IVW - Schriftenreihe Band 128
Institut für Verbundwerkstoffe GmbH - Kaiserslautern

Benedikt Hannemann

Multifunctional metal-carbon-fibre composites for damage tolerant and electrically conductive lightweight structures

Bibliografische Information Der Deutschen Bibliothek

Die Deutsche Bibliothek verzeichnet diese Publikation in der Deutschen Nationalbibliografie; detaillierte bibliografische Daten sind im Internet über <http://dnb.ddb.de> abrufbar.

Bibliographic information published by Die Deutsche Bibliothek

Die Deutsche Bibliothek lists this publication in the Deutsche Nationalbibliografie; detailed bibliographic data is available in the Internet at <http://dnb.ddb.de>.

Herausgeber: Institut für Verbundwerkstoffe GmbH
Prof. Dr.-Ing. Ulf Breuer
Erwin-Schrödinger-Straße
TU Kaiserslautern, Gebäude 58
67663 Kaiserslautern
http://www.ivw.uni-kl.de

Verlag: Institut für Verbundwerkstoffe GmbH

Druck: Technische Universität Kaiserslautern
ZBT – Abteilung Foto-Repro-Druck

D 386

Als Manuskript gedruckt. Printed in Germany.
ISSN 1615-021X
ISBN 978-3-944440-25-5

Multifunctional metal-carbon-fibre composites for damage tolerant and electrically conductive lightweight structures

Vom Fachbereich Maschinenbau und Verfahrenstechnik
der Technischen Universität Kaiserslautern
zur Verleihung des akademischen Grades

Doktor-Ingenieur (Dr.-Ing.)

genehmigte Dissertation

von Herrn
Dipl.-Ing. Benedikt Hannemann
aus Mainz

Tag der mündlichen Prüfung: 07.12.2017

Prüfungsvorsitzender:	Prof. Dr.-Ing. Joachim Hausmann
1. Berichterstatter:	Prof. Dr.-Ing. Ulf Paul Breuer
2. Berichterstatter:	Prof. Dr.-Ing. Gerhard Scharr
3. Berichterstatter:	Jun.-Prof. Dr.-Ing. Frank Balle

D 386

Vorwort

Die vorliegende Arbeit entstand im Rahmen meiner Tätigkeit als wissenschaftlicher Mitarbeiter an der Institut für Verbundwerkstoffe GmbH (IVW) in der Abteilung Bauteilentwicklung im Kompetenzfeld Crash und Energieabsorption.

Mein besonderer Dank gilt meinem Doktorvater Herrn Prof. Dr.-Ing. Ulf P. Breuer für die umfassende Betreuung und Unterstützung, die gewährten Freiräume bei der Gestaltung dieser Arbeit sowie für die Übernahme des Erstgutachtens. Außerdem danke ich Herrn Prof. Dr.-Ing. Gerhard Scharr vom Lehrstuhl für Konstruktionstechnik/Leichtbau der Universität Rostock sowie Herrn Prof. Dr.-Ing. Frank Balle vom Lehrstuhl für Werkstoffkunde der Technischen Universität Kaiserslautern für die freundliche Übernahme des Zweit- bzw. Drittgutachtens. Meinem Abteilungsleiter Herrn Prof. Dr.-Ing. Joachim Hausmann danke ich für seine Tätigkeit als Prüfungsvorsitzender.

Ferner gilt mein außerordentlicher Dank meinem Vorgesetzten Herrn Dr.-Ing. Sebastian Schmeer für die wissenschaftliche Betreuung meiner Arbeit. Sein Erfahrungsschatz sowie sein Engagement bei der Interpretation und Diskussion der erzielten Ergebnisse haben maßgeblich zum Gelingen dieser Arbeit und zur fachlichen Entwicklung meiner Person beigetragen.

Herrn Dipl.-Ing. Sebastian Backe vom Lehrstuhl für Werkstoffkunde der Technischen Universität Kaiserslautern danke ich für die konstruktive Zusammenarbeit im Rahmen des DFG-Projekts MCFK (BR 4262/2-1, BA 4073/6-1) und dessen Beiträge zur Messung des Ferritgehalts und der elektrischen Laminatleitfähigkeit.

Für die Unterstützung und Hinweise bei der Durchführung und Diskussion der Ultraschalluntersuchungen bedanke ich mich bei Herrn Prof. Dr.-Ing. Jens Schuster vom Institut für Kunststofftechnik Westpfalz der Hochschule Kaiserslautern.

Darüber hinaus bedanke ich mich bei der gesamten Belegschaft des IVW für die kollegiale Zusammenarbeit und die freundschaftliche Arbeitsatmosphäre. Besonders hervorheben möchte ich Yves Becker, Tobias Donhauser, Pia Eichert, Nora Feiden, Stefan Gabriel, Hermann Giertzsch, Werner Gölzer, Torsten Heydt, Alexander Huf, Benjamin Kelkel, Regina Köhne, Valentine Kessler, Janna Krummenacker, Nicole Motsch, Thomas Pfaff, Heidrun Plocharzik, Vitalij Popow, Jan Rehra, Thomas Rief,

Florian Rieger, David Scheliga, Ralf Schimmele, Florian Schimmer, Stefan Schmidt, Stefan Schmitt, Uwe Schmitt, Ralph Schneider, Petra Volk, Harald Weber und Torsten Weick. Auch den ehemaligen Kollegen Constantin Bauer, Marcel Bücker, Bernhard Helfrich, Michael Magin und Johannes Netz sei an dieser Stelle gedankt.

Den studentischen und wissenschaftlichen Hilfskräften Jonas Fischer, Frederik Oswald, Nils Oswald, Mario Sehnem und Fabian Wittkowski danke ich für deren tatkräftige Unterstützung bei der Materialfertigung.

Schließlich danke ich meiner Familie, die mir meine Ausbildung ermöglichte und mir durch ihre uneingeschränkte Unterstützung und Geduld den notwendigen Rückhalt beim Erstellen dieser Arbeit gab.

Oberwiesen, Dezember 2017

Contents

Abstract

Due to their superior weight-specific mechanical properties, carbon fibre epoxy composites (CFRP) are commonly used in aviation industry. However, their brittle failure behaviour limits the structural integrity and damage tolerance in case of impact (e.g. tool drop, bird strike, hail strike, ramp collision) or crash events. To ensure sufficient robustness, a minimum skin thickness is therefore prescribed for the fuselage, partially exceeding typical service load requirements from ground or flight manoeuvre load cases. A minimum skin thickness is also required for lightning strike protection purposes and to enable state-of-the-art bolted repair technology. Furthermore, the electrical conductivity of CFRP aircraft structures is insufficient for certain applications; additional metal components are necessary to provide electrical functionality (e.g. metal meshes on the outer skin for lightning strike protection, wires for electrical bonding and grounding, overbraiding of cables to provide electromagnetic shielding). The corresponding penalty weights compromise the lightweight potential that is actually given by the structural performance of CFRP over aluminium alloys.

Former research attempts tried to overcome these deficits by modifying the resin system (e.g. by addition of conductive particles or toughening agents) but could not prove sufficient enhancements. A novel holistic approach is the incorporation of highly conductive and ductile continuous metal fibres into CFRP. The basic idea of this hybrid material concept is to take advantage of both the electrical and mechanical capabilities of the integrated metal fibres in order to simultaneously improve the electrical conductivity and the damage tolerance of the composite. The increased density of the hybrid material is over-compensated by omitting the need for additional electrical system installation items and by the enhanced structural performance, enabling a reduction of the prescribed minimum skin thickness. Advantages over state-of-the-art fibre metal laminates mainly arise from design and processing technology aspects.

In this context, the present work focuses on analysing and optimising the structural and electrical performance of such hybrid composites with shares of metal fibres up to 20 vol.%. Bundles of soft-annealed austenitic steel or copper cladded low carbon steel fibres with filament diameters of 60 or 63 µm are considered. The fibre bundles

are distinguished by high elongation at break (32 %) and ultimate tensile strength (900 MPa) or high electrical conductivity (2.4×10^7 S/m). Comprehensive researches are carried out on the fibre bundles as well as on unidirectional and multiaxial laminates. Both hybrid composites with homogeneous and accumulated steel fibre arrangement are taken into account. Electrical in-plane conductivity, plain tensile behaviour, suitability for bolted joints as well as impact and perforation performance of the composite are analysed. Additionally, a novel non-destructive testing method based on measurement of deformation-induced phase transformation of the metastable austenitic steel fibres is discussed.

The outcome of the conductivity measurements verifies a correlation of the volume conductivity of the composite with the volume share and the specific electrical resistance of the incorporated metal fibres. Compared to conventional CFRP, the electrical conductivity in parallel to the fibre orientation can be increased by one to two orders of magnitude even for minor percentages of steel fibres. The analysis, however, also discloses the challenge of establishing a sufficient connection to the hybrid composite in order to entirely exploit its electrical conductivity.

In case of plain tensile load, the performance of the hybrid composite is essentially affected by the steel fibre-resin-adhesion as well as the laminate structure. Uniaxial hybrid laminates show brittle, singular failure behaviour. Exhaustive yielding of the embedded steel fibres is confined to the arising fracture gap. The high transverse stiffness of the isotropic metal fibres additionally intensifies strain magnification within the resin under transverse tensile load. This promotes (intralaminar) inter-fibre-failure at minor composite deformation. By contrast, multiaxial hybrid laminates exhibit distinctive damage evolution. After failure initiation, the steel fibres extensively yield and sustain the load-carrying capacity of angularly (e.g. ±45°) aligned CFRP plies. The overall material response is thus not only a simple superimposition but a complex interaction of the mechanical behaviour of the composite’s constituents. As a result of this post-damage performance, an ultimate elongation of over 11 % can be proven for the hybrid laminates analysed in this work. In this context, the influence of the steel fibre-resin adhesion on the failure behaviour of the hybrid composite is explicated by means of an analytical model. Long term exposure to corrosive media has no detrimental effect on the mechanical performance of stainless steel fibre reinforced composites. By trend, water uptake increases the maximum elongation at break of the hybrid laminate.

Moreover, the suitability of CFRP for bolted joints can partially be improved by the integration of steel fibres. While the bearing strength basically remains nearly unaffected, the bypass failure behaviour (ε_{max}: +363 %) as well as the head pull-through resistance ($E_{a,BPT}$: +81 %) can be enhanced. The improvements primarily concern the load-carrying capacity after failure initiation. Additionally, the integrated ductile steel fibres significantly increase the energy absorption capacity of the laminate in case of progressive bearing failure by up to 63 %.

However, the hybrid composite exhibits a sensitive low velocity/low mass impact behaviour. Compared to conventional CFRP, the damage threshold load of very thin hybrid laminates is lower, making them prone for delamination at minor, non-critical impact energies. At higher energy levels, however, the impact-induced delamination spreads less since most of the impact energy is absorbed by yielding of the ductile metal fibres instead of crack propagation. This structural advantage compared to CFRP gains in importance with increasing impact energy. The plastic deformation of the metastable austenitic steel fibres is accompanied by a phase transformation from paramagnetic γ-austenite to ferromagnetic α'-martensite. This change of the magnetic behaviour can be used to detect and evaluate impacts on the surface of the hybrid composite, which provides a simple non-destructive testing method. In case of low velocity/high mass impact, integration of ductile metal fibres into CFRP enables to address spacious areas of the laminate for energy absorption purposes. As a consequence, the perforation resistance of the hybrid composite is significantly enhanced; by addition of approximately 20 vol.% of stainless steel fibres, the perforation strength can be increased by 61 %, while the maximum energy absorption capacity rises by 194 %.

Kurzfassung

Kohlenstofffaserverstärkte Kunststoffe (CFK) sind aufgrund ihrer gewichtsspezifisch hervorragenden mechanischen Eigenschaften in Luftfahrtanwendungen weit verbreitet. Ihr sprödes Versagensverhalten begrenzt allerdings ihre Strukturintegrität und Schadenstoleranz gegenüber Schlagbeanspruchungen (z.B. Vogelschlag, Hagel, fallengelassenes Werkzeug) und im Versagensfall. Um eine ausreichende Robustheit sicherzustellen, ist daher eine Mindestwandstärke für die Primärstruktur vorgeschrieben, welche stellenweise jedoch Anforderungen an alle übrigen Gebrauchslasten aus Manövern am Boden oder in der Luft übersteigt. Eine Mindestwandstärke ist außerdem aus Gründen des Blitzschutzes und zur Gewährleistung gängiger, nietbasierter Reparaturverfahren erforderlich. Darüber hinaus weist der CFK-Rumpf keine ausreichende elektrische Leitfähigkeit auf. Zusätzliche Metallkomponenten sind erforderlich, um bestimmte elektrische Funktionen (Blitzschutz, Signaltransfer, elektromagnetische Abschirmung, Erdung u.a.) zu gewährleisten. Die damit einhergehenden Zusatzmassen schmälern den Gewichtsvorteil gegenüber Aluminium, welcher sich eigentlich aus der Verwendung von CFK als Strukturwerkstoff ergibt.

Untersuchungen, diesen Nachteilen gegenüber Metallen durch Modifikation des Harzsystems (bspw. durch Zugabe von leitfähigen oder zähmodifizierenden Partikeln) vollständig zu begegnen, konnten keine ausreichenden Verbesserungen belegen. Ein neuartiger Ansatz ist die Integration von besonders leitfähigen, hoch duktilen metallischen Endlosfasern in CFK. Die grundlegende Idee dieses Hybridkonzepts besteht darin, sowohl die elektrischen, als auch die mechanischen Eigenschaften der Metallfasern auszunutzen, um gleichzeitig die Schadenstoleranz und die elektrische Leitfähigkeit von CFK zu steigern. Die im Vergleich zu CFK höhere Dichte wird durch die eingesparten elektrischen Komponenten und die verbesserten mechanischen Eigenschaften des hybriden Verbundwerkstoffs kompensiert. Vorteile gegenüber Faser-Metall-Laminaten ergeben sich im Wesentlichen aus gestaltungs- und verarbeitungstechnischen Gründen.

Vor diesem Hintergrund beschäftigt sich die vorliegende Arbeit mit der Untersuchung und Optimierung der mechanischen und elektrischen Eigenschaften solcher hybrider Faserverbundwerkstoffe mit Metallfaservolumenanteilen bis etwa 20 vol.%. Dabei

werden Bündel aus hochlegierten austenitischen bzw. kupferbeschichteten niedriglegierten Stahlfasern mit Filamentdurchmessern von 60 bzw. 63 µm berücksichtigt. Diese zeichnen sich durch ihre hohe Bruchdehnung (32 %) bei gleichzeitig hoher Festigkeit (900 MPa) bzw. durch ihre hohe elektrische Leitfähigkeit (2.4×10^7 S/m) aus. Grundlegende Untersuchungen werden sowohl an den einzelnen Faserbündeln als auch an uni- und multiaxialen (Hybrid-) Laminaten durchgeführt. Hybridwerkstoffe mit homogener und lokal konzentrierter Stahlfaseranordnung werden analysiert. Die durchgeführten Untersuchungen zielen darauf ab, die elektrische Leitfähigkeit, das Zugverhalten, die Nieteignung sowie das Impakt- und Durchstoßverhaltens der Hybridlaminate zu analysieren. Darüber hinaus wird ein zerstörungsfreies Testverfahren basierend auf der Erfassung der Veränderungen des magnetischen Verhaltens der Stahlfasern infolge verformungsinduzierter Gefügeumwandlung diskutiert.

Die Leitfähigkeitsmessungen verifizieren eine lineare Abhängigkeit der elektrischen Leitfähigkeit von dem Volumenanteil und von dem spezifischen elektrischen Widerstand der integrierten Metallfasern. Verglichen mit CFK lässt sich die Leitfähigkeit in Faserrichtung bereits mit geringen Stahlfaservolumenanteilen um ein bis zwei Größenordnungen steigern. Die Messungen offenbaren allerdings auch die Herausforderung, eine hinreichend gute Kontaktierung zu dem Hybridmaterial herzustellen, um dessen elektrische Leitfähigkeit voll auszuschöpfen.

Im Falle von reiner Zugbeanspruchung wird das Verhalten des Hybridwerkstoffs wesentlich von der Laminatstruktur und der Metallfaser-Matrix-Anhaftung bestimmt. So weisen unidirektional verstärkte Hybridlaminate ein sprödes, singuläres Versagensverhalten auf. Ausgeprägt plastisches Fließen der Metallfasern ist auf den Bereich des entstehenden Bruchspalts begrenzt. Außerdem intensiviert die hohe Quersteifigkeit der isotropen Metallfasern die Dehnungsüberhöhung im Bereich der Matrix, wodurch die Bildung von Zwischenfaserbrüchen unter Querzugbeanspruchung begünstigt wird. Im Gegensatz dazu kann bei multiaxialen Hybridlaminaten ein ausgeprägtes Nachversagen nachgewiesen werden. Nach Versagensinitiierung sind die (noch intakten) Metallfasern in der Lage, plastisch zu fließen, Zwischenfaserbrüche zu überbücken und die Tragfähigkeit von unter einem Winkel (z. B. ±45°) angeordneten CFK-Lagen zu erhalten. Die Materialantwort ist folglich keine reine Überlagerung, sondern eine komplexe Interaktion des mechanischen Verhaltens der einzelnen Verbundbestandteile. Basierend auf dem

erzielten Nachversagen lässt sich mit den in dieser Arbeit untersuchten Hybridlaminaten eine Bruchdehnung von über 11 % nachweisen. Der Einfluss der Stahlfaser-Matrix-Anhaftung auf das Versagensverhalten wird dabei anhand eines analytischen Modells erläutert. Eine Auslagerung in korrosiven Medien hat keinen nennenswerten Einfluss auf die mechanischen Eigenschaften der edelstahlfaserverstärkten Hybridlaminate. Tendenziell bewirkt eine Wasseraufnahme eine Zunahme der maximalen Bruchdehnung der Hybridlaminate.

Durch die Integration von Metallfasern lässt sich ferner die Eignung von CFK für gebolzte Fügeverbindungen verbessern. Während die Lochleibungsfestigkeit nahezu unverändert bleibt, werden das Wangenzugverhalten (ε_{max}: +363 %) und der Kopfdurchzugwiderstand ($E_{a,BPT}$: +81 %) verbessert. Die Verbesserungen betreffen dabei vor allem das mechanische Verhalten nach Versagensinitiierung. Darüber hinaus lässt sich die Energieabsorption im Falle progressiver Lochleibungsbeanspruchung um bis zu 63 % steigern.

Allerdings ist der Hybridwerkstoff bei sehr geringen Laminatdicken empfindlicher gegenüber niederenergetischer Impaktbeanspruchung. Im Vergleich zu CFK sinkt die kritische Lastschwelle, ab der Versagen im Laminat initiiert wird. Impaktinduzierte Delaminationen breiten sich mit steigender Impaktenergie jedoch weniger stark aus, da Energie durch lokales Fließen der Stahlfasern anstelle von Risswachstum absorbiert wird. Dieser Vorteil gegenüber CFK nimmt mit zunehmender Impaktenergie zu. Die plastische Deformation der metastabilen Austenitfasern bewirkt eine verformungsinduzierte Phasenumwandlung von paramagnetischem γ-Austenit zu ferromagnetischem α‘-Martensit. Diese Veränderung des magnetischen Verhaltens kann zur zerstörungsfreien Schadensdetektion herangezogen werden. Im Falle von Penetrationsbeanspruchung ermöglicht die Integration der Metallfasern in CFK weitreichende Bereiche des Laminats zur Energieabsorption einzubeziehen, wodurch der Durchstoßwiderstand deutlich gesteigert wird. Bei Hybridlaminaten mit einem Stahlfaseranteil von etwa 20 vol.% steigt die maximale Durchstoßkraft um 61 %, während sich die maximale Energieabsorption um 194 % steigern lässt.

Glossary

Abbreviations

AFP	automated fibre placement
AITM	Airbus Industry test method
ATL	automated tape laying
bcc	body-centred cubic
BPT	bolt pull-through
BVID	barely visible impact damage
CAI	compression after impact
CCA	copper clad aluminium
CCS	copper clad steel
CFRP	carbon fibre reinforced polymer
CNC	computer numeric controlled
CNT	carbon nanotube
COA	centre of area
CPT	cured ply thickness
CTE	coefficient of thermal expansion
CVD	chemical vapour deposition
DC	direct current
DEA	dielectric analysis
DET	detailed inspection
DIC	digital image correlation
DSC	differential scanning calorimetry
DTL	damage threshold load
ECF	expanded copper foil
EDX	energy dispersive X-ray
EMF	expanded metal foil
EPT	electrical percolation threshold
ESI	electrical system installation
ESN	electrical structure network
FAW	fibre areal weight
fcc	face-centred cubic
FEA	finite element analysis
FFT	fast Fourier transform

FHT	filled hole tension
FML	fibre metal laminate
FZI	fracture zone of influence
GFRP	glass fibre reinforced polymer
GLARE®	glass laminate aluminium reinforced epoxy
GMR	giant magnetoresistance
GMT	glass mat reinforced thermoplastic
GNP	graphene nanoplatelet
hcp	hexagonal close-packed
HVI	high velocity impact
IWWF	inter-woven wire fabric
LOM	light optical microscopy
LSP	lightning strike protection
LVI	low velocity impact
MEMS	microelectromechanical
MFRP	metal fibre reinforced polymer
MWCNT	multi-walled carbon nanotube
MWM	meandering winding magnetometer
NCF	non-crimp fabric
OES	optical emission spectroscopy
PAN	polyacrylonitrile
PAW	ply areal weight
pax	passenger
PES	polyethylene succinate
PLB	pin load bearing
PR	penetration resistance
PT	plain tension
PTC	positive temperature coefficient
PVD	physical vapour deposition
RAW	resin areal weight
RVE	representative volume element
SCFRP	steel and carbon fibre reinforced polymer
SEA	specific energy absorption
SEM	scanning electron microscopy
SFRP	steel fibre reinforced polymer

SMA	shape memory alloy
SQUID	superconducting quantum interference device
SWCNT	single-walled carbon nanotube
TIG	tungsten inert gas
TMDSC	temperature-modulated differential scanning calorimetry
UD	unidirectional
VID	visible impact damage
WLI	white light interferometry
XRF	X-ray fluorescence

Latin symbols

a	µm	apothem of a fibre bundle's circumscribing hexagon
A	mm^2	cross-section of the electrical conductor
A	dB	amplitude
A_d	mm^2	delamination area
CPT	µm	cured ply thickness
CTE	K^{-1}	coefficient of thermal expansion
d	µm	diameter of a fibre bundle's circumscribing circle
d_f	µm	filament diameter
d_i	mm	indentation depth
DTL	N	damage threshold load
E	GPa	modulus of elasticity
e_a	J/mm^3	specific absorbed energy
E_a	J	absorbed energy
$E_{a,Fmax}$	J	energy absorbed up to maximum load
$E_{a,max}$	J	total absorbed energy
E_i	J	impact energy
EI	N/mm^2	bending stiffness
E_t	GPa	tangent modulus
f	-	element-specific reduction factor
F	N	load
FAW	g/m^2	fibre areal weight
f_d	-	delamination factor
F_{fail}	N	load at ultimate failure
f_{FZI}	%	relative length of the fracture zone of influence

F_{int}	N	load at failure initiation
F_{max}	N	maximum load
f_w	mm/rev	winding feed rate
F_{yield}	N	load at onset of yielding
G	GPa	modulus of shear
G	S	electrical conductance
G	J	Helmholtz free energy
G_{IIc}	J/mm^2	mode II fracture toughness
I	A	electrical current
l	m	length of the electrical conductor
l_{FZI}	mm	length of the fracture zone of influence
m	mg, kg	mass
m_r	mg	mass of a reference object
M	Nm	bending moment
M_d	°C	maximum temperature for deformation-induced martensite formation
M_{d30}	°C	temperature at which 50 vol.% of austenite is transformed to martensite when subjected to a true strain of 30 %
M_f	°C	martensite finish temperature
m_i	kg	impact mass
M_s	°C	martensite start temperature
M_s^σ	°C	temperature at which the mechanical stress equates to the yield strength of austenite
n	-	number of plies
n_f	-	number of filaments per bundle
p	bar	pressure
PAW	g/m^2	ply areal weight
$\dot{q}$	W/g	specific heat flow
Q	J	heat
R	Ω	electrical resistance
R	-	ratio of the absorbed energy after to the absorbed energy before maximum load
RAW	g/m^2	resin areal weight
R_C	Ω	electrical resistance of contact clips
R_c	Ω	electrical contact resistance

R_i	Ω	internal electrical resistance
R_L	Ω	electrical resistance of lead wires
R_{LC}	Ω	electrical resistance of lead wires and contact clips
R_m	Ω	electrical material resistance
s	mm	displacement
s_{Fint}	mm	displacement at failure initiation
s_{Fmax}	mm	displacement at maximum load
s_{int}	mm	displacement at failure initiation
s_{max}	mm	displacement at ultimate failure
s_p	mm	displacement at which the load is fallen to half of its maximum
s_{yield}	mm	displacement at onset of yielding
T	°C	temperature
$\dot{T}$	°C/min	heat-up or cooling rate
t	s	time
t	mm	laminate thickness
t	mm	specimen thickness
T_0	°C	reference temperature
T_0	K	equilibrium temperature
t_{bleed}	mm	laminate thickness reduction due to resin bleed
T_g	°C	glass transition temperature
U	V	electrical potential
U	V	standard electrode potential
v	m/s	velocity
V	mm^3	volume
v_i	m/s	impact velocity
w	mm	specimen width
y	-	year
z	mm	out-of-plane deformation

Greek symbols

α	°	orientation angle
α_{T0}	K^{-1}	resistance temperature coefficient
$\dot{\varepsilon}$	s^{-1}	nominal strain rate
ε	%	nominal strain
ε_{FZI}	%	nominal strain within the fracture zone of influence

ε_{int}	%	nominal strain at failure initiation
ε_{max}	%	nominal strain at ultimate failure
ε_{r}	%	residual nominal strain
ε_{yield}	%	nominal strain at onset of yielding
$\varepsilon_{\sigma max}$	%	nominal strain at maximum nominal stress, uniform elongation
η	Pas	dynamic viscosity
κ	S/m	specific electrical conductance
λ	tex	linear density
v	Ωcm	ion viscosity
v	-	Poisson ratio
ξ	vol.%	volume fraction of magnetic phase
ρ	g/cm^3	density
ρ^*	Ωm	specific electrical resistance
σ	MPa	nominal stress
σ	MPa	nominal bearing stress
σ_{max}	MPa	nominal tensile strength
σ_{max}	MPa	nominal bearing strength
σ_{mean}	MPa	mean nominal bearing stress
$\sigma_{p0.2}$	MPa	nominal offset yield strength
σ_{r}	MPa	residual nominal compressive strength
$\sigma_{\varepsilon max}$	MPa	nominal stress at ultimate failure
$\sigma_{\varepsilon max,CF}$	MPa	nominal stress at a nominal strain of $\varepsilon = \varepsilon_{max,CF}$
τ_{max}	MPa	interlaminar shear strength
φ	vol.%	volume fraction
ψ	wt.%	mass fraction

Indices

0	initial state
1,2,3	spatial direction (1 = fibre orientation) of an orthogonal coordinate system
c	calculated
C	carbon fibre
CF	carbon fibre
CFRP	carbon fibre reinforced polymer
crit	critical

dry	measured at air
ESI	electrical system installation
F	fibre
f	filament
fail	ultimate failure
FUS	fuselage
FZI	fracture zone of influence
i	index
int	failure initiation
LSP	lightning strike protection
m	measured
max	maximum
mech	mechanical
min	minimum
n	normal
R	resin
r	residual
ref	reference object
S	steel fibre
SF	steel fibre
SFRP	steel fibre reinforced polymer
therm	thermal
trig	trigger
w	water (immersion liquid)
wet	measured while submerged in immersion liquid
yield	onset of yielding
α’	α’-martensite
γ	γ-austenite

Mathematical symbols

∫	integral
Δ	difference
π	Ludolph's constant, π ≈ 3.1415

1 Introduction

Despite increasing requirements by customers, operators and authorities, the relative weight of aircraft primary structures could continuously be decreased to today's level of approximately 25 kg per passenger and 1000 km of range, figure 1.1 (left). The necessary weight savings have been achieved by improved load prediction, new design principles, elaborated design and sizing methods, improved manufacturing methods and application of enhanced materials. In this context, artificial composite technology has been continuously and progressively introduced to aeronautics over the past decades, figure 1.1 (right). By now, passenger aircraft of the latest generation such as Boeing B787 or Airbus A350 consist of more than 50 wt.% of composite materials ("full composite airframe"), in which carbon fibre reinforced polymers (CFRP) play a predominant role. CFRP offers not only superior weight-specific mechanical properties (high strength, high stiffness, low density) but also excellent fatigue behaviour ("no crack growth design concept") and pronounced media and corrosion resistance. [1]

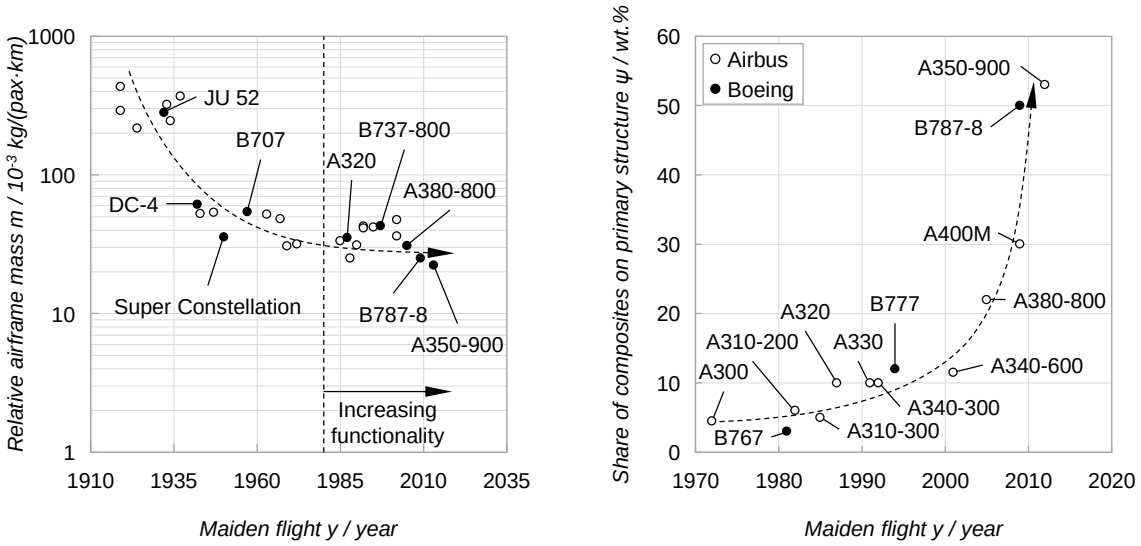

Figure 1.1 Development of (left) relative airframe mass (without engines) per passenger and 1000 km of range [2] and (right) proportion of composite materials on aircraft primary structures [3-5]

However, the lightweight potential of CFRP over modern aluminium alloys is still severely limited due to its relatively poor electrical conductivity. Different to aluminium structures, additional metal components are necessary to provide electrical

functionality to the aircraft primary structure, for example expanded metal foils on the outer skin for lightning strike protection, wires for electrical bonding and grounding or overbraiding of cables to provide sufficient electromagnetic shielding, figure 1.2.

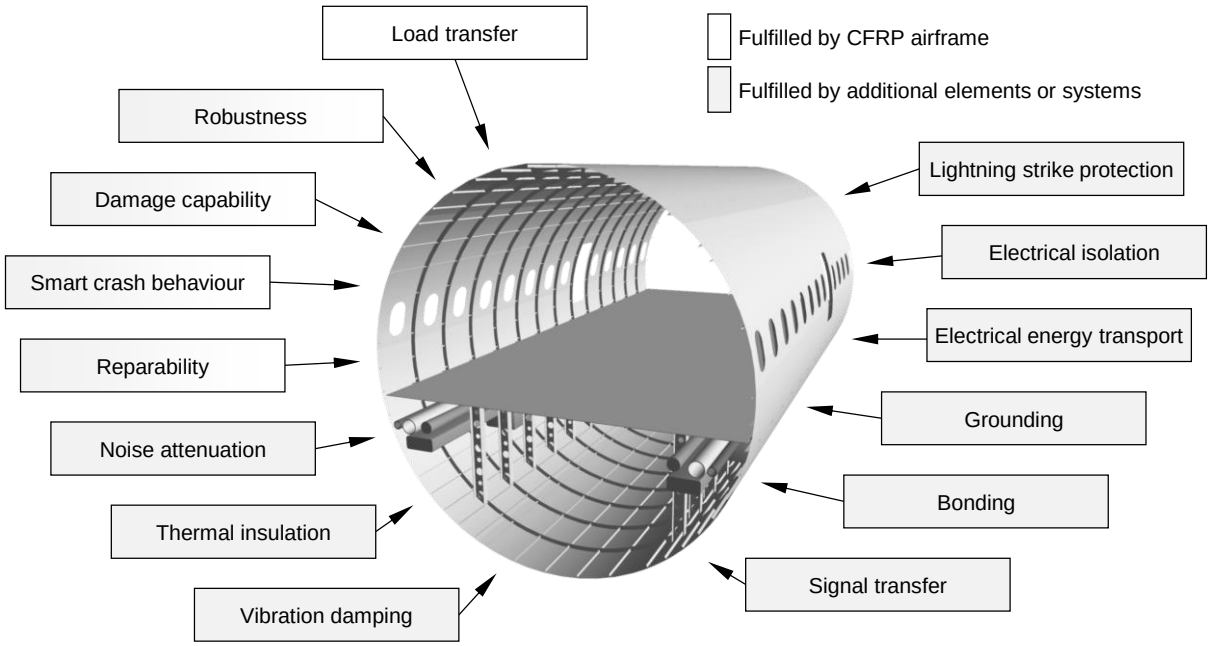

Figure 1.2 Assignment of tasks for a CFRP aircraft primary structure [1]

Moreover, the brittle failure behaviour of CFRP limits the damage tolerance and structural integrity in case of impact (e.g. tool drop, bird strike, hail strike, ramp collision) or crash events. To ensure adequate robustness, a minimum skin thickness is therefore prescribed for the fuselage, partially exceeding service load requirements from ground or flight manoeuvre load cases. A minimum skin thickness is also necessary to enable state-of-the-art structural bolted repair technology[1] (considering for example fastener pull-through resistance) and to guarantee structural integrity in case of lightning strike. Both the electrical systems and the minimum skin thickness are associated with additional weight, compromising the lightweight potential that is actually given by the application of CFRP in aircraft structures. In order to contribute to further mass reduction of next-generation aircraft, today's challenge is therefore to modify CFRP to provide the required electrical functionality for system installation purposes and to overcome the limiting minimum thickness criterion for monolithic structures in terms of damage tolerance and structural bolted joints. [1, 6]

[1] Adhesive joints, which offer a weight advantage over bolted joints, are state-of-the-art for cosmetic but not for structural repair. To date, the main challenge for the application of structural bonding repair is given by (non-destructive) proof testing of the load capacity required by the airworthiness authorities. [1]

1.1 Scope of work

Against this background, the present work develops and analyses the concept of a multifunctional hybrid composite consisting of highly conductive and ductile continuous metal fibres incorporated into CFRP. The basic idea of this hybrid material concept is to take advantage of both the electrical and load-bearing capabilities of the embedded metal fibres in order to synchronously improve the electrical conductivity as well as the damage tolerance of the composite. The density increase due to the metal fibre incorporation is over-compensated by omitting the

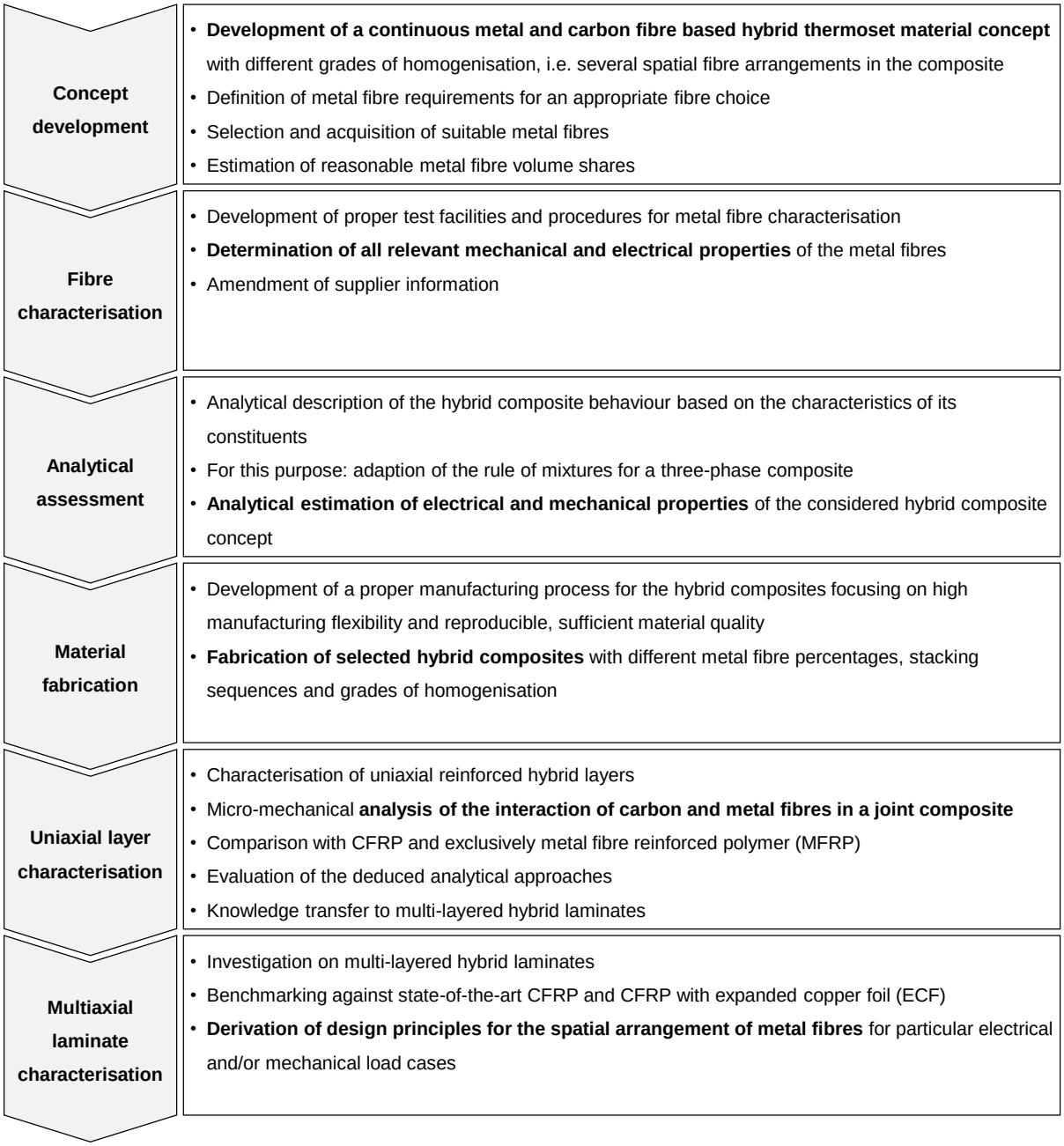

Figure 1.3 Procedural method and objectives of the present work

need for additional electrical system installation (ESI) items and by the enhanced structural performance, enabling a reduction of the prescribed minimum skin thickness. For this purpose, the content structure of this work follows the procedure given in figure 1.3. The procedural method aims to gradually develop various hybridisation concepts, elaborate the theoretical potential of the introduced hybrid material, experimentally prove its basic feasibility and functioning, understand the interrelation of highly ductile metal fibres with brittle carbon fibres in a joint composite and derive design recommendations for an optimal spatial arrangement of the metal fibres with regard to an improved electrical conductivity, bolted joint suitability and impact performance. Also, the study aims to highlight novel features in terms of damage monitoring and process enhancements which can be achieved by the integration of metal fibres into CFRP.

2 CFRP aircraft structures

The superior mechanical properties of CFRP have contributed to its increasing share in modern airframe design. Substantial parts of the aircraft primary structure (e.g. tailplane, pressurised fuselage or wing structure) of the latest generation of civil aircraft are made of this artificial composite. This chapter aims to provide a brief overview of state-of-the-art properties of CFRP and to discuss some important challenges that come with its application in aviation industry.

2.1 Mechanical properties

Carbon fibres are the predominant type of continuous reinforcing fibre for aircraft primary structures [1]. Depending on the precursor and the graphitisation process, they are commercially available in a wide range of properties. Increasing alignment of the graphite planes in parallel to the fibre axis (cf. molecular structure of carbon fibres) enhances the longitudinal tensile modulus and strength of the carbon filaments but impedes their properties in transverse direction, figure 2.1. The aligned arrangement of the graphite planes along a predominant direction (i.e. the fibre axis) consequently causes a distinctive anisotropy of the properties of carbon fibres. [7]

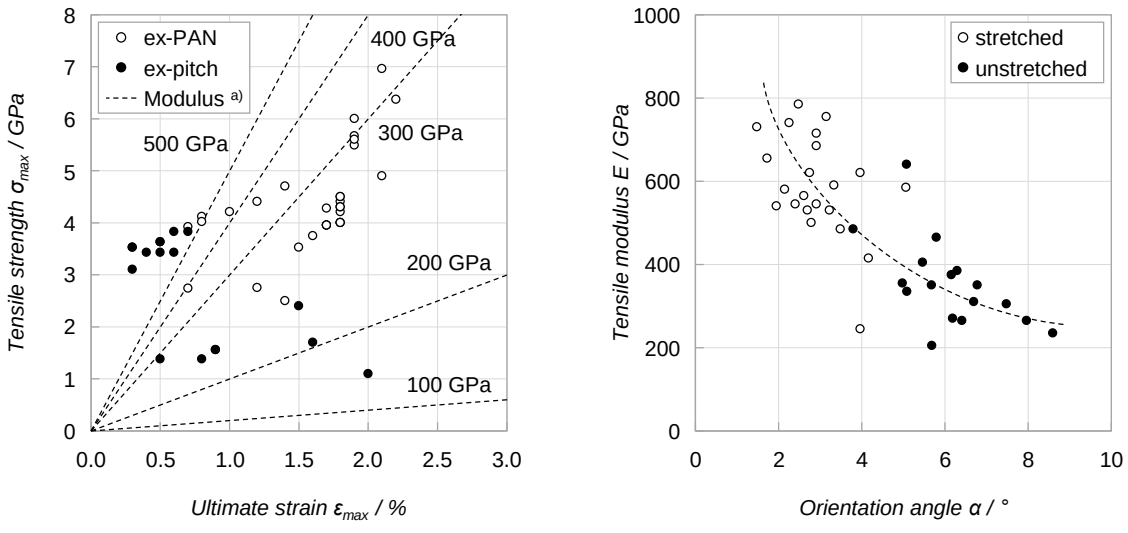

a) assuming a linear stress-strain relation

Figure 2.1 (left) Properties of commercially available continuous carbon fibres and (right) modulus of elasticity in dependence on the orientation angle of the graphite planes relatively to the longitudinal fibre axis [7]

In principle, carbon fibres are characterised by high tensile stiffness (155 to 920 GPa) and ultimate tensile strength (1380 to 7000 MPa) at low density (1.73 to 2.19 g/cm^3). Their stress-strain relation is nearly linear with a slight stiffness increase of approximately 10 % immediately before failure [7]. By trend, polyacrylnitrile-based (ex-PAN) carbon fibres feature better tensile properties than mineral oil-based (ex-pitch) carbon fibres. The minor elongation at break (0.3 to 2.2 %) as well as the brittle failure behaviour, however, can be detrimental in terms of fail-safe (load redistribution) or damage tolerance requirements and must be considered as drawback compared to ductile metals. Moreover, carbon fibres exhibit minor negative coefficient of thermal expansion (CTE) in the range of -1.5 to -0.1 × 10^{-6} K^{-1} along the fibre orientation, while the transverse CTE is positive. The mean diameter of carbon filaments varies between 4 and 11 µm.

The majority of load-carrying CFRP parts of the primary structure are based on epoxy resins. Beneficial characteristics include the ability to adapt the properties of the resin for particular application, thermal stability (upper dry service temperature of 150 °C for 180 °C curing systems) and safety of use due to low volatiles [8]. Due to the minor shrinkage of epoxy resins (2 to 5 % [7]), residual stresses after curing are less pronounced, which positively affects the fibre-resin-interface. The distinct adhesion of epoxy resins in particular to ex-PAN carbon fibres enhances the transverse tensile strength and fracture toughness of CFRP. In addition, CFRP is distinguished by excellent fatigue behaviour. As long as the maximum strain of a cyclically loaded CFRP structure remains below a certain value (0.3 to 0.4 %, depending on the specific material system [1]), cracks within the laminate, such as impact-induced delamination, do not propagate; the laminate can then be considered as fatigue endurable, which is a key advantage over aluminium alloys. Other beneficial characteristics of CFRP arise from the ability to manufacture large, complex shaped, integral components and the utilisation of laminate anisotropy for tailored strength, stiffness or stability design. Moreover, CFRP provides long-term stability against various aggressive media commonly encountered in aircraft usage (e.g. seawater, Skydrol (hydraulic fluid), kerosene, de-icing liquids or methyl-ethyl-ketone) due to the inertness of the carbon fibres and most epoxy resins. However, depending on the molecular structure and the degree of cure, epoxy resins tend to absorb a considerable amount of moisture (4 to 7 wt.% of water [8]), which must be taken into account in terms of corrosion of potential metal fibre reinforcement.

Most CFRP parts in civil aviation are manufactured from thermoset prepreg with resin contents of 35 to 40 wt.%. Typical values for the areal weight of applied unidirectional (UD) prepreg tapes are between 206 and 446 g/m^2, which corresponds to a cured ply thickness (CPT) of approximately 125 to 250 µm (depending on the resin loss during the curing process). However, multiaxial laminates built-up by thin layers typically exhibit superior mechanical properties compared to corresponding laminates consisting of thick individual plies. [1, 7]

2.2 Electrical conductivity

Depending on the precursor and the graphitisation process, carbon fibres offer a specific electrical resistance in parallel to the fibre orientation in the range of 0.2 to 2.8 × 10^{-5} Ωm. Ex-PAN carbon fibres tend to exhibit higher electrical conductivity than ex-pitch carbon fibres. Besides, the electrical conductivity generally rises with increasing alignment of the graphite planes in parallel to the fibre axis, i.e. with rising tensile modulus of elasticity, figure 2.2 (left). Application of metal coatings (e.g. copper, nickel, silver) enables reduction of the specific electrical resistance of carbon fibres by up to two orders of magnitude to the level of stainless steel fibres [9-12]. The coating can be applied e.g. by physical vapour deposition (PVD), chemical vapour deposition (CVD), electroplating or the colloid spray method. However, the coating process usually involves a degradation of the fibre strength and strain at failure. Moreover, coated carbon fibres are heavier and significantly more expensive (factor 5), table 2.1.

Table 2.1 Exemplary comparison of the properties of standard and nickel coated ex-PAN carbon fibres [12, 13]

Type	d_f / µm	ρ / g/cm^3	E / GPa	σ_{max} / MPa	ε_{max} / %	ρ* / Ωm
Toho Tenax HTS40	7.0	1.77	240	4300	1.8	1.6 × 10^{-5}
Toho Tenax HTS40 MC [a)]	7.5	2.70	230	2900	1.3	7.5 × 10^{-7}

[a)] nickel coated carbon fibre, 0.25 µm coating thickness

By contrast, unmodified epoxy resins exhibit dielectric behaviour with a volume resistivity in the range of 10^7 to 10^{15} Ωm [14]. The isolating effect of the resin causes a distinctive anisotropy of the electrical conductivity of unidirectional reinforced CFRP. Depending on the amount of filament-filament contacts, the ratio of the

specific conductance in parallel to transverse to the fibre orientation varies between 50 and 2000 [15]. The number of filament contacts again depends on the fibre volume fraction, fibre misalignments and fibre undulations. Still, even in parallel to the fibre orientation, the specific conductance of conventional CFRP is about one to three orders of magnitude lower compared to common metal alloys or fibre metal laminates (FML), e.g. GLARE® (glass laminate aluminium reinforced epoxy), table 2.2.

Table 2.2 Specific electrical resistance of various materials [13, 16-18]

Property	Copper Cu-0FE	Aluminium 7075-T6	GLARE® 4B-4/3-0.4 [a)]	Nickel Ni 99.2	Carbon steel 1.0338	Stainless steel 1.4301	Titanium Ti-6Al-4V	CFRP UD [b)]
ρ* / Ωm	1.7×10^{-8}	5.1×10^{-8}	6.4×10^{-8}	9.0×10^{-8}	1.5×10^{-7}	6.5×10^{-7}	1.7×10^{-6}	2.7×10^{-5}

[a)] GLARE® with three GFRP layers (CPT = 0.127 mm) and four layers of aluminium (2024-T3, t = 0.4 mm, ρ* = 5.2×10^{-8} Ωm)

[b)] epoxy based CFRP comprising 60 vol.% of HTS40 fibres, conductivity in parallel to the fibre orientation

Several attempts have been made in the past to optimise the electrical conductivity of CFRP by modification of the polymer matrix system or the fibre-resin-interphase, e.g. by addition of conductive particles, such as carbon black [19], carbon nanotubes (CNT), chopped or milled short carbon fibres [20], graphene or metallic nanowires [21]. The modification basically aims to enhance the electrical conductivity of the polymer and/or to network the conductive carbon fibres. However, a minimum amount of particles (electrical percolation threshold, EPT) must be added to the

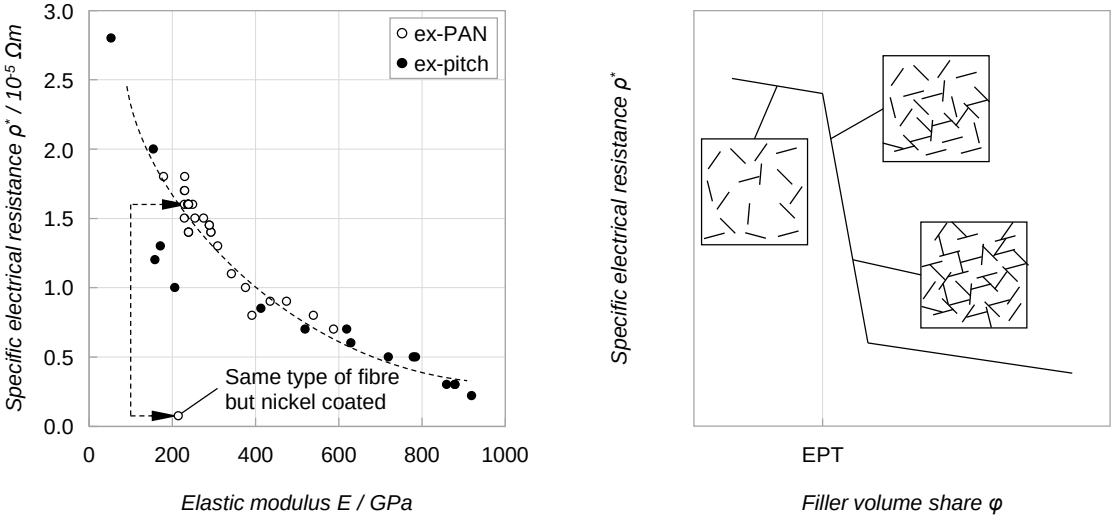

Figure 2.2 (left) Correlation of mechanical and electrical properties of commercially available carbon fibres and (right) schematic of the specific electrical resistance of modified epoxy resin as a function of the filler content [22]

polymer in order to generate a continuous conductive path throughout the composite. Further increase of the filler content erratically improves the electrical conductivity as more conductive pathways are created, figure 2.2 (right). In particular particles with large aspect ratio, random alignment and high intrinsic conductivity, as for example carbon nanotubes, enable high composite conductivity at low EPT value. [20, 22, 23]

Due to the large number of existing types of CNTs and processing methods, a wide range of electrical conductivity and EPT values for CNT-modified epoxy resins can be found in literature [14]. Sandler et al. [24] reported a specific conductance of 2 S/m for epoxy resin with 0.01 wt.% of aligned multi-walled CNTs (MWCNT), while Li et al. [25] verified an electrical conductivity of 10 S/m for a share of 15 wt.% of single-walled CNTs (SWCNT). Kim et al. [26] improved the electrical out-of-plane conductivity of CFRP by 144 % for 2 wt.% of SWCNTs. In many cases, the CNT-modification of the polymer additionally improves its mechanical and thermal properties, such as fracture toughness (cf. chapter 2.4) or thermal conductivity [14]. The addition of CNTs, however, also involves a gain of the resin viscosity in fused condition, which impedes its impregnation behaviour [27, 28]. Improvements by means of integration of graphene nanoplatelets (GNP) have been demonstrated by Qin et al. [29], who increased the electrical out-of-plane conductivity of CFRP by 165 % compared to the unmodified system. Wajid et al. [30] measured an increase of seven orders of magnitude for 0.46 wt.% graphene-modified epoxy resin compared to the baseline sample. Difficulties in case of GNP, however, arise with regard to a sufficient dispersion of the platelets in the composite. In this context, several studies reported synergetic effects when combining MWCNTs and graphene platelets [31, 32]. The MWCNTs prevent aggregation of the graphene platelets and additionally bridge intermediate gaps. A different approach to improve both the electrical in- and out-of-plane conductivity of CFRP consists of the application of silver coated knitting yarn and/or silver nanowires loaded interleaves (“fourth generation prepreg”) [33-35].

Despite the improvements achieved, a sufficient level of electrical conductivity of CFRP, which would guarantee electrical function integration similar to that of aluminium alloys or GLARE® structures, could not be demonstrated so far. In order to ensure proper functioning of the aircraft system, metallic elements already present in the pressurised zone of the composite fuselage are therefore joined to create an electrically conductive network, figure 2.3. This network must, however, be

complemented by additional metal components (e.g. wires, junctions, straps, raceways) to provide electrical continuity. Furthermore, additional metal parts must be added to the composite airframe in order to ensure failure current return, equipment bonding as well as lightning strike and electro-static discharge protection, hence to prevent loss of mechanical performance of CFRP due to unintended current injection (Joule heating) [36].

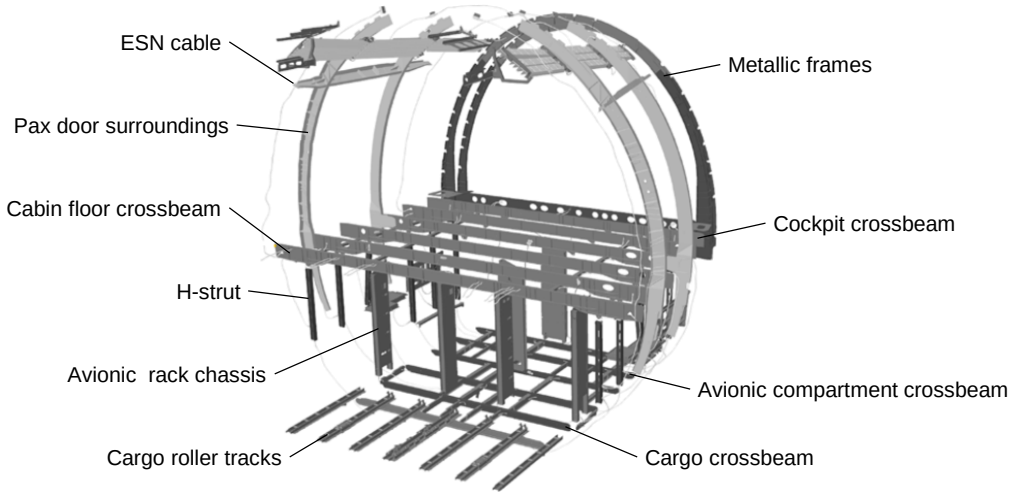

Figure 2.3 Elements of the electrical structure network (ESN) of an Airbus A350 [37]

2.3 Lightning strike protection

Lightning initially hits an aircraft at one spot and exits from another. Those spots are usually extremities of the aircraft, such as nose or wing tips. Since the aircraft flies more than its own length within the lifetime of most flashes, the entry point will change as the flash reattaches to other spots aft of the initial entry point (swept strokes). The exit point may do the same if the initial exit spot is at a forward position of the aircraft. Thus, for any flash there might be several entry or exit points. In general, there is no measureable difference in attachment point behaviour between metal and CFRP fuselages. [38-40]

Lightning strike causes damage to the aircraft structure due to mechanical and thermo-mechanical load. Heat introduction is given by the lightning plasma channel (direct heat flow, heat radiation) and indirectly by resistive heating due to the lightning current. In case of CFRP, Joule heating is of similar significance as direct plasma heat flow due to the poor electrical conductivity of the composite. The significant

heat-up of the material leads to material degradation in the form of resin embrittlement, resin vaporisation and, as a result, breakdown of the fibre-resin-adhesion. The temperature increase additionally causes mechanical load due to thermal expansion of the restrained structure. Moreover, mechanical loads arise from the shock wave caused by supersonic expansion of the plasma channel and from magnetic force effects. Secondary mechanical loads might occur due to explosive release of gas entrapped in the substrate (e.g. developing from the resin burn). Damages after lightning strike include fibre fracture, inter-fibre-failure, delamination and/or puncture (burn-through) of the laminate. In principle, the failure pattern is similar to that after mechanical impact. The most severe damages occur at the lightning attachment points, where the thermal and electrical load density is the highest. Additional threats are, among others, given by fuel vapour ignition caused by arcing and sparking at bonds, hinges and joints or by electromagnetic interferences with aircraft systems (e.g. electronics, communications). [38-43]

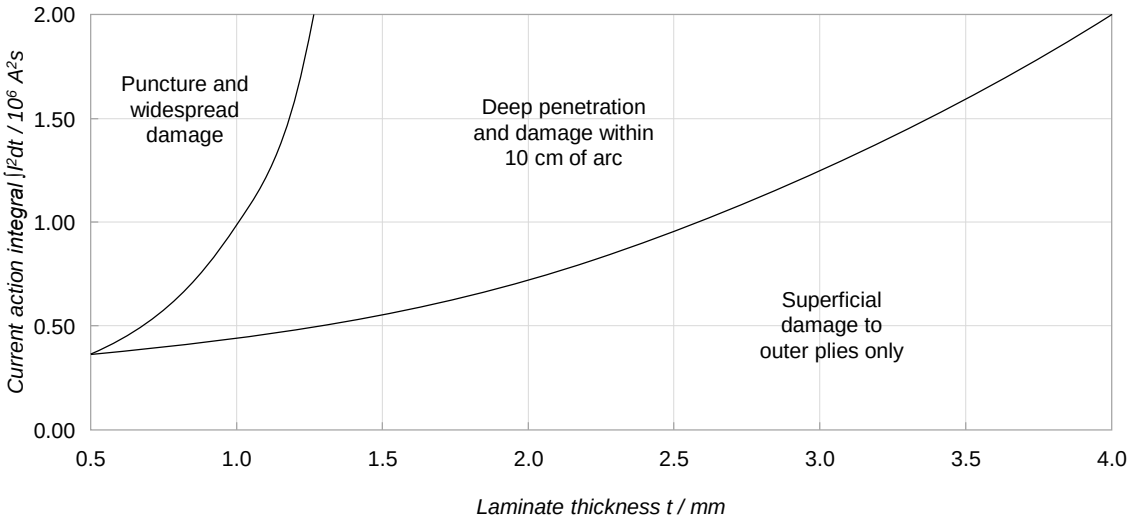

Figure 2.4 Approximate visible damage of unpainted CFRP in dependence on the laminate thickness and the lightning current introduced [44]

As demonstrated by various experimental and numerical studies, the extent of damage of unprotected CFRP after artificial lightning strike increases with rising lightning current load and/or decreasing laminate thickness, figure 2.4 [45-47]. Moreover, as shown by Feraboli et al. [41, 43], damages tend to be intensified and spread throughout the entire laminate height in the vicinity of filled holes (i.e. bolted joints). Due to the impact-like damage pattern, lightning strike deteriorates the load-bearing performance of unprotected CFRP structures similar as those after

mechanical impact (cf. chapter 2.4) and includes, for example, a significant decrease in laminate compressive strength [41, 43, 46, 48].

Composite parts in lightning strike prone areas must therefore comprise appropriate lightning strike protection (LSP). Current standard LSP measure is a metal film on the outer surface of CFRP structures. The metal film primarily aims to provide a continuous low resistance path[2] across the aircraft surface in order to reduce the amount of Joule resistive heating and to avoid electrical current flow inside the composite material [36]. Most common are expanded metal foils (EMF), which are fabricated by a milling process that perforates and stretches a solid metal foil. EMF thickness varies between 50 and 250 µm, while the areal weight ranges from 65 to 815 g/m^2 [49, 50]. The mesh structure of EMF promotes dielectric breakdown of overlaying primers and paints at multiplicity of points in the vicinity of the lightning attachment point. This divides the lightning arc into many conductive filaments of low intensity and thus disperses the lightning energy over a wider area [40]. The principles of woven wire meshes are very similar to those of EMF. The wires can either be woven to a separate fabric or co-woven with carbon fibres (inter-woven wire fabric, IWWF). The diameter of the mesh wires typically varies between 50 and 100 µm. Compared to the corresponding EMF with identical areal weight, the effective electrical in-plane conductivity is, however, significantly smaller due to the contact resistance at the intersection of the wires. Moreover, IWWF tend to provoke cracking of the laminate due to the differential CTE and/or explosion of the metallic wires caused by the lightning current loads. Solid, unperforated foils provide similar protection as EMF. The foils, however, do not encourage arc root dispersion. Disadvantages additionally arise due to the limited drapability, the difficulties in bonding to the substrate and the risk of blow-ups in case of resin vaporisation underneath. Another possibility for LSP consists of thin metal coatings, which can be applied by means of physical vapour deposition, thermal spraying or spark plasma sintering. The thickness of sprayed metal layers ranges from 100 to 200 µm. Most of the metallic LSP measures are based on soft-annealed aluminium or copper alloys. Aluminium provides superior weight-specific electrical conductivity but requires additional isolating interlayers (e.g. made of glass fibre reinforced polymers, GFRP) to ensure separation to the CFRP substrate and thus to prevent contact corrosion.

[2] There is no general value for the minimum electrical conductivity (e.g. required by authorities) which would ensure an acceptable extent of lightning strike damage [34, 38].

The selection of the appropriate LSP measure depends on various issues, such as lightning probability, protection effectiveness, electrochemical compatibility, additional weight, system costs, part geometry, part location (cf. lightning strike zones of an aircraft) or reparability. [39, 40, 51]

In the recent past, numerous studies have been carried out aiming to reduce the impact of lightning strike on CFRP structures by improving the electrical conductivity of CFRP primarily by modification of the polymer resin (cf. chapter 2.2) [11, 34, 38, 39, 52, 53]. Numerical and experimental test results indicate considerable diminution of the extent of damage of unprotected CFRP structures; the electrical conductivities achieved are, however, still insufficient for stand-alone LSP solutions [34, 39].

2.4 Impact behaviour

During their lifetime, aeronautical CFRP components are exposed to different kind of foreign body impact events, such as tool drop, bird impact, hail strike, runway debris, tire shrapnel or engine fragments. Potential impact velocities range over several orders of magnitude with very different consequences for the affected structure. In principle, low and high velocity impact events must be differed, figure 2.5.

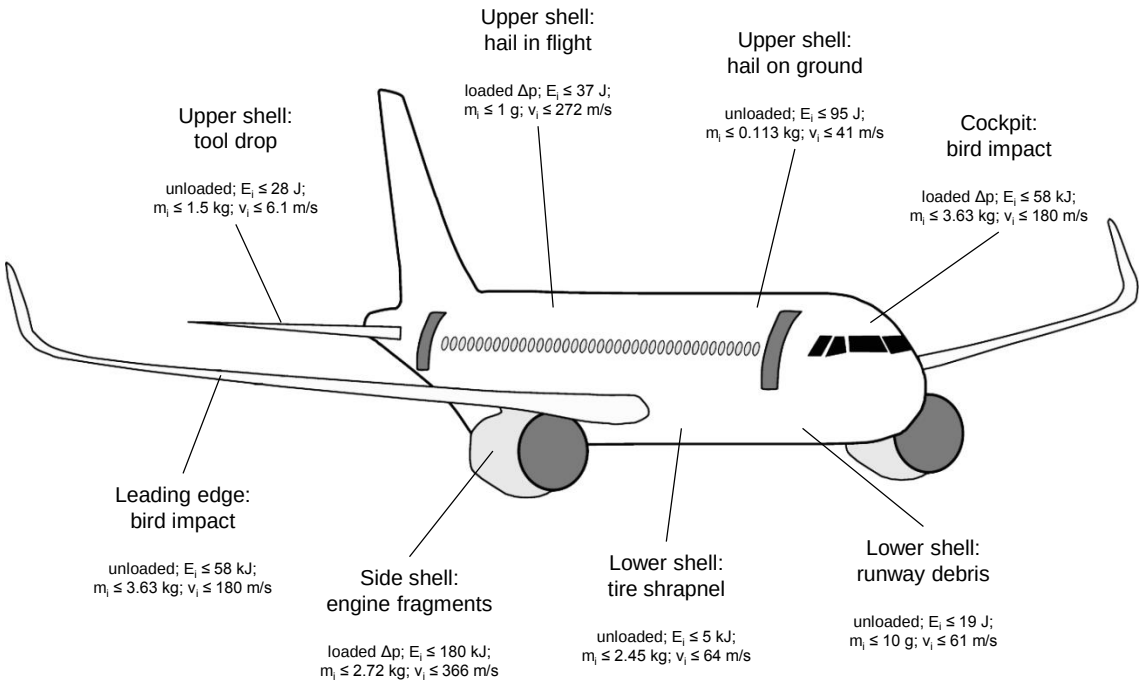

Figure 2.5 Potential impact events for aircraft structures [1]

Low velocity impacts (LVI) are characterised by a global structure response. The deformation mode is similar to that under static load. Impact energy is dissipated over extensive areas of the material. By contrast, high velocity impacts (HVI) are related to a localised structure response causing significant compressive stresses prior to any (elastic) deflection. As a result, damage is spatially confined but more pronounced. For a given impact energy, HVI loading therefore represents the more detrimental form of loading condition and provokes larger material degradation. The transition of LVI to HVI is considered to be in the range of 20 to 70 m/s. [54-57]

LVI damages basically result from superimposition of local laminate indentation and global (stiffness-dependent) structure bending. The induced contact force causes local impression (matrix crushing, fibre breakage) as well as interlaminar shear stresses, which promote initiation of delamination. The bending stresses cause fibre breakage and matrix cracking (transverse tensile failure) in particular at the impact-averted side of the laminate, which again facilitates formation of delamination, back face chipping and fibre peeling. [57, 58] In case of thick (rigid) laminates, high localised contact stresses below the impactor outweigh the bending stresses. The corresponding shear stresses lead to formation of matrix cracks, provoking delamination at ply interfaces, which again induces matrix cracking in adjacent plies. This leads to a pine-tree pattern as the size of the damage increases from the impacted surface, figure 2.6 (left). In case of thin (flexible) laminates, damages are primarily caused by laminate deflection. The bending stresses cause transverse tensile failure of the impact-averted outer layer of the laminate, inducing delamination

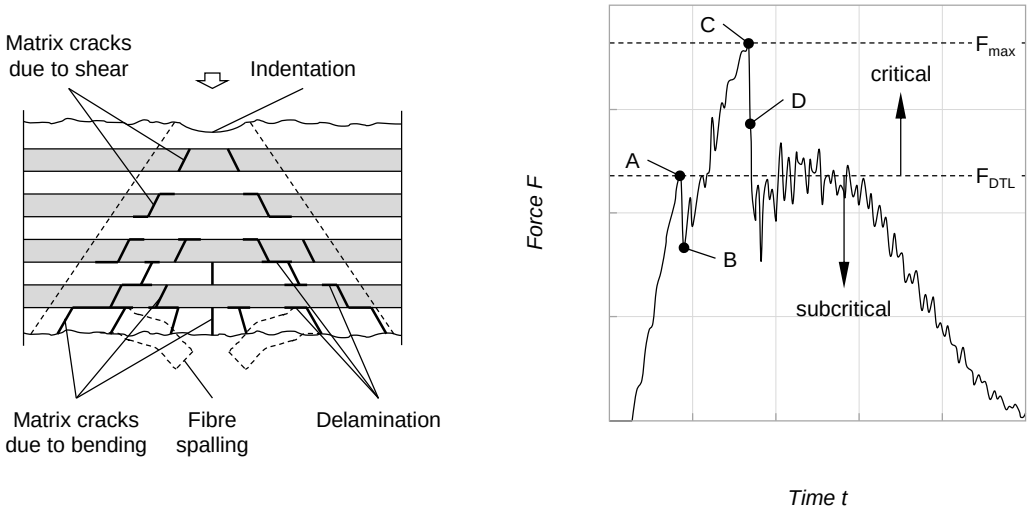

Figure 2.6 Typical (left) damage modes and (right) force history trace of a LVI [59]

at the adjacent interface. The failure initiation is followed by a sequence of matrix cracks and delamination that propagates upwards, resulting in a reversed pin-tree pattern. [57, 60] High modulus and/or high-tenacity reinforcing fibres facilitate initiation and propagation of delamination, representing the main energy absorbing mechanism. By contrast, fibres with minor strength or high permanent energy absorption capacity (e.g. by means of plastic deformation) allow energy absorption by means of deformation and fibre fracture, reducing the extent of delamination to a smaller (circular) area in the vicinity of the impact location.

Damage to the laminate, however, only occurs when exceeding a critical contact force (damage threshold load, DTL), figure 2.6 (right). This threshold load indicates onset of delamination. The subsequent distinctive load drop (A-B) is attributed to sudden, unstable propagation of delamination throughout the laminate, causing a significant loss of flexural stiffness. Typically, the more pronounced the following oscillations of the force history trace (cyclic process of damage propagation and arrest), the more impact energy is dissipated in the form of delamination instead of fibre breakage and consequently the greater is the resulting delamination area. A second characteristic load drop (C-D) at higher value of load might appear, indicating pronounced tensile fibre failure at the impact-averted side of the laminate. In this case, the delamination area arising is typically smaller since a considerable amount of energy is dissipated by means of fibre breakage. An analytical estimation of the critical contact load is given by Davies and Zhan, eq. 2.1, validated by a series of experimental studies. [59, 61]

$$\mathrm{DTL} = \sqrt{\frac{8 \cdot \pi^2 \cdot \mathrm{E} \cdot \mathrm{t}^3}{9 \cdot (1 - \nu^2)} \cdot \mathrm{G_{IIc}}} \qquad \text{(Eq. 2.1)}$$

According to this theoretical approach, the DTL primarily depends on the laminate thickness t but also on the mode II fracture toughness G_{IIc} of the composite, the elastic modulus E and the Poisson ratio v of the laminate. Conversely, the threshold load has been shown to be independent of the impact energy and seems also to be independent of the in-plane load of the structure during impact.

The impact-induced damages significantly reduce the load-carrying capability of the structure. Generally, the compressive strength is the most affected property with loss of up to 70 to 75 % [56, 62]. The strength reduction is usually attributed to a number of potential failure mechanisms. Local buckling of the delaminated sub-laminates

promotes unstable delamination growth perpendicular to the load direction and, as a result, premature global buckling. Latter is additionally facilitated by asymmetric loading due to impact-induced residual deformation of the structure and by the lower buckling stability of the (thin) sub-laminates compared to the (thick) pristine laminate. Moreover, compressive failure of reinforcing fibres aligned in load direction might appear, starting at pre-existing damages close to the impact location and spreading transverse to the load direction. [56, 62] The post-impact compressive performance of CFRP therefore primarily depends on the mode I and mode II fracture toughness of the composite. Reduction of the tensile properties is attributed to impact-induced fibre breakage. In principle, the extent of damage in terms of indentation depth and projected size of damage area increases with rising impact energy. In addition, compressive pre-load during impact causes an increase in structure deflection and consequently more pronounced defects [63]. The damage extent can be assessed by different non-destructive testing methods, such as ultrasonic testing, computed tomography, thermal imaging, shearography or electrical impedance tomography.

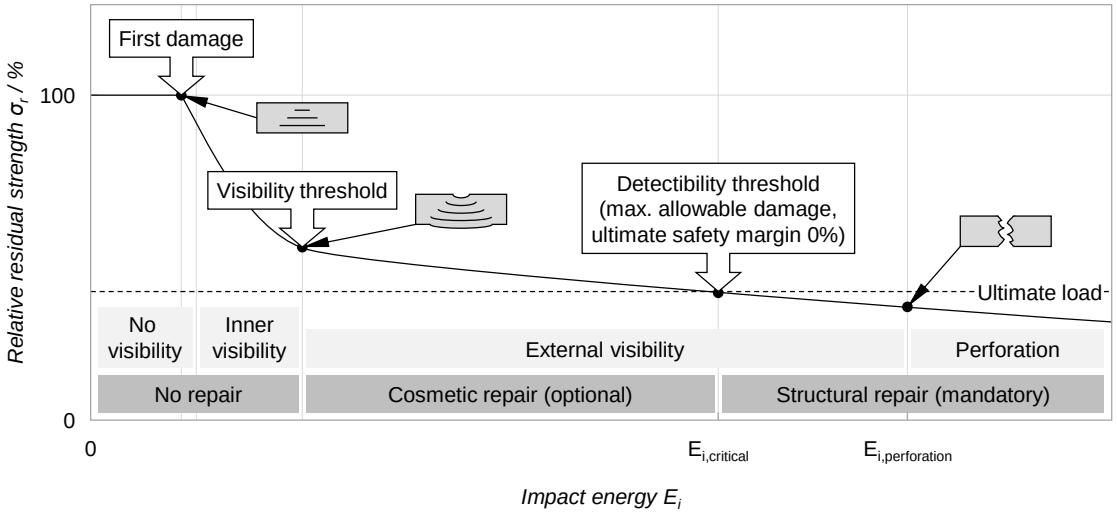

Figure 2.7 Residual strength of a CFRP structure as a function of the impact energy [1]

Figure 2.7 illustrates the residual strength of a CFRP structure as a function of the impact energy. For minor impact events, damages do not appear and the residual strength remains unaffected. If the impact energy increases, damages (intra- and interlaminar inter-fibre-failure) arise inside the laminate (inner visibility), which are, however, not visible from the outside. As a consequence of the internal damages, the residual strength of the structure decreases. At a certain level of impact energy,

permanent dents remain on the CFRP surface (external visibility). As long as the residual strength capability of the CFRP structure is above ultimate load (1.5 times of limit load), these impact damages are classified as barely visible impact damages (BVID). Cosmetic repair is possible but not required. The detectability threshold is reached at impact energy levels at which the residual strength of the structure falls below ultimate load. At this point, structural repair is mandatory and appropriate laminate design must ensure that the dent depth on the CFRP surface at the impact location is large enough to be detected during visual (scheduled) inspection (VID). A typical indentation depth for the VID criterion is 0.3 mm. Further increase of the impact energy causes perforation of the composite structure.

Structural improvements of the absolute residual compressive strength are basically feasible by increasing the laminate thickness. As demonstrated by Stavropoulos and Papanicolaou [64], the compressive performance can be further enhanced if the increase in laminate thickness results from in increase of ply thickness instead of an increased number of plies. Moreover, the impact damage tolerance of monolithic thin-walled CFRP structures has gradually been improved by the introduction of polymer toughening agents (“second generation prepreg”). Dissolvable thermoplastic polymers, such as polyethersulphone and polyetherimide, were introduced in epoxy matrix systems in different ways, enabling substantial improvements of fracture toughness. Another development are interleaf prepregs (“third generation prepreg”), which additionally consist of a thin film of thermoplastic particles on their top, figure 2.8. These particles are insolvable in the epoxy resin system and retain a constant

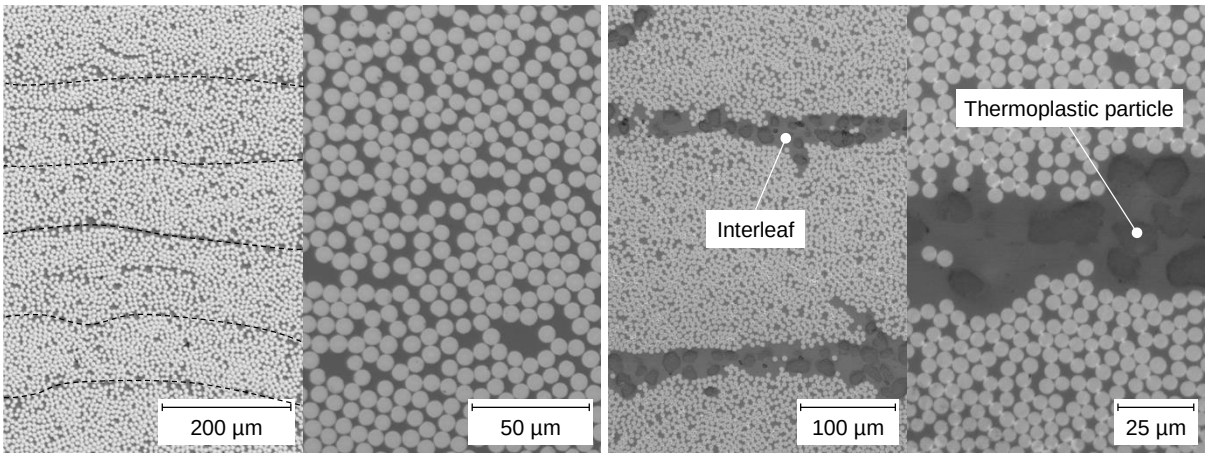

Figure 2.8 CFRP prepreg of (left) second (977-2/HTS) and (right) third generation with interleaf (M21E/IMA) in comparison

gap between the individual prepreg layers of the cured laminate. The propagation of initiated cracks is inhibited by the particles itself and by a hackling mechanism. Toughened resins are, however, usually 5 to 10 times more expensive than unmodified resins. [35, 65] Comprehensive researches on the modification of epoxy resins and the influence of the neat resin properties (e.g mode II fracture toughness, strain at failure) on the impact performance of CFRP tapes or non-crimp fabrics is given by Gilliot [66].

Further improvements of the fracture toughness of CFRP are feasible by incorporation of carbon nanoparticles, such as CNT or graphene. Numerous experimental studies in this regard can be found in literature. Detailed surveys of experimental studies carried out are provided by Domun et al. [67] or Spitalsky et al. [14]. Basically, CNTs act as toughening material by bridging the lamina interfaces [68]. However, beyond a certain filler content, CNTs aggregate easily and act as a defect, contributing to stress concentrations and weakening of the composite. Homogeneous dispersion of CNTs throughout the resin during processing is therefore essential yet very challenging for the performance of the composite.

In addition to modification of the resin or the fibre-resin-interface, enhancements of the impact tolerance of CFRP laminates can be achieved by out-of-plane reinforcement, e.g. z-pinning. The z-pins (diameter 0.15 to 1.00 mm), typically made of metal wires (e.g. titanium) or pultruded composite rods, can be inserted into uncured prepreg tapes or dry fabrics, either normal or at an off-axis angle to the laminate surface [69]. They are used at volume contents between 0.5 and 5 % [8]. As experimentally demonstrated, z-pinning can significantly improve the in-plane shear strength, interlaminar fracture toughness and finally the impact damage resistance of CFRP laminates [69-73]. Freitas et al. [74] showed that the amount of impact damage experienced by carbon/epoxy composites is reduced by 30 % to 50 % by means of z-pinning. Moreover, z-pinning increases the resistance of the composite to crack propagation caused by cyclic interlaminar stress loading [8, 75]. In principle, the improved delamination resistance results from a bridging effect of the z-pins, which exert a closure traction force that lowers the tensile strain acting on the crack tip [65]. Out-of-plane reinforcement of CFRP laminates can also be achieved by three-dimensional fibre architectures [65]. Commonly used techniques are weaving, braiding, knitting, stitching and tufting. However, those techniques can only be applied to dry fabrics and are therefore limited in application in aviation industry.

Through-thickness reinforcements are, however, typically associated with a degradation of static and cyclic in-plane properties of the laminate (especially tensile and compression strength), mainly due to lateral displacement of the in-plane fibres and thus local deviations of the ideal fibre orientation (deviation up to 25° [8]). In addition, in-plane fibres might be damaged or broken during the introduction of the out-of-plane reinforcement. The degradation is particularly pronounced in case of composites with high and ultra-high modulus reinforcing carbon fibres. Through-thickness reinforcements are not state-of-the-art for primary airframe series solution today. [65, 70, 76-79]

2.5 Bolted joints

Mechanical fastening represents the main joining technology for composite elements in aircraft application. Bolted joining is well-established and provides advantages in terms of reliability, automated installation, detachability and inspectability. However, the inevitable boreholes considerably lower the strength of the laminate due to interruption or deviation of the reinforcing fibres, reduction of the cross-sectional area and stress concentration (notch effect) at the borehole edge. Moreover, the anisotropic, brittle performance of CFRP causes complex fracture behaviour with a wide variety of failure modes, which all have to be accounted in order to create an optimal joint design. The main failure modes of bolted CFRP joints are depicted in figure 2.9, exemplarily for a single-lap joint.

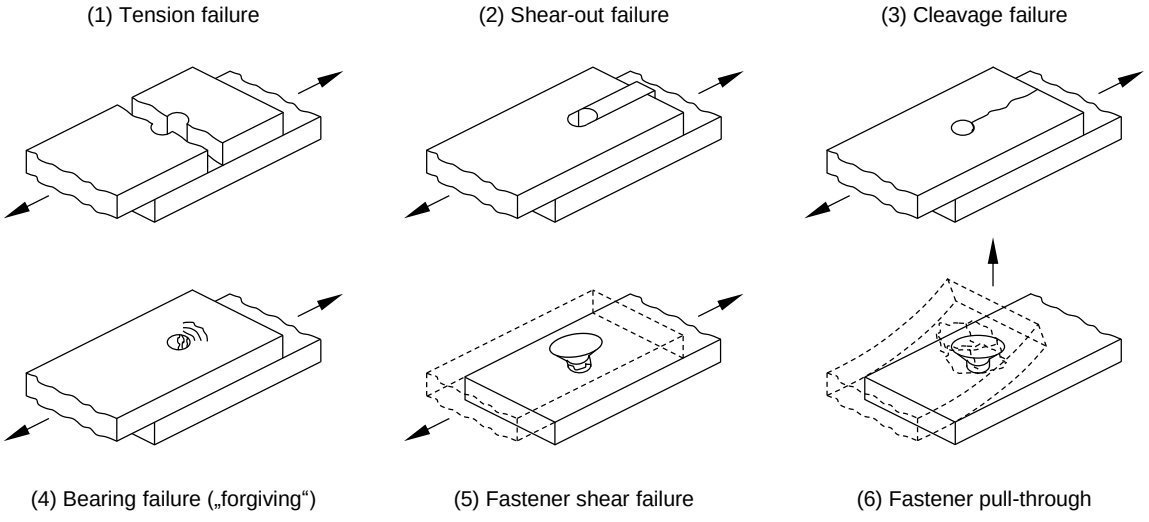

Figure 2.9 Typical failure modes of bolted composite joints [80]

Tension failure is likely if the edge distance of the fastener is too small or in case of laminates with an insufficient amount of reinforcing fibres in parallel to the load direction. This failure mode typically originates at the borehole due to local stress magnification. Shear-out failure is promoted by too little edge spacing of the fastener or by laminate design with insufficient shear strength, i.e. excessive share of fibres aligned in load direct. Cleavage failure occurs if the transverse laminate strength is too small (insufficient amount of fibres in ±45° and 90° relatively to the load direction). This failure mode is additionally promoted by a tight press fit of the fastener. Bearing failure indicates a balanced laminate design and is usually the desired failure mode. Exceeding the bearing strength causes local stiffness degradation of the laminate by means of fibre shear buckling, intralaminar inter-fibre-failure or delamination in front of the bolt, which again leads to a diminution of local stress peaks and load rearrangement. Unlike the other failure modes, bearing failure prevents sudden separation of the join partners. Fastener shear failure occurs in case of an under-dimensioned fastener (shaft) diameter. Fastener pull-through is likely if the laminate thickness, i.e. the cylindrical height of the fastener hole, is too small or if the ratio of hole diameter to laminate thickness is too big. Fasteners with (aerodynamically beneficial) countersunk heads[3] are more susceptible to pull-through failure than fasteners with protruding head due to the higher contact pressure underneath the fastener head. In addition, countersunk bolts increase the bearing stress in the shaft area since the conical fastener head transfers a significantly lower amount of bearing stress than the cylindrical shaft. [7, 8]

In order to prevent complete separation of the join partners and thus to ensure fail-safe behaviour, the laminate design must promote bearing failure. In addition to local thickening of the laminate, a laminate structure with fibres in 0° and ±45° relatively to the load direction is recommended for this purpose. The 0° fibres are used to counter the bearing stress, while the fibres orientated in ±45° prevent cleavage and shear-out failure. According to experimental investigations, the optimum proportion of the fibres aligned in load direction is 50 %. Part of the ±45° fibres is typically replaced by fibres orientated in 90°. A favourable laminate structure is (0/±45/90) (50 %/40 %/10 %) [7].

[3] Countersunk heads typically exhibit a cone angle of 100° and a head diameter of 1.6 or 2 times the shaft diameter. This “tension type” is beneficial in terms of head pull-through due the minor contact pressure underneath the fastener head. However, the cone angle significantly lowers the shaft length and thus increases the bearing stress. For join connections primarily exhibited to tensile load, countersunk heads with a cone angle of 140° (“shear type”) are to be preferred. Such fastener provides larger shaft length but the same head diameter (e.g. to ensure a certain preload). [7]

Such laminate stacking sequence, however, might not be the primary choice for the design of the structure regarding service loads. The application of countersunk heads additionally requires a minimum laminate thickness in order to prevent fastener pull-through and to ensure a minimum shaft length. Considering bolted repair requirements (with countersunk heads) for the primary aircraft structure, such laminate design must be provided to the entire fuselage skin. Structural joining thus represents an essential design driver for the basic laminate design and might cause significant penalty weight to the CFRP fuselage due to the minimum laminate thickness prescribed. [1, 6, 7]

Besides an adaption of the laminate thickness and design, various concepts have been developed in the past in order to improve the joint efficiency of thermoset CFRP structures. A promising approach to increase the bearing strength entails local hybridisation by means of thin metal foils. The foils are embedded into the composite by gradually replacing the weakest composite plies. Recent studies include titanium and austenitic steel sheets [81, 82]. Titanium is characterised by high weight-specific strength and stiffness, relatively low CTE mismatch and excellent galvanic compatibility to carbon fibres, whereas austenitic steel features high absolute strength and stiffness and low material costs but also higher CTE mismatch and weight. In principle, those fibre metal laminates take advantage of the isotropic properties of metals foils to simultaneously increase the bearing, shear and notched strength of the laminate. A comprehensive overview on this topic is given by Camanho and Fink [83]. Disadvantages arise in terms of manufacturing effort; the thin metal sheets are difficult to handle and require complex pre-treatment to guarantee reliable adhesion to adjacent composite plies [84, 85]. A similar concept has been investigated by Bosbach et al. [86], who replaced the solid foils by (permeable) metallic woven mesh. The investigation proves an increase of the bearing strength by 15 %.

Due to the ease of integration and the superior weight specific performance, progressive bearing failure of bolted joints particularly suit for structural integrated energy absorption purposes. The crushing zone in front of the bolt is characterised by local compression load. According to Farley and Jones [87], four main failure modes can be differed: transverse shearing, laminate bending, brittle fracturing and local buckling, figure 2.10.

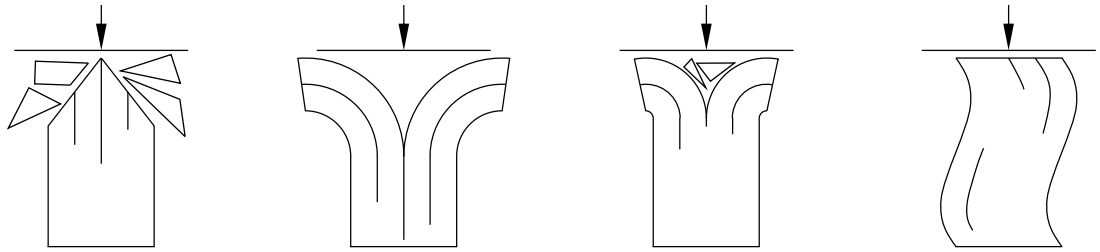

Figure 2.10 Crushing modes of fibre reinforced composites under compression load [88]

Transverse shearing is characterised by one or multiple short inter- and intralaminar cracks, which form discrete laminate bundles. The cracks propagate until the edges of the bundles are crushed, forming a wedge-shaped cross-section. Besides crack growth, the main energy absorbing mechanism is fracturing of the laminate bundles. Laminate bending is characterised by pronounced inter- or intralaminar cracking. The laminate bundles show extensive bending deformation but do not fail instantly. Crack growth is thus the principal energy absorbing mechanism. Additionally, friction between the laminate bundles as well as the bundles and the bolt contributes to energy absorption. Brittle fracturing represents a combination of both transverse shearing and laminate bending. The crack length is significantly smaller than in case of the laminate bending mode. Laminate bundles thus exhibit some bending but can break near their base. Subsequently, load is redistributed within the material and the cyclic process of crack growth, laminate bundle bending and fracture is repeated. The progressive bending deformation of the laminate bundles is additionally facilitated by the wedge caused by fragments and abrasion in the centre of the laminate. Local buckling mainly occurs to (quasi-) ductile composites. Energy is absorbed by means of plastic deformation of the reinforcing fibres and the resin as well as cracking and delamination caused by interlaminar shear stress at the buckles. A comprehensive study on the bearing mode absorber is given by Bergmann [88]; the investigation indicates an advantage of brittle over ductile reinforcing fibres with regard to the weight-specific energy absorption (SEA) capacity. SEA values of 155 J/g could be demonstrated. Ductile fibres, by contrast, enable to address larger areas of the composite material for energy absorption mechanisms and thus facilitate higher absolute energy absorption capacity.

2.6 Future challenges

Considering the application of CFRP in aviation industry, challenges result from insufficient electrical conductivity, brittle failure behaviour, susceptibility to impact loading and limited suitability for bolted joints. The specific characteristics of CFRP lead to a minimum skin thickness criterion, which is driven by countersunk fastener installation (baseline design, repair concept), robustness (demonstrating ultimate load capability for the aircraft primary structure in presence of non-visible damages), hail impact and lightning strike protection [6]. With today's epoxy based prepreg, a minimum skin thickness of approximately 1.625 mm can be achieved [1, 6]. Moreover, the insufficient electrical conductivity of CFRP laminates requires additional metallic components (e.g. wires, metallic measures for LSP) in order to ensure electrical functionality. Both, the minimum skin thickness and the metal parts for electrical purposes cause additional weight to the aircraft structure, compromising the lightweight potential that is actually given by the application of CFRP as structure material. Former research attempts tried to overcome these deficits by modifying the resin system (e.g. by addition of conductive particles or toughening agents) but could not prove sufficient, holistic and economic enhancements. Against this background, today's challenge is to efficiently modify CFRP in order to provide the required electrical functionality for system installation purposes and to overcome the limiting minimum thickness criterion for damage tolerance.

3 Hybridisation concept

The basic idea of combining two different types of reinforcing fibres in a single composite is to merge their individual strengths and to alleviate certain disadvantageous of the composite, figure 3.1.

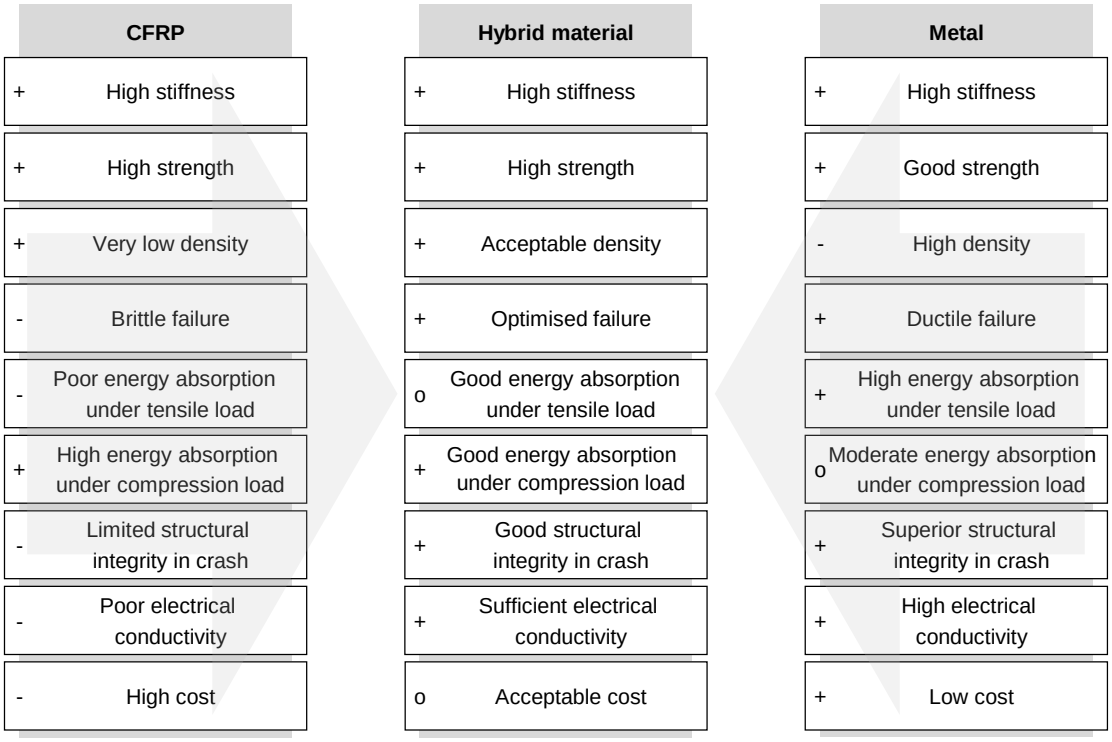

Figure 3.1 Beneficial properties of a hybrid composite by combination of the individual strengths of CFRP and metal

As introduced in the previous chapter, CFRP is distinguished by superior weight specific mechanical properties, such as high stiffness, high tensile strength and high energy absorption capacity under compression load. Drawbacks, however, arise in terms of damage tolerance and structural integrity in particular under tensile or impact load, suitability for bolted joints as well as electrical conductivity. By contrast, metals typically offer excellent electrical conductivity and superior failure performance under both tensile and compression load. In case of overload, their deformability enables load redistribution, hence fail-safe behaviour. Compared to CFRP, the main disadvantages of metals are usually their higher density and worse mechanical and fatigue properties. The integration of electrically conductive and ductile continuous metal fibres into CFRP aims to combine the beneficial properties of both materials in a joint composite and is a promising new approach to composite multifunctionality.

3.1 Metal reinforced composites

Fibre-metal-laminates are among the best known hybrid materials. GLARE® comprises alternating layers of aluminium and GFRP. The thickness of the applied aluminium sheets (e.g. AA2024-T3 or AA7475-T761) typically varies between 0.2 and 0.5 mm, while the cured ply thickness of the GRFP layers is typically 0.127 mm. Compared to aluminium alloys, GLARE® is characterised by low density, improved impact performance, beneficial fatigue behaviour (GFRP layers serve as crack arrester) and high fire resistance. Fibre-metal-laminates such as titanium- or stainless steel-CFRP-laminates usually provide even lower density, higher stiffness and strength, higher notch insensitivity and better fatigue properties than GLARE®. Main disadvantages of fibre-metal-laminates are the complex pre-treatment of the metal sheets prior to bonding, limited drapability, considerable (manual) manufacturing effort and high material cost. [18, 83, 89]

Improvements of the structural integrity and energy absorption capacity of long-fibre-reinforced polypropylene by means of steel wire mesh integration (1.4301) have already been demonstrated in previous studies [91, 92]. The large diameter of the metal wires (0.1 to 0.2 mm), however, limits the drapability of the wire mesh and the minimum ply thickness. Higher flexibility is basically given by the application of thin metal filaments. Comprehensive researches regarding continuous steel fibre reinforced polymers were carried out by Callens and colleagues. Austenitic steel fibres (1.4404, 30 µm, 1k) were processed both as quasi-UD and biaxial textiles. Despite the application of brittle epoxy resin, the analyses proved pronounced ductile behaviour of steel fibre reinforced composites with an elongation at break in the range of 10 to 15 % while local bundling of steel fibres was advantageous over an overall homogeneous fibre distribution [93]. High local fibre percentages, however, were also found to cause stress concentration in adjacent transverse orientated plies and consequently to lower the strength of these layers. Similar results were obtained in case of polypropylene-based steel fibre reinforced composites [94]. Further investigations carried out by Callens et al. indicated higher strain at failure of steel fibre reinforced composites when using ductile polyamide as matrix material instead of brittle epoxy resin [95]. This was attributed to a better fibre-resin-adhesion, which delayed debonding of the steel fibres, onset of necking and finally failure of the steel filaments. In all cases, the strain at failure of the composite was lower than the elongation at break of the integrated steel fibres. By contrast, investigations on UD

steel fibre reinforced epoxy resin (1.4404, 30 µm, 0.275k) conducted by Allaer et al. [96] proved nearly identical strain at failure of composite and dry metal fibres.

McBride et al. [97] analysed the mechanical behaviour of UD hybrid glass/steel fibre reinforced epoxy composites (1.4401, 30 µm). The test results indicated a decrease in tensile strength in case of plain and open hole tensile load with increasing steel fibre share. Enhancement of the strain at failure was only achieved in case of pure steel fibre reinforcement. Hybrid composites (combination of steel fibres and self-reinforced polypropylene) were also studied by Swolfs et al. [98], who measured an improvement of the penetration resistance in case of steel fibre reinforced layers located on top of the laminate. Van den Abeele [99] described the development of a full-scale beam consisting of steel fibre cords embedded in a glass mat reinforced thermoplastic (GMT) for improved structural integrity and energy absorption in case of bending load. A function-oriented approach was analysed by Ahmed [100], who investigated the concept of a structural integrated de-icing system based on resistive heat-up of embedded stainless steel fibres (1.4401, 70 µm). Successful integration of SMA (shape memory alloy) wires for active, reversible deformation of fibre reinforced polymers was demonstrated by Hübler [2].

Only little research has been carried out regarding the integration of continuous metal fibres into CFRP. Callens [101] analysed the tensile properties of an epoxy-based hybrid composite with a share of 31.3 vol.% of austenitic steel fibres (1.4404, 30 µm, 1k) and 9.2 vol.% of carbon fibres. The investigation proved pronounced post-damage performance of the UD hybrid composite after failure of the high-tenacity carbon fibres. Again, the ultimate elongation at break of the hybrid composite (6 %) remained below the strain at failure of the corresponding pure steel fibre reinforced composite (15 %) or the dry steel fibres (20 %). In another study, Mosleh et al. [102] reported considerable enhancement of the penetration resistance of cross-ply polyamide-based CFRP by addition of austenitic steel fibre reinforced top layers (1.4404, 30 µm, 1k). Improvements of the bending and impact behaviour of epoxy-based CFRP by means of steel wire integration (1.4301, 0.3 to 0.5 mm) were reported by Lehmann et al. [103]. Moreover, QinetiQ [104] presented a hybrid material comprising titanium alloy wires woven into a carbon fibre reinforced polymer, which offered enhanced penetration resistance. A first approach to multifunctional CFRP was published by Breuer et al. [105]; integration of austenitic steel fibres (1.4404, 1k, 30 µm) in cross-ply epoxy-based CFRP enabled simultaneous

improvements in terms of electrical conductivity, bending-tensile load and penetration resistance.

3.2 Concept idea

The basic idea of the present hybrid material concept is to partially re-integrate specific electrical features, for example grounding, bonding, signal transfer or lightning strike protection, into the load-carrying structure of the aircraft (function integration as in case of an aluminium fuselage). The necessary enhancement of the electrical conductivity of the structure material (CFRP) is achieved by incorporation of highly conductive and ductile continuous metal fibres. Simultaneously, the metal fibre integration is utilised to improve CFRP in terms of damage tolerance, crashworthiness and suitability for bolted joints. The increase in density caused by the metal fibre incorporation is over-compensated by eliminating additional electrical system installation items and by reducing the present minimum skin thickness prescribed, taking advantage of the improved mechanical and electrical performance of the hybrid composite.

The application of thin metal filaments is advantageous for design reasons. Different to fibre metal laminates, such as GLARE® or titanium-CFRP-laminates, where the semi-finished metal material is integrated as a thin sheet, the fibre based approach enables utilisation of anisotropy for (both mechanical and electrical) load tailored laminate design and wrinkle-free draping of multiple shaped structures. Moreover, the large fibre surface alleviates bonding to the polymer resin while the permeable structure facilitates (through-thickness) impregnation of the composite. The easy handling of hybrid textiles and the possible application of established, fully automated manufacturing technologies, such as automated tape laying (ATL) or automated fibre placement (AFP), additionally provides the chance of simple process integration, manufacturing cost savings and reduced scrap rate, hence lower buy-to-fly ratio.

3.3 Hybridisation concepts

A crucial aspect of the considered hybrid material concept is the spatial distribution of the different reinforcing fibres in the composite. Basically, three different grades of homogenisation can be distinguished as illustrated in figure 3.2. The most elementary approach is the combination of layers with different kinds of reinforcing fibres stacked

on each other (**separated layer concept**). This approach enables accumulation of metal or carbon fibres at certain z-positions of the laminate and can be beneficial in terms of manufacturing effort and cost. The grade of homogenisation can be further increased by intra-layer hybridisation (**homogenised layer concept**). For this purpose, carbon and metal fibre bundles are co-woven into a hybrid textile or grouped in a (unidirectional) hybrid non-crimp fabric. The most homogeneous fibre distribution is achieved by intra-yarn hybridisation, for example by commingling carbon and metal filaments of similar diameter to a hybrid roving. In this case, both types of reinforcing fibres are randomly distributed within the roving in a defined ratio. The fabrication of such hybrid roving, however, requires processing of monofilaments or untwisted fibre bundles. Moreover, the individual concepts can be combined to more complex configurations. A quantifiable measure for the dispersion of the fibres is given by the edge length of the smallest repeat unit of the composite; the smaller this value, the greater is the grade of homogenisation. [106, 107]

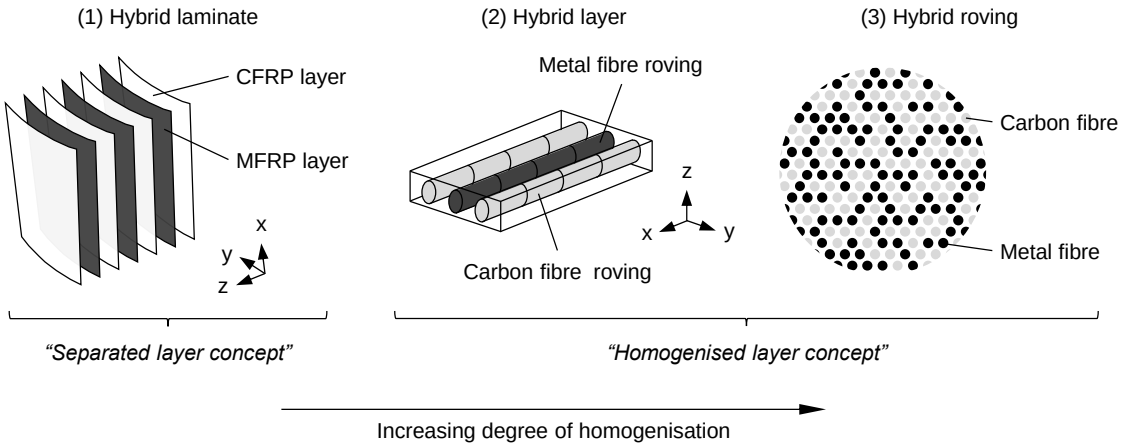

Figure 3.2 Hybridisation concepts with different grades of homogenisation

Increasing degree of homogenisation requires decreasing diameter of the metal filaments. In case of the hybrid roving, the diameter of the metal and carbon fibres should be of similar magnitude to ensure homogeneous distribution and common processing. Both the hybrid layer and the hybrid laminate concept enable thicker metal filaments; in principle, the metal fibre diameter can be as large as the cured ply thickness of the composite. However, compared to thick monofilaments with identical linear density, bundles comprising of several thin filaments are more flexible and enable smaller bending radii. Hybrid fabrics consisting of thins filament will therefore show better drapability.

3.4 Metal fibre selection

Suitable metal fibres have to meet various requirements, figure 3.3. The metal fibres should primarily exhibit high weight-specific electrical conductivity in order to enable sufficient enhancement of the composite's electrical conductivity with only minor increase in density. In addition, the metal fibres must offer high elongation at break (in any case higher than the applied carbon fibres) to facilitate pronounced post-damage performance by providing the composite with alternative load pathways after failure of the brittle carbon fibres. Moreover, in order to ensure sufficient load-carrying capacity of the hybrid material in the post-damage stage and to minimise any deterioration of the composite's stiffness and ultimate strength (e.g. in case of a load-controlled load case), the metal fibres to be incorporated should offer a stiffness close to that of carbon fibres and high ultimate strength. Ultimate strength and strain at failure are typically of opposing trend; however, as shown in chapter 7.3, the elongation at break is of superordinate meaning. Furthermore, the yield strength of the metal fibres should be high enough to allow sufficient (cyclic) elastic deformation of the hybrid composite without plastic deformation; otherwise, minor elongation of the composite would result in permanent deformation of the steel fibres, which would

Mechanical	**Electrical**	**Thermal**
• Stiffness ↑ • Yield strength ↑ • Ultimate tensile strength ↑ • Strain at failure ↑ • Energy absorption capacity ↑ • Strain rate sensitivity ↓	• Specific electrical conductivity ↑ • Tolerable current density ↑	• Thermal expansion ↓ • Thermal conductivity ↑
Selection criteria for metal fibres		
• Corrosion and media resistance ↑ • Galvanic compatibility to carbon fibres ↑	• Costs ↓ • Availability (as fibre) ↑	• Density ↓ • Surface condition ↓↑ • Filament diameter ↓↑ • Bundle twist ↓↑ • Processibility ↑ • Cold formability ↑
Chemical	**Economical**	**Miscellaneous**

↑: as high as possible, ↓: as low as possible, ↓↑: case dependant

Figure 3.3 Selection criteria for metallic reinforcing fibres for the present hybrid material concept

cause inter- or intralaminar residual stresses. As shown in the further course of this work, the functionality of the hybrid composite is strongly affected by the quality of the interface between the metal fibres and the surrounding resin, which again depends on the fibre surface topology and the fibre surface condition. The fibre-resin-interface must be able to transfer shear stresses and avoid premature adhesive inter-fibre-failure but must also enable unhindered metal fibre deformation. Moreover, the corrosion resistance of the metal fibres and the galvanic compatibility to carbon fibres are crucial for long-term stability of the hybrid composite. Particularly in case of high modulus metal fibres, distinct mismatch of the coefficient of thermal expansion of carbon and metal fibres excites inter- and intralaminar thermal stresses (e.g. during manufacturing or in service)[4], which generally promotes inter-fibre-failure, delamination and aggravation of the composite's fatigue performance. Moreover, high thermal conductivity will facilitate homogeneous distribution of local heat input (e.g. in case of lightning strike) over extensive areas of the composite. An overview of concept-relevant properties of potential metal alloys is given in table 3.1 and figure 3.4.

Table 3.1 Typical properties of selected metal alloys in comparison with a standard high-tenacity carbon fibre

Material	ρ / g/cm^3	E / GPa	$\sigma_{p0.2}$ / MPa	σ_{max} / MPa	ε_{max} / %	CTE / 10^{-6} K^{-1}	ρ^* / Ωm	Reference
HTS40	1.77	240	-	4300	1.8	-0.1	1.6×10^{-5}	[13]
CuSn6-R380	8.82	118	170	380…480	50	18	1.1×10^{-7}	[108]
CuZn37-R360	8.44	110	160	360…450	33	19	6.6×10^{-8}	[109]
Ti-6Al-4V	4.41	110…119	785…910	860…1200	10…14	9	1.7×10^{-6}	[16]
Ti-15V-3Cr-3Sn-3Al [a)]	4.75	108…113	750…775	770…785	21…22	10	1.3×10^{-6}	[16]
AA2024-T6	2.75	72…76	345…380	425…470	5…6	24	4.2×10^{-8}	[16]
AA5028-H116	2.67	72	330…345	400…405	12…13	24	5.9×10^{-8}	[110]
1.0338 [a)]	7.85	200…220	140…210	270…350	38…44	11…13	1.5×10^{-7}	[16]
1.4301 [a)]	7.85	190…203	205…310	510…620	45…60	16…18	6.5×10^{-7}	[16]

[a)] in soft-annealed condition

[4] In case of a steel/carbon fibre hybrid composite (steel fibres: 1.4301, carbon fibres: HTS40, $\varphi_{CF} : \varphi_{SF} = 2 : 1$), a temperature decrease of 160 °C (e.g. cooling after laminate cure) excites thermal stresses of up to 364 MPa within the steel fibres and -182 MPa within the carbon fibres, assuming perfect adhesion between steel and carbon fibres, stress-free initial condition and neglecting any influence of the polymer matrix. In fact, the compliancy of the epoxy resin is expected to reduce the thermal-induced stresses to a lower level.

Copper fibres are widely used as electrical conductor due to their minor (absolute) specific electrical resistance. Typically, they offer high corrosion resistance and good cold formability. Drawbacks are given by their low stiffness, low strength and high density. Titanium alloys are characterised by high specific strength, excellent galvanic compatibility to carbon fibres, minor thermal expansion and average specific electrical conductivity. However, the diversity of commercially available titanium fibres is limited. From a weight-specific point of view, fibres made of aluminium alloys are of particular interest. They are distinguished by superior weight-specific electrical conductivity and mechanical properties. However, aluminium fibres show great thermal expansion. Moreover, in presence of electrolytes and in contact with carbon fibres, aluminium tends to ineligible galvanic corrosion, table 3.2. Improvements of the contact corrosion resistance as well as the electrical conductivity can partially be achieved by additional copper cladding (copper clad aluminium, CCA).

Table 3.2 Standard electrode potential for various metal alloys in combination with carbon fibres [7, 16]

Property	Stainless steel	Titanium alloys	Copper alloys	Low carbon steel	Aluminium alloys
Potential difference ΔU / V [a)]	0.27 (non-critical)	0.33 (non-critical)	0.40 (critical)	0.57 (critical)	0.90 (supercritical)

[a)] in relation to carbon in a 3 % NaCl solution, ΔU should be below 0.4 V to preclude contact corrosion

Corrosion is of no relevance for alloyed steel fibres with a sufficient amount of chromium and nickel. Stainless steel fibres are commercially available with a wide range of mechanical properties and appearances. The steel fibres can be purchased either as monofilaments or as twisted or untwisted bundles comprising of up to several thousand filaments. Depending on the production process (individual or multiple wire drawing), the shape of the steel fibres can be circular or polygonal with a filament diameter down to 1 µm. The ultimate tensile strength of high-tenacity steel fibres can be up to over 3000 MPa. By soft-annealing, the strain at failure can be maximised to over 35 %, which is, however, accompanied by a loss of yield and ultimate tensile strength. The stiffness of standard modulus carbon and steel fibres is of similar magnitude. Compared to standard high-tenacity ex-PAN carbon fibres, the electrical conductance of stainless steel fibres is approximately 23 times higher. Due to less alloying, low carbon steel fibres have an even higher specific conductance but worse mechanical properties and corrosion resistance. By nickel or copper cladding, the electrical conductivity can be further enhanced by a factor of 140 and 378,

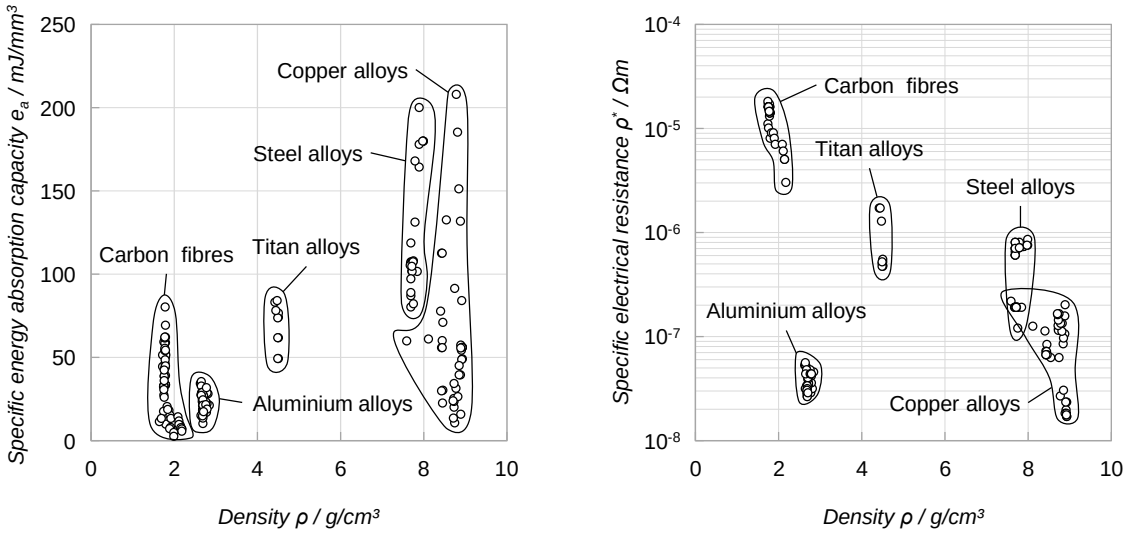

Figure 3.4 (left) Specific energy absorption capacity under tensile load[5] and (right) specific electrical resistance of various metal alloys in dependence on their density [16]

respectively. The cladding of the fibres additionally provides corrosion resistance to the (low carbon) steel core. Main drawbacks of steel fibres are their high density and the CTE mismatch to carbon fibres. Latter particularly applies to austenitic steel fibres. Still, stainless steel fibres offer the best trade-off between absolute electrical and mechanical properties, corrosion resistance and diversity of appearance and are therefore chosen for the further course of this work.

3.5 Steel fibre fabrication

Steel fibres are produced by means of wire drawing, i.e. by pulling a wire through a series of drawing dies to a certain diameter. In case of large cross-section reduction, several draws with intermediate soft-anneal of the semi-finished fibre are required. The monofilaments can subsequently be processed to a twisted bundle. The twist does not only stabilise the structure of the bundle but also ensures homogeneous load distribution among the individual filaments; otherwise, the shortest filament would bear the highest proportion of load. Coatings for improved processibility, electrical conductivity and/or corrosion resistance are feasible by various methods. One possible process consists of initial inserting the wire into an open tube made of

[5] The specific energy absorption capacity under tensile load is calculated by integrating the stress-strain relation, assuming a bi-linear behaviour defined by Young's modulus, yield strength, ultimate tensile strength and elongation at break of the alloy.

the designated metallic cladding material. This tube is then closed using rollers before being TIG (tungsten inert gas) welded in a protective atmosphere, figure 3.5 (left). Subsequent drawing and thermal treatments metallurgically bond the coating material to the steel fibre core. By this process, a particularly resistant cladding is achieved. Other relevant coating technologies to adjust the surface condition are hot dip (e.g. zinc or zinc-aluminium), electro deposition (e.g. copper or zinc), lacquering or extrusion of polymers. In order to produce fibres with very small filament diameter (a few microns), several copper-coated wires are bundled into a tube and then drawn together. The covering tube and the copper are subsequently dissolved in acid, leaving a bundle of single filaments with rough surface and polygonal (regular or irregular hexagonal) cross-section, figure 3.5 (right). [111]

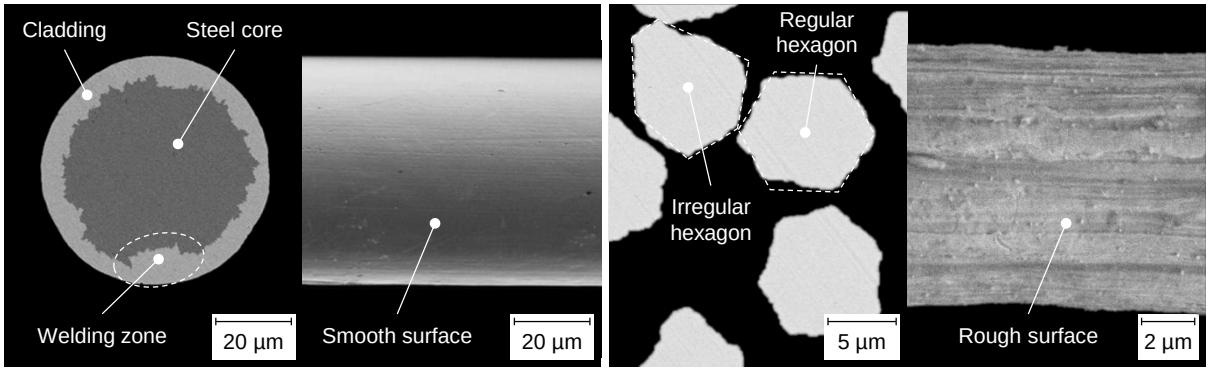

Figure 3.5 Comparison of the cross-section and surface roughness of (left) single and (right) multiple wire drawn steel fibres

Due to strain hardening, the drawing process increases the yield strength and ultimate tensile strength while reducing the ductility of the steel fibres. A final soft-anneal in an inert atmosphere is therefore required to increase both strain at failure and electrical conductivity. Surface contamination of the steel fibres might occur due to lubrication (in order to minimise friction drag and die wear) during the drawing process. Depending on their kind and the dimensions of the filaments, the contamination can be removed by mechanical and/or chemical-physical purification methods. [111, 112]

3.6 Allowable steel fibre proportion

The mass of steel fibres which can maximally be incorporated into the structure material without detrimentally affecting the overall mass of the aircraft primary structure equates to the weight of the electrical system installation items and lightning strike protection measures to be substituted, figure 3.6. For the further course of this

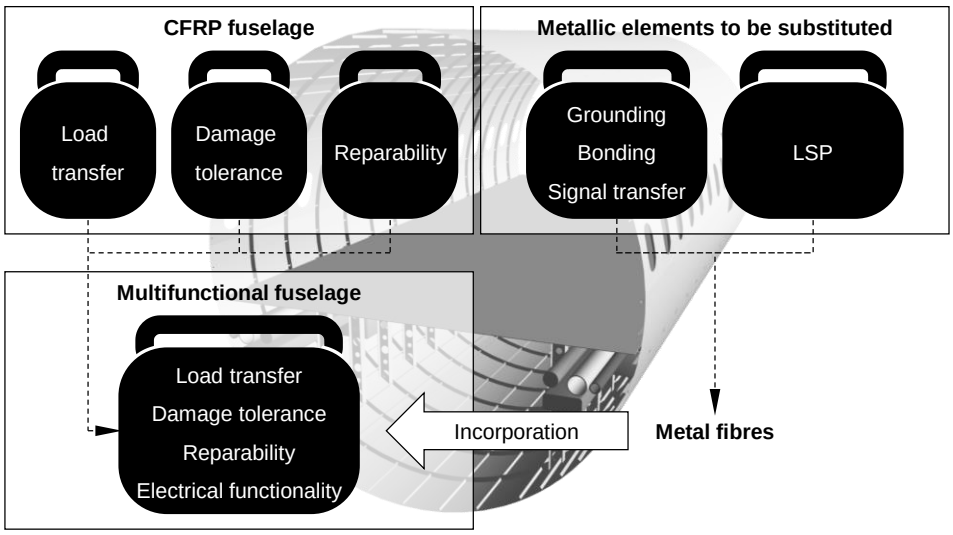

Figure 3.6 Re-integration of electrical functions into the load-carrying CFRP fuselage structure by means of mass transfer

work, this weight is converted into an allowance for the steel fibre volume share of the hybrid composite as described below, figure 3.7, exemplarily for a single-aisle, short to medium range aircraft.

In a first step, the mass of the fuselage panels (i.e. skin, stringer, assembly) is approximated by 2000 kg. This simplified yet conservative approach neglects local reinforcements (i.e. increase in laminate thickness) at loaded and unloaded cut-outs (windows, passenger and cargo doors) or at panel and section junctions. Assuming the structure to be entirely made of CFRP with a density of 1.59 g/cm^3, this mass corresponds to a material volume of 1.26 m^3. For the electrical system installation items to be replaced (e.g. cables, metallic strips, junctions, overbraidings), a weight of 450 kg is supposed. The mass of expanded metal foil for lightning strike protection is considered by 160 kg. Both masses can be converted into a steel volume equivalent by dividing by the density of steel (7.95 g/cm^3). Next, an overall fibre share of 60 vol.%[6] is defined for the hybrid composite. Moreover, a distinction must be made whether the wall thickness of the structure retains its original value or increases as a result of the steel fibre incorporation. In case of a constant wall thickness, the original volume of the fuselage panels equates to the overall volume of the hybrid material. According to the previous made specification, 40 % of this volume consists of resin. The corresponding weight is calculated by multiplying this

[6] This value equates to a technical upper limit. Higher fibre percentages are feasible but would lead to insufficient wetting of the fibres by the surrounding resin and thus to deficient mechanical composite properties [7].

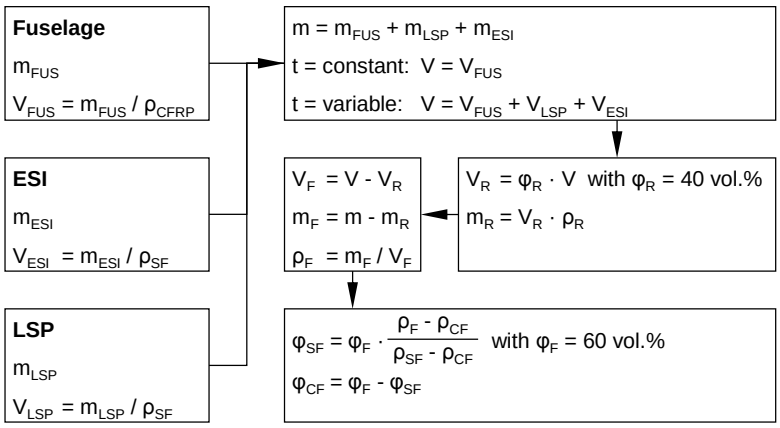

V: volume, m: mass, ρ: density, φ: volume share, t: laminate thickness

FUS: fuselage, CF: carbon fibre, SF: steel fibre, F: fibre, R: resin

Figure 3.7 Procedure for determining an allowance for the steel fibre volume share

volume with the resin density (1.31 g/cm^3). The remaining volume and mass plus the weight of the elements to be substituted (with an average density) is assigned to the reinforcing fibres. Considering the density of the steel (7.95 g/cm^3) and carbon fibres (1.77 g/cm^3) and applying the rule of mixtures on the average density yields the portion of steel fibres on the overall fibre volume share. Multiplying this value with the previously defined value of 60 vol.% for the overall fibre percentage yields the steel fibre volume share of the hybrid composite. In case of a variable wall thickness, the overall volume is given by the original volume of the fuselage panels and additionally by the volume of the steel equivalent of the electrical system installation items and lightning strike protection measures to be replaced. The further estimation is analogue to that with a constant wall thickness. Following this approach, a maximum steel fibre share of approximately 5 to 10 vol.% can be estimated as a reasonable range for the present hybrid material concept, table 3.3.

Table 3.3 Reasonable steel fibre shares for the considered hybrid material concept for a single-aisle aircraft

Concept	m_{FUS} / kg	m_{ESI} / kg	m_{LSP} / kg	V / m^3	m_F / kg	m_R / kg	φ_{CF} / vol.%	φ_{SF} / vol.%	φ_R / vol.% [a)]
t = constant	2000	450	160	1.26 (= V_{FUS})	1949	661	52	8	40
t = variable	2000	450	160	1.34	1909	701	54	6	40

[a)] per definition

Obviously, this simplified appraisal has to be considered as first approximation only. Nonetheless, in order to assess the structure-mechanical and electrical effects of the

steel fibre integration on the performance of the hybrid composites more clearly, steel fibre shares of up to 20 vol.% are studied in the further course of this work. Moreover, the derivation re-emphasises the fact that the increase in composite density is solely caused by a mass transfer from electrical system installation items to be eliminated to incorporated steel fibres and does not mean a rise in the total mass of the aircraft structure. In principle, the present multifunctional material concept also allows an increase in laminate thickness if the steel fibres are added on top of the baseline CFRP structure. From a structure-mechanical point of view, this would be particularly advantageous, for example regarding bending stiffness or bolted joint suitability.

The estimated range for the steel fibre share applies to the entire fuselage airframe as homogenised value. In fact, spatial concentration of steel reinforcing fibres (local steel fibre share up to 60 vol.%) at certain areas of the aircraft structure might be beneficial to realise specific electrical and/or mechanical improvements. Stringer, for example, might exhibit higher steel fibre shares than frames in order to provide distinct electrical conductivity along the longitudinal axis of the aircraft while demonstrating enhanced bending stiffness and crashworthiness. Moreover, discrete straps of steel fibres could enable several individual conductive pathways. Another example is a fuselage with pure steel fibre reinforced top layers on the outer skin to simultaneously provide lightning strike protection as well as improved impact resistance.

4 Fibre characterisation

Within the scope of this work, two different kinds of continuous, soft-annealed steel fibres are selected: stainless steel fibres (Bekinox VNM A 60.7) and copper cladded low carbon steel fibres (Bekiflex LR A 63.7). Both types of steel fibres are processed as bundles consisting of seven circular filaments, each with a diameter of (60.0 ± 0.4) or (63.4 ± 0.5) µm. The bundles are twisted with a Z-lay direction and a lay length[7] of approximately 1.00 cm in case of the stainless steel and 1.43 cm in case of the copper cladded low carbon steel fibres. Micrographs of the bundle cross-sections obtained by scanning electron microscopy (SEM) are shown in figure 4.1.

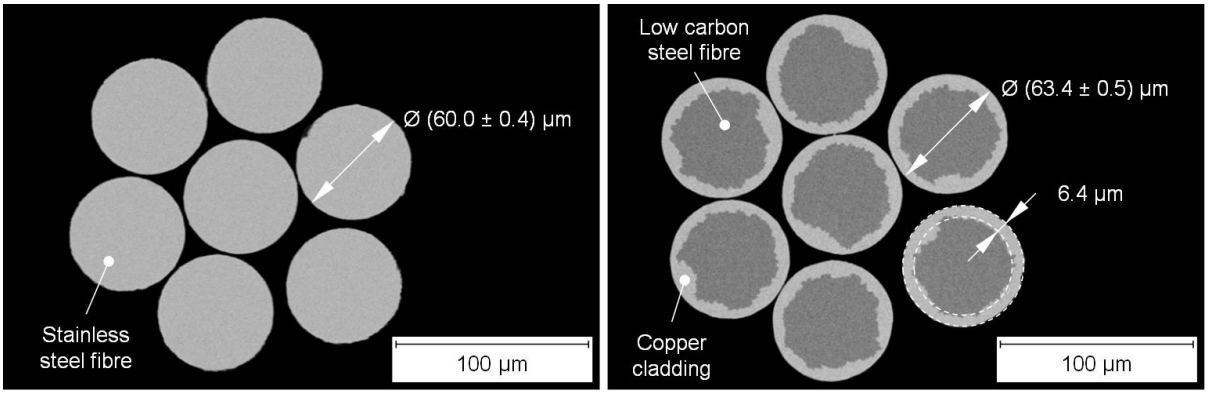

Figure 4.1 Micrographs of the cross-section of one (left) stainless steel and (right) copper cladded low carbon steel fibre bundle

As depicted in the micrograph, each filament of Bekiflex LR A 63.7 includes a closed copper coating. According to the cross-section polish, the copper cladding represents 36 % of the filament cross-sectional area, which again correlates with an average coating thickness of 6.4 µm. In fact, as a result of the coating process, the cladding is irregularly shaped; the actual thickness varies between 3 and 12 µm.

In order to complement the supplier information on the fibre properties, fundamental tests are carried out on both types of steel fibre bundles. The experimental analyses in this chapter aim to determine the alloy composition, mass density, strain rate dependent tensile properties and specific electrical resistance of the steel fibres. The obtained characteristic values are subsequently used to analytically predict possible property enhancements of CFRP as a result of the steel fibre integration.

[7] The lay length is the longitudinal distance along the bundle required for one complete helical wrap, i.e. the total bundle length divided by the total number of wraps.

4.1 Alloy composition

The alloy composition of the applied steel fibre bundles is determined according to DIN EN 10088-3 [114] and DIN EN 10025-2 [115] by means of optical emission spectroscopy (OES) and X-ray fluorescence (XRF) spectroscopy. The results of the analysis are summarised in table 4.1. For the copper cladded low carbon steel fibres, the alloy composition of the steel core is additionally estimated by excluding the copper share from the analysis. This approach has to be considered as first order approximation since this simplification disregards the small amount of copper that is included even in low carbon steel alloys, while conversely the cladding material most probably consists not only of elemental but alloyed copper.

Table 4.1 Alloy composition of the applied metal fibre bundles [116, 117]

Bekinox VNM A 60.7: 1.4301 / X5CrNi1810 / AISI 304 [a]									
C	Si	Mn	Mo	Ni	Cr	N_2	O_2	H_2	B
0.023	0.52	0.35	0.16	8.11	18.43	0.033	0.024	0.005	< 0.005
Pb	Ta	Co	Cu	Sn	Ti	Nb	S	P	Fe
0.011	< 0.005	0.08	0.1	0.007	0.01	0.03	0.006	0.008	(residual)

Bekiflex LR A 63.7 [a]									
C	Si	Mn	Mo	Ni	Cr	N_2	O_2	H_2	B
0.02	0.18	0.16	0.012	0.05	0.05	0.005	0.022	0.007	< 0.005
Pb	Co	Cu	Sn	Ti	Nb	S	Fe		
< 0.005	< 0.005	38.14	< 0.005	< 0.005	< 0.005	0.024	61.39		

Bekiflex LR A 63.7 - analysis result excluding copper proportion: 1.0338 / S235JR / AISI 1006 [a]									
C	Si	Mn	Mo	Ni	Cr	N_2	O_2	H_2	B
0.03	0.29	0.26	0.019	0.08	0.08	0.008	0.036	0.011	< 0.008
Pb	Co	Cu	Sn	Ti	Nb	S	Fe		
< 0.008	< 0.008	0 [b]	< 0.008	< 0.008	< 0.008	0.039	99.24		

[a] all data given in wt.%

[b] per definition

According to the maximum permissible values mentioned in the relevant standard, an austenitic stainless steel alloy of type 1.4301 is determined for Bekinox VNM A 60.7. This chromium-nickel austenitic grade of stainless steel is characterised by high

ductility and ultimate tensile strength but comparatively low tensile stiffness (190 to 200 GPa) and yield strength. Due to its specific mechanical characteristics, the alloy features excellent drawability. Moreover, the high percentage of chromium (17.5 to 19.5 wt.%) and nickel (8.0 to 10.5 wt.%) provides distinctive corrosion resistance, particularly in natural environmental media and in absence of considerable amounts of chlorine. Nevertheless, this alloy is prone for intergranular corrosion because of possible precipitation of chromium carbides at grain boundaries. Compared to carbon steel alloys, the coefficient of thermal expansion is high (16 to 18 × 10^{-6} K^{-1}), while the thermal conductivity is low (14 to 17 W/Km). Considering the negative thermal expansion of carbon fibres, the large CTE of stainless steel fibres might be detrimental for the application in hybrid composites regarding residual stresses induced during laminate cure or in-service. Typical values for the specific electrical resistance ranges from 6.5 to 7.7 × 10^{-7} Ωm. In principle, the alloy is paramagnetic. However, by means of cold forming at temperatures below M_d = 47 °C (cf. appendix A.3), the metastable microstructure transforms from paramagnetic γ-austenite to ferromagnetic α‘-martensite. This γ-α‘-transformation can be determined by proper magneto-sensitive sensors. As shown in chapter 8.7, this effect basically allows non-destructive detection of permanent, non-visible damages of the hybrid composite. Further details on the martensite transformation are given in appendix A.3. [16, 118]

In case of Bekiflex LR A 63.7, the alloy distortion caused by the copper cladding prevents explicit identification of the steel core alloy. The analysis merely enables a classification of the core material to be a low alloyed carbon steel. However, the supplier information suggests a carbon steel of type 1.0338. The threshold values for this alloy composition are in moderate agreement with the values of the copper-freed analysis result. In principle, this low carbon steel is characterised by high stiffness (200 to 220 GPa), low yield strength as well as moderate ultimate tensile strength and particularly suits for cold forming processes. The minor percentage of alloying elements enables low electrical resistivity (1.5 to 2.9 × 10^{-7} Ωm) and good thermal conductivity (43 to 55 W/Km) but also prevents decent corrosion resistance. The coefficient of thermal expansion is comparatively small (11 to 13 × 10^{-6} K^{-1}). The copper cladded low carbon steel fibre is paramagnetic. The combination of a low carbon steel core surrounded by copper is known as copper clad steel (CCS) [119]. CCS wires particularly suit for high frequency signal applications since high frequency currents mainly travel in the outer (high conductive) skin of the conductor. [16]

4.2 Mass density

The density of the steel fibre bundles is determined by means of the liquid displacement method in accordance with ISO 10119 [120] at an ambient temperature of 21 °C. This method particularly suits for an accurate density determination of small and complex shaped structures since explicit measurement of the sample dimensions is not required [121]. For the determination of the density, the desiccated specimen is initially weighed in air (subscripted with dry) and then weighed again while entirely submerged in double distilled, degassed water (subscripted with wet). The difference between the two weights m correlates linearly with the buoyancy force of the specimen (Archimedes' principle). Dividing the weight difference by the density of the water ρ_w yields the volume of the specimen V, eq. 4.1.

$$V = \frac{m_{dry} - m_{wet}}{\rho_w} \quad \text{(Eq. 4.1)}$$

The specimen weight in air divided by the volume yields the sample density ρ, eq. 4.2.

$$\rho = \frac{m_{dry}}{V} \quad \text{(Eq. 4.2)}$$

To avoid additional uplift by adhering air bubbles on the surface and thus distorted test results, the submerged specimen is placed under a light vacuum for deaeration prior to measurement. Furthermore, a wetting agent is added to the water to reduce the surface tension and consequently the affinity for blistering. The density of the applied immersion liquid is determined by an analogue procedure. For this purpose, the weight of a reference object m_{ref} with a defined volume V_{ref} is determined in air and again while entirely submerged in water. The difference between the two weights divided by the object's volume V_{ref} yields the density of the water ρ_w, eq. 4.3.

$$\rho_w = \frac{m_{ref,dry} - m_{ref,wet}}{V_{ref}} \quad \text{(Eq. 4.3)}$$

Temperature related variation of the water's density during measurement is prevented by stabilising the ambient temperature. The measurements are conducted for steel fibre sections with a length of 1000 mm. Five specimens from different bobbins are analysed for each type of steel fibre. By this procedure, a density of (7.95 ± 0.01) g/cm^3 for the stainless steel and (8.25 ± 0.02) g/cm^3 for the copper cladded low carbon steel fibre bundles is determined. The density of the carbon

fibres (1.77 g/cm^3 [13]) and the epoxy resin (1.31 g/cm^3 [113]) is taken from the supplier data sheets.

4.3 Tensile properties

In order to determine the tensile properties of the steel fibre bundles, tests are carried out on a modified hydraulic tensile testing machine (Zwick Roell HTM 5020). The tensile tests are performed on 160 mm long bundle sections, which are provided with 30 mm long end tabs made of adhesive tapes. The end tabs simplify the handling of the specimen and enable an accurate positioning in the flat, roughened clamping jaws. The free clamping length of the specimen is 100 mm. All tests are captured by a high-speed camera system, which allows an optical elongation measurement of the specimen by motion tracking of the clamping jaws with the software Motion Studio [122]. The frame rate of the camera is set to 25 Hz/(mm/s). The load is measured by a piezo-electric load cell with a calibrated range of 25 N. The test setup and a representative sequence of the fibre tensile tests are depicted in figure 4.2.

In order to assess the strain rate sensitivity of the tensile properties, three monotonic crosshead speeds of 2, 20 and 200 mm/s are tested. These loading speeds comply with nominal strain rates of 0.02, 0.2 and 2 s^{-1}. For each type of metal fibre and testing velocity, ten specimens from different bobbins are tested to failure. Testing is considered as valid if the bundle fails at a distance of more than 5 mm from the

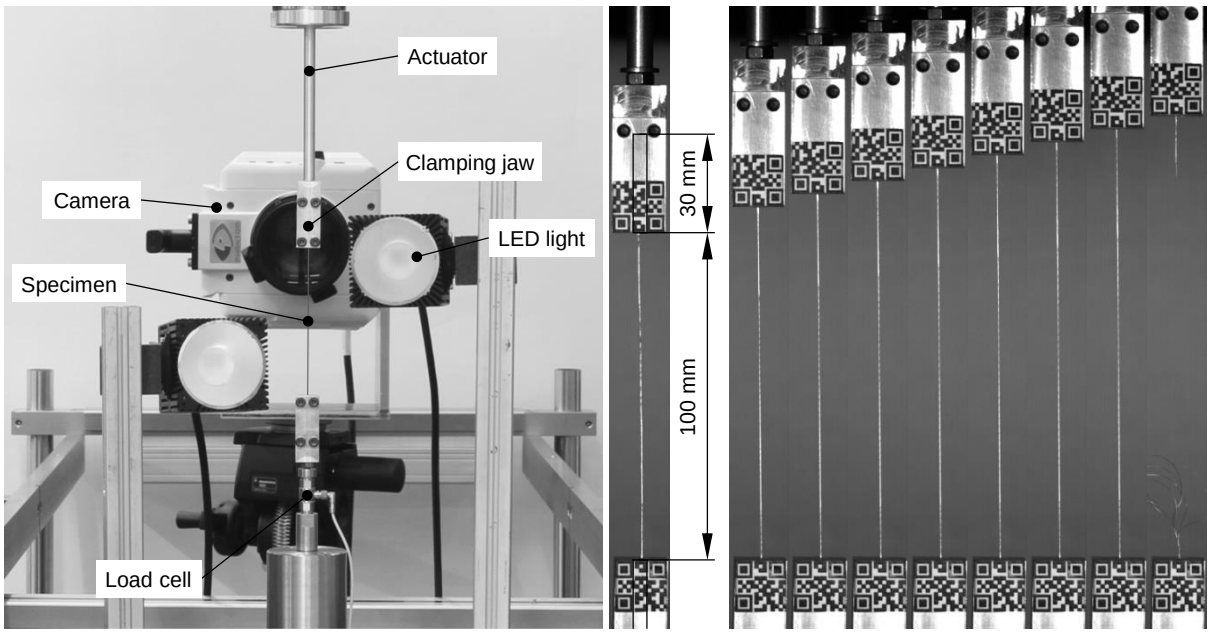

Figure 4.2 (left) Test setup and (right) test sequence of the fibre tensile tests

clamping jaws. Following the tests, 0.2 % offset yield strength $\sigma_{p0.2}$, ultimate tensile strength σ_{max}, uniform elongation $\varepsilon_{\sigma max}$ and elongation at break ε_{max} are derived from the obtained stress-strain data. The strain at failure is defined as the total nominal elongation at which the first filament of the bundle fails. The tensile stiffness E is determined by linear regression within 10 and 50 % of the offset yield strength. Integrating the stress-strain relation up to ε_{max} yields the volume-specific energy absorption capacity $e_{a,max}$. Mean stress-strain curves are depicted in figure 4.3. The corresponding characteristic values are summarised in table 4.2.

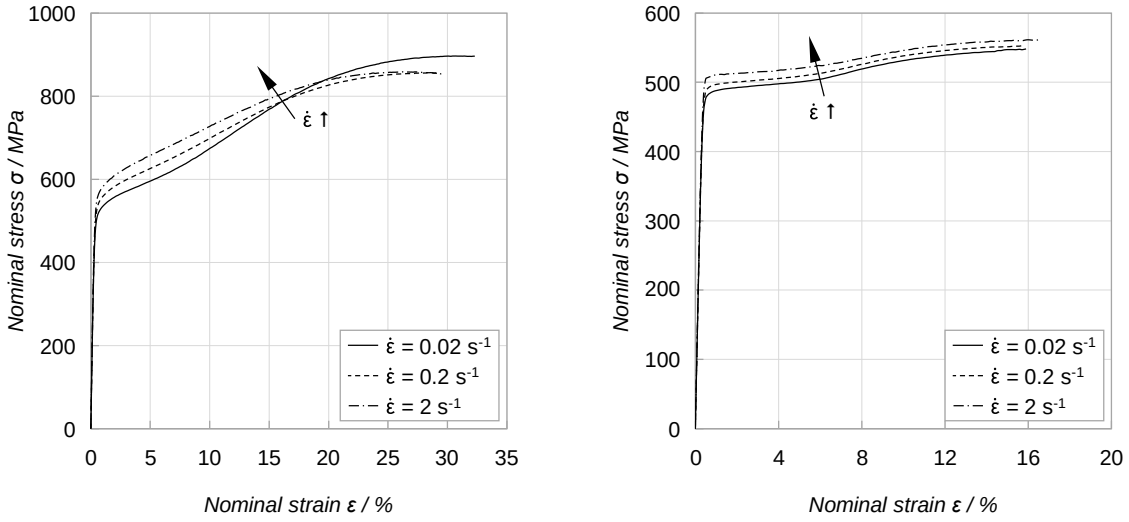

Figure 4.3 Mean stress-strain curves of (left) the stainless steel and (right) copper cladded low carbon steel fibre bundles as a function of the strain rate

Both kind of steel fibre bundles are characterised by pronounced ductility. Compared to the carbon fibres processed in this work (Toho Tenax HTS40 F13 12k, cf. table 4.4), the elongation at break is 18 times higher in case of the stainless steel and 8 times higher in case of the copper cladded low carbon steel fibres bundles. By contrast, the tensile stiffness (-26 % or -41 %) and the ultimate tensile strength (-79 % or -87 %) are significantly lower. A distinctive yield point, which would indicate onset of permanent plastic deformation, cannot be identified for both kinds of steel fibre bundles. Due to the pronounced ductility, the stainless steel as well as the copper cladded low carbon steel fibres provide a high volume-specific energy absorption capacity, which is 6 times higher or twice as high compared to the brittle high-tenacity carbon fibres.

Table 4.2 Tensile properties of the metal fibre bundles as a function of the strain rate

Material	$\dot{\varepsilon}$ / s^{-1}	E / GPa	$\sigma_{p0.2}$ / MPa	σ_{max} / MPa	$\varepsilon_{\sigma max}$ / %	ε_{max} / %	$e_{a,max}$ / mJ/mm^3
	0.02	176 ± 7	504 ± 5	897 ± 2	30.62 ± 1.46	32.31 ± 2.01	244 ± 17
Bekinox VNM A 60.7	0.2	178 ± 8	526 ± 4	856 ± 3	28.17 ± 0.80	29.23 ± 1.16	217 ± 9
	2	187 ± 12	547 ± 4	860 ± 2	26.57 ± 0.77	29.54 ± 0.55	225 ± 4
	0.02	142 ± 5	479 ± 4	545 ± 4	14.77 ± 1.26	15.00 ± 1.29	77 ± 7
Bekiflex LR A 63.7	0.2	142 ± 4	489 ± 6	552 ± 2	15.60 ± 0.63	15.84 ± 0.64	82 ± 3
	2	150 ± 6	506 ± 5	561 ± 3	15.90 ± 1.45	16.53 ± 1.59	88 ± 9

In case of the stainless steel fibre bundles, failure of the individual filaments occurs synchronously, which indicates homogeneous loading of the bundle. Moreover, the stainless steel fibres show a distinct strain hardening, indicated by a small yield ratio (ratio of $\sigma_{p0.2}$ to σ_{max}) of 0.56. This is caused by the high concentration of alloying elements, which cause lattice distortion and thus higher resistance against dislocation motion during plastic deformation. In addition, elongation at temperatures below M_{d30} = 47 °C (cf. appendix A.3) causes deformation-induced phase transformation from γ-austenite (initial phase) to α'-martensite. The formation of α'-martensite, which exhibits higher strength but lower ductility than γ-austenite, causes additional hardening of the metastable austenitic steel fibres. Typically, the γ-α'-transformation as a function of the plastic deformation is sigmoidal in shape, which again is reflected by the shape of the measured yield curve. In case of the copper cladded low carbon steel fibre bundles, erratic failure signifies a more heterogeneous load distribution among the individual filaments, which can be attributed to the lower twist of the fibre bundles. Due to the minor concentration of alloying elements, hardening mainly relies on strain and grain boundary hardening and is, as indicated by a yield ratio of 0.90, less pronounced.

Both kinds of steel fibre bundles exhibit a low tensile stiffness. For the alloy of the stainless steel fibres of type 1.4301, a low Young's modulus in the range of 190 to 200 GPa is well known [16]. However, the tensile stiffness of the quasi-statically loaded stainless steel fibre bundles is about 7 % lower. In fact, manufacturing of the fibres is expected to cause an alignment of the microstructure along the drawing direction, i.e. the longitudinal axis of the fibre, which should result in an increase in tensile stiffness. Moreover, heterogeneous (asynchronous) loading of the individual filaments is avoided by the twist of the fibre bundles and can additionally be excluded

due to the missing toe region in the stress-strain curve. In principle, inaccurate determination of the bundle's stiffness might occur during calculation of the nominal tensile stress from the force signal as a result of an imprecise calculation of the fibre cross-sectional area. However, the experimentally determined filament diameter of the steel fibres merely exhibits negligible scattering (cf. figure 4.1). Moreover, inaccuracies might result from an imprecise strain measurement. Slipping of the bundles out of the clamping jaws can verifiably be excluded. However, there is the chance that the steel fibers partly elongate within the clamping jaws. This would increase the effective free clamping length and cause an overestimation of the specimen's elongation or underestimation of the bundle's stiffness. The particularly low tensile stiffness of the copper cladded low carbon steel fibre bundles is additionally caused by the parallel connection of high modulus steel core and low modulus copper cladding (approximately 110 to 130 GPa [16]).

4.3.1 Influence of the strain rate

In case of the austenitic steel fibres, increasing strain rate changes the shape of the stress-strain curve, figure 4.3 (left). Compared to the quasi-static material response, both tensile stiffness (+1.16 % or +6.29 %) and offset yield strength (+4.36 % or +8.64 %) rise with increasing strain rate. However, hardening is less pronounced, which finally lowers the ultimate tensile strength of the fibre bundles by -4.60 % or -4.13 %. The yield ratio consequently increases to 0.61 or 0.64. The nominal strain at failure declines by 9.55 % and 8.57 %, respectively. This distinctive strain rate sensitivity is characteristic for metastable austenitic steel alloys and is caused by superimposition of two contrariwise processes. Increasing strain rate is accompanied by a rise of the material resistance against dislocation motion and consequently by an increase of the mechanical stress required for plastic deformation. This increases the offset yield strength. With progressive elongation, adiabatic heat-up of the metal fibres (which gains in importance with rising strain rate) stabilises the austenitic microstructure and delays or prevents deformation-induced martensite formation (cf. appendix A.3). Compared to quasi-static deformation, the higher share of residual austenite reduces the strength of the stainless steel fibres. Superimposition of both effects finally causes flattening of the sigmoidal shaped yield curve, hence a reduction of the ultimate tensile strength. In addition, the restrained dislocation motion reduces the elongation at break.

In case of the copper cladded low carbon steel fibres, increasing strain rate causes a rise of the material resistance against dislocation motion, which shifts the stress-strain curve to higher stresses. The basic curve progression, however, remains unchanged, figure 4.3 (right). As a result, both offset yield strength (+2.07 % or +5.60 %) and ultimate tensile strength (+1.37 % or +3.03 %) are increased. The yield ratio rises slightly to 0.89 and 0.90, respectively. Additionally, the tensile stiffness of the fibre bundles alters by -0.15 % or +5.79 %. The maximum elongation atypically increases by 5.60 % and 10.25 %, respectively.

4.3.2 Influence of the fibre processing

Moreover, the influence of the laminate fabrication (cf. chapter 6.1), i.e. filament winding and laminate cure, on the mechanical properties of the steel fibre bundles is analysed. For this purpose, steel fibre bundles are wound in dry condition on a winding core. All parameters, in particular the filament drag, correspond to the setup used for laminate fabrication. The wound fibre bundles are subsequently released from the winding core. Moreover, pristine bundle sections are fixed on peel ply with polyimide adhesive tape, bagged in a vacuum bag and exposed in an autoclave to the temperature and pressure profile emulating the laminate cure cycle (cf. figure 6.1 (left)). Samples of both separated treatments are subsequently tested with regard to their tensile properties ($\dot{\varepsilon} = 0.02\ s^{-1}$) according to the procedure introduced at the

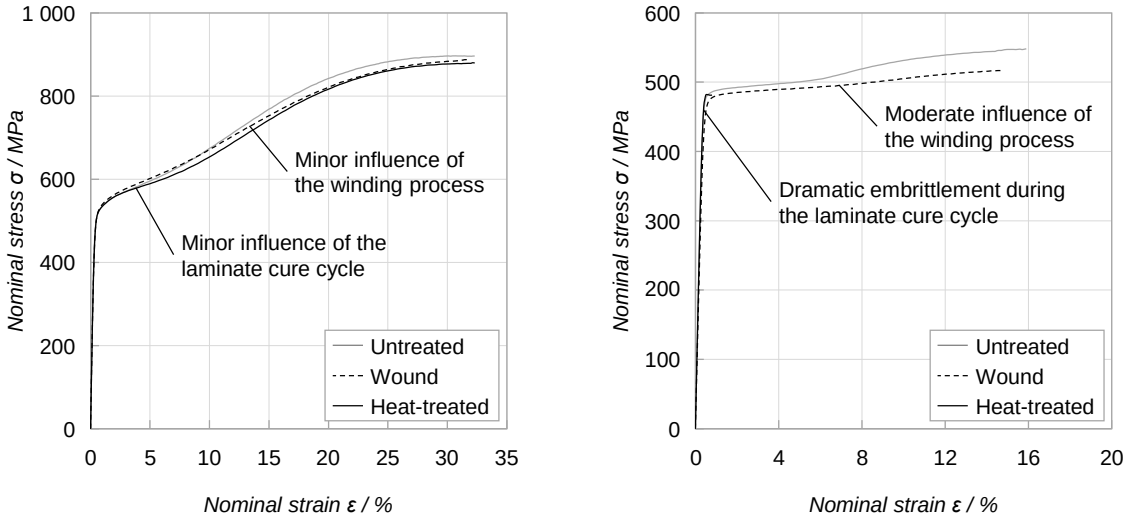

Figure 4.4 Influence of the filament winding and autoclave cure cycle on the tensile behaviour of (left) the stainless steel and (right) copper cladded low carbon steel fibres

Table 4.3 Influence of the filament winding and autoclave cure cycle on the tensile properties of the metal fibre bundles

Material	Cond.[a)]	E / GPa	$\sigma_{p0.2}$ / MPa	σ_{max} / MPa	$\varepsilon_{\sigma max}$ / %	ε_{max} / %	$e_{a,max}$ / mJ/mm^3
Bekinox VNM A 60.7	r	176 ± 7	504 ± 5	897 ± 2	30.62 ± 1.46	32.31 ± 2.01	244 ± 18
	w	167 ± 8	506 ± 3	886 ± 6	31.65 ± 1.03	31.99 ± 1.19	238 ± 11
	a	163 ± 6	507 ± 2	879 ± 4	31.38 ± 0.61	32.34 ± 0.57	238 ± 5
Bekiflex LR A 63.7	r	142 ± 5	479 ± 4	545 ± 4	14.77 ± 1.26	15.00 ± 1.29	77 ± 7
	w	121 ± 8	469 ± 7	516 ± 2	14.11 ± 0.45	14.76 ± 0.53	72 ± 3
	a	137 ± 2	482 ± 2	483 ± 2	0.28 ± 0.15	0.87 ± 0.12	3 ± 1

[a)] r: raw condition (as delivered), w: after filament winding, a: after autoclave (heat) treatment

beginning of this chapter. The results are given in figure 4.4 and table 4.3.

Neither the winding process nor the laminate cure cycle has a considerable influence on the tensile properties of the stainless steel fibre bundles. All concept relevant mechanical characteristics, such as offset yield strength (+0.42 % or +0.58 %), ultimate tensile strength (-1.23 % or -2.06 %) and elongation at break (-1.00 % or +0.08 %), basically remain unaffected. The tensile stiffness of the stainless steel fibre bundles, however, decreases slightly by 5.17 % or 7.01 %.

In case of the copper cladded low carbon steel fibre bundles, the winding process has an ambivalent influence on the tensile properties. Offset yield strength (-2.12 %), ultimate tensile strength (-5.23 %) as well as total elongation at break (-1.57 %) decreases slightly, while the tensile stiffness considerably declines by 14.67 %. By contrast, the autoclave cure cycle severely affects the performance of the copper cladded low carbon steel fibre bundles. While the offset yield strength (+0.56 %) and the tensile stiffness (-3.68 %) remain nearly unchanged, the ultimate tensile strength (-11.44 %) and the strain at failure (-94.23 %) are significantly reduced. As a consequence, the volume-specific energy absorption capacity decreases by -95.71 %. The reason for this severe deterioration could not conclusively be clarified within this study. Quenching of the steel fibres can be excluded due to the low temperatures (T_{max} = 180 °C) and minor cooling rate ($\dot{T}$ = 2 °C/min) of the laminate cure cycle. The loss of ductility might be caused by galvanic corrosion of the (ignoble) low carbon steel fibre core in contact with the (noble, cf. galvanic series of metals) copper cladding, accelerated by the increased temperature and pressure during the autoclave process.

4.4 Electrical conductivity

In order to determine the specific direct current (DC) conductance of the steel fibre bundles, measurements are carried out by using the four-terminal-sensing-method (Kelvin connection) on a digital sourcemeter (Keithley 2601A) at a constant ambient temperature of 21 °C. The sourcemeter consists of a voltmeter, an amperemeter and a controlled power supply. Amperemeter and power supply are separately connected to the bundle sample via four rotating clip jaws. The output of the power supply is controlled by the voltmeter, ensuring a defined voltage drop across a specified measuring length. Synchronously, the resulting electric current is measured by the amperemeter. The test setup and its equivalent circuit diagram are shown in figure 4.5.

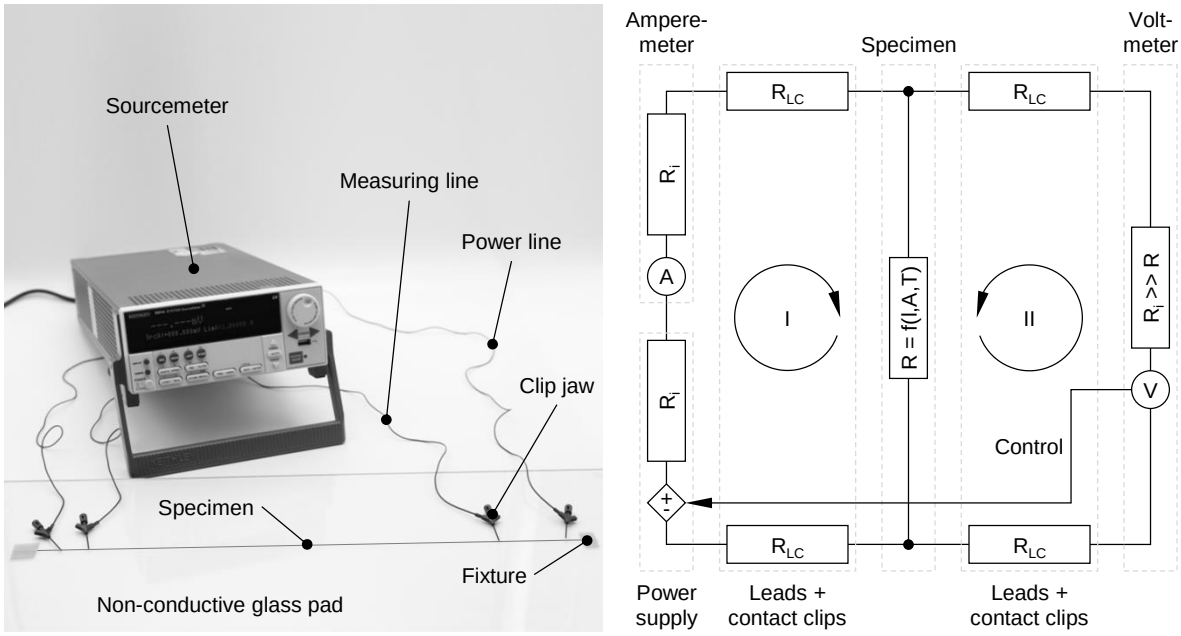

Figure 4.5 (left) Test setup and (right) equivalent circuit diagram of the fibre conductivity measurements

Voltage drops in the range of 0.1 mV to 0.1 V are examined. Considering Ohm's law, the absolute electrical resistivity is determined from the obtained current-voltage data using linear regression with a compelled zero-crossing. The reading is repeated for five different measuring lengths between 200 and 600 mm. In compliance with Pouillet's law, the absolute resistance R correlates linearly with the measuring length l, considering a constant cross-sectional area A of the steel fibre bundles, eq. 4.4 [123].

$$R = \rho^* \cdot \frac{l}{A} \qquad \text{(Eq. 4.4)}$$

The proportionality factor of the resistance-to-length correlation is obtained by linear regression with an enforced zero-crossing. Multiplying this value with the sample cross-sectional area yields the specific electrical resistance ρ*. The procedure is illustrated in figure 4.6.

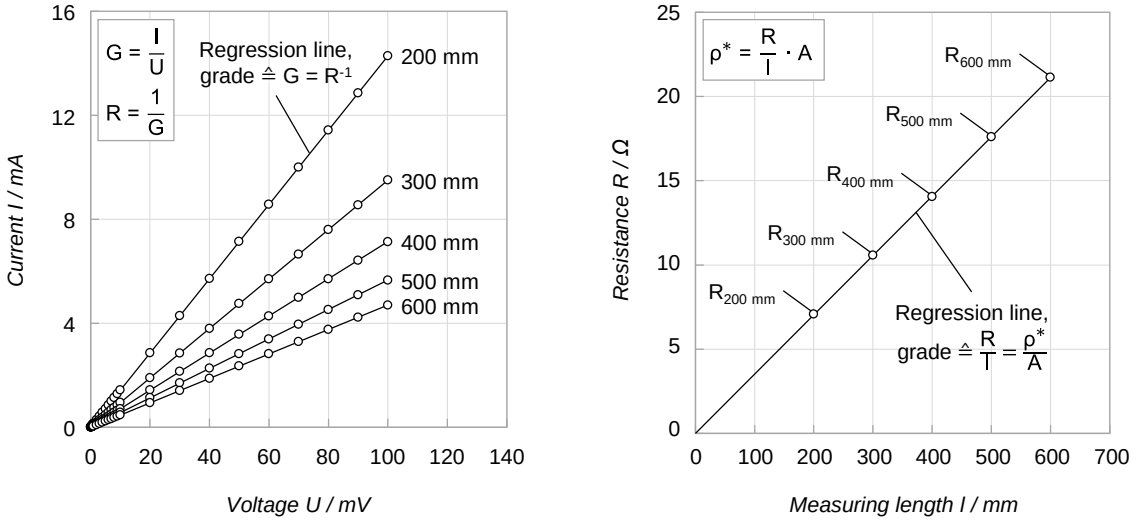

Figure 4.6 Procedure to determine the electrical resistivity of the steel fibre bundles: (left) determination of the absolute resistivity as a function of the measuring length by measuring the current-voltage characteristics and (right) subsequent determination of the length-dependent resistivity and derivation of the specific electrical resistance

The method is repeated for five specimens from different bobbins for each type of steel fibre. By this means, a specific electrical resistance of $(6.97 \pm 0.02) \times 10^{-7}$ Ωm for the stainless steel and $(4.23 \pm 0.04) \times 10^{-8}$ Ωm for the copper cladded low carbon steel fibre bundles is determined. The electrical resistivity of the applied carbon fibres (1.60×10^{-5} Ωm [13]) is known from the supplier data sheet. Due to the lack of manufacturer information, a specific electrical resistance of 1.00×10^{13} Ωm has to be supposed for the dielectric epoxy resin. Compared to the applied carbon fibres, the electrical conductivity of the steel fibre bundles is one to two orders of magnitude higher (factor 23 or 378). The excellent conductance of the copper cladded low carbon steel fibres results from a combination of low alloyed steel core and highly conductive copper cladding. Their specific electrical resistance is only 2.5 times higher than the electrical resistivity of pure copper (1.70×10^{-8} Ωm [17]).

Determination of the specific electrical resistance is additionally carried out on steel

fibre bundles which have been exposed to the temperature and pressure profile emulating the laminate cure cycle. In compliance with the tensile tests, the analysis proves a degradation of the copper cladded low carbon steel fibres. Their specific electrical resistance increases by 4.98 % to $(4.44 \pm 0.18) \times 10^{-8}$ Ωm. The electrical resistivity of the stainless steel fibres, by contrast, remains at $(6.96 \pm 0.08) \times 10^{-7}$ Ωm (-0.25 %).

The four-point-probe-method particularly suits for determination of minor electrical resistances. Since the internal resistance of the voltmeter significantly exceeds the sample resistance, current flow and therefore voltage drop across the lead and the contact clips in the measuring circuit (loop I in figure 4.5 (right)) can be neglected. The measured voltage equates to the voltage drop across the specimen. Current exclusively flows in the source circuit (loop II in figure 4.5 (right)) across the specimen, the amperemeter and the power supply and is therefore entirely captured by the amperemeter. For this reason, the measured current and voltage match the load of the specimen. Consequently, resistances caused by the wiring and the connecting clips do not affect the test result. [123]

However, as a consequence of the current flow, the specimen resistively heats up. The amount of released heat Q is proportional to the converted energy, i.e. the product of voltage U and current I (Joule-Lenz law), eq. 4.5.

$$Q \sim U \cdot I \qquad \text{(Eq. 4.5)}$$

For a positive temperature coefficient (PTC) resistor, such as the steel fibres, the increased temperature raises the electrical resistivity of the specimen. Within certain limits, the resistivity changes linearly with the temperature shift $T - T_0$, eq. 4.6. The proportionality factor α_{T0} is referred to as resistance temperature coefficient. [123]

$$\rho^*(T) = \rho^*(T_0) \cdot \left[1 + \alpha_{T_0} \cdot (T - T_0)\right] \qquad \text{(Eq. 4.6)}$$

In consideration of Ohm's law and assuming a constant current supply, the increased resistivity leads to a higher voltage and therefore to further heating of the specimen (self-enhancing process). By contrast, with a constant voltage feed, a temperature-caused increase of the resistance lowers the current flow and reduces the released heat. Using a constant voltage source therefore autonomously prevents improper heating of the specimen and finally distorted conductivity values (self-stabilising process).

4.5 Properties overview

The essential outcome of the previous steel fibres characterisation is summarised in table 4.4. The overview is complemented by supplier information about the resin and the carbon fibres which are applied within the present work. In general, the stainless steel fibres are distinguished by superior mechanical properties (high ultimate tensile strength, high strain at failure) and corrosion resistance, while the copper cladded low carbon steel fibres provide excellent electrical conductivity. In the following chapter, the listed characteristic values are used to analytically predict the mechanical and electrical properties of uniaxial reinforced composites with different proportions of continuous steel and carbon fibres.

Table 4.4 Properties of the applied resin and fibres [13, 113]

Property	Carbon fibre [a]	Stainless steel fibre [b]	Copper cladded low carbon steel fibre [b]	Epoxy resin [a]
Supplier	Toho Tenax	Bekaert	Bekaert	Cytec
Type	HTS40 F13 12k	Bekinox VNM A 60.7	Bekiflex LR A 63.7	Cycom 977-2
Density ρ / g/cm^3	1.77	7.95 ± 0.01	8.25 ± 0.02	1.31
Young's modulus E / GPa	240	176 ± 7	142 ± 5	3.52
Offset yield strength $\sigma_{p0.2}$ / MPa	-	504 ± 5	479 ± 4	-
Ultimate tensile strength σ_{max} / MPa	4300	897 ± 2	545 ± 4	81.4
Strain at failure ε_{max} / %	1.80	32.31 ± 2.01	15.00 ± 1.29	-
Specific energy absorption e_a / mJ/mm^3	39	244 ± 18^3	77 ± 7	-
Specific electrical resistance ρ^* / Ωm	1.6×10^{-5}	$(6.97 \pm 0.02) \times 10^{-7}$	$(4.23 \pm 0.04) \times 10^{-8}$	-
Filament diameter d_f / µm	7	60.0 ± 0.4	63.4 ± 0.5	-
Filaments per bundle n_f	12k	7	7	-
Linear density λ / tex	799	157	180	-
Glass transition temperature T_g / °C	-	-	-	212 (dry)

[a] data sheet values

[b] measurements on fibre bundles in raw condition (as delivered by supplier)

5 Analytical assessment

Certain properties of a unidirectional continuous fibre reinforced polymer composite can be analytically estimated by means of the rule of mixtures. The derivation of this theoretical approach is based on a micromechanical consideration of the composite and correlates the volume share and the characteristic values of its constituents with the effective (homogenised) properties of the UD layer. Within this chapter, the rule of mixtures is applied to assess prospective property enhancements of the hybrid composite as a function of the steel fibre share, having regard to the characteristic values of the reinforcing fibres and the resin determined in chapter 4. The derived relations are used in chapter 7 to evaluate the results of the experimental UD layer characterisation.

5.1 Density

The density of a material is defined as the ratio of its mass to its volume. For a composite, the total mass or volume is given by the sum of the individual masses or volumes of its components. Considering the volume fraction φ_i and the density ρ_i of each constituent, the mean density of a composite ρ can therefore be expressed as follows, eq. 5.1.

$$\rho = \sum_i \rho_i \cdot \varphi_i \qquad \text{(Eq. 5.1)}$$

If considered as individual phase, eq. 5.1 is valid even in the presence of voids[8]. The density of entrapped air at 20 °C can then be appraised by 1.20×10^{-3} g/cm^3. In the further course of this work, laminates are, however, assumed to be void-free.

5.2 Tensile stiffness

The effective stiffness of an ideal unidirectional continuous fibre reinforced polymer composite can be estimated based on the elastic properties of its constituents. In parallel to the fibre orientation, the composite can be considered as a parallel connection of stiffnesses (Voigt model). The individual components of the composite must bear the same elongation (iso-strain condition), while the total stress is given by

[8] For many structural parts in aeronautical applications, a maximum void content of 2 vol.% is proven acceptable [1].

the sum of the individual loads. Considering Hooke's law, the effective modulus of elasticity of a UD layer in parallel to its fibre orientation E_1 is consequently given by accumulating the individual products of longitudinal elastic modulus $E_{1,i}$ and volume share φ_i of each constituent, eq. 5.2. Typically, this linear rule of mixtures provides an effective Young's modulus which is in good agreement with the experimentally determined value [7].

$$E_1 = \sum_i E_{1,i} \cdot \varphi_i \qquad \text{(Eq. 5.2)}$$

Transverse to the fibre orientation, the composite can be considered as a series connection of stiffnesses (Reuss model). Each constituent of the composite is exposed to the same stress (iso-stress condition). The total strain is given by the sum of the individual strains. As first approximation, the effective modulus of elasticity transverse to the fibre direction E_2 (or E_3) can therefore be estimated in consideration of volume share φ_i and transverse modulus of elasticity $E_{2,i}$ of each constituent according to the inverse rule of mixtures, eq. 5.3.

$$E_2 = \left(\sum_i \frac{\varphi_i}{E_{2,i}} \right)^{-1} \qquad \text{(Eq. 5.3)}$$

However, since the lateral contraction of the resin is limited by the longitudinal stiffness of the reinforcing fibres, the matrix modulus E_R is typically replaced by an increased modulus $\bar{E}_R$, having regard to the Poisson ratio ν_R of the resin, eq. 5.4 [7].

$$\bar{E}_R = \frac{E_R}{1 - \nu_R^2} \qquad \text{(Eq. 5.4)}$$

The simplifying assumptions used in this theoretical approach (e.g. perfect fibre-resin-adhesion, homogeneous microstructure, ideally aligned fibres) are, however, rarely achieved in genuine composites. For this reason, the inverse rule of mixtures for the stiffness of a composite transverse to its fibre orientation is typically extended by a semi-empirical approach, which is adjusted and validated by a series of experimental tests. Typical extensions developed for two-component composites (e.g. by Puck [7]) are therefore not valid for this novel three-phase hybrid material.

Generally, the transverse modulus of the orthotropic carbon fibres is significantly lower than the modulus in parallel to the fibre orientation. The transverse modulus can be appraised by approximately 10 % of the longitudinal modulus [7]. Still, the

transverse modulus of carbon fibres is typically one order of magnitude greater than the isotropic modulus of epoxy resins. By contrast, transverse and longitudinal modulus of the isotropic metal fibres can be considered as equal, neglecting a potential influence of the wire drawing process and, as in case of the copper cladded low carbon steel fibres, the divergent stiffness of coating and core material. This discrepancy in the transverse stiffness of reinforcing fibres and epoxy resin causes significant inhomogeneity in the local material deformation (strain magnification) under transverse load.

Following the analytical approach, both the longitudinal and transverse elastic modulus of a three-component UD layer with a constant resin proportion of 40 vol.% are calculated. For the stainless steel and copper cladded low carbon steel fibres, an isotropic elastic modulus of 176 or 142 GPa is applied (cf. table 4.4). The elastic modulus of the carbon fibres in parallel to the fibre orientation (240 GPa) is taken from the data sheet, while the transverse elastic modulus is appraised by one tenth of the longitudinal modulus (24 GPa). For the epoxy resin, an isotropic elastic modulus of 3.52 GPa is applied according to the supplier information, while for its Poisson ratio a literature value of 0.35 is assumed [7]. For the stainless steel fibre reinforced hybrid laminate, the analytical values are additionally compared with values obtained by numerical simulation. The derivation of these values is described in appendix A.1.

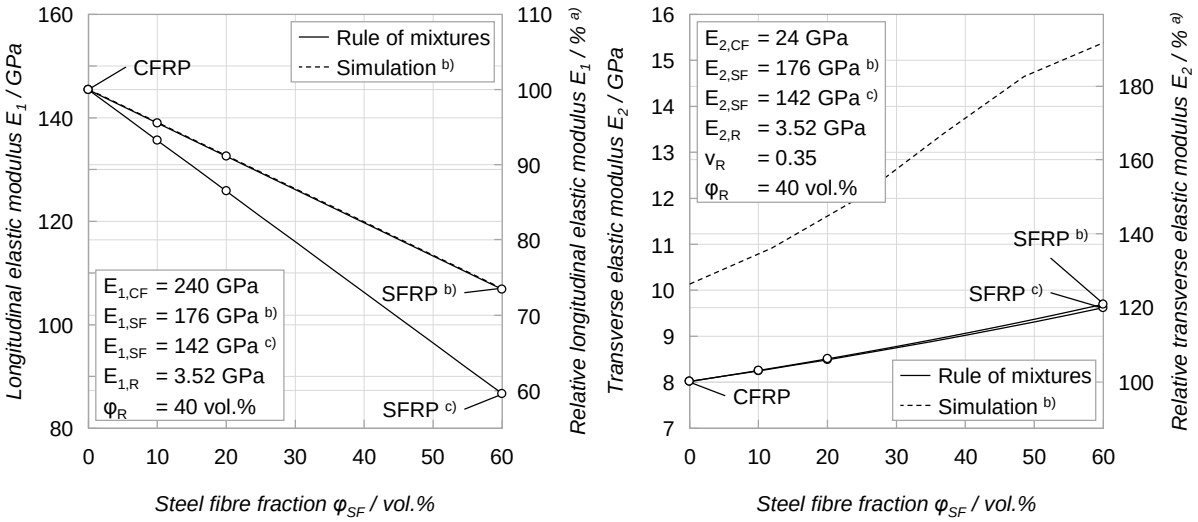

a) compared to unmodified CFRP b) stainless steel fibre c) copper cladded low carbon steel fibre

Figure 5.1 (left) Longitudinal and (right) transverse elastic modulus of unidirectional reinforced (hybrid) composites as a function of the type and volume share of the reinforcing steel fibres

As depicted in figure 5.1 (left), incorporation of steel fibres into CFRP causes a decrease of the laminate tensile modulus in parallel to the fibre orientation[9]. The diminution is caused by the minor elastic modulus of the steel fibre bundles relatively to the longitudinal modulus of the carbon fibres. In case of a stainless steel/carbon fibre hybrid composite, the effective modulus decreases by 4 % for a steel fibre share of 10 vol.% and by 9 % for a steel fibre portion of 20 vol.%. The maximum decrease is 27 % in case of pure stainless steel fibre reinforcement (steel fibre reinforced polymer, SFRP). In case of the copper cladded low carbon steel fibre reinforced composite, the longitudinal modulus is lowered by 7 % or 13 %. For a pure copper cladded low carbon steel fibre reinforced composite, the modulus of elasticity is 40 % lower compared to unmodified CFRP. Simultaneously, incorporation of steel fibres into CFRP leads to an increase of the transverse elastic modulus, figure 5.1 (right). The rise is caused by the isotropy of the steel fibres, i.e. their significantly higher transverse modulus in comparison with the orthotropic carbon fibres. Compared to CFRP, the maximum increase is 21 % for a pure stainless steel fibre reinforced composite and 20 % for a pure copper cladded low carbon steel fibre reinforced composite. In case of the elastic modulus in parallel to the fibre orientation, the analytical approach conforms to the numerical simulation. The maximum deviation is less than 0.2 %. By contrast, transverse to the fibre orientation the deviation of the analytical estimation with respect to the numerical simulation is significantly higher and ranges from 21 to 38 %. This considerable divergence originates from simplifying assumptions of the analytical model (e.g. simplified consideration of the impediment of transverse strain, negligence of the random fibre distribution, disregard of the circular fibre cross-section) which are limited in their validity especially in case of high fibre volume fractions.

[9] In principle, the rule of mixtures suits to predict the effective longitudinal stiffness of a hybrid composite. The estimated values serve to dimension hybrid laminates or to review experimental test results. However, this analytical approach disregards the fact that the multifunctional material concept allows an increase of the laminate thickness without detrimentally affecting the overall weight of the structure (cf. chapter 3.6). Consequently, integration of metal fibres into CFRP does not (necessarily) mean a diminution of the absolute stiffness of a structure despite the decrease in the composite's modulus of elasticity. The same applies to the (longitudinal tensile) strength of a hybrid composite (cf. chapter 5.3). For example: Assuming that the steel fibres (including the corresponding amount of resin) are additionally added to CFRP, a UD reinforced stainless steel/carbon fibre hybrid composite (φ_{SF} = 20 vol.%, φ_{CF} = 40 vol.%, φ_{R} = 40 vol.%) would exhibit 37 % greater absolute stiffness and 7 % higher absolute tensile strength compared to the baseline CFRP (φ_{CF} = 60 vol.%, φ_{R} = 40 vol.%).

5.3 Tensile strength

In order to estimate the longitudinal tensile strength of a hybrid composite, two cases must be distinguished (assuming the following failure sequence: carbon fibres → epoxy resin → steel fibres): In case of minor steel fibre percentages, the effective tensile strength of the composite is dominated by the brittle high-tenacity carbon fibres. After failure of the brittle carbon fibres and the epoxy resin, load is transferred to the steel fibres (due to their higher elongation at break). The load redistribution leads to progressive elongation of the integrated steel fibres. Despite the associated strain hardening (cf. chapter 4.3), the steel fibres themselves are, due to their insufficient strength and/or volume share, unable to bear higher absolute load than the complete hybrid composite prior to failure of the carbon fibres. The effective tensile strength of the hybrid composite therefore corresponds to the mean stress at the moment of failure initiation and can be estimated by means of a linear rule of mixtures (according to the Voigt model). In addition to the respective volume shares φ_i and the ultimate tensile strength of the carbon fibres $\sigma_{1,max,CF}$, the tensile stress of the epoxy resin $\sigma_{1,R}$ and the steel fibres $\sigma_{1,SF}$ at the elongation at break of the carbon fibres $\varepsilon_{1,max,CF}$ must be taken into account, eq. 5.5.

$$\sigma_{1,\max} = \sum_{i} \sigma_{1,(\max),i} \cdot \varphi_i \qquad \text{(Eq. 5.5)}$$

In case of sufficiently high ultimate tensile strength and/or percentage of the integrated steel fibres, the effective tensile strength of the hybrid composite in parallel to its fibre orientation is dominated by the steel fibres. After failure of the carbon fibres and the epoxy resin, the steel fibres are capable of bearing further load increase by strain hardening or phase transformation. The mean stress of the composite at the moment of steel fibre failure surpasses the stress at the moment of carbon fibre failure. The effective tensile strength of the composite is then exclusively given by the product of ultimate tensile strength $\sigma_{1,max,SF}$ and volume fraction of the incorporated steel fibres φ_{SF}, eq. 5.6.

$$\sigma_{1,\max} = \sigma_{1,\max,SF} \cdot \varphi_{SF} \qquad \text{(Eq. 5.6)}$$

Usually, the analytical approach over-estimates the experimentally determined strength of the composite. The reasons are premature damage of the reinforcing fibres during processing, misalignments of the fibres (i.e. heterogeneous load distribution among the individual filaments) or residual stresses within the composite.

According to this analytical approach, the longitudinal tensile strength of a three-component UD layer with a constant resin proportion of 40 vol.% is estimated. The ultimate tensile strength of the carbon fibres (4300 MPa) is taken from the supplier data sheet. For the epoxy resin, the nominal stress at an elongation of 1.80 % (i.e. the strain at failure of the carbon fibres) is calculated assuming a modulus of elasticity of 3.52 GPa and linear elastic behaviour (63 MPa). The corresponding values for the steel fibres are derived from the quasi-static stress-strain curves (cf. chapter 4.3). By this means, a tensile stress of 554 MPa for the stainless steel or 492 MPa for the copper cladded low carbon steel fibres is determined. Moreover, an ultimate tensile strength of 897 or 545 MPa is applied for the steel fibre bundles (cf. table 4.4).

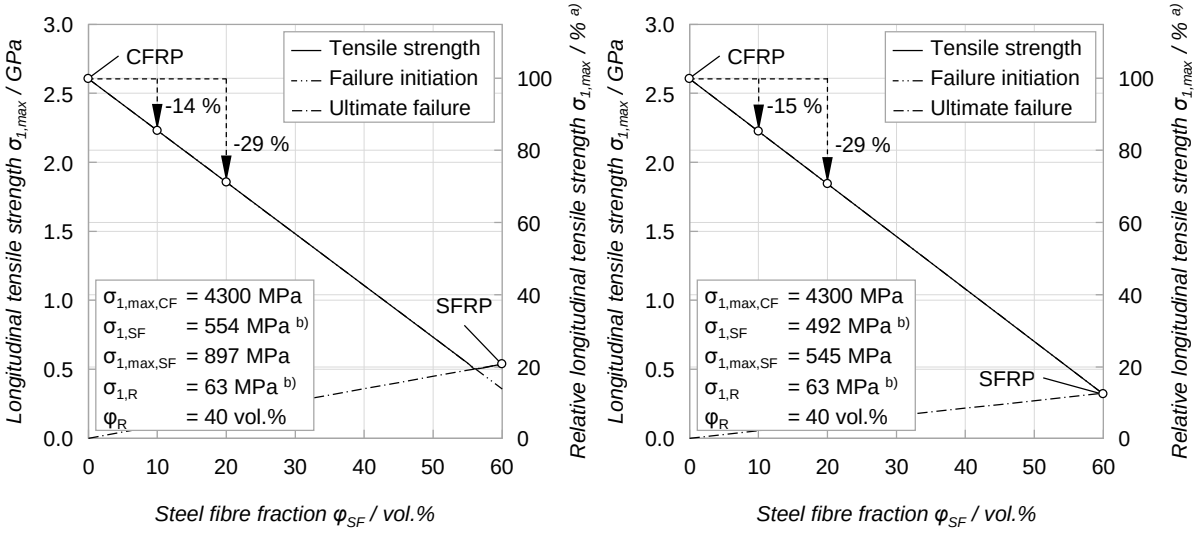

a) compared to unmodified CFRP b) stress at an elongation of $\varepsilon_{1,max,CF}$

Figure 5.2 Tensile strength of unidirectional reinforced (hybrid) composites with (left) stainless steel and (right) copper cladded low carbon steel fibre reinforcement in parallel to the fibre orientation

As depicted in figure 5.2, incorporation of steel fibres into CFRP causes a distinctive decrease of the effective tensile strength of the composite in parallel to its fibre orientation[9]. In case of a stainless steel/carbon fibre hybrid composite, the strength decreases by 14 % for a steel fibre share of 10 vol.% and by 29 % for a steel fibre share of 20 vol.%. A minimum of the effective tensile strength is achieved at a share of stainless steel fibres of 56 vol.%. Up to this share, the effective tensile strength of the composite is dominated by the carbon fibres; the tensile strength is reached at failure initiation, i.e. at the elongation at break of the carbon fibres. For larger shares of stainless steel fibres, the effective tensile strength of the hybrid composite is

dominated by the steel fibres and occurs when exceeding their strain at failure. The tensile strength of pure SFRP reinforced by stainless steel fibres is 538 MPa, which is 79 % less compared to the tensile strength of the unmodified CFRP. In case of the copper cladded low carbon steel fibre reinforced composite, the tensile strength is lowered by 15 % or 29 %. Due to the comparatively low strength of the copper cladded low carbon steel fibres, the carbon fibres define the effective tensile strength of the hybrid composite in any case. The tensile strength of pure SFRP reinforced by copper cladded low carbon steel fibres is 327 MPa, which is 87 % less compared to CFRP.

The transverse tensile strength of a composite is strongly affected by the quality of the fibre-resin-interface and by local stress peaks in the proximity of the reinforcing fibres (notch effect). High transverse stiffness of the fibres causes excessive loading of the resin material (strain magnification, cf. chapter 5.2), which facilitates inter-fibre-failure. The strength of the reinforcing fibres is generally of subordinate importance. Typically, the transverse tensile strength of a composite is therefore experimentally determined. For this reason, an analytical approach for the transverse tensile strength of a multi-phase composite is omitted at this point.

5.4 Electrical conductivity

The specific conductance measures a material's ability to conduct electric current. For a conductor with a uniform cross-section and a homogeneous current distribution, the electrical conductivity κ is defined by the absolute conductance G, the cross-sectional area A and the conductor's length l, eq. 5.7. [123]

$$\kappa = \mathrm{G} \cdot \frac{\mathrm{l}}{\mathrm{A}} \qquad \text{(Eq. 5.7)}$$

The reciprocal value of the specific conductance is denominated as the specific electrical resistance ρ*, eq. 5.8.

$$\rho^* = \kappa^{-1} \qquad \text{(Eq. 5.8)}$$

In fibre direction, an ideal unidirectional continuous fibre reinforced polymer composite can be considered as a parallel circuit of conductors. In this case, the total conductance is given by the sum of the individual conductivities of each conductor. The mean specific conductance in parallel to the fibre orientation κ_1 can therefore be calculated by the rule of mixtures considering the volume fraction φ_i and the longitudinal electrical conductivity $\kappa_{1,i}$ of each constituent, eq. 5.9.

$$\kappa_1 = \sum_i \kappa_{1,i} \cdot \varphi_i = \rho_1^{*-1} \qquad \text{(Eq. 5.9)}$$

Perpendicular to the fibre orientation, the composite can be considered as a series connection of conductors. In this case, the overall resistance is given by the sum of the individual resistances of each conductor. The mean specific conductance transverse to the fibre direction κ_2 (or κ_3) can therefore be calculated having regard to the volume fraction and the transverse electrical conductivity $\kappa_{2,i}$ (or $\kappa_{3,i}$) of each constituent, eq. 5.10. However, the conductivity of the composite perpendicular to the fibre orientation is typically dominated by the dielectric resin and can be neglected (cf. chapter 2.2).

$$\kappa_2 = \left(\sum_i \frac{1}{\kappa_{2,i} \cdot \varphi_i} \right)^{-1} = \rho_2^{*-1} \qquad \text{(Eq. 5.10)}$$

Figure 5.3 illustrates the rule of mixtures for the specific electrical resistance of a three-component UD composite with a constant resin share of 40 vol.% in parallel to the fibre orientation, assuming a volume resistivity of 6.97×10^{-7} Ωm for the stainless steel fibres, 4.23×10^{-8} Ωm for the copper cladded low carbon steel fibres and 1.60×10^{-5} Ωm for the carbon fibres. For the epoxy resin, a specific electrical

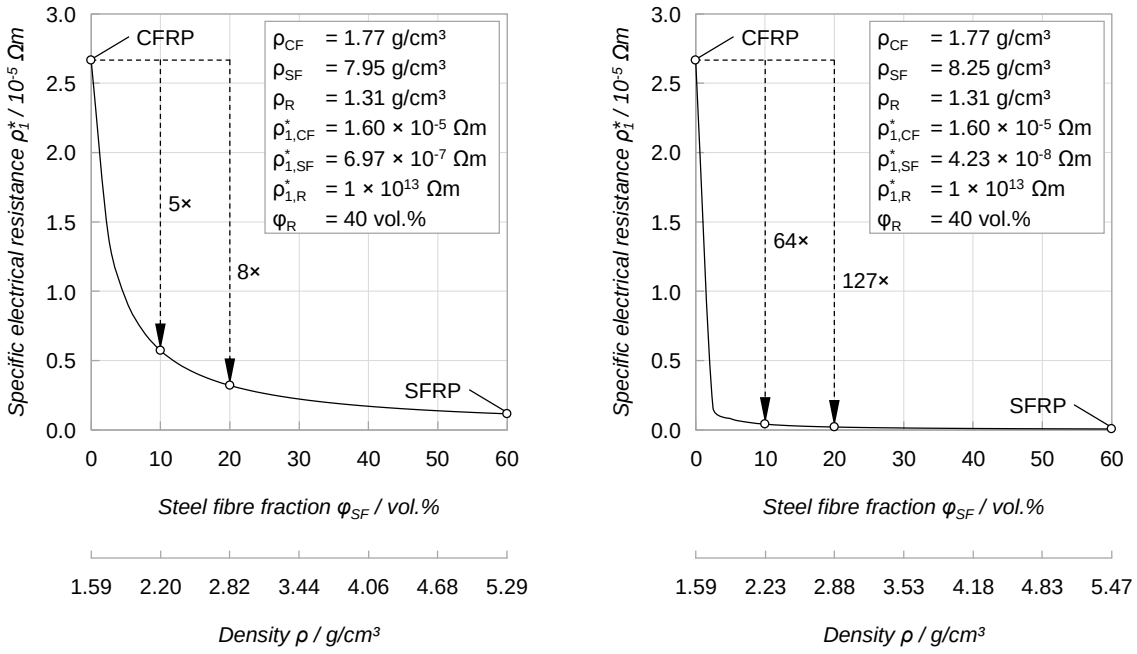

Figure 5.3 Specific electrical resistance in parallel to the fibre orientation of unidirectional reinforced (hybrid) composites with (left) stainless steel and (right) copper cladded low carbon steel fibre reinforcement

resistance of 1.00×10^{13} Ωm is supposed (cf. table 4.4).

Following the analytical approach, a stainless steel/carbon fibre hybrid composite demonstrates an electrical conductivity in parallel to the fibre direction of more than 5 times the conductivity of conventional CFRP (2.67×10^{-5} Ωm) for a steel fibre share of 10 vol.% (5.73×10^{-6} Ωm) and 8 times for a steel fibre fraction of 20 vol.% (3.21×10^{-6} Ωm). Simultaneously, the density rises from 1.59 g/cm^3 to 2.20 g/cm^3 or 2.82 g/cm^3. In case of the copper cladded low carbon steel fibres, the electrical conductivity of the hybrid composite is increased by a factor of 64 (4.18×10^{-7} Ωm) and 127 (2.10×10^{-7} Ωm), respectively. The density rises to 2.23 g/cm^3 or 2.88 g/cm^3. Further enhancements of the electrical conductivity can be achieved by higher steel fibre portions; in case of pure steel fibre reinforcement, the specific conductance rises by a factor of 23 (1.16×10^{-6} Ωm) for the stainless steel fibres and by a factor of 378 (7.05×10^{-8} Ωm) for the copper cladded low carbon steel fibres. The density then increases to 5.29 g/cm^3 and 5.47 g/cm^3, respectively.[10]

[10] For comparison: The specific electrical resistance of aluminium alloys ranges from 2.70 to 6.10×10^{-8} Ωm at a density of 2.59 to 2.91 g/cm^3 [16].

6 Material preparation

In order to provide different laminate configurations for the experimental study on the influence of the hybridisation of CFRP, an in-house manufacturing process, which focuses on production flexibility and manufacturing quality, is established. The process enables systematic and accurate deposition of individual steel fibre bundles, hence different grades of hybridisation and spatial arrangements of the steel fibres within the composite. In the following chapter, the applied manufacturing process is described in detail. Moreover, the individual steps of the specimen preparation are specified.

6.1 Material fabrication

The hybrid composites are manufactured using a combination of tape deposition and filament winding technology. Unidirectional layers of pre-impregnated carbon fibres of type Cycom 977-2-35-12KHTS-134 are stacked on a plain steel winding core and wrapped in dry steel fibre bundles. The deposition rate of the bundles is set to 5 m/min, which corresponds to 0.79 g/min for the stainless steel or 0.90 g/min for the copper cladded low carbon steel fibre bundles. The resin required for steel fibre impregnation originates from the resin excess (bleed) of the prepreg layers and/or additional resin films of type Cycom 977-2-40, respectively. Pure SFRP is prepared

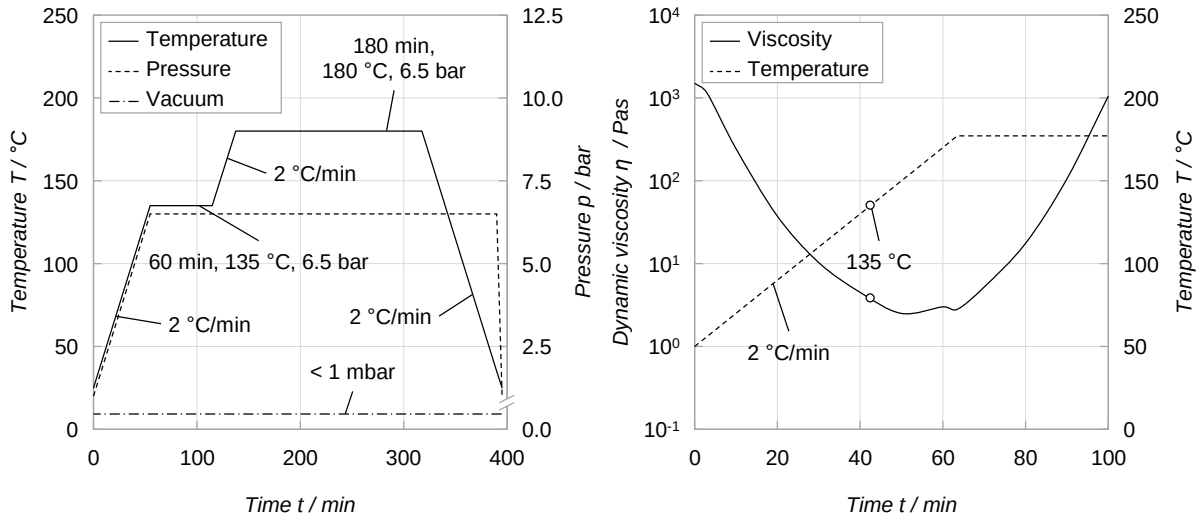

Figure 6.1 (left) Laminate cure cycle and (right) dynamic viscosity of the applied epoxy resin as a function of the temperature [113]

by an analogue procedure. As reference material, conventional CFRP is manufactured by an open moulding prepreg lay-up process. All laminates are cured using autoclave technology. The two-stage cure cycle consists of a one hour dwell

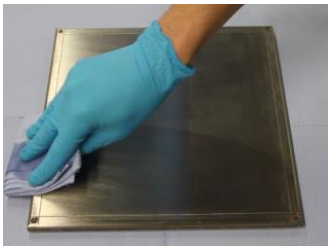	• Careful removal of coarse contaminations (e.g. cured resin) from the tooling (winding core and caul plates) with a glass scraper • **Cleaning and degreasing of the tooling** with acetone • Repeated **application of release agent** (Frekote 770-NC) to the tooling • Fixture of peel ply (Tygavac 60BR) on the winding core with polyimide adhesive tape
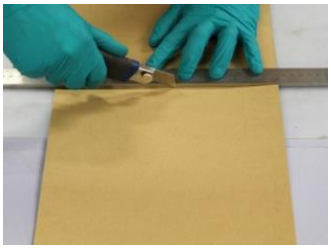	• Thawing of the bagged prepreg and resin films to room temperature • Unpacking the prepreg and resin film • **Pre-cut of resin and prepreg plies** (260 mm × 260 mm) with 0° and 45° fibre orientation
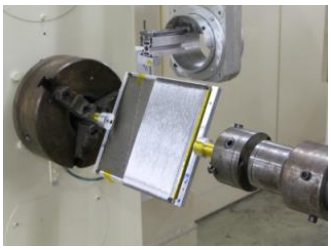	• **Winding of the steel fibre bundles and tape deposition** according to the designated laminate stacking sequence (fibre deposition rate: 5 m/min) • During winding: controlling the drag of the steel fibre bundle by a tensioner • Pressing the prepreg plies with a teflon roller to adjacent plies • Taping the margins of each steel fibre ply to provide pristine, plane edges for the next winding layer
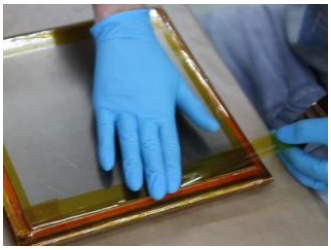	• Fixture of peel ply with polyimide adhesive tape on top of the laminates • Application of caul plates (255 mm × 255 mm) on top of the laminates • **Sealing of the tooling** with polyimide adhesive tape to avoid resin bleed • Minor perforation of the sealing with a needle to allow evacuation of entrapped air within the composite
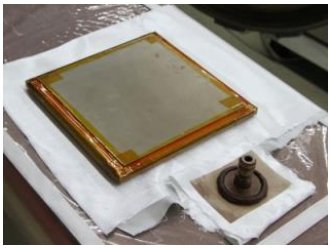	• Draping breather (glass fibre fabric) around the laminate/tooling package • **Vacuum bagging of the laminate/tooling assembly** • Evacuation of the vacuum bag (< 1 mbar)
	• **Curing by means of autoclave technology** (2 °C/min, 1 h/135 °C/6.5 bar, 3 h/180 °C/6.5 bar) • Removal of vacuum bag, breather fabric and caul plates • Demoulding of the composite sheets • Edge trimming of the composite sheets (250 mm × 250 mm)

Figure 6.2 Stepwise description of the applied manufacturing process of hybrid and pure steel fibre reinforced composites

time at 135 °C followed by a three hour cure time at 180 °C. The heat-up and cooling rate is 2 °C/min. Full pressurisation of 6.5 bar is applied from the beginning of the 135 °C stage to the end of the cure cycle, figure 6.1 (left). During the initial heat-up, the resin viscosity decreases and attains nearly its minimum at 135 °C, figure 6.1 (right). By interrupting the heating at this temperature, cross-linking of the epoxy resin accompanied by a re-gain of its dynamic viscosity is delayed. The minor viscosity facilitates impregnation and consolidation of the laminates as well as removal of entrapped air and volatiles. This is of particular interest for the hybrid and pure steel fibre reinforced laminates, which contain process-related gaps between the steel fibre bundles and thus considerable air inclusion prior to cure. A detailed analysis of the cure behaviour of the resin for the applied autoclave cycle is given in appendix A.2. Finally, the cured hybrid or SFRP laminates are released from the tooling by removing the steel fibres at the end faces of the winding core. By this procedure, multi-layered laminates with different steel and carbon fibre proportions, steel fibre distributions and stacking sequences are prepared. The individual steps of the manufacturing process are described in figure 6.2.

In case of uniaxial hybrid laminates, the steel fibre bundles are pressed into adjacent CFRP plies by the consolidation pressure during laminate cure. The carbon fibres fill the gaps between the steel fibre bundles and closely adapt to their outer cavities, figure 6.3. The twist of the steel fibre bundles, however, prevents individual carbon fibres to penetrate into the spacing between the steel filaments, figure 6.3 (left).

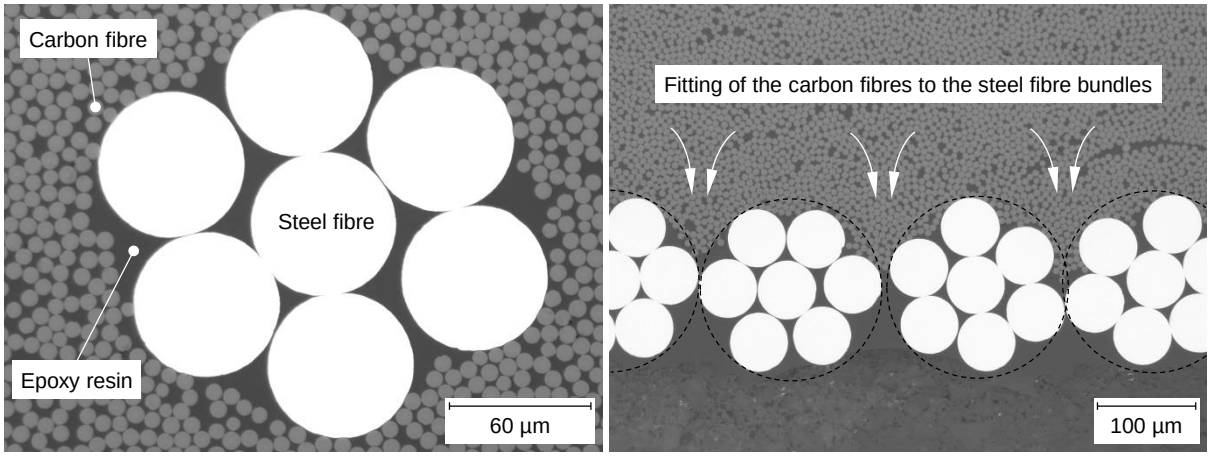

Figure 6.3 Interaction of steel and carbon fibres in case of unidirectional reinforced hybrid composites with (left) homogeneous and (right) concentrated steel fibre arrangement

Exploiting this effect, hybrid composites with a homogeneous steel fibre distribution (according to the homogeneous layer concept, cf. figure 3.2) are manufactured by alternating prepreg and intermittent steel fibre layers. By contrast, selecting a winding feed of approximately the diameter of the bundles envelope enables to manufacture pure steel fibre reinforced layers, hence laminates according to the separated layer concept or pure SFRP. In this case, individual steel fibre bundles are arranged next to each other. Carbon or steel fibres of adjacent plies with common fibre orientation, however, still fit to the outer gaps of the steel fibre reinforced layer. Straight-lined borders to adjacent plies are consequently not given, figure 6.3 (right).

If the adjacent layers are of different fibre orientation, the individual plies are clearly separated from each other. The thickness of the steel fibre reinforced layers is then inherently given by the structure of the steel fibre bundles. The twist of the bundles mostly prevents a disintegration of their hexagonal packing. As a consequence, the nominal thickness of the steel fibre layers ranges between 164 to 180 µm[11] for the stainless steel fibre and 175 to 192 µm[11] for the copper cladded low carbon steel fibre bundles, figure 6.4 (left). The remaining space between the steel fibres is entirely filled with resin. The structural integrity of the steel fibre bundles, however, also involves the risk of inducing out-of-plane waviness in adjacent plies by intersecting steel fibre bundles (e.g. as a result of insufficient bundle drag during the winding process), figure 6.4 (right).

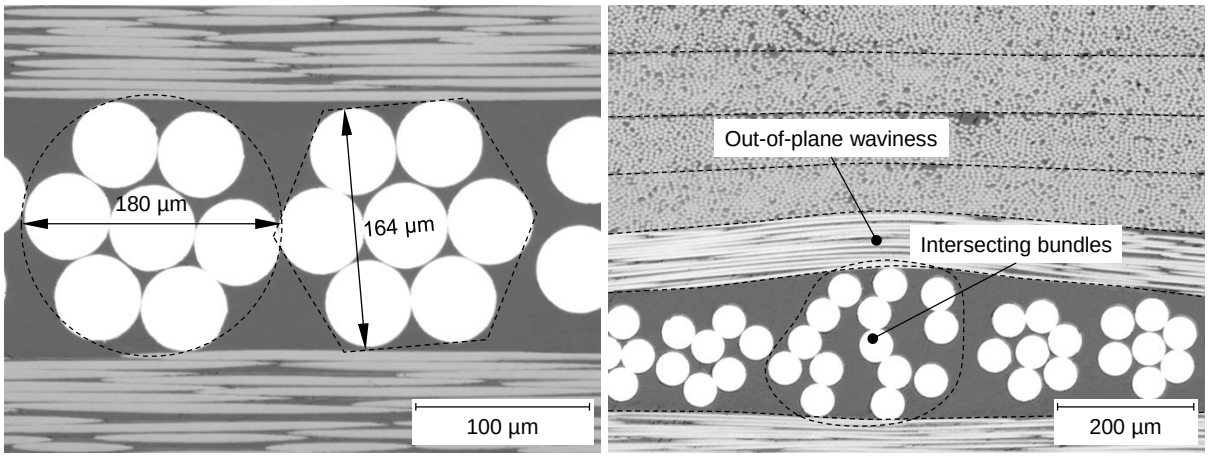

Figure 6.4 Interaction of steel and carbon fibres in case of multiaxial hybrid laminates with concentrated steel fibre arrangement

[11] The stated values correspond to the double apothem a of the circumscribing hexagon ($2 \cdot a = d_f + \sqrt{3} \cdot d_f$) or the diameter d of the circumscribing circle ($d = 3 \cdot d_f$) of the fibre bundles (with d_f as filament diameter).

6.2 Laminate design

The amount of steel fibres per layer can be adjusted by the feed rate of the winding process. The resulting fibre areal weight (FAW) and the corresponding apparent[12] cured ply thickness (CPT) for pre-dimensioning the laminate can be calculated in consideration of the feed rate of the filament winding process f_w, the density of the steel fibres ρ_{SF}, the mean filament diameter d_{SF} and the number of filaments per bundle n_{SF}, eq. 6.1 and eq. 6.2. Since the steel fibres are wound without prior resin impregnation, the fibre areal weight equals the ply areal weight (PAW).

$$FAW_{SF} = \rho_{SF} \cdot \left[\left(\frac{\pi}{4} \cdot d_{SF}^2\right) \cdot n_{SF}\right] \cdot \frac{1}{f_w} \quad \text{(Eq. 6.1)}$$

$$CPT_{SF} = \left[\left(\frac{\pi}{4} \cdot d_{SF}^2\right) \cdot n_{SF}\right] \cdot \frac{1}{f_w} \quad \text{(Eq. 6.2)}$$

Table 6.1 Design relevant properties of the processed prepreg, resin film, steel fibre reinforced non-crimp fabrics and LSP copper mesh [49, 113, 124]

Property	Prepreg 977-2-12k-HTS	Resin film 977-2	Steel NCF Bekiflex LR A 63.7		
Winding feed f_w / mm/rev	-	-	1.720	0.860	0.200
Fibre density ρ_f / g/cm^3	1.77	-	8.25	8.25	8.25
Resin density ρ_R / g/cm^3	1.31	1.31	-	-	-
Ply areal weight PAW / g/m^2	206	40	105	209	901
Fibre areal weight FAW / g/m^2	134	-	105	209	901
Resin areal weight RAW / g/m^2	72	40	-	-	-
Cured ply thickness CPT / µm	131	31	13	25	109

Property	Steel NCF Bekinox VNM A 60.7				LSP copper mesh 3CU7-100FA
Winding feed f_w / mm/rev	1.560	0.780	0.195	0.190	-
Fibre density ρ_f / g/cm^3	7.95	7.95	7.95	7.95	8.92
Resin density ρ_R / g/cm^3	-	-	-	-	-
Ply areal weight PAW / g/m^2	101	202	807	828	195
Fibre areal weight FAW / g/m^2	101	202	807	828	195
Resin areal weight RAW / g/m^2	-	-	-	-	-
Cured ply thickness CPT / µm	13	25	101	104	22

[12] As discussed before, the thickness of the steel fibre layers is given by the structure of the twisted bundles and additionally depends on the interaction with the adjacent plies. However, for the design process of the laminate (e.g. calculation of the volume shares or the overall laminate thickness), an apparent CPT, which equates to the thickness of a compact steel ply with identical areal weight, can be calculated.

For the prepreg, resin film and LSP copper mesh (Dexmet 3CU7-100FA) applied in this study, the corresponding values are taken from the supplier data sheets. Within the present work, steel fibre reinforced layers with different fibre areal weights are manufactured to realise various uni- and multiaxial reinforced laminates (cf. figure 7.1 and figure 8.1). Table 6.1 summarises the characteristics of the wound and/or applied non-crimp fabrics (NCF).

With this data, the overall thickness t of the cured laminates can be calculated according to eq. 6.3, allowing for the number n_i and types of layers. Due to the resin uptake by the peel ply of type Tygavac 60BR [125] applied on both sides of the laminates, a resin loss t_{bleed} of 100 µm (or 131 g/m^2) has to be considered.

$$t = \sum_i n_i \cdot CPT_i - t_{bleed} \qquad \text{(Eq. 6.3)}$$

Moreover, correlation of laminate thickness, fibre areal weights and fibre densities yields the volume shares φ_i of carbon and metal fibres, eq. 6.4. The remaining portion consists of resin, assuming a void-free laminate.

$$\varphi_i = \frac{1}{t} \cdot \left(n_i \cdot \frac{FAW_i}{\rho_i} \right) \qquad \text{(Eq. 6.4)}$$

For the homogeneous, uniaxial reinforced hybrid laminates, variation of the steel fibre share is achieved by adapting the winding feed (cf. figure 7.1). In this way, a most homogeneous distribution of the steel fibres is ensured. For all the other hybrid laminate configurations, the winding feed is kept consistent. Different steel fibre percentages are then realised by varying the ratio of carbon and steel fibre reinforced layers or the number of resin films.

6.3 Alternative manufacturing processes

Main drawbacks of the established manufacturing process are the minor material output, the restriction of the steel fibre layers on two orthogonal orientations and the limited complexity of the producible part geometry. Even though these deficiencies are acceptable for analysing the basic functionality of the hybrid material on coupon level, more efficient processes are required for advanced investigations and future industrial applications. In principle, established processes such as weaving or prepreg fabrication are suitable to prepare dry or pre-impregnated woven or non-crimp fabrics, which can then be integrated in established lay-up processes. Prepreg

manufacturing (e.g. hot melt or solvent dip process) provides pre-impregnated fabrics with pre-assigned resin content (approximately 10 wt.% of resin corresponds to 60 vol.% of steel fibres). By contrast, weaving enables manufacturing of dry fabrics. Undulations can be minimised by application of compliant thermoset weft or warp yarn (fabrication of quasi-UD non-crimp fabrics), figure 6.5 (left). Both technologies allow processing of monofilaments, bundles or rovings. Processing of rovings, however, requires proper methods to homogeneously spread the individual filaments (e.g. by means of bassets, ultrasonic vibration, Fukui principle or curved rollers).

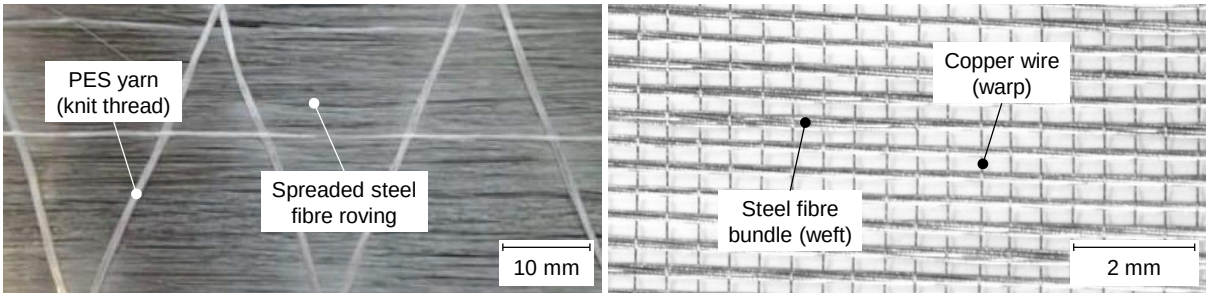

Figure 6.5 Exemplary configurations of quasi-UD steel fibre fabrics: (left) non-twisted 1.4401 steel fibre rovings with polyethylene succinate (PES) yarn [97] and (right) 1.4301 steel fibre bundles with copper warp wires

6.4 Specimen preparation

Following material manufacturing, specimens are extracted from the composite sheets by band saw cutting with a guided, diamond-studded saw band (Diagrit K, grit 91). After machining, all edges of the specimens are wet-polished with abrasive paper (grit 1200) to eliminate any existing notches. Drill holes in the specimens are created using a CNC (computer numeric controlled) milling machine with solid carbide drill bits with a W-shaped tip and a recommended cutting speed (peripheral velocity) of 120 m/min. The special tip geometry minimises the risk of peel-up delamination by cutting the reinforcing fibres of the composite at the edge of the drill hole and thus improves roundness and edge quality of the drill hole. In order to avoid steel fibre pull-outs at near-surface layers or push-out delamination at the exit of the drill bit, specimens are co-drilled with GFRP plates pressed to both sides of the laminate [126]. Evaluation of the drill hole quality by means of white light interferometry (WLI) and light optical microscopy (LOM) proves minor differences between CFRP and the hybrid composites, figure 6.6. Typically, the delamination factor f_d is slightly higher on the drill bit exit compared to the entry side. In case of

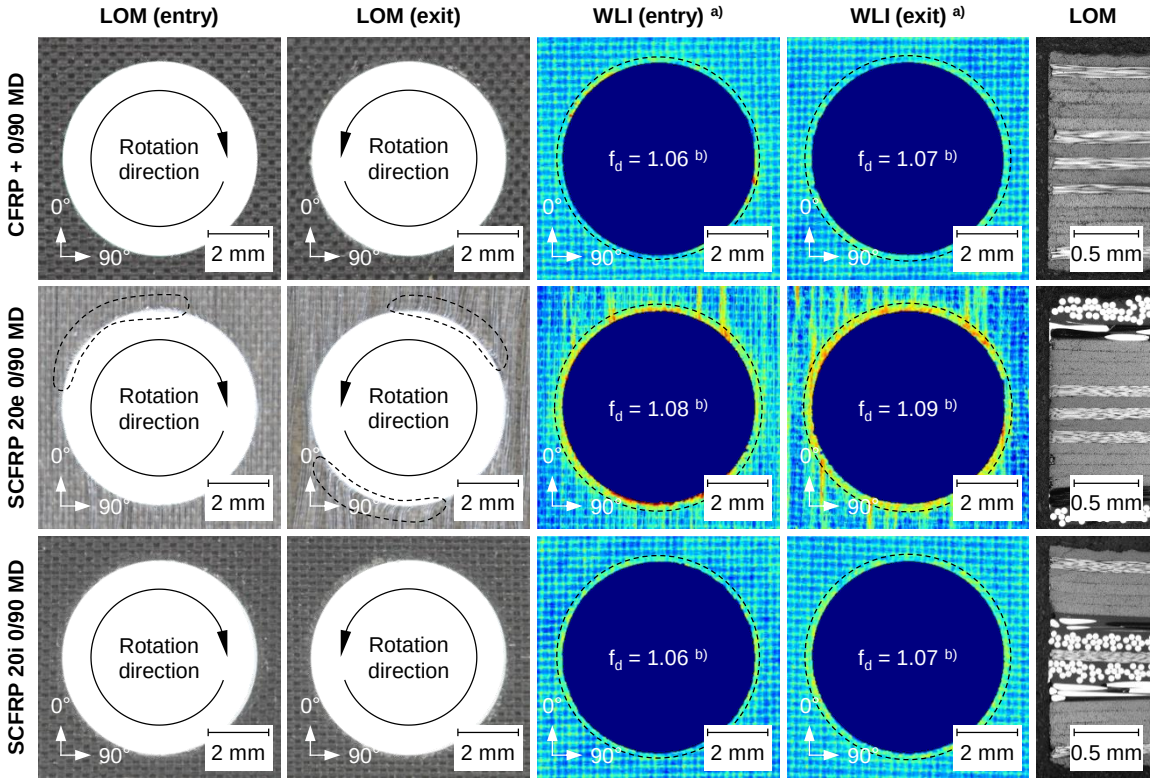

a) The illustration of the out-of-plane shape of the laminate surface ranges from -0.05 (blue) to 0.10 mm (red).

b) The delamination factor f_d is defined as the ratio of maximum damage diameter to nominal drill hole diameter.

Figure 6.6 Comparison of the drill hole quality between CFRP and hybrid composites with SFRP layers on top or at the centre of the laminate

steel fibre reinforced top layers, the ductile steel fibres tend to be displaced tangentially to the drill hole edge at the quadrants with a cutting angle (angle enclosed by the fibre orientation and the cutter engagement) of 0 to 90° due to insufficient lateral material support. If required by the relevant test specification, specimens are provided with chamfered end tabs made of 1 mm thick GFRP cross-ply laminate. Prior to application, the tabs are roughened with abrasive paper (grit 180) and cleaned with acetone. The tabs are subsequently bonded to the specimen with epoxy-based two-component adhesive of type UHU plus endfest 300 [127]. The adhesive is cured for 10 min at a temperature of 100 °C. The specimen tabs enable application of coarse grip surfaces and consequently low grip pressure while preventing surface damage to the specimen. Additionally, the tabs serve to reduce stress concentrations induced at the specimen restraints [128]. Finally, to remove absorbed moisture (e.g. originating from cooling lubricant or ambient air) and to ensure defined material conditions, all specimens are desiccated in a drying oven for 168 hours at a temperature of 50 °C and a pressure of 30 mbar.

7 Uniaxial layer characterisation

In the following chapter, the mechanical and electrical properties of uniaxial reinforced (hybrid) composites are experimentally analysed. For this purpose, different hybrid composites with steel fibre shares between 10.4 and 21.4 vol.% are prepared and tested. Both homogeneous and separated layer concept are considered. For comparison reasons, pure CFRP and SFRP are taken into account. The microstructure, stacking sequence and calculated characteristics of the manufactured material configurations are specified in figure 7.1. The composites are tested with regard to their fibre-resin-adhesion, plain tensile behaviour, bending-tensile properties and electrical conductivity. Material configurations which contain

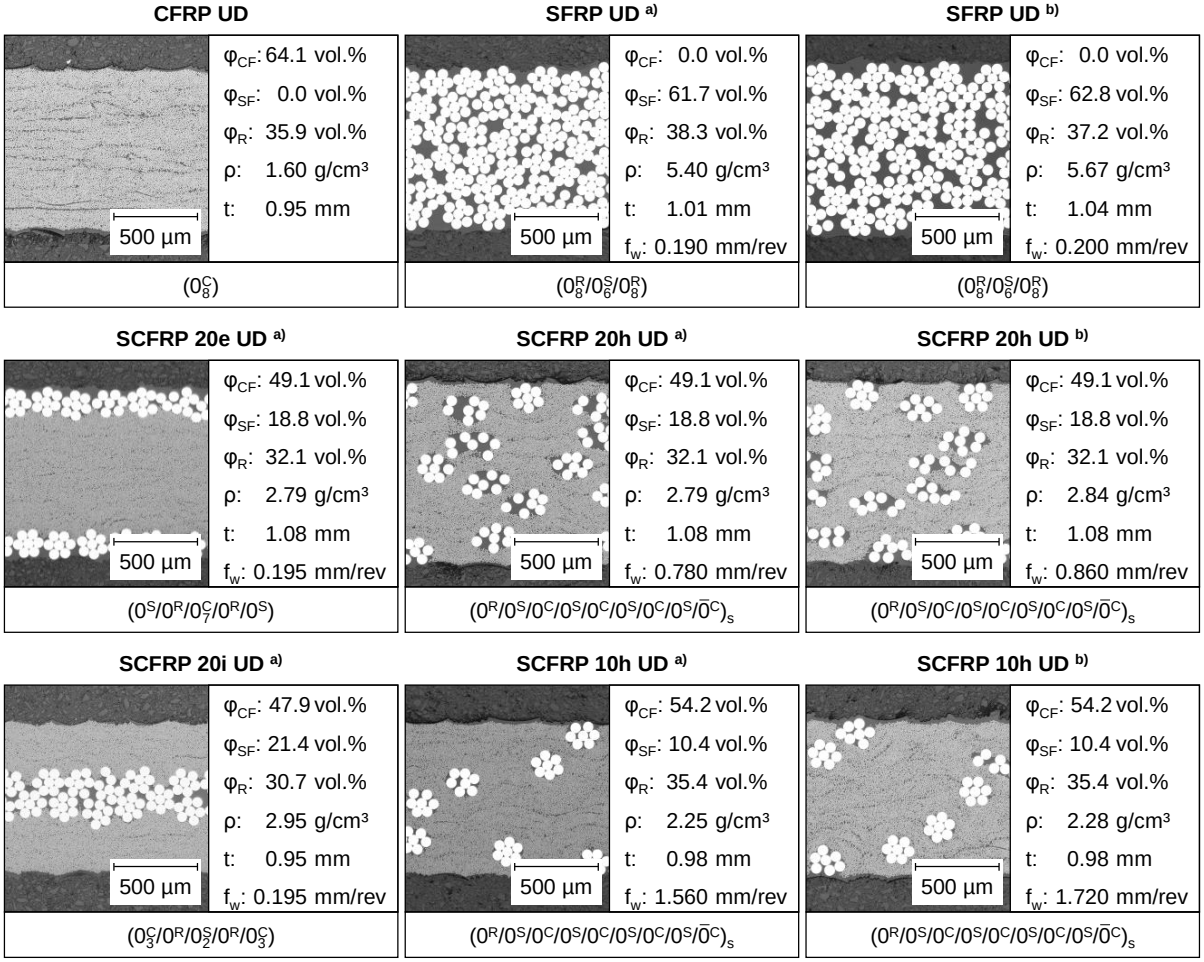

C: carbon, S: steel, R: resin, φ: volume share, ρ: density, t: laminate thickness, f_w: winding feed rate

a) stainless steel fibre reinforced b) copper cladded low carbon steel fibre reinforced

Figure 7.1 Microstructure and calculated characteristics of the manufactured and analysed uniaxial reinforced (hybrid) composites

copper cladded low carbon steel fibres are, however, tested only regarding their electrical conductivity due to their embrittlement during laminate cure (cf. chapter 4.3.2).

7.1 Density

The volume fractions listed in figure 7.1 are analytically determined by means of eq. 6.4 and the ply areal weights specified in table 6.1. In order to verify the accuracy of these values, the density of the UD composites is experimentally determined and compared with values calculated by the rule of mixtures. Due to the pronounced surface roughness of the composites caused by the application of peel ply, the density measurements are carried out by means of the liquid displacement method (cf. chapter 4.2). For each material configuration, two rectangular specimens with a length of 30 mm and a width of 25 mm are analysed. The calculated densities are obtained by means of the rule of mixtures using the fibres and resin densities listed in table 4.4 as well as the calculated volume shares given in figure 7.1.

Table 7.1 Comparison of calculated and measured densities of unidirectional reinforced (hybrid) composites

Material	Density (calculated) ρ_c / g/cm^3	Density (measured) ρ_m / g/cm^3	Deviation ρ_m to ρ_c / %
CFRP UD	1.60	1.60 ± 0.00	-0.04
SCFRP 10h UD [a)]	2.25	2.26 ± 0.02	+0.41
SCFRP 20h UD [a)]	2.79	2.75 ± 0.01	-1.24
SCFRP 20e UD [a)]	2.79	2.85 ± 0.00	+2.16
SCFRP 20i UD [a)]	2.95	3.00 ± 0.00	+1.63
SFRP [a)]	5.40	5.53 ± 0.03	+2.25
SCFRP 10h UD [b)]	2.28	2.28 ± 0.01	-0.21
SCFRP 20h UD [b)]	2.84	2.80 ± 0.01	-1.47
SFRP [b)]	5.67	5.57 ± 0.00	-1.73

[a)] stainless steel fibre reinforced

[b)] copper cladded low carbon steel fibre reinforced

As shown in table 7.1, the measured densities are in good agreement with the estimated values. The deviations range from -1.73 % for SFRP reinforced by copper cladded low carbon steel fibres to +2.25 % for SFRP reinforced by stainless steel fibres. The least difference occurs in case of CFRP. Assuming exact values for the applied fibre and resin densities, the minor deviations confirm proper values of the

calculated volume shares. In the following chapters, these volume shares can therefore be applied to evaluate the measured mechanical and electrical layer properties by comparison with characteristic values determined by means of numerical simulation or the analytical approaches derived in chapter 5.

7.2 Fibre resin adhesion

The load transfer of the fibre-resin-interface is of major concern for the overall performance of the (hybrid) composite. The interface can be influenced by modifications of the resin (e.g. by addition of functional groups) or the fibre surface (e.g. by application of coupling agents). Poor fibre-resin-adhesion promotes adhesive failure of the interface (inter-fibre-failure). In addition, insufficient adhesion or minor intralaminar gaps facilitate moisture ingress, which is of particular meaning in terms of corrosion of reinforcing metal fibres. As shown in chapter 7.3, perfect bonding to the resin conversely prevents unrestrained elongation of the embedded steel fibres, which detrimentally affects the post-damage performance of the hybrid composite. The optimal surface condition is consequently a trade-off between conflicting requirements. In this subsection, the delivery condition and possible modifications of the surface of the applied stainless steel fibre are therefore investigated.

In a first step, the delivery condition of the stainless steel fibre surface is characterised by means of SEM and EDX (energy dispersive X-ray) spectroscopy. The analysis reveals minor organic and inorganic contamination of the metal fibres, which result from wire drawing (lubrication) and cord making, figure 7.2.

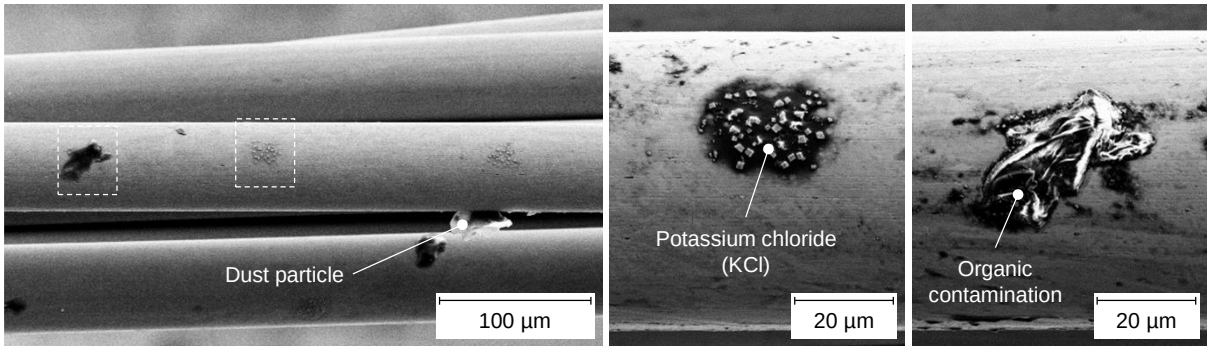

Figure 7.2 Typical contamination of the stainless steel fibre surface in delivery condition (as provided by supplier)

In order to remove the detected contamination and to ensure defined, reproducible surface conditions, the stainless steel fibre bundles are pre-treated by a two-step

purification process. Coarse and inorganic depositions (e.g. dust particles or salt impurities) are initially removed by means of hot distilled water purge (T = 50 °C). The passively dried fibres are subsequently treated by atmospheric pressure plasma (PlasmaTreat FG1001/RD1004) to eliminate any organic residue and to chemically activate the fibre surface. Alternative cleaning methods, such as ultrasonic cleaning in distilled water, lead to a similar purification quality. Moreover, a second surface condition aiming to minimise the fibre-resin-adhesion by selective contamination of the stainless steel fibre bundles is prepared. For this purpose, the purified fibres are additionally irrigated with release agent of type Loctite Frekote 770-NC [129].

A qualitative evaluation of the fibre pre-treatment by means of SEM is given in figure 7.3. As shown, impurities are almost completely removed by the applied purification process. Subsequent application of release agent generates a homogeneous but discontinuous coating of the steel fibre surface.

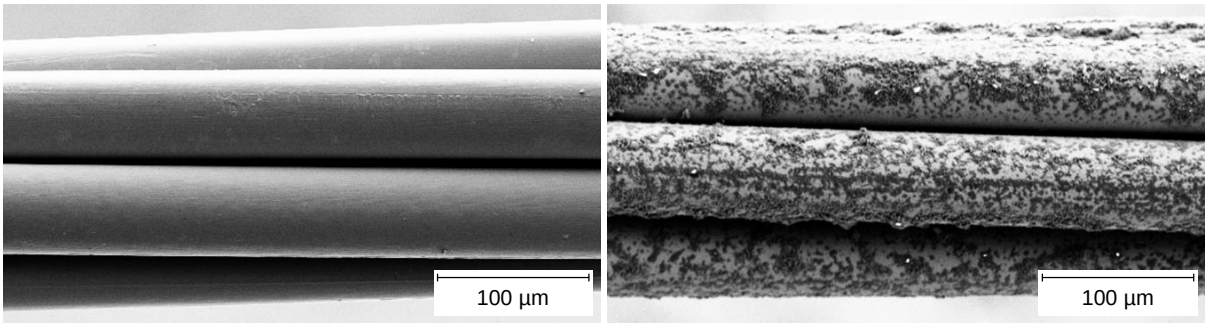

Figure 7.3 Surface condition of the stainless steel fibre bundles: (left) cleaned by hot water purge and atmospheric plasma and (right) additionally coated with release agent of type Loctite Frekote 770-NC

In order to quantify the influence of the surface modification on the fibre-resin-adhesion, short beam bending tests are carried out according to DIN EN 2563 [130]. The test method involves loading of the material (stainless steel fibre reinforced SFRP with different fibre surface treatments) under symmetrical three-point bending load. By choosing a small span length-to-specimen thickness ratio of 5 (in compliance with the applied standard), the laminate is exposed to a shear stress dominated stress state. This is possible since the shear stress is independent of the bearing distance, whereas the bending stresses depend linearly on the support length. According to Euler-Bernoulli beam theory, the induced shear stress varies parabolically from zero on the specimen top and bottom surfaces to a maximum at the specimen midplane. As a consequence, single or multiple shear failure typically

occurs at or near the neutral axis of the coupon. The apparent interlaminar shear strength τ_{max} is then calculated in consideration of the load at failure F_{max}, the width w and thickness t of the specimen, eq. 7.1.

$$\tau_{max} = \frac{3 \cdot F_{max}}{4 \cdot w \cdot t} \qquad \text{(Eq. 7.1)}$$

Since the interlaminar failure resistance primarily depends on the fibre-resin-adhesion, the ascertained values can be used to assess the outcome of the surface pre-treatment. For each surface configuration, five specimens are analysed. Table 7.2 summarises the obtained results. The interlaminar shear strength is given both as absolute value and relatively to the corresponding unmodified composite.

Table 7.2 Influence of the surface pre-treatment on the steel fibre-resin-adhesion of stainless steel fibre reinforced SFRP

Surface condition	Interlaminar shear strength τ_{max} / MPa	Rel. interlaminar shear strength τ_{max} / %
Raw (as delivered)	101.0 ± 1.4	100.0 ± 1.3
Cleaned (hot water & atmosphere plasma)	100.7 ± 1.7	99.7 ± 1.7
Contaminated (release agent)	73.1 ± 1.6	72.4 ± 1.6

As shown by the measurements, extensive purification of the fibre surface has no significant influence on the bond between the steel fibres and the resin. Compared to the composite with the untreated fibres, the interlaminar shear strength remains unaffected. By contrast, a considerable diminution of the steel fibre-resin-adhesion can be achieved by selective contamination of the steel fibre surface; application of release agent to the steel fibres reduces the interlaminar shear strength by approximately 28 %. Nonetheless, due to the considerable effort, fibre surface pre-treatments are omitted in the further course of this work.

7.3 Longitudinal tensile behaviour

In order to assess the influence of the integration of ductile steel fibre on the tensile properties of CFRP, in particular on the failure behaviour, tensile tests in parallel to the fibre orientation are conducted with a hydraulic testing machine (Zwick Roell HTM 5020) in dependence on DIN EN ISO 527-5 [131]. The rectangular specimens with a length of 250 mm and a width of 15 mm are provided with 1 mm thick, chamfered GFRP end tabs. The specimens are clamped with a free length of 150 mm and loaded with a monotonic crosshead speed of 3 mm/s. This loading speed complies

with a nominal strain rate of 0.02 s^{-1}, which again corresponds to the slowest strain rate used for the fibre tensile tests (cf. chapter 4.3). All tests are captured by a camera system with a frame rate of 200 Hz in order to evaluate the deformation of the specimen's surface by means of digital image correlation (DIC). For each laminate configuration, five specimens are tested to failure. Tensile strength $\sigma_{1,max}$ and maximum elongation $\varepsilon_{1,max}$ are derived from the obtained stress-strain data. The tensile stiffness E_1 is determined by means of linear regression within 0.05 and 0.25 % nominal longitudinal strain. Mean stress-strain curves are shown in figure 7.4. The corresponding characteristic values are summarised in table 7.3.

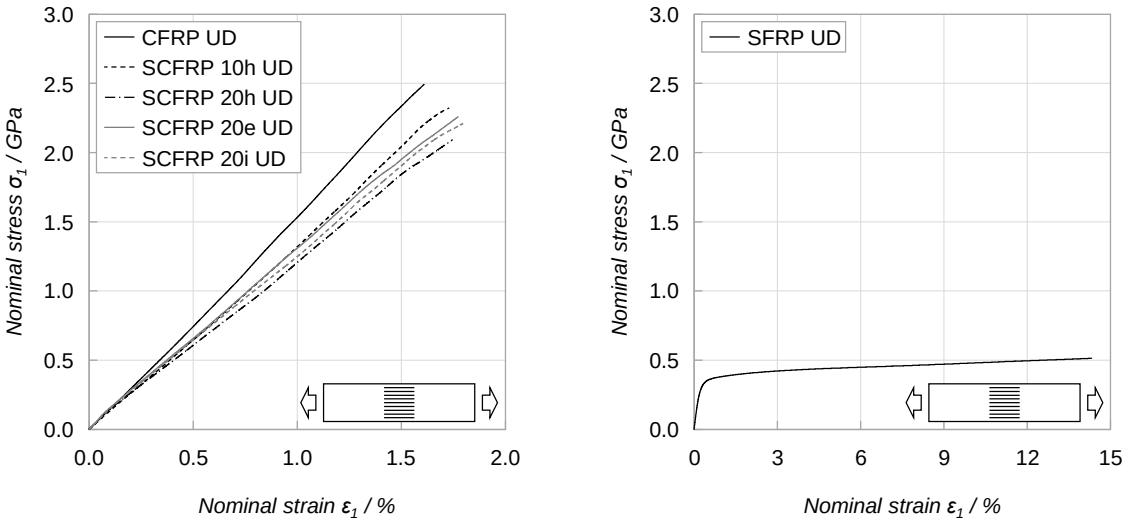

Figure 7.4 Mean stress-strain curves of the analysed uniaxial reinforced (hybrid) layers in case of tensile load in parallel to the fibre orientation

In case of tensile load in parallel to the fibre orientation, both CFRP and the hybrid composites exhibit linear-elastic brittle material behaviour with similar elongation at break. Incorporation of stainless steel fibres into CFRP lowers the stiffness and tensile strength of the composite. Despite the integration of highly ductile stainless steel fibres, a gradual failure or quasi-ductile behaviour after failure initiation (failure of the carbon fibres) cannot be observed. Compared to CFRP, the tensile stiffness of the hybrid composite with homogeneously distributed stainless steel fibres decreases by 12 % for a steel fibre share of 10.4 vol.% and by 17 % for a steel fibre fraction of 18.8 vol.%. The tensile strength is reduced by 7 % or 16 %, while the strain at failure increases by 8 % or 9 %, respectively. In case of the hybrid composites with stainless steel fibres concentrated at the top or core layers of the laminate, the tensile stiffness decreases by 11 %. The tensile strength is lowered by 11 % or 9 %, while the strain

Table 7.3 Tensile properties of uniaxial reinforced (hybrid) composites in parallel to the fibre orientation

Material	E_1 / GPa [a)]	$\sigma_{1,max}$ / MPa [a)]	$\varepsilon_{1,max}$ / % [a)]	E_1 / GPa [b) d)]	$\sigma_{1,max}$ / MPa [b) d)]	E_1 / GPa [c) d)]
CFRP UD	146.1 ± 5.2	2492 ± 85	1.61 ± 0.06	155.0 (+6 %)	2778 (+11 %)	155.2 (+6 %)
SCFRP 10h UD	127.8 ± 4.2	2323 ± 74	1.73 ± 0.04	149.6 (+17 %)	2412 (+4 %)	150.1 (+17 %)
SCFRP 20h UD	120.9 ± 5.0	2093 ± 72	1.75 ± 0.09	152.1 (+26 %)	2237 (+7 %)	152.2 (+26 %)
SCFRP 20e UD	129.7 ± 3.5	2259 ± 78	1.77 ± 0.04	152.1 (+17 %)	2237 (-1 %)	152.2 (+17 %)
SCFRP 20i UD	130.3 ± 2.5	2211 ± 34	1.80 ± 0.04	153.7 (+19 %)	2198 (-1 %)	155.4 (+19 %)
SFRP UD	136.9 ± 2.9	514 ± 7	14.77 ± 0.96	109.7 (-20 %)	553 (-8 %)	110.1 (-20 %)

[a)] experimentally determined

[b)] calculated by the rule of mixtures

[c)] determined by numerical simulation

[d)] deviation from the experimentally determined value in percent

at failure increases by 12 % or 10 %. By contrast, pure stainless steel fibre reinforced SFRP exhibits pronounced ductility; still, the elongation at break remains below the one of the pristine stainless steel fibre bundles.

In principle, the determined stiffness of the composites is in moderate accordance with the values estimated by means of numerical simulation[13]. The simulation typically overestimates the measured tensile stiffness. The deviation ranges from +6 % in case of CFRP to +26 % in case of the hybrid composite with 20 vol.% of homogeneously distributed stainless steel fibres. In case of SFRP, the stiffness is underestimated by 20 %. Similar results are obtained by the rule of mixtures. Regarding the tensile strength of the composites, the deviation of the calculation ranges from -1 % in case of the hybrid composites with steel fibres concentrated at the outer layers to +11 % in case of CFRP, assuming a stress of 554 MPa for the steel fibres and 63 MPa for the epoxy resin at the moment of failure initiation. In case of SFRP, the difference is +8 %. The minor strengths measured might be caused by insufficient edge quality of the specimens (decrease in strength due to notches) or minor misalignment of the reinforcing fibres from the load direction.

The explanation of the apparent (macro-mechanical) brittle failure mode of the hybrid composites requires a detailed (micro-mechanical) consideration of the fracture mechanics. For this purpose, the general force-displacement curve of the tensile-

[13] The applied numerical simulation corresponds to the one presented in appendix A.1. However, the volume shares are adapted to the actual proportions of the experimentally analysed laminates (cf. figure 7.1).

loaded hybrid composite is divided into several states, figure 7.5 (left) and figure 7.6. The corresponding stress conditions of the steel fibres or the carbon fibres are illustrated in figure 7.5 (right). In this context, the following simplifying assumptions are made:

(1) The carbon fibres as well as the epoxy resin exhibit linear-elastic stress-strain relation. Both components are perfectly bonded together and fail simultaneously when exceeding the elongation at break of the carbon fibres ($\varepsilon_{max,R} = \varepsilon_{max,CF}$). For convenience, they are considered as combined phase with homogenised properties, denominated as surrounding CFRP.

(2) The steel fibre bundles exhibit non-linear elastic-plastic stress-strain relation. Failure of all filaments occurs uniformly when exceeding their strain at failure.

(3) All three components exhibit similar behaviour under compression and tensile load.

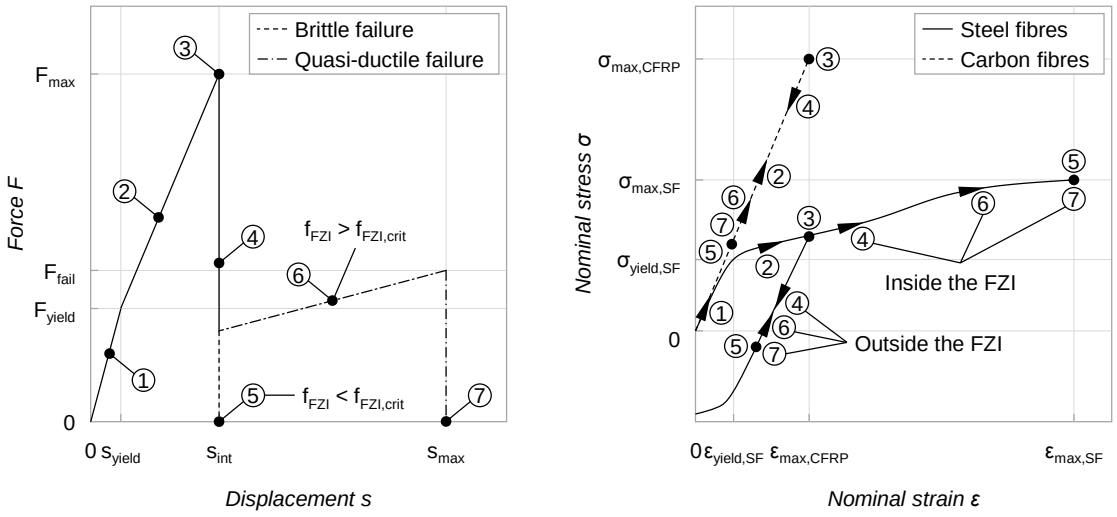

Figure 7.5 Schematic representation of (left) the force-displacement curve of a UD hybrid composite under tensile load in parallel to the fibre orientation and (right) the corresponding stress-strain states of the embedded steel and carbon fibres

State 1: The global elongation of the composite leads to a homogeneous strain state within the entire hybrid composite; the local elongation of each constituent corresponds to the global deformation of the composite. Initially, both the steel fibres and the surrounding CFRP are elastically elongated. Due to the homogeneous elastic deformation, potential (elastic) energy is stored in the entire volume of the material.

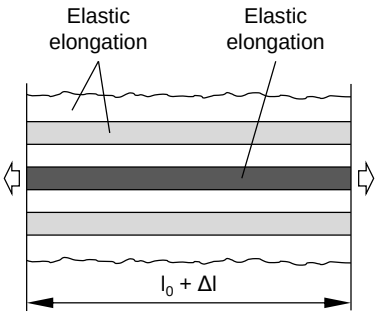

$\Delta l = l_0 \cdot \varepsilon,\ 0 < \varepsilon < \varepsilon_{yield,SF},\ \varepsilon_{SF} = \varepsilon$

State 1: Uniform elastic elongation

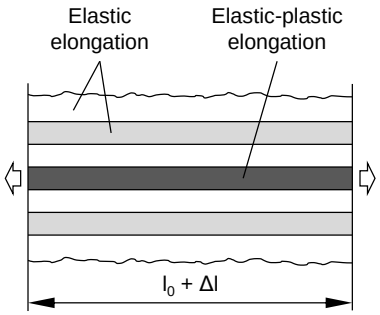

$\Delta l = l_0 \cdot \varepsilon,\ \varepsilon_{yield,SF} < \varepsilon < \varepsilon_{max,CF},\ \varepsilon_{SF} = \varepsilon$

State 2: Uniform elastic-plastic elongation

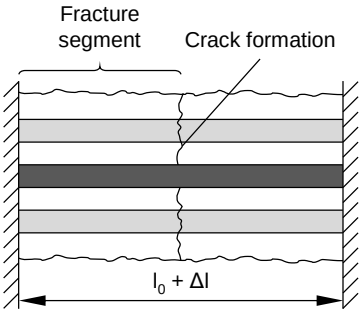

$\Delta l = l_0 \cdot \varepsilon,\ \varepsilon \rightarrow \varepsilon_{max,CF},\ \varepsilon_{SF} = \varepsilon$

State 3: Failure initiation

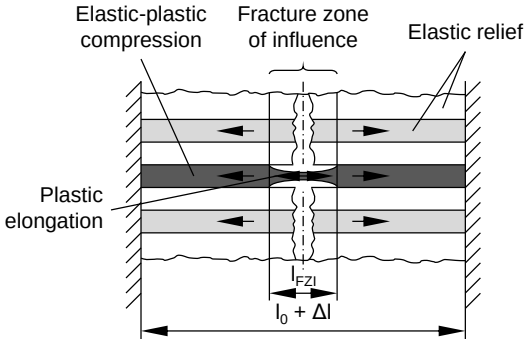

$\Delta l = l_0 \cdot \varepsilon,\ l_{FZI} = f_{FZI} \cdot (l_0 + \Delta l),\ \varepsilon = \varepsilon_{max,CF},\ \varepsilon_{max,CF} < \varepsilon_{FZI,SF} < \varepsilon_{max,SF}$

State 4: Fracture gap generation

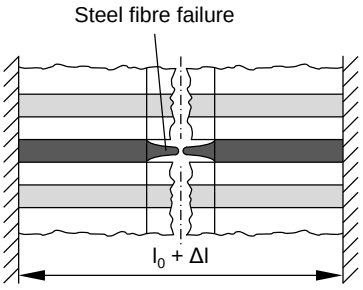

$\Delta l = l_0 \cdot \varepsilon,\ \varepsilon = \varepsilon_{max,CF},\ \varepsilon_{FZI,SF} > \varepsilon_{max,SF}$

State 5: Brittle composite failure ($f_{FZI} < f_{FZI,crit}$)

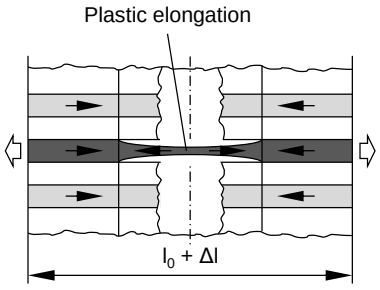

$\Delta l = l_0 \cdot \varepsilon,\ \varepsilon_{max,CF} < \varepsilon < \varepsilon_{max,SF},\ \varepsilon_{max,CF} < \varepsilon_{FZI,SF} < \varepsilon_{max,SF}$

State 6: Post-failure yielding ($f_{FZI} > f_{FZI,crit}$)

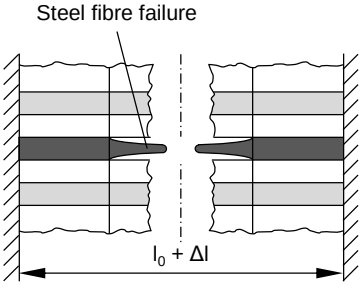

$\Delta l = l_0 \cdot \varepsilon,\ \varepsilon_{max,CF} < \varepsilon < \varepsilon_{max,SF},\ \varepsilon_{FZI,SF} > \varepsilon_{max,SF}$

State 7: Quasi-ductile composite failure ($f_{FZI} > f_{FZI,crit}$)

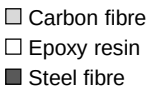

Figure 7.6 Schematic illustration of the failure process of a UD hybrid composite under tensile load in parallel to the fibre orientation

State 2: After exceeding their yield strain ($\varepsilon_{yield,SF} \approx 0.29$ %), the stainless steel fibres are plastically elongated. Their deformation, however, still occurs uniformly on the entire length of the loaded composite. Onset of plastic deformation leads to a degradation of the stiffness of the steel fibres and thus of the hybrid composite. The progressive elongation of the composite causes further storage of elastic energy by CFRP and permanent energy absorption by plastic deformation of the steel fibres.

State 3: The global elongation of the composite and thus of each constituent equates to the elongation at break of the carbon fibres ($\varepsilon_{max,CF} = 1.80$ %), which causes tensile failure initiation of the carbon fibres and the epoxy resin. For small steel fibre percentages, the stress at this elongation conforms to the tensile strength of the hybrid composite (cf. chapter 5.3). Due to their higher elongation at break, the so far uniformly elongated steel fibres remain as load-bearing part of the composite.

State 4: The failure of the carbon fibres and the epoxy resin leads to an elastic unloading of the fracture halves. This highly transient process occurs without global change in length of the composite (deformation-controlled loading of the material) but exclusively by relative displacement between its constituents. In this context, two different areas in the composite have to be distinguished: Over a defined length in the proximity of the growing fracture gap, the steel fibres can deform freely (no fibre-resin-adhesion at all). This area is denominated as fracture zone of influence (FZI)[14]. The relative length of the fracture zone of influence f_{FZI} is given as ratio of length of the fracture zone of influence l_{FZI} to the free length of the specimen l, eq. 7.2, cf. figure 7.6. This definition applies until ending of the fracture gap generation (state 4).

$$f_{FZI} = \frac{l_{FZI}}{l} \qquad \text{(Eq. 7.2)}$$

Outside this area, the steel fibres are perfectly bonded to the surrounding material. Within the FZI, the carbon fibres and the epoxy resin are completely elastically relieved. Conversely, the steel fibres in this area are further elongated to bypass the growing fracture gap. Outside the FZI, the steel fibres are first elastically relieved and then, if necessary, elastic-plastically compressed due to the elastic spring-back of the adhesive surrounding CFRP. The relaxation of the CFRP in this area is, however, incomplete due to the permanent deformation of the steel fibres outside and the

[14] In this consideration, the extent of the fracture zone of influence is assumed to be consistent until fracture gap generation and in the further course of the composite deformation. In fact, the fracture zone of influence propagates due to the transversal contraction of the steel fibres and the corresponding steel fibre-resin-detachment.

tensile load exerted by the steel fibres inside the FZI. The degree of the remaining deformation depends on the extent of the FZI as well as the share and the properties (strain hardening) of the embedded steel fibres. In general, the totality of released elastic energy is either dissipated by generation of inter-fibre-failure, fibre fracture, fragmentation and friction (heat) between arising laminate bundles, or absorbed by yielding of the embedded steel fibres.

State 5: During the energy transfer, the steel fibres within the FZI fail if they are strained beyond their elongation at break. In this case, ultimate failure of the hybrid material occurs without any further global elongation since failure initiation. Macroscopically, the hybrid composite then exhibits brittle failure behaviour (similar to neat CFRP). The elongation at break corresponds to that of the carbon fibres.

State 6: If the energy redistribution during the fracture gap generation causes an elongation of the steel fibres within the FZI without exceedance of their strain at failure, the hybrid composite sustains its structural integrity and can bear further global deformation after failure of the carbon fibres, albeit on a lower level of load. The hybrid composite then exhibits pronounced post-failure behaviour. Progressive elongation of the composite is accompanied by hardening of the steel fibres, hence re-gain of the mean composite stress. Simultaneously, increasing tensile stress of the steel fibres within the FZI causes a slight rise of the elongation of the fracture halves.

State 7: Ultimate failure of the hybrid composite finally occurs after local (within the FZI) exceedance of the strain at failure of the reinforcing steel fibres. However, since the steel fibres primarily yield within the FZI (heterogeneous strain distribution of the composite) the global elongation at break of the composite falls below the one of the dry steel fibre bundles. In the remaining parts of the composite, the available ductility of the steel fibres is far from being exhausted.

According to this theoretical model, the macroscopic failure pattern (brittle failure or pronounced after-damage stage) of the hybrid composite is determined by the size of the fracture gap generated and whether the integrated steel fibres are capable of bypassing this gap. This depends on various parameters, in particular the extent of the fracture zone of influence (i.e. the steel fibre-resin-adhesion), the strain at failure of the applied steel fibres, the ratio of steel to carbon fibres, the effective stiffness of the surrounding CFRP and the strain hardening (or strength) of the steel fibres.

The greater the FZI, the larger is the area at which the embedded steel fibres are able to elongate without restriction and thus the lower is the local elongation of the steel fibres which is necessary to bypass the growing fracture gap. Above a critical length of the fracture zone of influence $f_{FZI} > f_{FZI,crit}$, the strain of the steel fibres within the FZI is lower than their strain at failure (state 6 and 7); the hybrid composite can bear further elongation after failure initiation and exhibits quasi-ductile behaviour. Besides, the more pronounced the FZI, the lower is the load level in the post-damage stage (depends on the steel fibre share) and the higher is the ultimate elongation at break of the hybrid laminate. In case of $f_{FZI} = f_{FZI,crit}$, the steel fibres within the FZI are strained right to their maximum elongation. For $f_{FZI} < f_{FZI,crit}$, the fracture gap generation elongates the steel fibres beyond their strain at failure (state 5); the hybrid composite then exhibits brittle failure behaviour. In this case, the total strain at failure of the composite equates to the elongation at break of the carbon fibres.

The size of the fracture gap generated results from a balance of forces between the fracture halves and the steel fibres within the FZI. The greater the elongation of the steel fibres within the FZI, the more pronounced is their (strain) hardening and thus the greater is the force which they execute on the fracture halves. This consequently increases the residual deformation of the fracture halves and again lowers the size of the fracture gap generated. A comparable influence is given by an increasing percentage of steel fibres or a decreasing effective stiffness of the surrounding CFRP. The greater the residual deformation of the fracture halves, the lower is the necessary deformation of the steel fibres within the FZI to bypass the fracture gap. Higher steel fibre percentages, lower effective stiffness of the surrounding CFRP or pronounced hardening of the steel fibres therefore increase the probability of a post-failure behaviour of the hybrid composite.

In principle, the estimation of the critical extent of the fracture zone of influence requires an iterative calculation. However, in a first approximation, the critical extent of the fracture zone of influence can be estimated by the ratio of the strain at failure of the carbon fibres to the strain at failure of the steel fibres, neglecting the residual elongation of the fracture segments[15]. This conservative approximation applies for the case of overdamping (the fracture segments return to their steady state free of

[15] This approach also disregards a possible strain rate dependence of the strain at failure of the applied steel fibres (cf. chapter 4.3.1 and 9.1.1). However, strain rate sensitivity is relevant since the fracture gap generation is a highly dynamic process.

oscillation and overshoot; elastic energy is dissipated by the mechanisms mentioned above); the actual value of $f_{FZI,crit}$ is smaller (due to the residual deformation of the fracture halves). In case of an underdamped system, the fracture segments return to their steady state by oscillation. The maximum amplitude of the overshoot equates to the previous laminate elongation (undamped oscillator). The estimated value of $f_{FZI,crit}$ must then be doubled. In appendix A.4, a simplified analytical approach is used to exemplarily estimate the post-damage behaviour of SCFRP 20h UD in dependence on the fracture zone of influence $f_{FZI,crit}$.

Following the theoretical description of the fracture mechanics described above, several strategies can be derived in order to achieve pronounced post-failure behaviour with the given hybrid material:

(1) Increasing the fracture zone of influence, i.e. **reduction of the steel fibre-resin-adhesion** (cf. chapter 7.2), enables unrestrained elongation of the steel fibres on longer distances. However, this strategy is expected to compromise other important properties such as transverse tensile strength (cf. chapter 7.4), bending strength, impact resistance or fatigue performance.

(2) Improvements are also feasible by **higher steel fibre fractions**. This would downsize the fracture gap generated and thus reduce the necessary elongation of the steel fibres within the FZI but would also cause higher (inappropriate) laminate density.

(3) **Reducing the effective stiffness of the surrounding CFRP** in comparison with the integrated steel fibres (as for example by multiaxial laminate stacking sequence) diminishes the restoring force for the elastic spring-back of the fracture halves and thus increases the significance of the steel fibres to the surrounding CFRP. Consequently, this would downsize the fracture gap generated and have a similar effect as a higher steel fibre percentage.

Application of annealed **steel fibres with higher elongation at break** basically reduces the critical length of the FZI. In case of $f_{FZI} > f_{FZI,crit}$, a rise of the strain at failure of the steel fibres additionally increases the ultimate strain at failure of the hybrid composite.

7.4 Transverse tensile behaviour

In order to analyse the influence of the steel fibre incorporation on the transverse tensile properties of the hybrid composites, measurements are carried out in dependence on DIN EN ISO 527-5 [131]. For this purpose, rectangular specimens with a length of 150 mm and a width of 15 mm are provided with 1 mm thick, chamfered GFRP end tabs. The specimens are restrained with a free clamping length of 50 mm and loaded with a monotonic crosshead speed of 1 mm/min. Again, all tests are captured by a camera system with a frame rate of 10 Hz in order to evaluate the deformation of the specimen's surface by DIC. For each laminate configuration, five specimens are tested to failure. Tensile strength $\sigma_{2,max}$ and elongation at break $\varepsilon_{2,max}$ are derived from the obtained stress-strain data. The tensile stiffness E_2 is determined by means of linear regression within 0.05 and 0.25 % nominal strain. Mean stress-strain curves and characteristic properties of the tested laminates are summarised in figure 7.7 and table 7.4.

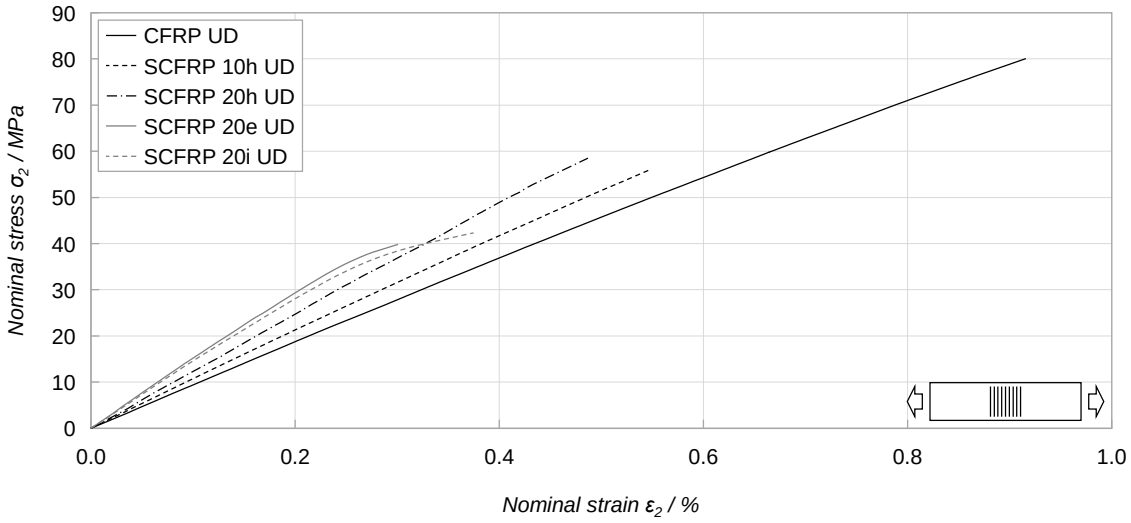

Figure 7.7 Mean stress-strain curves of uniaxial reinforced (hybrid) composites transverse to the fibre orientation

CFRP exhibits a linear stress-strain relation with a tensile stiffness of (9.3 ± 0.2) GPa. Failure occurs abruptly at a nominal elongation of (0.92 ± 0.03) % or at a nominal tensile stress of (80 ± 3) MPa. Incorporation of metal fibres into CFRP increases the stiffness of the composite but significantly lowers its strain at failure and ultimate tensile strength. Compared to CFRP, the tensile stiffness of the hybrid composite with homogeneously distributed stainless steel fibres increases by 13 % for a steel

Table 7.4 Tensile properties of uniaxial reinforced (hybrid) composites transverse to the fibre orientation

Material	E_2 / GPa [a]	$\sigma_{2,max}$ / MPa [a]	$\varepsilon_{2,max}$ / % [a]	E_2 / GPa [b] [d]	E_2 / GPa [c] [d]
CFRP UD	9.3 ± 0.2	80 ± 3	0.92 ± 0.03	8.6 (-8 %)	11.0 (+18 %)
SCFRP 10h UD	10.5 ± 0.2	56 ± 2	0.55 ± 0.02	9.0 (-15 %)	12.1 (+15 %)
SCFRP 20h UD	12.4 ± 0.5	59 ± 3	0.49 ± 0.03	9.9 (-21 %)	13.9 (+12 %)
SCFRP 20e UD	14.1 ± 0.2	40 ± 1	0.30 ± 0.01	9.9 (-30 %)	13.9 (-1 %)
SCFRP 20i UD	13.4 ± 0.1	42 ± 0	0.38 ± 0.01	10.2 (-24 %)	15.0 (+12 %)

[a] experimentally determined

[b] calculated by the rule of mixtures

[c] determined by numerical simulation

[d] deviation from the experimentally determined value in percent

fibre share of 10.4 vol.% and by 33 % for a steel fibre fraction of 18.8 vol.%. The ultimate tensile strength decreases by 30 % and 27 %, respectively, while the strain at failure declines by 40 % or 47 %. In case of the hybrid composites with stainless steel fibres concentrated at the top or core layers of the laminate, the tensile stiffness rises by 52 % and 44 %, respectively. The ultimate tensile strength decreases by 50 % or 48 %, while the strain at failure is reduced by 67 % or 59 %.

In principle, the experimentally determined transverse tensile stiffness of the composites is only in moderate accordance with the values estimated by means of numerical simulation[13]. The calculation typically surpasses the measured tensile stiffness with a deviation between -1 and +18 %. Larger deviations arise in case of the hybrid materials with steel fibres concentrated at either the top or core layers of the laminate. Possible reasons for this deviation are defects in the laminate and a limited fibre-resin-adhesion, which are not taken into account by the numerical simulation. By contrast, the rule of mixtures clearly underestimates the tensile stiffness of the composites. The deviation increases with the steel fibre share and ranges from -30 to -8 %. Typical reasons for this underestimation are given in chapter 5.2. Accordingly, both (unmodified) methods are inappropriate to precisely predict the transverse tensile stiffness of the hybrid composites.

The differences between the transverse tensile properties of CFRP and the hybrid composites are caused by different grades of isotropy of the reinforcing fibres. Unlike orthotropic carbon fibres, metal fibres exhibit isotropic properties (neglecting a possible influence of the wire drawing process), i.e. similar moduli of elasticity transverse and in parallel to the fibre orientation. Since the overall transverse tensile

stiffness of the laminate is given proportionately by the stiffness of the composite's constituents (cf. chapter 5.2), incorporation of steel fibres into CFRP increases the tensile stiffness. Moreover, under transverse tensile load, the high stiffness of the reinforcing fibres must be compensated by large deformation of the compliant epoxy resin. As a consequence, local deformation of the matrix significantly exceeds the global strain of the composite. The significance of this strain magnification increases with portion and transverse tensile stiffness of the reinforcing fibres. Incorporation of isotropic steel fibres into CFRP consequently promotes large local deformation of the epoxy resin, hence cohesive inter-fibre-failure at minor laminate deformation. Additionally, the unsized steel fibre surface facilitates adhesive failure at the fibre-resin-interface. This assumption is supported by SEM micrographs of the fracture surfaces. As shown in figure 7.8, the epoxy resin detaches extensively from the stainless steel fibres (adhesive failure), while the carbon fibres are still covered by the polymer (cohesive failure). The reduction of the strain at failure outweighs the stiffness increase, which finally provokes a diminution of the transverse tensile strength of the hybrid composites.

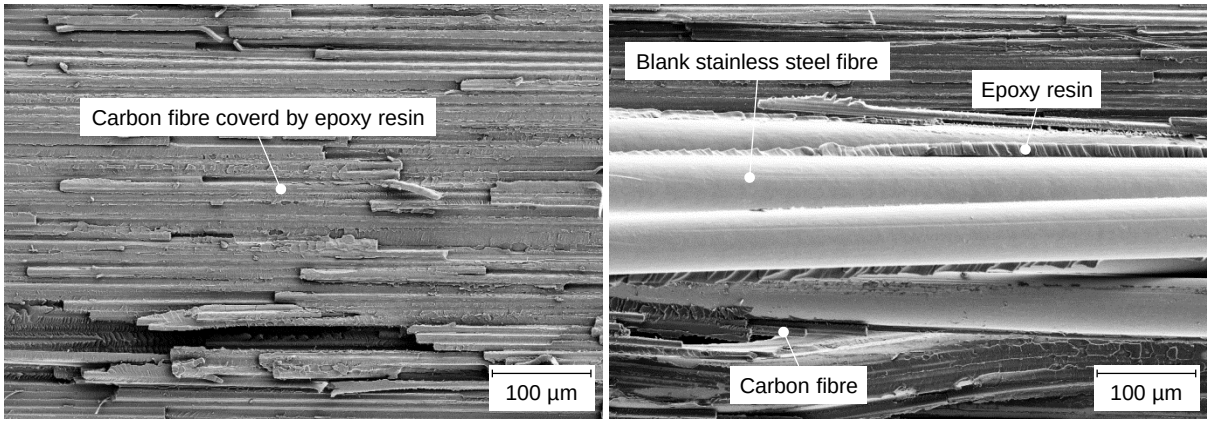

Figure 7.8 Fracture surface of (left) conventional CFRP and (right) a hybrid composite with homogeneously distributed steel fibres

The effect of strain magnification is particularly pronounced at metal fibre rich areas, such as pure steel fibre reinforced layers. High local fibre percentages and reinforcement exclusively by isotropic fibres promote crack formation at small laminate deformation. Due to their proximity, initiated cracks can easily coalesce, causing a proceeding reduction of the load-bearing cross-section and thus degradation of the effective laminate stiffness. In case of unidirectional reinforced laminates, cracks can propagate freely into adjacent CFRP plies, causing ultimate

failure of the composite. As a consequence, strain at failure and finally transverse tensile strength of hybrid composites with conglomerated steel fibre reinforcement are even lower than of composites with homogeneous steel fibre distribution.

7.5 Bending-tensile behaviour

In order to review the essential outcome of the longitudinal tensile tests (cf. chapter 7.3), bending-tensile tests are carried out on a conventional testing machine (Zwick 1474). Rectangular coupons in the form of 125 mm long and 15 mm wide flat strips are restrained at their short edges with a remaining span of 50 mm while the reinforcing fibres are orientated in parallel to the long edge of the specimen. The transverse loading is symmetrically applied to the specimen by an indenter at a constant displacement rate of 2 mm/min. Both indenter and specimen support are chamfered with a radius of 5 mm. The deflection is given by the distance travelled by the indenter during the test. For each material, a number of five specimens is tested to failure. The material response is characterised by the maximum load experienced F_{max}, the corresponding deflection s_{Fmax} and the deflection at ultimate failure of the specimen s_{max}. Integrating the force-displacement trace up to s_{Fmax} or s_{max} yields the absorbed energy $E_{a,Fmax}$ and $E_{a,max}$, respectively. An illustration of the test setup and representative force-displacement curves are given in figure 7.9. The corresponding characteristic values are summarised in table 7.5.

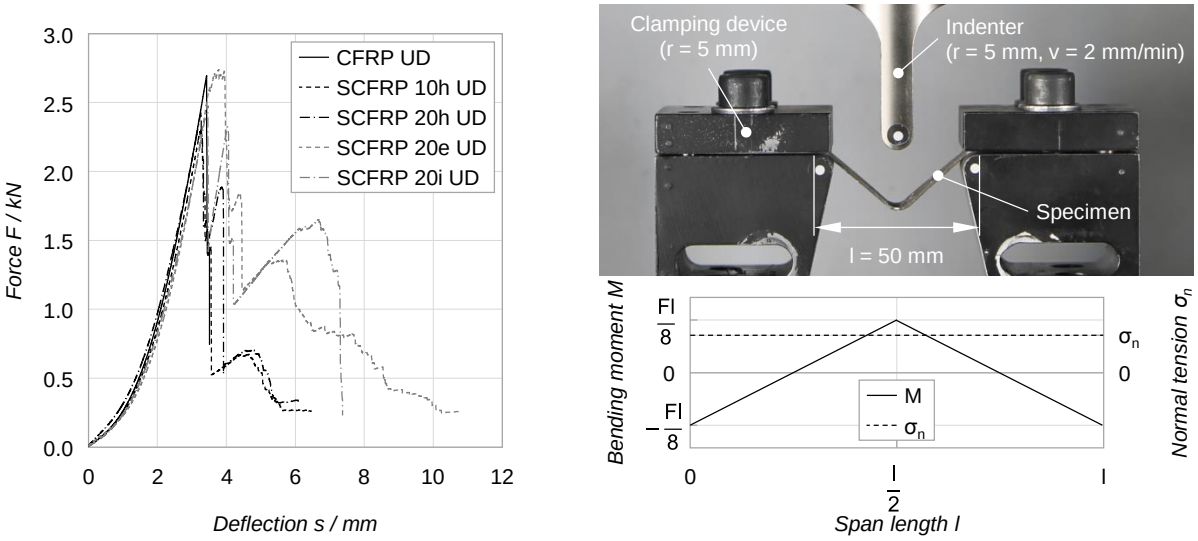

Figure 7.9 (left) Representative force-deflection curves of uniaxial reinforced (hybrid) composites under bending-tensile load and (right) corresponding test setup with illustration of the load distribution [132]

Table 7.5 Bending-tensile properties of uniaxial reinforced (hybrid) composites in parallel to the fibre orientation

Material	F_{max} / N	s_{Fmax} / mm	$E_{a,Fmax}$ / J	s_{max} / mm	$E_{a,max}$ / J
CFRP UD	2715 ± 105	3.41 ± 0.04	3.14 ± 0.09	3.58 ± 0.12	3.38 ± 0.09
SCFRP 10h UD	2396 ± 93	3.36 ± 0.07	2.74 ± 0.14	6.11 ± 0.28	4.24 ± 0.21
SCFRP 20h UD	2406 ± 57	3.22 ± 0.07	2.73 ± 0.11	6.33 ± 0.36	5.16 ± 0.34
SCFRP 20e UD	2710 ± 115	3.90 ± 0.08	3.96 ± 0.21	10.09 ± 0.58	9.41 ± 0.48
SCFRP 20i UD	2566 ± 58	3.48 ± 0.01	3.02 ± 0.07	7.32 ± 0.29	8.47 ± 0.46

CFRP exhibits brittle material behaviour. Failure occurs singularly at a bearable deformation of (3.58 ± 0.12) mm or at a maximum force of (2715 ± 105) N, respectively. By contrast, the hybrid composites reinforced by stainless steel fibre bundles generally prove multistage failure behaviour. In case of the hybrid composites with a share of 10.4 or 18.8 vol.% homogeneously distributed stainless steel fibres, failure is initiated at a slightly lower deflection (-2 % or -6 %). The maximum force decreases by 12 % and 11 %, respectively. However, after failure initiation, the hybrid composites can bear further deflection, albeit on a reduced level of load. Ultimate failure occurs at a significantly increased deflection of 6.11 mm (+71 %) and 6.33 mm (+77 %), respectively. As a consequence, the ultimate energy absorption consequently rises by a factor of 1.25 or 1.53 compared to CFRP. An even better material performance is achieved by concentrating the steel fibres at either the outer or the core layers of the laminate. First failure occurs at 3.90 mm (+14 %) and 3.48 mm (+2 %), respectively. The maximum force is slightly reduced by 1 % and 6 %. However, the deflection at ultimate failure extensively increases by 182 % and 105 %. The energy absorption is consequently improved by a factor of 2.79 and 2.51, respectively.

Unlike the plain tensile test, the flexure-tension test is characterised by a complex, inhomogeneous stress state, figure 7.9 (right). While the normal stress due to the elongation of the composite is constant over the specimen length, the bending (tensile and compression) stress caused by the deflection of the laminate varies over both the specimen thickness and length (cf. Euler-Bernoulli beam theory), figure 7.9 (right). Superposition of both load cases involves stress maxima at the clamping or below the indenter, while stress in the rest of the composite is significantly lower. In case of CFRP, tensile failure of the carbon fibres is therefore initiated at the convexly

curved outer layer of the laminate underneath the indenter[16]. Analogue to the tensile tests, the failed carbon fibres elastically relieve, which is accompanied by an energy transfer to the adjacent layer. However, since the carbon fibres of the adjacent layer are already loaded to a similar level as the failed fibres (close to their limit load), their energy absorption capacity is nearly exhausted. The energy transfer consequently exceeds the absorption capacity and causes failure of the adjacent ply. This energy transfer and thus crack propagation proceeds continuously through the entire laminate. Due to the minor laminate thickness, the fracture penetrates the entire laminate, causing sudden failure before the crack propagation can be stopped by energy absorption mechanisms of the laminate.

In principle, the failure process of the hybrid composites with homogeneous steel fibre distribution is similar to that of CFRP. However, different to the carbon fibres, the ductile stainless steel fibres are able to absorb a significantly higher amount of energy by means of plastic deformation (factor 6.32, cf. table 4.4). As a consequence, propagation of the initiated crack is stopped after a certain distance. The hybrid laminate can bear further deflection before cracking is re-initiated. By this means, the crack propagates incrementally through the composite. For this reason, the hybrid composites exhibit gradual failure process. The higher the proportion of ductile steel fibres, the faster the crack is stopped and the higher is the attainable load level after failure initiation. Interlocking of the coarse fracture surfaces, i.e. friction between protruding, elongated steel fibres, finally causes a certain level of load prior to ultimate separation of the composite, figure 7.10 (top right).

In case of the hybrid composite with steel fibre reinforced top layers, deflection of the laminate initially causes yielding of the metal fibres. Further deflection of the hybrid laminate initiates failure of carbon fibres lying further inside. Similar to conventional CFRP, the crack promptly spreads inwards, reducing the effective cross-sectional area of the composite and thus of the composite load. However, since the carbon fibres are aligned closer to the neutral axis, the deflection required for failure initiation is higher. Crack propagation is restrained when reaching the upper steel fibre reinforced layer. Extensive yielding of the steel fibres (cf. figure 7.10

[16] According to the theoretically predicted stress state (cf. figure 7.9), failure could occur underneath the indenter or at the clamping of the specimen. In fact, the high tensile load during testing leads to a minimal tilting of the fixation due to the finite stiffness of the test setup. As a result, the bending load of the laminate in this area is slightly reduced, which promotes failure underneath the indenter.

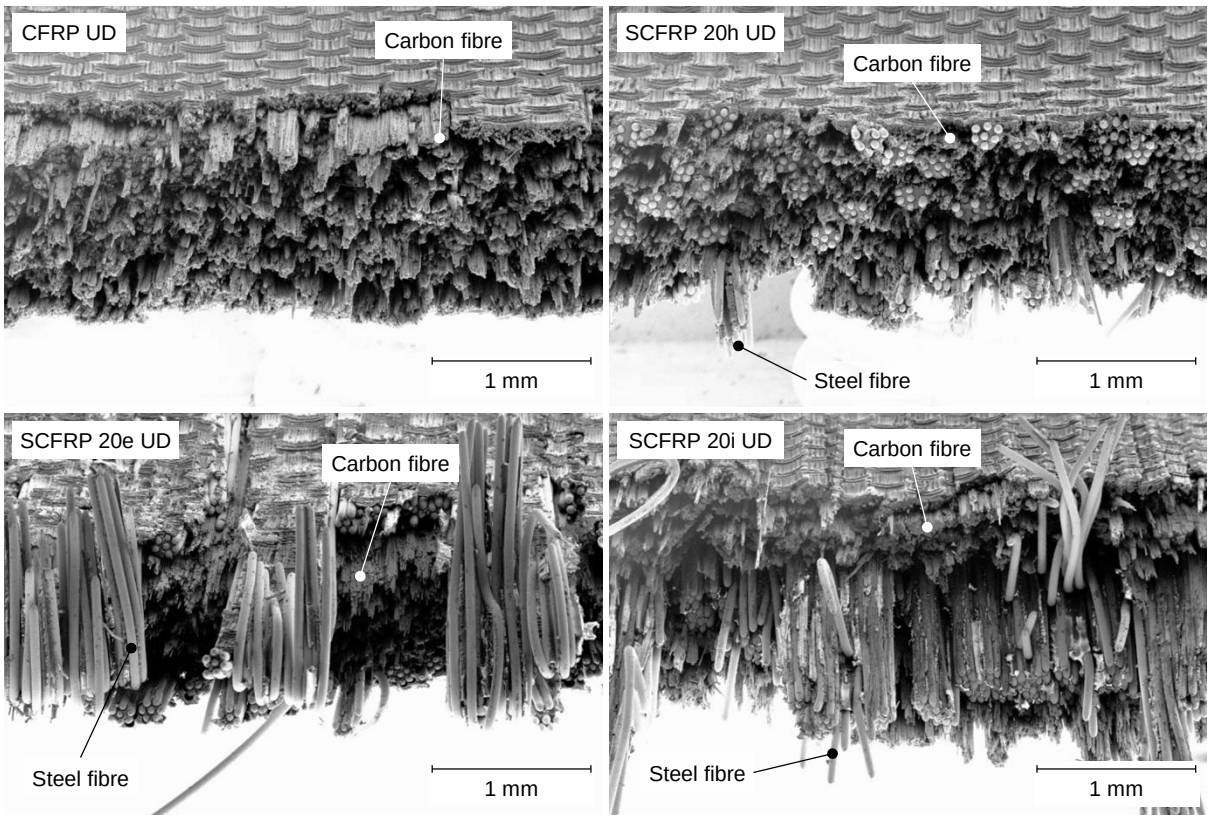

Figure 7.10 Fracture surface of uniaxial reinforced (hybrid) composites after bending-tensile loading

(bottom left)) sustains the moment of inertia, i.e. the bending stiffness, which enables further loading of the laminate. Increasing deflection causes failure of the lower SFRP layer, accompanied by a second load drop. Ultimate failure occurs after exceeding the elongation at break of the steel fibres of the top SFRP layer.

In case of the hybrid composites with steel fibres arranged at the neutral axis of the composite, the failure sequence is initially identical to that of CFRP. However, due to their distinctive energy absorption capacity, the steel fibres are able to sustain the energy transfer by means of yielding when the tip of the propagating crack reaches the inner SFRP layers. Further deflection is initially accompanied by plastic elongation of the metal fibres, which results in a renewed increase of the contact force. Subsequently, failure is initiated at the CFRP area of the upper half of the composite while the steel fibres are still able to yield. Progressive degradation (gradual failure) of the steel fibre layers (superimposed by intralaminar friction between the steel fibres) leads to a continuous diminution of the effective cross-sectional area and thus of the bearable load. Again, interlocking of protruding steel fibres (cf. figure 7.10 (bottom right)) provides additional load-bearing capacity.

7.6 Electrical conductivity

Measurements of the electrical DC conductivity in parallel to the fibre orientation are carried out by the two-wire-method. The test setup mainly consists of a constant-current source, a voltmeter and a data logging system. Constant direct current in the range of 50 to 250 mA is introduced via flat silver sputtered copper electrodes to the end faces of the 15 mm wide, rectangular specimen. Synchronously, the voltage drop across the specimen is taped at the very same electrodes. The test setup and the corresponding equivalent circuit diagram are depicted in figure 7.11.

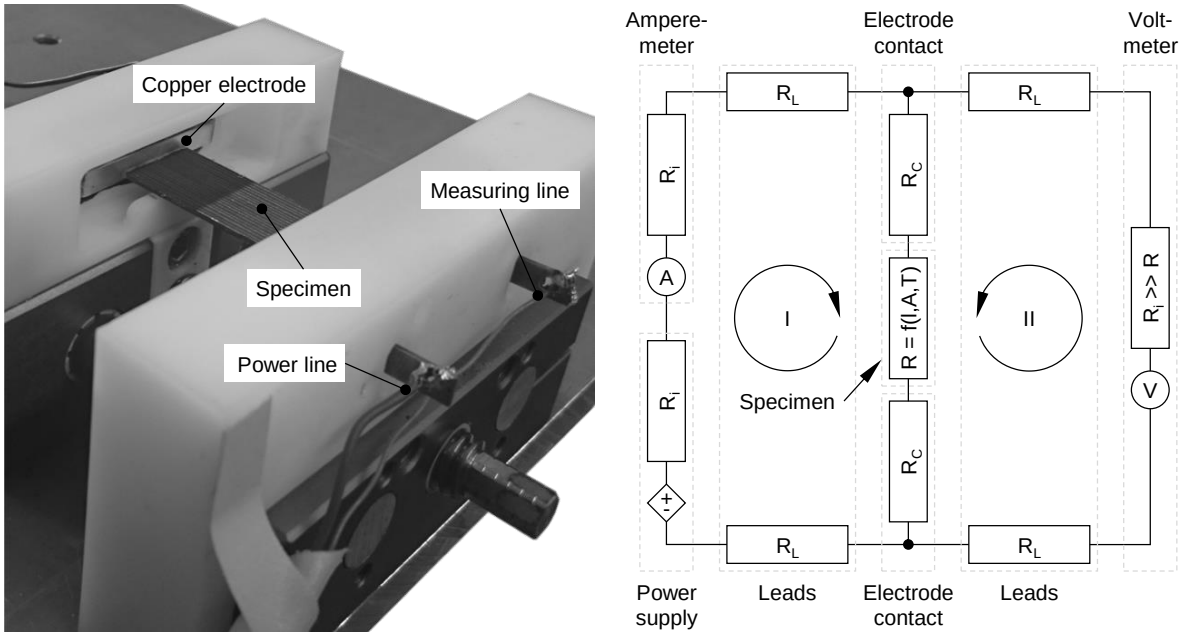

Figure 7.11 (left) Test setup[17] and (right) equivalent circuit diagram of the laminate conductivity measurements

Main issue of the two-wire-method is the influence of the contact resistances caused by the electrodes and their interfaces to the specimen. Across the contact resistances the introduced test current leads to a distinctive voltage drop. The voltage measured by the voltmeter consequently equates to the sum of both the voltage drop across the specimen and across the contact resistances. In order to consider this systematic error, several specimen lengths of 50, 70 and 90 mm are analysed for each material configuration. By means of Ohm's law, the measured current-voltage data yields an electrical resistance comprising the contact resistances and the length-

[17] Development of the test setup, specimen preparation and material testing were realised by the Institute of Materials Science and Engineering (WKK) of the University of Kaiserslautern.

dependent resistance of the specimen. The gradient of the overall resistance-to-length correlation, which exclusively corresponds to the length-dependent resistance of the specimen, is obtained by linear regression. Multiplying this value with the sample cross-sectional area yields the specific electrical resistance of the composite (cf. chapter 4.4). The intercept of this regression line with the ordinate equates to the sum of the contact resistances (cf. figure 7.14). However, this procedure presumes constant contact resistances for each specimen (length) of a material configuration. For this reason, the contact surfaces of the specimen are specially prepared in order to ensure a homogeneous and reproducible electrical connection to the electrodes. The end faces of the specimens are initially polished with a grinding paper (grit 1200) and subsequently treated with a picosecond laser to expose the ends of the steel fibres by removing the surrounding CFRP, figure 7.12. [163]

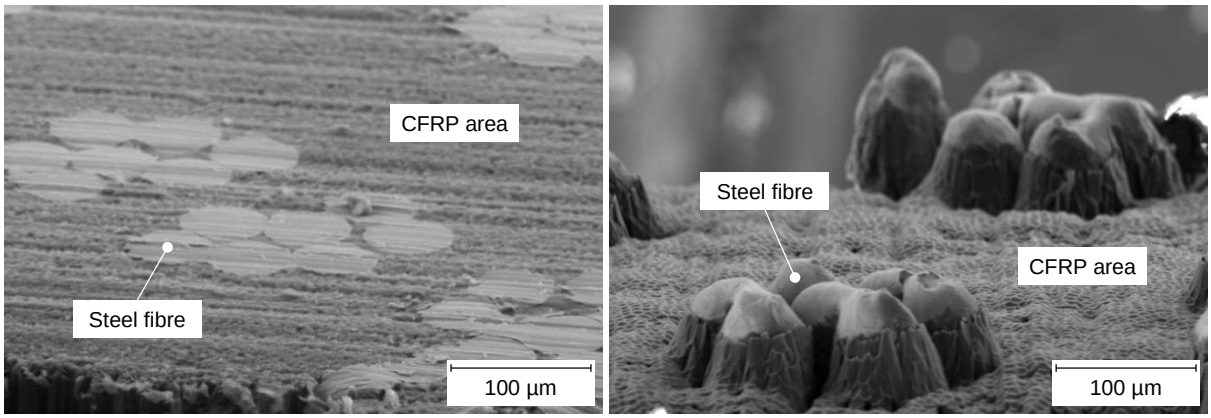

Figure 7.12 End face of a stainless steel fibre reinforced hybrid composite after (left) grinding and (right) treatment with a picosecond laser[18] [163]

Afterwards, the contact surfaces are cleaned with ethanol and coated with silver conductive paste. Finally, the copper electrodes are pressed to the specimen with a consistent pressure of 35 MPa in order to enable a reproducible electrical connection, hence consistent contact resistances. During the measurement, improper heating of the specimen caused by the constant current supply (cf. chapter 4.4) is excluded by limiting the applied current. Monitoring the surface temperature of the specimen by a thermography system proves a subcritical temperature increase of less than 2 °C for the maximum current introduced of 250 mA.

[18] Laser treatment was performed by the Photonik-Zentrum Kaiserslautern e.V..

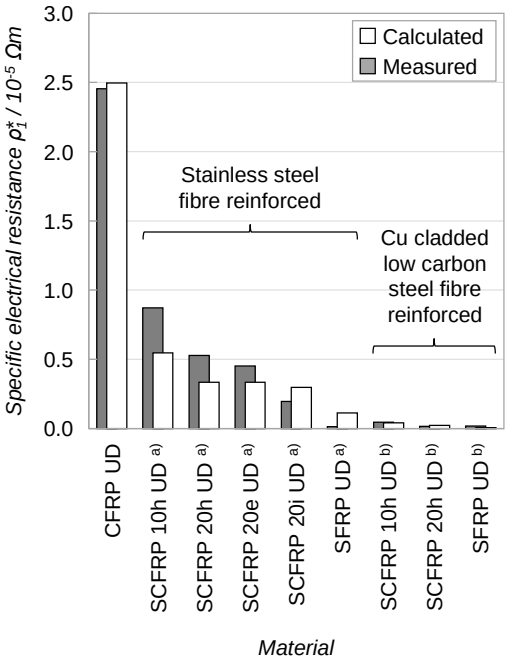

Material	ρ_1^* / 10^{-5} Ωm		Deviation / %
	Calculated	Measured	
CFRP UD	2.50	2.45	-2
SCFRP 10h UD [a]	0.55	0.87	+60
SCFRP 20h UD [a]	0.33	0.53	+59
SCFRP 20e UD [a]	0.33	0.45	+36
SCFRP 20i UD [a]	0.30	0.20	-34
SFRP UD [a]	0.11	0.01	-88
SCFRP 10h UD [b]	0.04	0.05	+14
SCFRP 20h UD [b]	0.02	0.02	-30
SFRP UD [b]	0.01	0.02	+158

[a] Stainless steel fibre reinforced
[b] Copper cladded low carbon steel fibre reinforced

Figure 7.13 Comparison of the calculated and experimentally determined specific electrical resistance of unidirectional reinforced (hybrid) laminates, acc. to [163]

The results of the conductivity measurements are summarised in figure 7.13. The experimental findings show a pronounced increase of the electrical conductivity as a function of the volume share and the specific electrical resistance of the incorporated metal fibres. Compared to CFRP, the specific conductance of the hybrid composite reinforced by homogeneously distributed stainless steel fibres is about 3 times higher for a steel fibre fraction of 10.4 vol.% and 5 times higher for steel fibre fraction of 18.8 vol.%. Further enhancements are feasible by concentrating the metal fibres in two adjacent core layers. By this means, the electrical conductivity is increased by a factor of 12. In case of the hybrid composites reinforced by copper cladded low carbon steel fibres, the specific conductance is enhanced by a factor of 53 for a steel fibre fraction of 10.4 vol.% and 158 for a steel fibre fraction of 18.8 vol.%. Both SFRPs are characterised by the highest electrical conductivity. Compared to CFRP, the specific conductance is 189 times higher for SFRP reinforced with stainless steel fibres and 141 times higher for SFRP reinforced with copper cladded low carbon steel fibres.

The measured specific electrical resistance of CFRP of 2.45×10^{-5} Ωm is in good accordance with the estimated value (2.50×10^{-5} Ωm), basically proving the accuracy of the applied measuring method and of the analytical approach (rules of mixtures).

By contrast, the measured values of the hybrid composites and the pure steel fibre reinforced materials significantly differ from the calculated values. Both over- and underestimation of the electrical conductivity is found. The deviation is particularly pronounced for SFRP with copper cladded low carbon steel fibre reinforcement.

The deviations are partially caused by misalignments of the steel fibres. Fibres which are properly contacted on one side of the specimen do not entirely run through the specimen, i.e. do not contribute to the specimen's conductivity and consequently cause an underrating of the specific electrical conductivity. The significance of this error rises with increasing specimen length. A certain deviation of the ideal fibre orientation is inherently given by the feed of the winding process ($\delta < 0.2°$)[19], in particular for the hybrid composites with low steel fibre percentages, i.e. large winding feeds, cf. figure 7.1.

Additionally, an influence of the autoclave process on the electrical properties of the copper cladded low carbon steel fibres must be taken into account. As shown in chapter 4.4, the specific electrical resistance of the copper cladded low carbon steel fibres increases by 4.98 % to $(4.44 \pm 0.18) \times 10^{-8}$ Ωm. Assuming the same degradation for the embedded steel fibres yields a theoretical electrical resistivity of 5.47×10^{-6} Ωm for the hybrid composite with a steel fibre percentage of 10.4 vol.% and of 3.33×10^{-6} Ωm for a steel fibre percentage of 18.8 vol.%. The deviation of the measured values is then +9 % and -34 %, respectively. In case of the pure copper cladded low carbon steel fibre reinforced composite, the estimated electrical resistivity still differs by +146 % (7.07×10^{-8} Ωm).

Furthermore, the accuracy of the applied measurement procedure significantly relies on the consistency of the electrical connection between specimens and electrodes, i.e. on constant contact resistances for different specimen lengths. Only in case of their consistency, the contact resistances can be analytically eliminated by the introduced gradient-method. Conversely, a large variation of the contact resistances reduces the accuracy of the determination of the material-related length-dependent resistance and finally of the specific electrical resistance. The significance of this error gains in importance for minor specimen resistances, i.e. in case of contact resistances with similar order of magnitude as the sample resistance, figure 7.14.

[19] The winding angle δ is given by the arc tangent of the ratio of winding feed rate f_w to the perimeter of the winding core p. Within the entire study, a winding core with a perimeter of 577.85 mm is used.

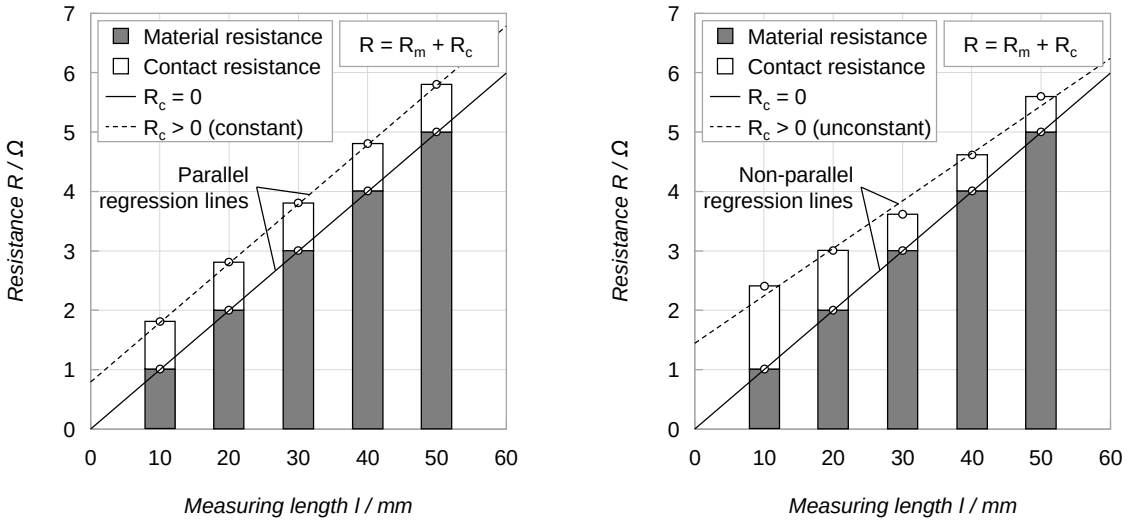

Case 1: Constant contact resistance

- → Constant resistance offset on material resistance
- → Parallel regression lines
- → Identical gradients
- → Gradient of regression line of measured resistances corresponds to specific material resistance
- → Offset of regression line of measured resistances equals contact resistance

Case 2: Inconsistent contact resistance

- → Inconsistent resistance offset on material resistance
- → Non-parallel regression lines
- → Non-identical gradients
- → Gradient of regression line of measured resistances merely approximates specific material resistance
- → Offset of regression line of measured resistances has no meaning

R_c: Contact resistance, R_m: Material resistance, R: Overall (measured) resistance

Figure 7.14 Influence of the contact resistance on the accuracy of the determination of the specific electrical resistance (schematic diagram)

Despite particular efforts (e.g. consistent end face preparation, constant contact pressure of the electrodes), inconsistent contact resistances must be assumed in case of the present analysis. Since certain samples exhibit higher overall resistances than shorter but otherwise identical samples, a dominant influence of the contact resistances on the obtained test results must be supposed. Especially in case of pure steel fibre reinforced composites, i.e. in case of the material configurations with low specific electrical resistivity, the contact resistances demonstrate a similar order of magnitude as the sample resistance. For this reason, the present analysis of the specific electrical resistance only applies to a first approximation.

More accurate tests results are expected by a greater number of test items (i.e. more sampling points for the gradient-method), larger specimens (i.e. more dominant specimen resistance compared to the contact resistances) and repeated conductivity measurements on each specimen (i.e. statistical averaging of the contact resistances).

8 Multiaxial laminate characterisation

The findings of the UD layer characterisation are transferred to multiaxial laminates. As reference material, a 13-layered CFRP laminate with a typical aeronautical stacking sequence (15 %/23 %/62 %) is manufactured [6]. For benchmark reasons, a second configuration of the 13-layered CFRP laminate but with an additional LSP

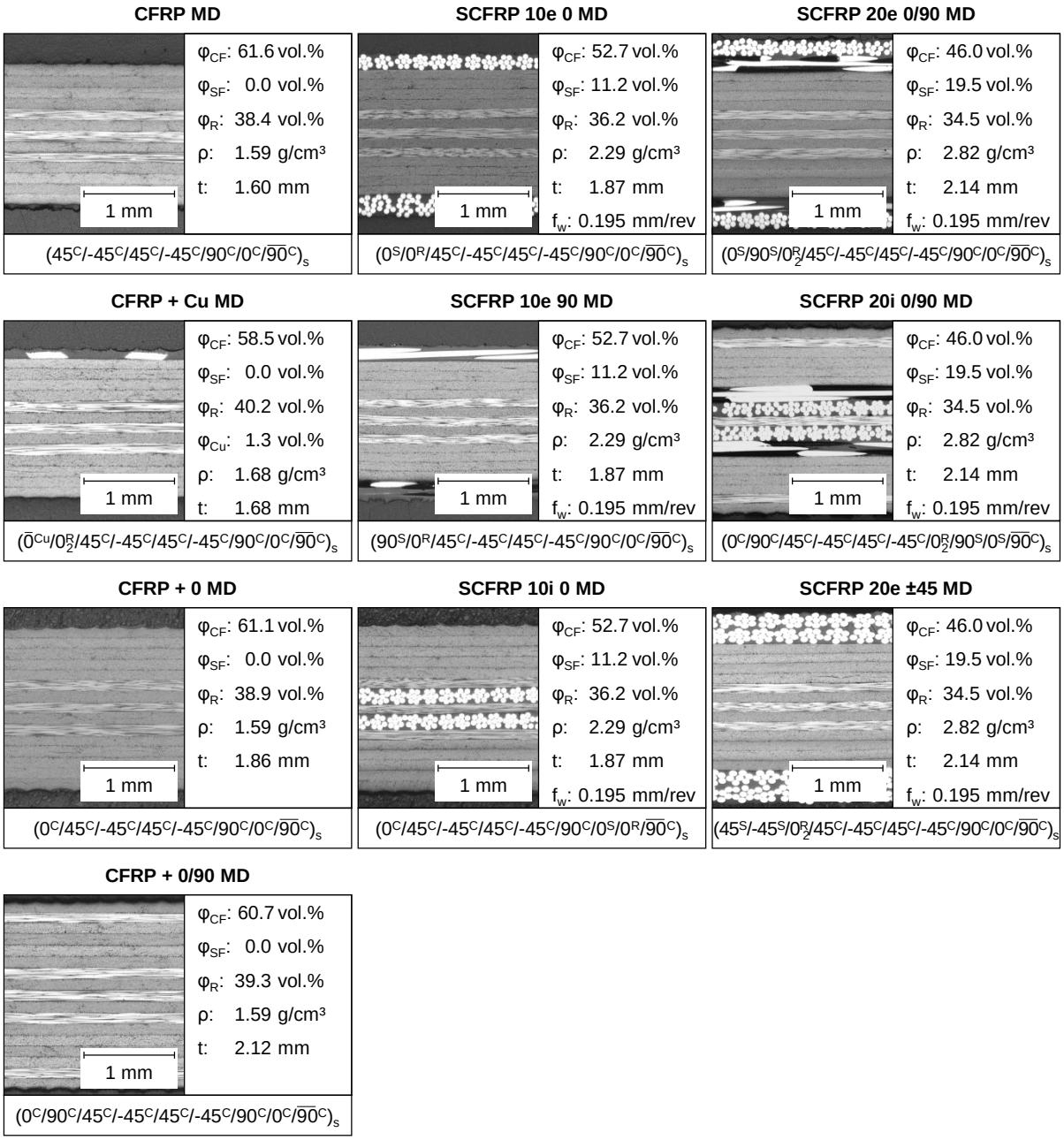

C: carbon, S: steel, R: resin, Cu: copper, φ: volume share, ρ: density, t: laminate thickness, f_w: winding feed rate

Figure 8.1 Microstructure and calculated characteristics of the manufactured and analysed multiaxial reinforced (hybrid) laminates

copper mesh (expanded copper foil) on top is prepared. The hybrid composites consist of the 13-layered CFRP base laminate and two or four additional SFRP plies either as top or core layers with 0°, ±45° or 90° orientation relatively to the material coordinate system. Only the stainless steel fibre bundles are used as metallic reinforcement. For comparison reasons, further CFRP configurations with identical stacking sequences (or laminate thicknesses) as the hybrid composites are taken into account. The microstructure, stacking sequences and calculated characteristics of the different multiaxial reinforced laminates are given in figure 8.1. The laminates are tested regarding their plain tensile behaviour, bolted joint suitability, head pull-through resistance, impact sensitivity and penetration resistance.

8.1 Density

As for the UD composites, the density of the multiaxial laminates is experimentally determined in order to verify the calculated volume shares listed in figure 8.1. Again, the density measurements are carried out by means of the liquid displacement method. For each composite material, two rectangular specimens with a length of 30 mm and a width of 25 mm are analysed. The measured values are compared with the laminate densities estimated by means of the rule of mixtures, applying the calculated volume shares listed in figure 8.1 as well as the fibre and resin densities given in table 4.4.

Table 8.1 Comparison of measured and calculated densities of multiaxial reinforced (hybrid) laminates

Material	Density (calculated) ρ_c / g/cm^3 a)	Density (measured) ρ_m / g/cm^3 b)	Deviation ρ_m to ρ_c / %
CFRP MD	1.59	1.60 ± 0.00	+0.17
CFRP + Cu MD	1.68	1.69 ± 0.00	+0.54
CFRP + 0 MD	1.59	1.59 ± 0.00	-0.18
CFRP + 0/90 MD	1.59	1.59 ± 0.00	-0.03
SCFRP 10e 0 MD	2.29	2.32 ± 0.00	+1.36
SCFRP 10e 90 MD	2.29	2.32 ± 0.02	+1.21
SCFRP 10i 0 MD	2.29	2.27 ± 0.00	-0.91
SCFRP 20e 0/90 MD	2.82	2.80 ± 0.02	-0.43
SCFRP 20i 0/90 MD	2.82	2.79 ± 0.00	-1.00
SCFRP 20e ±45 MD	2.82	2.81 ± 0.00	-0.31

As shown in table 8.1, the measured densities are in good agreement with the estimated values. The deviations range from -1.00 to +1.36 %. Assuming exact values for the applied fibre and resin densities, the minor deviations confirm proper values of the analytically determined volume shares listed in figure 8.1.

8.2 Plain tension behaviour

Monotonic plain tensile (PT) tests are conducted in compliance with DIN EN ISO 527-4 [133]. The rectangular specimens with a length of 250 mm and a width of 25 mm are provided with 1 mm thick, chamfered GFRP end tabs. The specimens are clamped with a free length of 150 mm and loaded with a monotonic crosshead speed of 2 mm/min in line with the 0° orientation of the laminates. All tests are captured by a camera system with a frame rate of 4 Hz in order to analyse the in-plane deformation of the specimen's surface by means of DIC. Using this data, the nominal longitudinal elongation of the specimens is determined within a gauge length of 150 mm. The specimens are initially tested in dry condition (cf. chapter 6.4). In order to asses any potential influence of corrosive media on the tensile characteristics, i.e. to simulate in-service conditions, specimens are additionally tested after being exposed to corrosive fluids. Two different kinds of ageing fluids specified by DIN EN 2379 [134] are selected: distilled water and phosphate ester based hydraulic oil (Skydrol 500B-4). In accordance with DIN EN 2489 [135], specimens are aged by immersion for four weeks

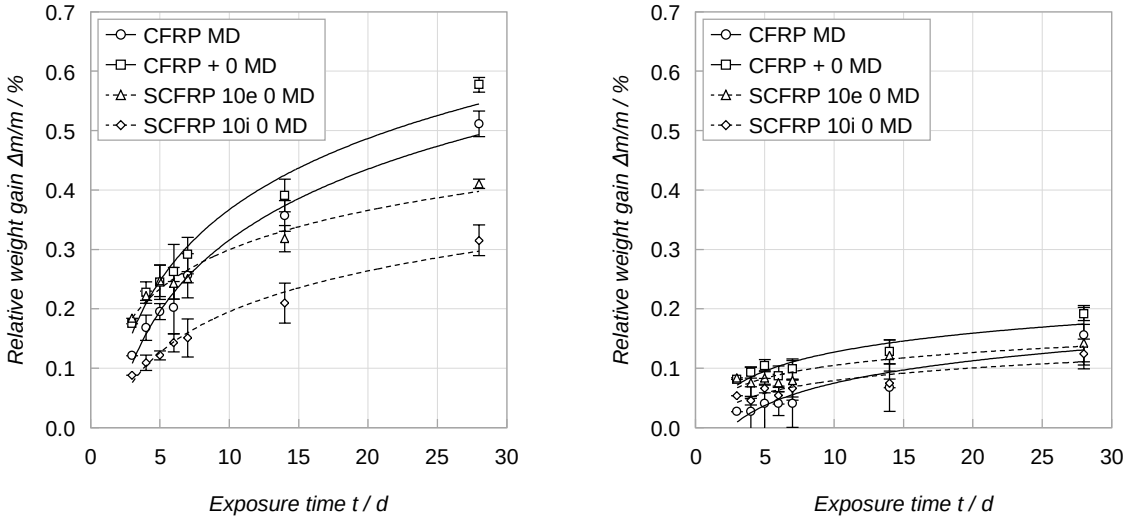

Figure 8.2 Relative weight gain of multiaxial reinforced (hybrid) laminates due to immersion in (left) distilled water and (right) phosphate ester based hydraulic oil of type Skydrol 500B-4

(672 h) at a constant temperature of 23 °C under exclusion of light. During this period, weight changes of the specimens (e.g. due to moisture uptake or corrosion) are monitored by regular weighing. As shown in figure 8.2, both CFRP and the hybrid composites exhibit continuous (logarithmically shaped, cf. Fick's law of diffusion) moisture uptake. Basically, absorption of water is more pronounced than uptake of hydraulic fluid. The relative weight gain of SCFRP, which is lower compared to CFRP, is partly related to the higher material density, i.e. higher initial sample weight, but can also be attributed to the smaller overall boundary surface of the embedded steel fibres to the surrounding resin. An externally visible change of the materials (e.g. due to corrosion), in particular of the hybrid composites, cannot be observed.

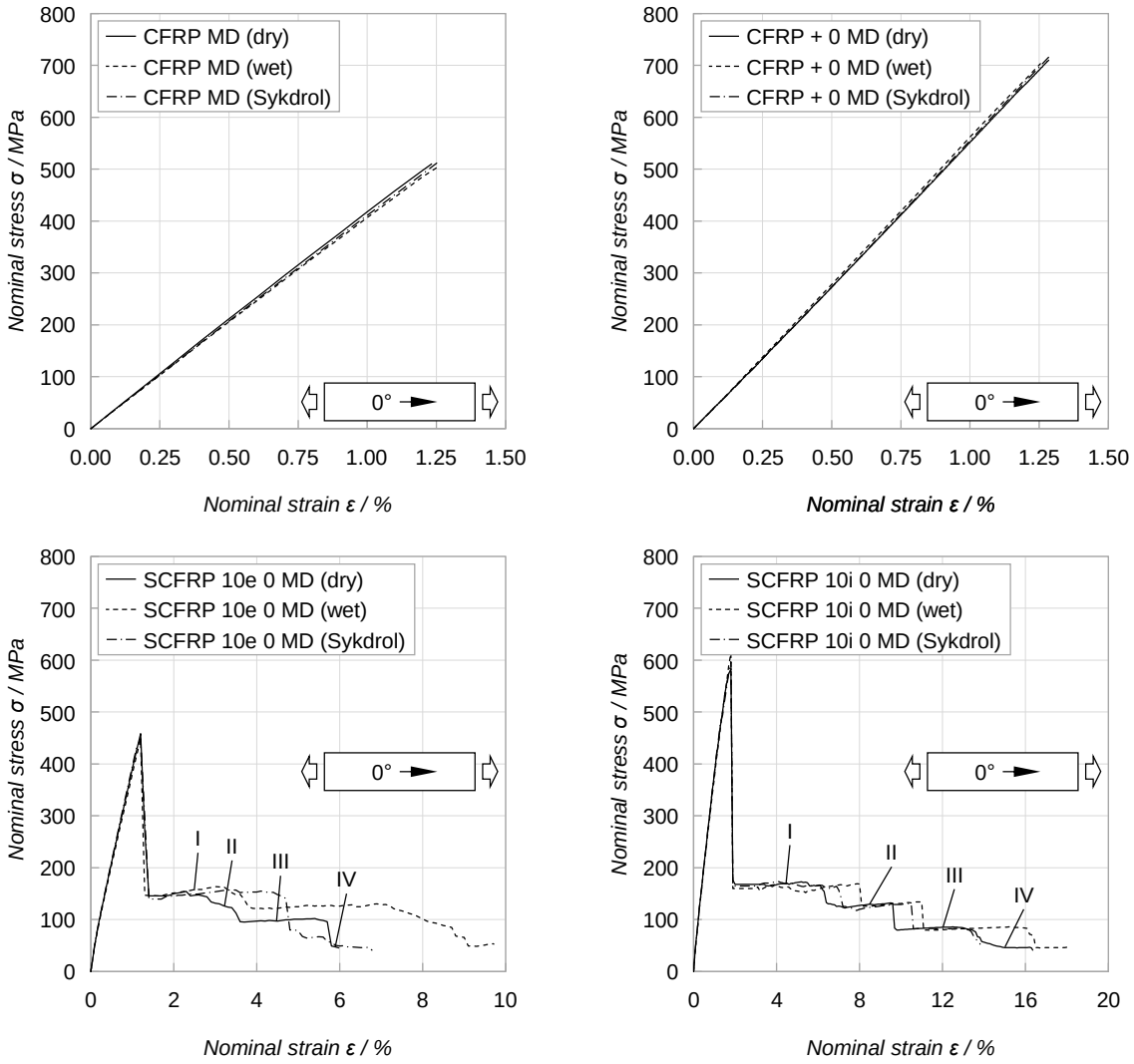

Figure 8.3 Representative stress-strain curves of the plain tension tests on multiaxial reinforced (hybrid) laminates in dependence on the specimen condition

For each laminate configuration and ageing condition, five specimens are loaded to failure. Following testing, the nominal tensile stress and secondary characteristic values are calculated in consideration of the initial cross-sectional area of the specimen. The nominal tensile strength σ_{max}, the corresponding nominal elongation $\varepsilon_{\sigma max}$ and the ultimate nominal elongation ε_{max} are derived from the obtained measuring data. Furthermore, the tensile stiffness E is ascertained by linear regression within a range of 10 to 50 % of the maximum nominal stress experienced. Mean stress-strain curves are depicted in figure 8.3. The corresponding characteristics are given in table 8.2.

Table 8.2 Results of the plain tension tests on multiaxial reinforced (hybrid) laminates in dependence on the specimen condition

Material	Condition	E / GPa	σ_{max} / MPa	$\varepsilon_{\sigma max}$ / %	ε_{max} / %
CFRP MD	dry	42.2 ± 0.7	510 ± 19	1.23 ± 0.06	1.23 ± 0.06
	wet	41.0 ± 0.2	503 ± 2	1.25 ± 0.01	1.25 ± 0.01
	Skydrol	41.4 ± 0.1	513 ± 5	1.26 ± 0.01	1.26 ± 0.01
CFRP + 0 MD	dry	56.2 ± 1.5	703 ± 22	1.25 ± 0.06	1.25 ± 0.06
	wet	55.1 ± 0.1	710 ± 22	1.28 ± 0.05	1.28 ± 0.05
	Skydrol	55.6 ± 0.7	721 ± 9	1.29 ± 0.01	1.29 ± 0.01
SCFRP 10e 0 MD	dry	38.5 ± 0.1	457 ± 6	1.22 ± 0.05	7.66 ± 1.49
	wet	37.5 ± 0.2	460 ± 11	1.43 ± 0.13	9.98 ± 1.03
	Skydrol	38.6 ± 0.3	461 ± 5	1.25 ± 0.10	7.96 ± 1.48
SCFRP 10i 0 MD	dry	36.7 ± 0.2	597 ± 13	1.84 ± 0.06	11.77 ± 4.95
	wet	36.0 ± 0.4	622 ± 7	1.84 ± 0.04	19.91 ± 3.01
	Skydrol	36.7 ± 0.3	592 ± 11	1.83 ± 0.04	11.55 ± 4.76

In dry condition, the reference CFRP exhibits a linear elastic stress-strain relation with a tensile stiffness of (42.2 ± 0.7) GPa. Failure occurs singularly at an elongation of (1.23 ± 0.06) % or at a tensile stress of (510 ± 19) MPa. Addition of two 0° CFRP top layers enhances the stiffness by 33 % and the tensile strength by 38 %, while the strain at failure increases insignificantly by 2 %. By contrast, both hybrid laminates demonstrate a bi-linear stress-strain relation (slightly reduced stiffness from approximately 0.2 % nominal elongation), followed by a gradual failure behaviour. In case of the hybrid laminate with two additional 0° SFRP top layers, the average tensile stiffness is 9 % lower compared to the reference CFRP. Failure is initiated at a

comparable elongation of (1.22 ± 0.05) %. The failure initiation is accompanied by a significant load drop, followed by a distinctive post-failure behaviour. At this stage, four different, slightly increasing levels of load can be identified. Compared to the reference CFRP, the ultimate elongation of the laminate is increased by 522 %. In case of the hybrid laminate with two inner 0° SFRP layers, the tensile stiffness is decreased by 13 %, while the elongation at failure initiation is enhanced by 49 %. As a consequence, the tensile strength increases by 17 % compared to the reference CFRP. Again, four different levels of load can be distinguished at the post-failure stage. The ultimate elongation at break rises by 856 % compared to the reference CFRP.

The bi-linear stress-strain behaviour of the hybrid composites is caused by onset of plastic deformation of the embedded steel fibres. The yielding of the steel fibres is accompanied by progressive diminution of their tensile stiffness, which then lowers the stiffness of the hybrid laminates from an elongation of approximately 0.2 %. The pronounced post-damage behaviour of the hybrid laminates can be attributed to the significantly lower stiffness of the multiaxial aligned CFRP. As deduced in chapter 7.3, the lower stiffness of the CFRP portion significantly reduces the amount of elastic energy which is generated in the laminate until failure initiation. This lowers the restoring force acting during fracture gap generation. In addition, different to UD hybrid composites, a considerable amount of released elastic energy during failure of the 0° CFRP plies can be dissipated in the form of interlaminar crack propagation or inter-fibre-failure within the ±45° and 90° CFRP layers. All together lowers the load exerted on the steel fibres within the fracture zone of influence during failure initiation. Minor plastic elongation of the steel fibres suffices to dissipate the remaining energy, which is released during fracture gap generation. As a consequence, formation of the fracture gap does not exceed the strain at failure of the integrated soft-annealed stainless steel fibres within the FZI. Even with a distinct steel fibre-resin-adhesion and/or a steel fibre share of approximately 10 vol.%, a pronounced post-damage performance with a considerable load-carrying capacity in the after-damage stage is therefore feasible. Moreover, in case of pure CFRP, a considerable amount of elastic energy, which is released during failure of the 0° CFRP layers, is dissipated by failure of the ±45° CFRP layers. This entirely devastates their load-carrying capacity. Both CFRP laminates therefore exhibits brittle failure. By contrast, in case of the hybrid laminates, the ±45° CFRP plies have to absorb less elastic energy during failure

initiation since part of the released elastic energy is dissipated by yielding of the adjacent SFRP layers. As a consequence, the ±45° CFRP layers are not entirely damaged but sustain a certain level of load-carrying capacity. The interaction of both effects leads to the observed post-damage performance with four discriminable levels of load; both lower stress levels (cf. figure 8.3, III + IV) correspond to yielding of the steel fibre reinforced layers, while the upper two levels (I + II) relate to further shear deformation of the (pre-damaged) ±45° CFRP layers. The overall stress-strain relation of the hybrid laminates is consequently not only a superimposition of the stress-strain behaviours of multiaxial CFRP and pure SFRP but a complex interaction of both types of layers.

In principle, the release of elastic energy during failure initiation causes burst (delamination, fibre splintering, elastic out-of-plane deformation due to unbalanced, asymmetric laminate fragments) of the laminate. In case of the hybrid composite with steel fibre reinforced top layers, the intact steel fibres enclose and impede the blast of the laminate, which causes additional load to the integrated steel fibres. If the steel fibre layers are arranged at the centre of the laminate, the energy release can freely develop outwards, causing less impairment to the SFRP layers. As a consequence, the embedded steel fibres are less affected by the burst of the CFRP layers. The plain tensile performance of the hybrid laminate with SFRP layers at its centre is therefore superior to that with SFRP top layers.

Ageing of the composites in aggressive media has no detrimental influence on the plain tensile performance of the hybrid laminates. By trend, water uptake increases the ultimate elongation at break (which is a well-known effect for epoxy-based CFRP [7]) but might also be related to an aggravation of the steel fibre-resin-bond based on the water uptake, causing an increase of the fracture zone of influence. Corrosion of the stainless steel fibres, by contrast, is not observed.

8.3 Bypass failure behaviour

In order to analyse the bypass failure behaviour of the laminates, filled hole tensile (FHT) tests are carried out in accordance with AITM 1-0007 [136]. The specimen appearance and the testing procedure basically corresponds to the plain tension tests described in chapter 8.2. Main differences are the increased specimen width of 32 mm and the cylindrical hole in the centre of the specimen. The hole has a

diameter of 6.35 mm (0.25 inch) and is filled with a titanium (Ti-Al6-V4), close-tolerance fastener with a protruding head. The fastener is installed with a steel washer (same outer diameter as the fastener head) and tightened with a torque of 7 Nm. Again, each test is captured by a camera system with a frame rate of 4 Hz in order to analyse the in-plane deformation of the specimen's surface by means of DIC with a special regard to the heterogeneous strain distribution in the immediate vicinity of the fastener hole. For each laminate configuration, five specimens are tested to failure. Following testing, the nominal tensile stress and secondary characteristic values are calculated in consideration of the initial gross cross-sectional area of the specimen ("far-field stress"), disregarding the cross-section reduction caused by the fastener hole. In addition to the filled hole tensile strength σ_{max} and the corresponding nominal elongation $\varepsilon_{\sigma max}$, the ultimate nominal elongation ε_{max} is determined. Furthermore, the tensile stiffness E is ascertained by linear regression within a range of 10 to 50 % of the maximum stress experienced. Mean stress-strain curves are depicted in figure 8.4. Table 8.3 contains the derived characteristic values.

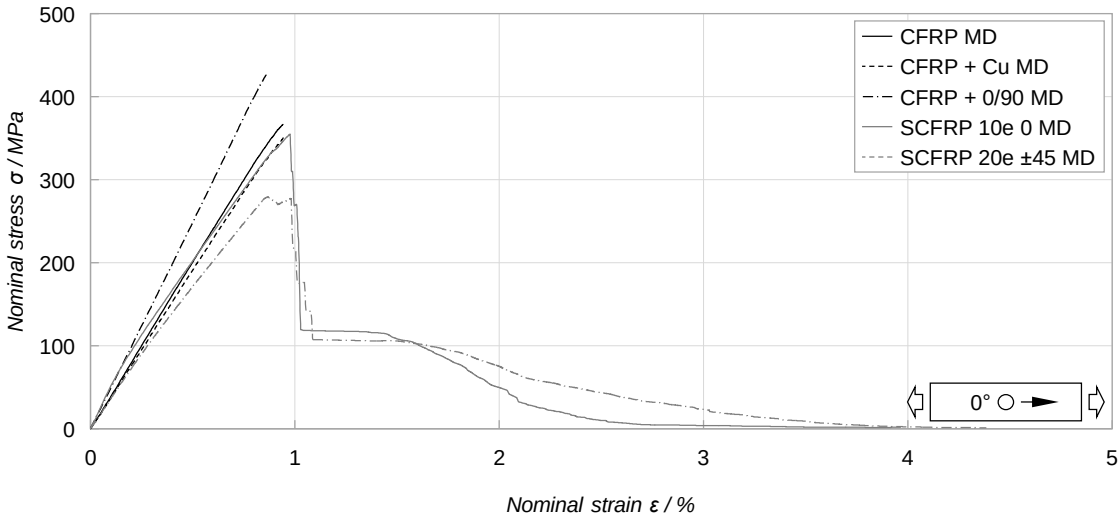

Figure 8.4 Mean stress-strain curves of the filled hole tension tests on multiaxial reinforced (hybrid) laminates

The reference CFRP exhibits a linear stress-strain relation with a tensile stiffness of (40.6 ± 0.5) GPa. Failure occurs singularly at an elongation of (0.94 ± 0.02) % or at a tensile stress of (366 ± 6) MPa. Addition of two 0° and two 90° CFRP layers on top increases the stiffness of the laminate by 22 % and the tensile strength by 16 %, while the strain at failure is reduced by 9 %. By contrast, a copper mesh on top of the laminate has a negligible influence on the bypass failure behaviour of CFRP.

Table 8.3 Results of the filled hole tension tests on multiaxial reinforced (hybrid) laminates

Laminate	E / GPa	σ_{max} / MPa	$\varepsilon_{\sigma max}$ / %	ε_{max} / %
CFRP MD	40.6 ± 0.5	366 ± 6	0.94 ± 0.02	0.95 ± 0.02
CFRP + Cu MD	38.4 ± 0.6	353 ± 9	0.95 ± 0.02	0.97 ± 0.02
CFRP + 0/90 MD	49.6 ± 0.8	426 ± 14	0.86 ± 0.01	0.86 ± 0.01
SCFRP 10e 0 MD	38.3 ± 0.8	361 ± 7	1.00 ± 0.02	3.96 ± 0.53
SCFRP 20e ±45 MD	34.4 ± 0.5	286 ± 7	0.95 ± 0.04	4.38 ± 0.19

Compared to the reference CFRP, the tensile stiffness (-5 %) and the ultimate tensile strength (-4 %) are slightly reduced due to the poor mechanical properties of the LSP copper mesh[20]. The ultimate strain at failure of the laminate remains unchanged. Addition of two additional 0° SFRP top layers causes a bi-linear stress-strain relation; as in case of the plain tensile tests, the stiffness of the composite decreases from an elongation of approximately 0.2 %. Compared to CFRP, the average tensile stiffness is lowered by 6 %. Failure is initiated at an elongation of (1.00 ± 0.02) % or at a tensile stress of (361 ± 7) MPa. The failure initiation is accompanied by a significant load drop, followed by a continuous degradation of the load-bearing capacity of the composite. Compared to CFRP, the ultimate elongation of the laminate is increased by 319 %. The hybrid laminate with four additional ±45° SFRP top layers exhibits a slightly declining stress-strain relation. In comparison with the reference CFRP, the stiffness and the tensile strength are reduced by 15 % and 22 %. The elongation at failure initiation equates to the strain at failure of the reference CFRP. Similar to SCFRP 10e 0 MD, this hybrid laminate configuration shows a pronounced post-failure performance. Compared to the reference CFRP, the ultimate elongation at break is increased by 363 %.

Due to the cross-section reduction at the borehole and the corresponding load transfer, the filled hole tensile test is characterised by a heterogeneous strain state with a butterfly-shaped strain distribution around the drill hole. Stress concentrations are produced in the laminate close to the borehole. Local stress consequently exceeds the far-field stress condition. According to the point stress criterion for notched strength prediction, failure occurs when the stress at a characteristic

[20] Reduction of the cross-sectional area by the nominal thickness of the applied LSP copper mesh (0.076 mm) yields stiffness and strength values which are identical to those of the reference CFRP.

distance from the drill hole exceeds the unnotched tensile strength of the composite. As a consequence, the ultimate strain at failure of the reference CFRP is considerably lower than the longitudinal elongation at break of unidirectional CFRP or of the applied carbon fibres. Since the effect of the stress concentrations depends on the laminate anisotropy (ratio of E_1 to E_2), the ultimate strain at failure of CFRP + 0/90 MD is lower compared to CFRP MD. In case of the hybrid composites, incorporation of steel fibres causes a diminution of the longitudinal stiffness of the laminates since the modulus of elasticity of the integrated stainless steel fibres is lower than that of the applied carbon fibres. Onset of plastic deformation of the steel fibre bundles (accompanied by a progressive reduction of their tensile stiffness) leads to an additional reduction of the effective tensile stiffness of the hybrid laminate and finally to the bi-linear stress-strain relation. However, local stiffness degradation due to yielding of the steel fibres also enables to minimise stress concentrations in the immediate vicinity of the borehole and thus to increase the elongation at failure initiation. Similar to the plain tension tests, the embedded steel fibres of the hybrid laminates are able to endure the fracture process of the longitudinal carbon fibres by means of plastic deformation. After damage initiation (failure of the 0° CFRP layers), the hybrid laminates can bear further load by including the SFRP and ±45° CFRP layers but due to the reduction of the effective cross-sectional area on a lower level of load. Progressive shearing of the ±45° CFRP layers and increasing damage extent of the composite continuously decrease the load-carrying capacity. Moreover, a certain load-carrying capacity in the after-damage stage is given by interlocking (friction) of the fragmented fracture surfaces, which, however, becomes less important with increasing laminate elongation. In case of SCFRP 20e ±45 MD, progressive shear deformation of the ±45° SFRP top layers causes a continuous diminution of the load-carrying capacity in the after-damage stage. Besides, the minor strength of the ±45° SFRP top layers in load direction decreases the tensile stiffness and strength of the hybrid laminate compared to the reference CFRP.

8.4 Bearing behaviour

In order to analyse the influence of the steel fibre incorporation on the bearing strength of CFRP, pin load bearing (PLB) tests are carried out according to AITM 1-0009 [137]. The rectangular specimens are 150 mm long and 42 mm wide. The thickness depends on the tested laminate configurations (cf. figure 8.1) but generally

falls below the recommendation of the mentioned standard (4 mm). At one end, the specimens are provided with 1 mm thick, chamfered GFRP tabs, while at the opposite end the specimens include a drill hole with a diameter of 6.35 mm (0.25 inch). The bearing load is introduced to the specimens via two steel loading plates and a titanium (Ti-Al6-V4), close-tolerance fastener with a shank diameter of 6.35 mm (0.25 inch). The fastener is tightened with a torque of 5 Nm, allowing the jig to maintain a gap of 0.5 mm either side of the specimen. The specimens are loaded with a constant crosshead speed of 1 mm/min until a load drop greater than 30 % or a crosshead displacement of 5 mm is achieved. For each material configuration, a number of five test specimens is tested. The only valid failure mode is bearing failure. The bearing stress at any time during the test is calculated by dividing the tensile load by the bearing area, i.e. the product of nominal bolt diameter and specimen thickness. The ultimate bearing strength of the tested materials is listed in table 8.4.

Table 8.4 Bearing strength and load of multiaxial reinforced (hybrid) laminates

Property	CFRP MD	SCFRP 10e 0 MD	SCFRP 10i 0 MD	SCFRP 20e 0/90 MD	SCFRP 20e ±45 MD
F_{max} / N	5306 ± 499	5823 ± 690	5454 ± 699	6785 ± 370	6444 ± 798
σ_{max} / MPa	490 ± 49	488 ± 59	453 ± 58	476 ± 23	466 ± 60

All tested laminate configurations exhibit similar bearing response: with increasing hole deformation, the bearing stress increases nearly linearly (slightly declining) up to a maximum value. After exceeding the ultimate bearing strength, the bearing stress drops to a lower level. Accumulation of displaced material in front of the pin and the associated friction to the loading plates subsequently causes a re-gain of the apparent bearing stress. An initial peak or inflection point on the bolt bearing test curve is observed for none of the investigated material configurations. In principle, the bearing failure corresponds to a compression failure of the laminate in front of the pin. Initial failure occurs in the form of inter- and intralaminar cracks (inter-fibre-failure, delamination), causing local stiffness degradation, load redistribution and thus a reduction of stress concentrations. The bearing failure is finally related to an exceedance of the compression strength (buckling stability) of the fibres which are aligned in load direction in front of the pin. By contrast, reinforcing fibres which are aligned at an angle to the load direction serve to prevent splitting of the laminate.

The integration of stainless steel fibres in load direction has no significant influence on the bearing performance of CFRP. In principle, addition of 0° SFRP layers increases the absolute bearing strength of the laminate. Still, since the stiffness and strength of the steel fibres is lower compared the applied carbon fibres, the specific bearing strength is comparable to that of the reference CFRP. By contrast, adding steel fibres perpendicularly to the load direction lowers the specific bearing strength by 8 %. Advantages are only obtained in the stage after bearing failure. Similarly, the combination of two additional 0° and 90° SFRP layers on top of the reference slightly lowers the specific bearing strength by 3 %. Addition of four ±45° SFRP top layers to the reference CFRP decreases the specific bearing strength by 5 % due to the minor support of the fastener by the diagonal arranged steel fibres (compared to fibres straight aligned in load direction). However, with increasing pin displacement after bearing failure, the steel fibres are subjected to tensile load. Distinct onset of plastic elongation and the associated strain hardening causes a much faster re-gain of the bearing stress in comparison with CFRP MD. In this context, the ductile steel fibre deformation in the post-damage stage is beneficial in terms of energy absorption purposes and is therefore analysed in the following chapter.

8.5 Progressive bearing behaviour

In order to analyse the behaviour of the laminates under progressive bearing load, dynamic bearing tests are carried out on a testing machine of type Zwick HTM 5020. For this purpose, rectangular specimens with a width of 70 mm and a length of 75 mm are fixed by a U-shaped clamping device. At the lower end, the composite plates include a borehole with a diameter of 6.35 mm (0.25 inch). The drill hole is filled with a stainless steel bolt with a shank diameter of 6.35 mm (0.25 inch). Using a CFRP loop, the bolt is continuously pulled through the specimen with a constant crosshead speed of 1 m/s. The load is measured by a piezo-electric load cell with a calibrated range of 50 kN. The test setup and a representative sequence of the progressive bearing tests are depicted in figure 8.5. For each material configuration, a number of five specimens is tested. Average stress-displacement curves and the corresponding characteristics are given in figure 8.6 and table 8.5. Representative failure patterns are shown in figure 8.7.

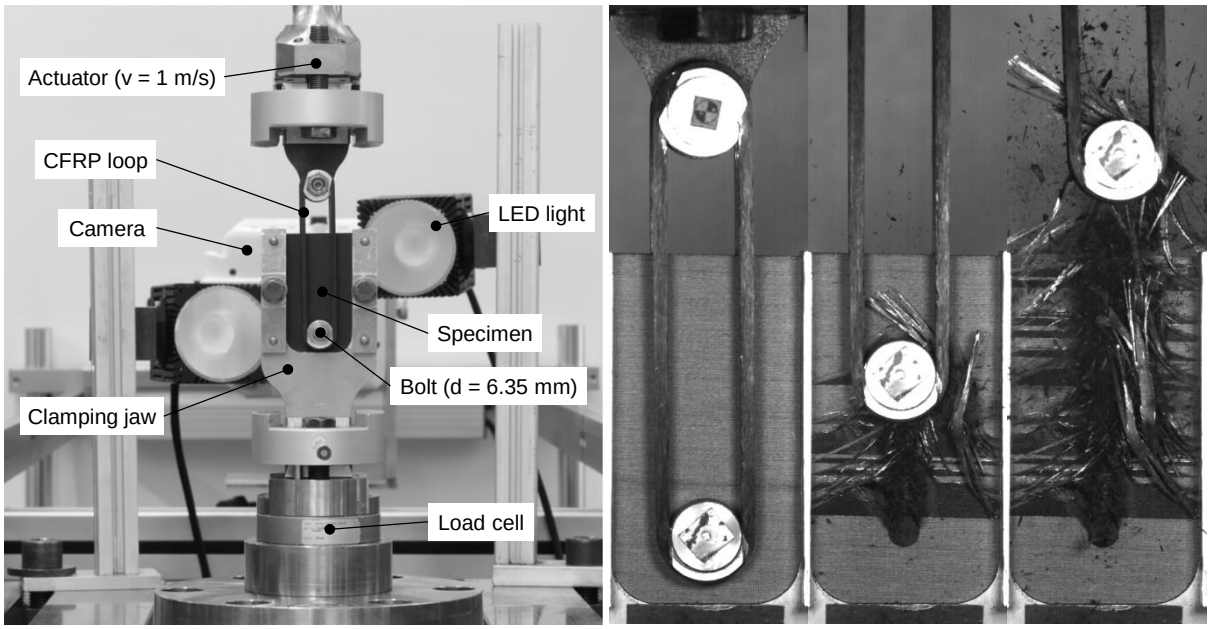

Figure 8.5 (left) Test setup and (right) exemplary sequence of the progressive bearing tests on multiaxial reinforced (hybrid) laminates

In principle, all tested laminate configurations exhibit a similar material response: after exceeding an initial trigger stress σ_{trig}, the bearing stress drops to a lower level and oscillates around a nearly constant level σ_{mean}. Integration of the mean stress-displacement curves yields the specific energy $e_{a,max}$ which is absorbed by the specimens. However, the laminate configurations clearly differ in their failure pattern. In case of the reference CFRP, damage is limited to a narrow corridor along the trace of the pin. The failure mode is dominated by brittle fracturing of the carbon fibres

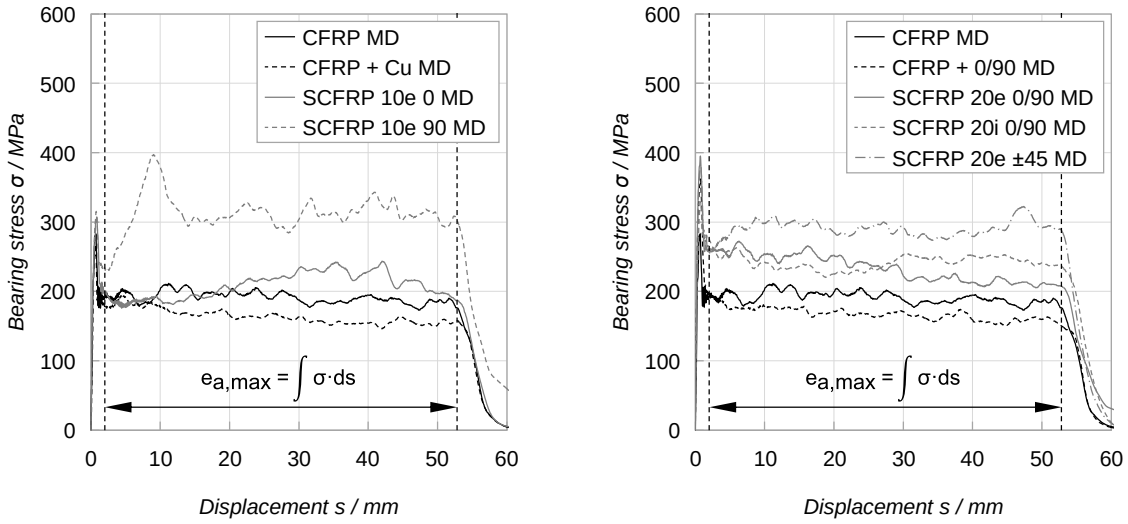

Figure 8.6 Mean stress-displacement curves of the progressive bearing tests on multiaxial reinforced (hybrid) composites

Table 8.5 Results of the progressive bearing tests on multiaxial reinforced (hybrid) laminates

Laminate	σ_{trig} / MPa	σ_{mean} / MPa	$e_{a,max}$ / J/mm^2
CFRP MD	292 ± 16	191 ± 8	10.63 ± 0.45
CFRP + Cu MD	269 ± 18	164 ± 22	9.17 ± 1.19
CFRP + 0/90 MD	369 ± 58	167 ± 12	9.49 ± 0.63
SCFRP 10e 0 MD	317 ± 25	209 ± 13	11.61 ± 0.62
SCFRP 10e 90 MD	318 ± 16	313 ± 17	17.40 ± 1.02
SCFRP 20e 0/90 MD	402 ± 52	233 ± 16	13.18 ± 0.91
SCFRP 20i 0/90 MD	331 ± 8	242 ± 12	13.69 ± 0.66
SCFRP 20e ±45 MD	391 ± 37	290 ± 12	16.16 ± 0.67

mainly under compression load (cf. figure 2.9). Increasing the laminate thickness by four additional CFRP layers (CFRP + 0/90 MD) enhances the initial trigger stress by 26 % but lowers the mean bearing stress by 14 %. An additional copper mesh on top of the reference CFRP has no relevant influence on the bearing performance of the composite. Due to the minor stiffness and strength of the copper mesh and despite its high ductility, the initial trigger stress decreases by 8 % compared to the reference CFRP, while the mean bearing stress is reduced by even 14 %. The failure pattern corresponds to that of pure CFRP. Adding two SFRP top layers in parallel to the pin motion direction has only a minor influence on the progressive bearing resistance of the laminate. The steel fibres in front of the pin are coiled and subsequently displaced without significant plastic deformation. As a consequence, additional energy absorption is primarily attributed to bending crushing of the SFRP layers. The mean bearing stress therefore increases only by 9 % compared to the reference CFRP. By contrast, adding two SFRP top layers perpendicularly to the pin motion direction significantly improves the bearing performance. Caused by the expulsion of the pin, the steel fibres detach from the inner CFRP layers along the entire width of the specimen and are free to yield. Extensive areas lateral to the track of the pin are degraded and involved for energy absorption purposes. Compared to the reference CFRP, energy is additionally absorbed by the SFRP layers by means of inter- and intralaminar crack growth as well as plastic deformation of the steel fibres. Moreover, friction between laminate bundles as well as between the laminate bundles and the pin additionally contributes to energy absorption. As a consequence, the mean bearing stress and finally the energy absorption capacity increase by 63 % compared to the reference CFRP. In case of SCFRP 20e 0/90 MD, the detachment of the 90°

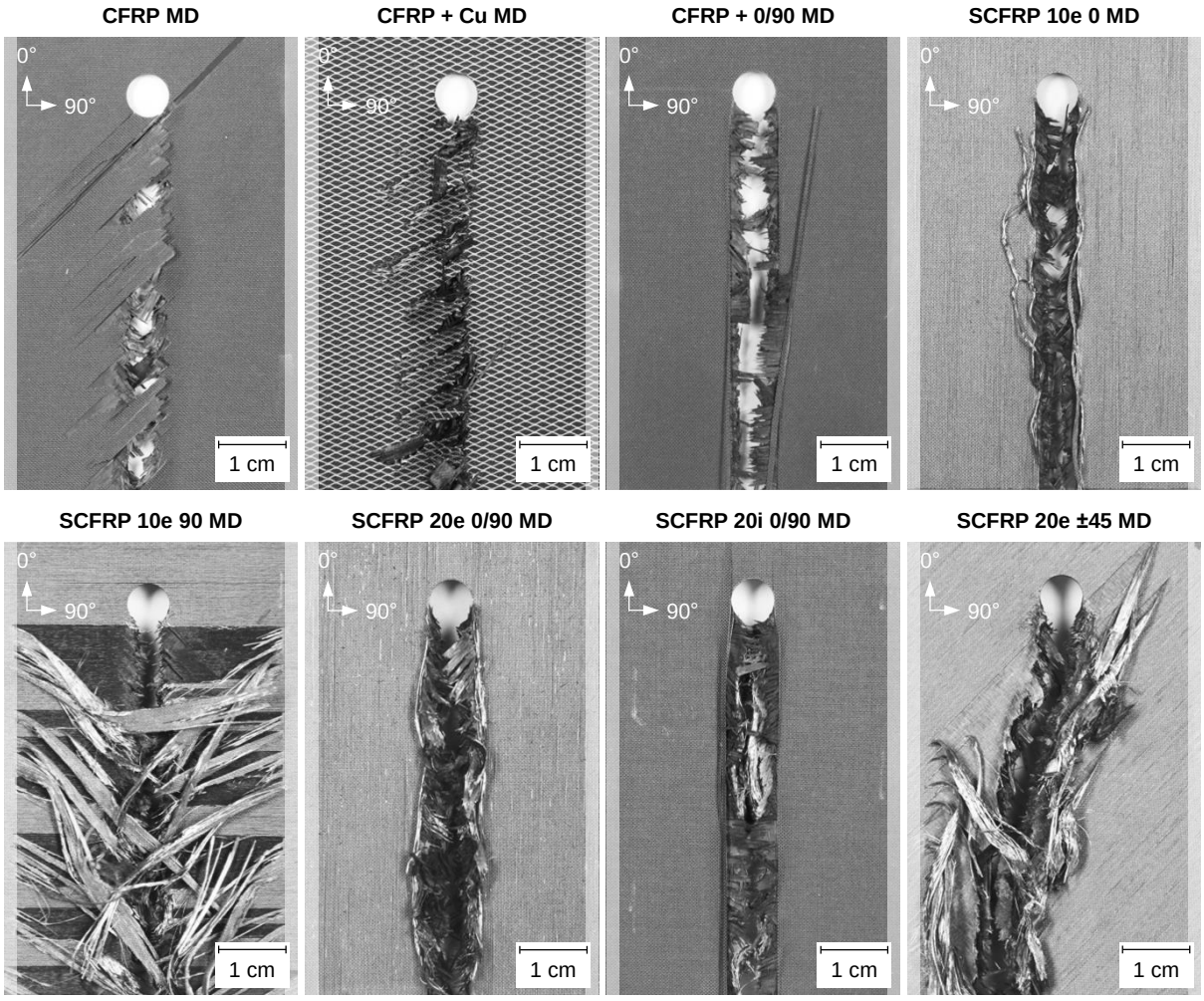

Figure 8.7 Representative failure modes after progressive bearing tests on multiaxial reinforced (hybrid) laminates

SFRP layers and thus yielding of the steel fibres is impeded by the 0° SFRP top layers. The energy absorption mechanisms observed for SCFRP 10e 90 MD are therefore limited to a much smaller extent, reducing the bearing resistance of the hybrid composite. As a result, the mean bearing stress and the specific energy absorption capacity increases by only 22 % compared to the reference CFRP. However, the initial trigger force is enhanced by 38 %. A very similar material response is given in case of SCFRP 20i 0/90 MD. The mean bearing stress and the specific energy absorption capacity increases by 26 %, while the initial trigger stress rises by 12 % compared to the reference CFRP. Adding four ±45° SFRP top layers on top of the reference CFRP significantly improves both the initial trigger stress (+34 %) and the mean bearing stress (+52 %). Steel fibres of the outermost layers delaminate from the subjacent layers, yield to their maximum elongation and fail under tensile load.

8.6 Bolt pull-through resistance

In order to determine the resistance of the laminates against penetration of a fastener head (pull-out/pull-through strength), bolt pull-through (BPT) tests are carried out in dependence on AITM 1-0066 [138]. For this purpose, plain quadratic specimens with an edge length of 60 mm and a central drill hole with a diameter of 6.35 mm (0.25 inch) are fixed in a test rig. The clamping device consists of a support ring and a clamping ring, both with an inner diameter of 40 mm and chamfered with a 1 mm radius. Subsequently, a titanium (Ti-Al6-V4), close-tolerance fastener with a shank diameter of 6.35 mm (0.25 inch) and a protruding head is inserted from the bottom of the specimen and attached to a yoke with a self-locking nut. The nut is installed with a torque of 2 Nm. During the test, a uniaxial tensile force is applied to the yoke, leading to a tensile loading of the fastener and thus to an out-of-plane loading of the specimen. For each material configuration, five specimens are tested to failure with a constant crosshead speed of 1 mm/min. The force exerted on the specimens is measured by a load cell with a calibrated range of ±10 kN, while the nominal displacement of the fastener is given by the crosshead displacement. The material response is characterised by the force at first failure F_{int}, the maximum force F_{max}, the corresponding displacements s_{Fint} and s_{Fmax}, the displacement at which the force has fallen to half its maximum value s_p and the energies which are expended up to the maximum force $E_{a,Fmax}$ or complete pull-trough $E_{a,7\,mm}$. Moreover, the ratio R of the energy absorbed after maximum load to the energy absorbed prior to maximum

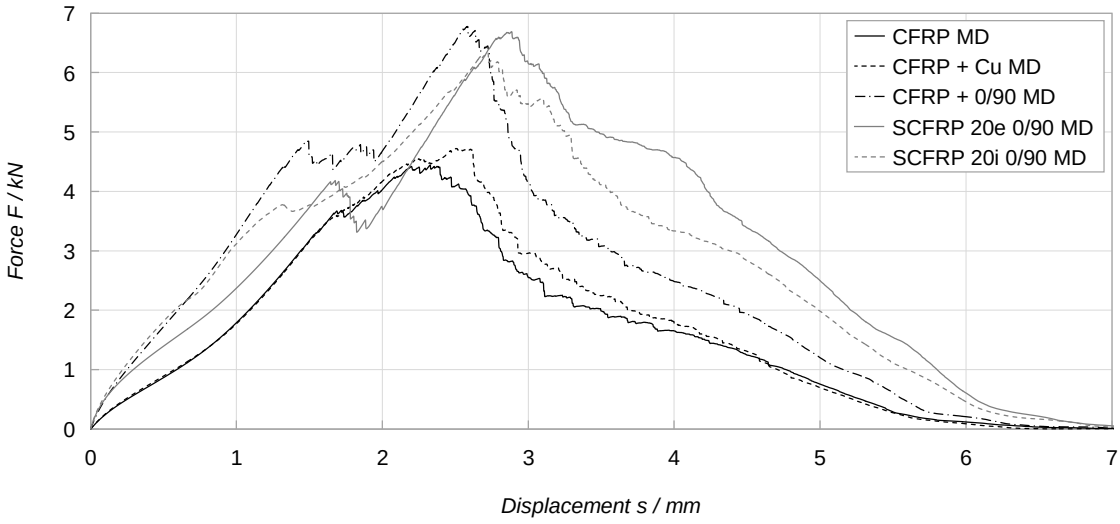

Figure 8.8 Mean force-displacement curves of the head pull-through tests on multiaxial reinforced (hybrid) laminates

Table 8.6 Results of the head pull-through resistance tests on multiaxial reinforced (hybrid) laminates

Laminate	F_{int} / kN	s_{Fint} / mm	F_{max} / kN	s_{Fmax} / mm	$E_{a,Fmax}$ / J	s_p / mm	$E_{a,7\,mm}$ / J	R
CFRP MD	3.74 ± 0.17	1.72 ± 0.13	4.68 ± 0.16	2.45 ± 0.11	5.88 ± 0.35	3.15 ± 0.15	11.37 ± 0.31	0.94 ± 0.08
CFRP + Cu MD	3.76 ± 0.22	1.75 ± 0.05	4.83 ± 0.24	2.47 ± 0.19	6.09 ± 0.91	3.27 ± 0.23	12.01 ± 0.26	1.02 ± 0.37
CFRP + 0/90 MD	4.93 ± 0.27	1.49 ± 0.13	7.05 ± 0.36	2.69 ± 0.09	10.17 ± 0.43	3.27 ± 0.17	17.51 ± 0.37	0.72 ± 0.06
SCFRP 20e 0/90 MD	4.37 ± 0.21	1.71 ± 0.05	6.78 ± 0.30	2.89 ± 0.04	9.52 ± 0.23	4.49 ± 0.18	20.61 ± 0.42	1.17 ± 0.06
SCFRP 20i 0/90 MD	3.95 ± 0.09	1.33 ± 0.02	6.45 ± 0.13	2.77 ± 0.04	9.75 ± 0.30	4.15 ± 0.03	19.48 ± 0.43	1.00 ± 0.03

load is determined. Mean force-displacement curves and the corresponding characteristic values are summarised in figure 8.8 and table 8.6. Typical failure patterns for each laminate configuration are depicted in figure 8.9.

In case of the reference CFRP, the specimen bends upwards due the tensile load exerted by the fastener in the initial phase of the BPT test. At a deflection of (1.72 ± 0.13) mm or at a force of (3.74 ± 0.17) kN, failure in the form of matrix cracking and delamination is initiated. This is accompanied by a degradation of the effective bending stiffness and thus by unloading of the laminate (indicated by a first load drop). Further increase of the rivet displacement causes penetration of the laminate by the fastener head, which is accompanied by delamination propagation and fibre breakage. Ultimate BPT failure of the composite occurs after loss of the bending stiffness below the fastener head, causing a continuous diminution of the head pull-through resistance. A certain resistance is, however, still given by friction between fastener head and fracture surface (protruding laminate bundles). Addition

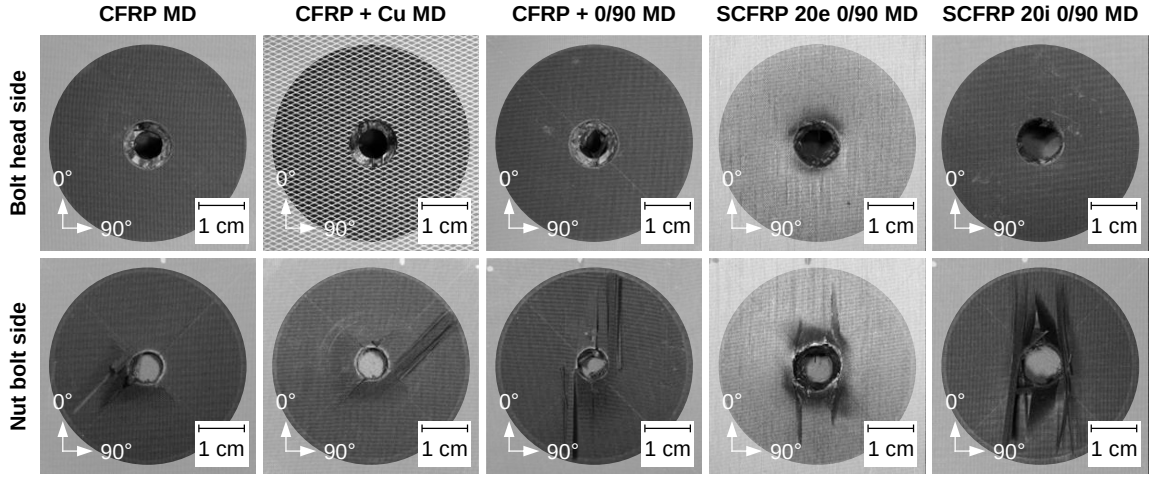

Figure 8.9 Representative failure modes after head pull-through tests on multiaxial reinforced (hybrid) laminates

of four additional CFRP layers (CFRP + 0/90 MD) basically increases the bending stiffness as a result of the higher laminate thickness. The load for failure initiation increases by 32 %, while the necessary deformation decreases by 13 %. The ultimate BPT strength rises by 51 %, while the corresponding deflection increases by 9 %. The basic failure pattern, however, remains unchanged. An additional LSP copper mesh on top of the compression loaded side of CFRP has no relevant meaning for the BPT resistance of the laminate. Both failure pattern and force-displacement curve are similar to that of the reference CFRP. By contrast, adding two SFRP layers on both sides of the reference CFRP (SCFRP 20e 0/90 MD) increases the initial bending stiffness of the composite (due to the increased moment of inertia) compared to the reference CFRP. The bending stiffness, however, declines again prior to first failure due to onset of yielding of the steel fibres. Still, compared to the reference CFRP, first failure occurs at a similar displacement but on a higher level of load (+17 %). The ultimate BPT strength significantly enhances by 45 %. The associated displacement increases by 18 %. Different to the reference CFRP, continuous yielding of the steel fibres causes a slower degradation of the laminate bending stiffness after exceeding the maximum force. As a consequence, the energy which is required for complete pull-through of the fastener rises by 81 % compared to the reference CFRP. Addition of four SFRP layers to the core of the laminate (SCFRP 20i 0/90 MD) has a similar influence on the BPT performance. The larger laminate thickness causes an increase in bending stiffness. However, different to SCFRP 20e 0/90 MD, onset of plastic deformation of the embedded steel fibres has (due to their arrangement close to the neutral axis of the laminate) only a negligible influence on the bending stiffness of the laminate. Compared to the reference CFRP, the deflection for failure initiation decreases by 23 % (due to the higher bending stiffness), while the load at failure initiation increases by 6 %. Moreover, unlike the brittle CFRP layers, the structural integrity of the SFRP layers prevents sudden penetration of the fastener. The force drop after failure initiation is significantly lower compared to SCFRP 20e 0/90 MD. Compared to the reference CFRP, the ultimate BPT strength increases by 38 %; the corresponding displacement rises by 13 %. The total energy for complete pull-trough of the fastener increases by 71 %.

8.7 Impact behaviour

In order to assess the low velocity/low mass impact sensitivity of the laminates, compression strength after impact (CAI) tests are conducted in dependence on AITM 1-0010 [139]. The specimen thickness is given by the laminate configurations to be tested (cf. figure 8.1), which is less than recommended in the relevant standard (4 mm). The test procedure involves two distinctive parts: damage generation by impact and post-impact damage propagation by mechanical compression loading.

The impact damage is generated on a drop tower by a falling impactor slide with a total weight of 4.87 kg and a hemispherical indenter with a diameter of 20 mm. The desired impact energy E_i is set by the drop height. The rectangular specimens with a length of 150 mm and a width of 100 mm are secured to a flat mounting plate using four snap fasteners. The support jig has a central cut-out of 125 by 75 mm. The contact force F is measured by a piezo-electric load cell with a calibrated range of ±60 kN, which is mounted between indenter and impactor slide, while the motion of the impactor slide is captured by a single-point laser vibrometer (Polytec OFV-525/

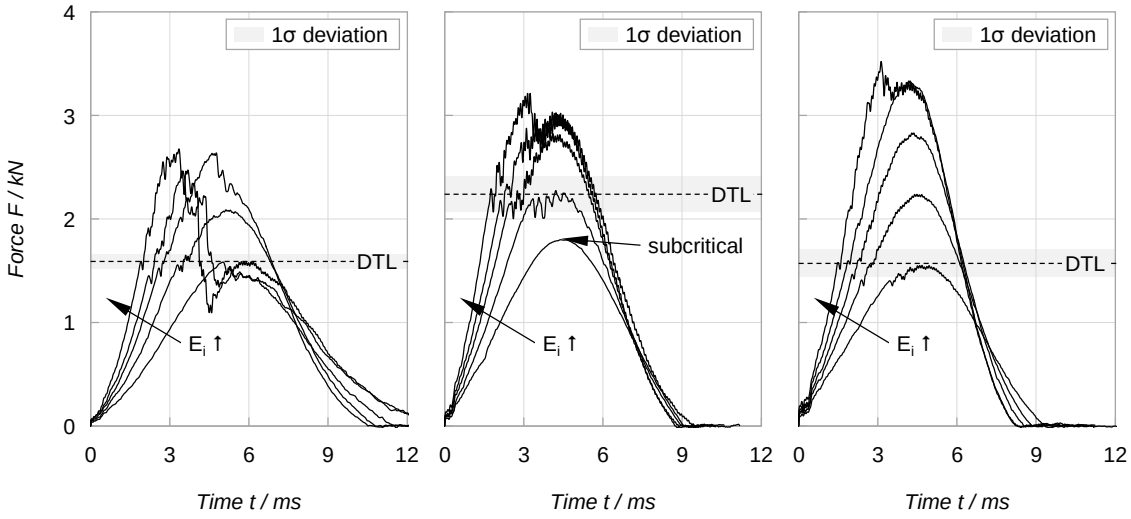

Figure 8.10 Contact force history trace of the impact tests for (left) CFRP MD, (middle) CFRP + 0/90 MD and (right) SCFRP 20e 0/90 MD as a function of the impact energy (3, 5, 7, 9, 13 J) with indication of the average damage threshold load (DTL)[21]

[21] In order to determine the DTL of a laminate configuration, the first local maximum (followed by a significant drop and pronounced oscillations, cf. chapter 2.4) of the unfiltered force history trace is identified for each specimen (or impact energy) tested. Averaging these values yields the DTL of the respective laminate configuration.

-5000-S). Repeated hits by the indenter are prevented by using a suitable arresting device. Five impact energies between the threshold level and that causing perforation of the laminates are investigated. The resulting contact force-time traces are depicted in figure 8.10.

After the impact, the permanent indentation depth d is measured using a non-contact profilometer (white light interferometry). For this purpose, the sample surface is scanned with a grid spacing of 0.2 mm, a vertical resolution of 30 nm and a maximum vertical scan range of 3 mm. Impact-induced global warpage of the hybrid laminate samples is excluded by defining a plane of reference according to the best-fit position of an annulus (inner diameter: 16 mm, outer diameter: 20 mm) concentrically arranged around the impact location. The dent depth is then determined by the maximum indentation perpendicularly to the plane of reference.

In order to determine the extent of the impact-induced internal damages (delamination area A), all samples are non-destructively tested by ultrasonics using the double-through-transmission technique with an auxiliary reflector. This technique allows ultrasonic testing of thin samples without front and back surface echo affecting

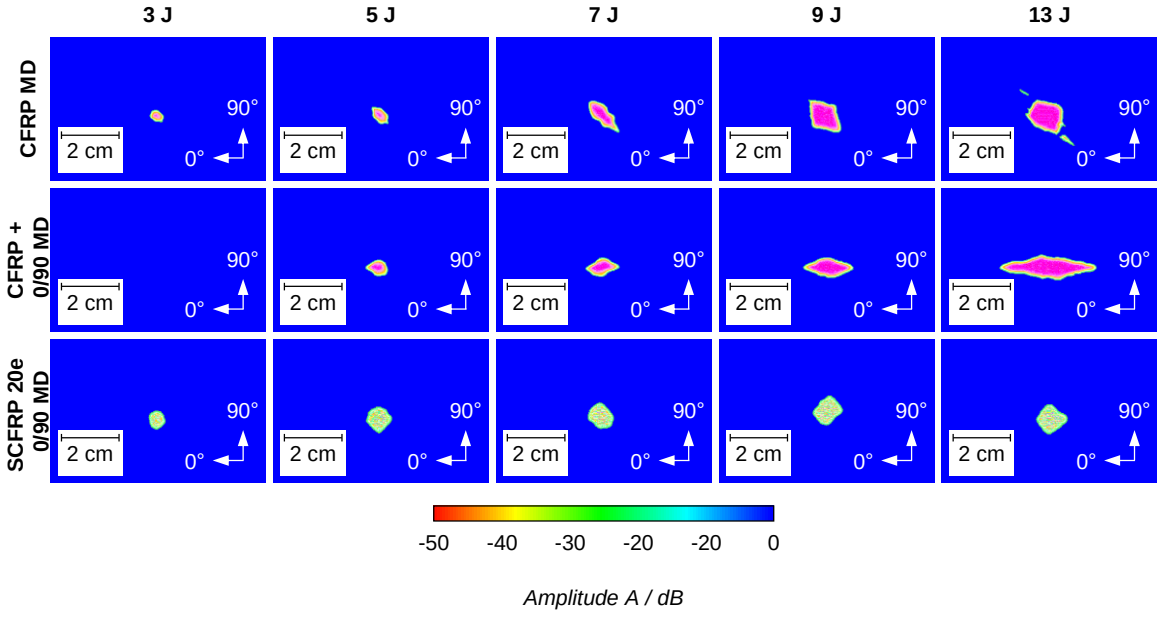

Figure 8.11 Visualisation of the impact-induced damages by means of ultrasonic testing (C-scans) with an evaluation damage threshold level of 16 dB[22]

[22] Ultrasonic inspections were performed by the Institute for Plastic Technology Palatinate of the University of Applied Sciences Kaiserslautern.

the evaluating gate, which is set around the reflector echo. The distance between the rear side of the samples and the reflector is 5 mm to clearly separate back surface echo and reflector echo. The inspections are accomplished with an ultrasonic transducer providing a frequency of 5 MHz while having a focal length of 50 mm. The focal point is targeted on the auxiliary reflector. The step width is chosen to 0.2 mm. The damage threshold level for evaluation is set to 16 dB. The resulting C-scans are depicted in figure 8.11.

Additionally, impact-induced variation of the magnetic volume fraction within the metastable austenitic steel fibre reinforced near-surface layers is measured. For this purpose, the area around the dent on front and back surface of the specimen is scanned with a magnetic inductive measuring device (cf. appendix A.3). The grid spacing is set to 5 mm. The measuring device quantifies deformation-induced phase transformations from paramagnetic γ-austenite to ferromagnetic α'-martensite. The distribution of the absolute magnetic volume share ξ after impact is visualised in figure 8.12.

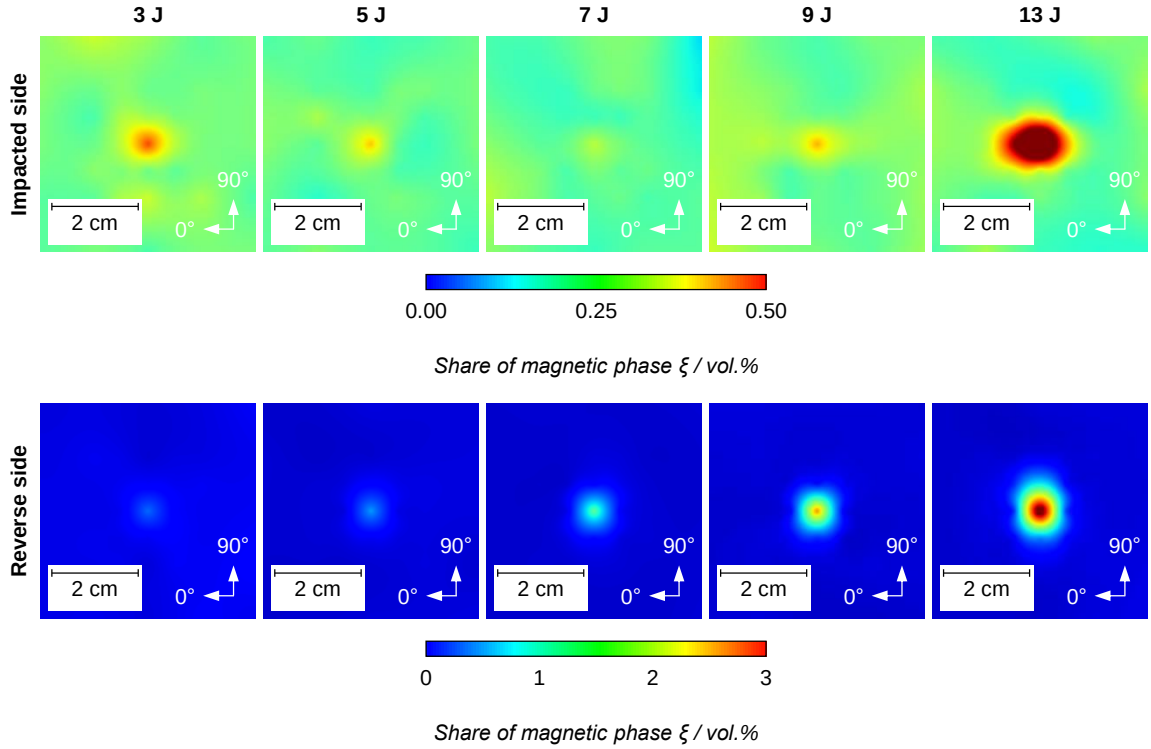

Figure 8.12 Magnetic volume fraction within the metastable austenitic steel fibre reinforced near-surface layers of SCFRP 20e 0/90 MD after impact[23] [164]

[23] Measurement of the magnetic volume fraction has been carried out by the Institute of Materials Science and Engineering (WKK) of the University of Kaiserslautern.

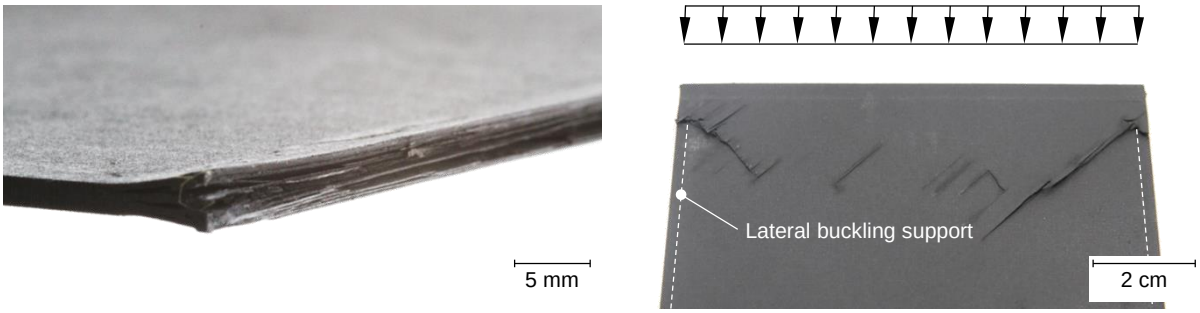

Figure 8.13 Exemplary invalid failure modes during end-loading compression: (left) specimen end brooming and (right) local buckling due stress magnification at the ends of the lateral support

After non-destructive testing, the residual compression strength σ_r of the pre-damaged coupons is determined by end-loading compression testing in line with the 0° orientation of the laminates. For this purpose, the specimens are fixed in a two-part compression kit, which prevents global buckling failure of the loaded specimens. The bottom and the sides of the specimens are restrained by a single fixture unit, while the top of the specimens are fixed by a separate clamp. The restraining plates on top and bottom are flat to prevent crushing of the specimens' ends, figure 8.13 (left). The lateral anti-buckling support is knife-edged and greased to minimise friction to the specimens. Different to the compression kit proposed in the applied standard, which exhibits unsupported areas at the corners of the specimen, the lateral

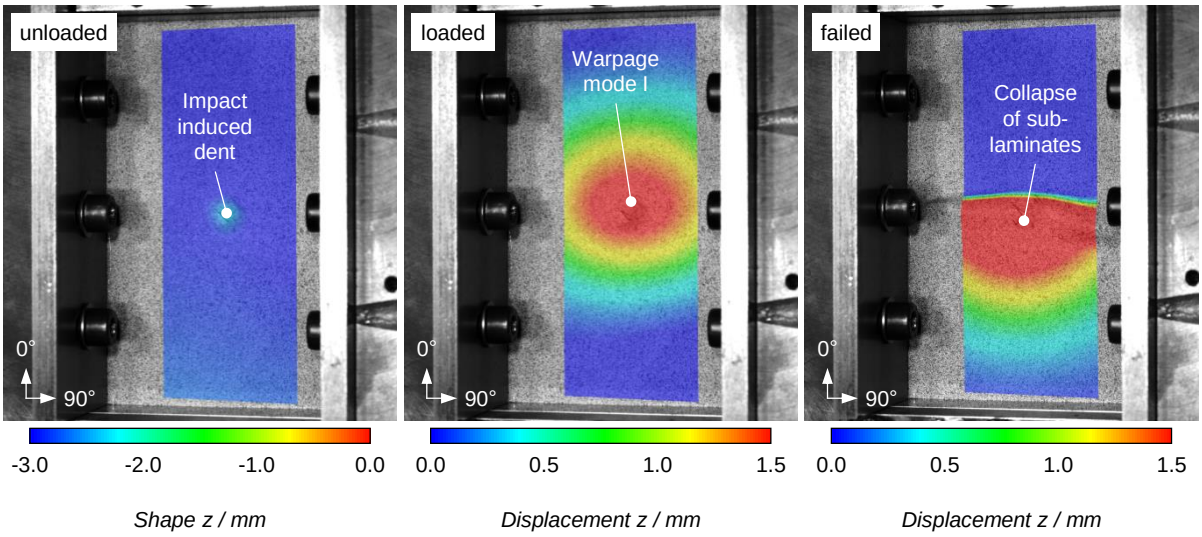

Figure 8.14 Out-of-plane deformation of pre-impacted specimen: (left) visible impact-induced dent in the centre of the unloaded specimen, (middle) valid warpage mode I of the compression-loaded specimen and (right) failed specimen

anti-buckling support is extended to the entire length of the specimens. By this means, carving of the ends of the anti-buckling support into the surface of the loaded specimens and therefore unintended local stress magnification are avoided, figure 8.13 (right). However, as a consequence, the specimens are end-loaded on their top only on a reduced width of 80 mm. Each specimen is compressed to failure with a constant displacement rate of 0.5 mm/min. In order to determine the three-dimensional deformation, i.e. the warpage mode of the specimens, the compression tests are additionally captured by a stereo camera system with a frame rate of 1 Hz and evaluated by DIC. A valid failure mode is considered to be one in which local warpage (mode I) of the impact-generated sub-laminates passes through the pre-damaged area, figure 8.14. The residual compression strength after impact is finally

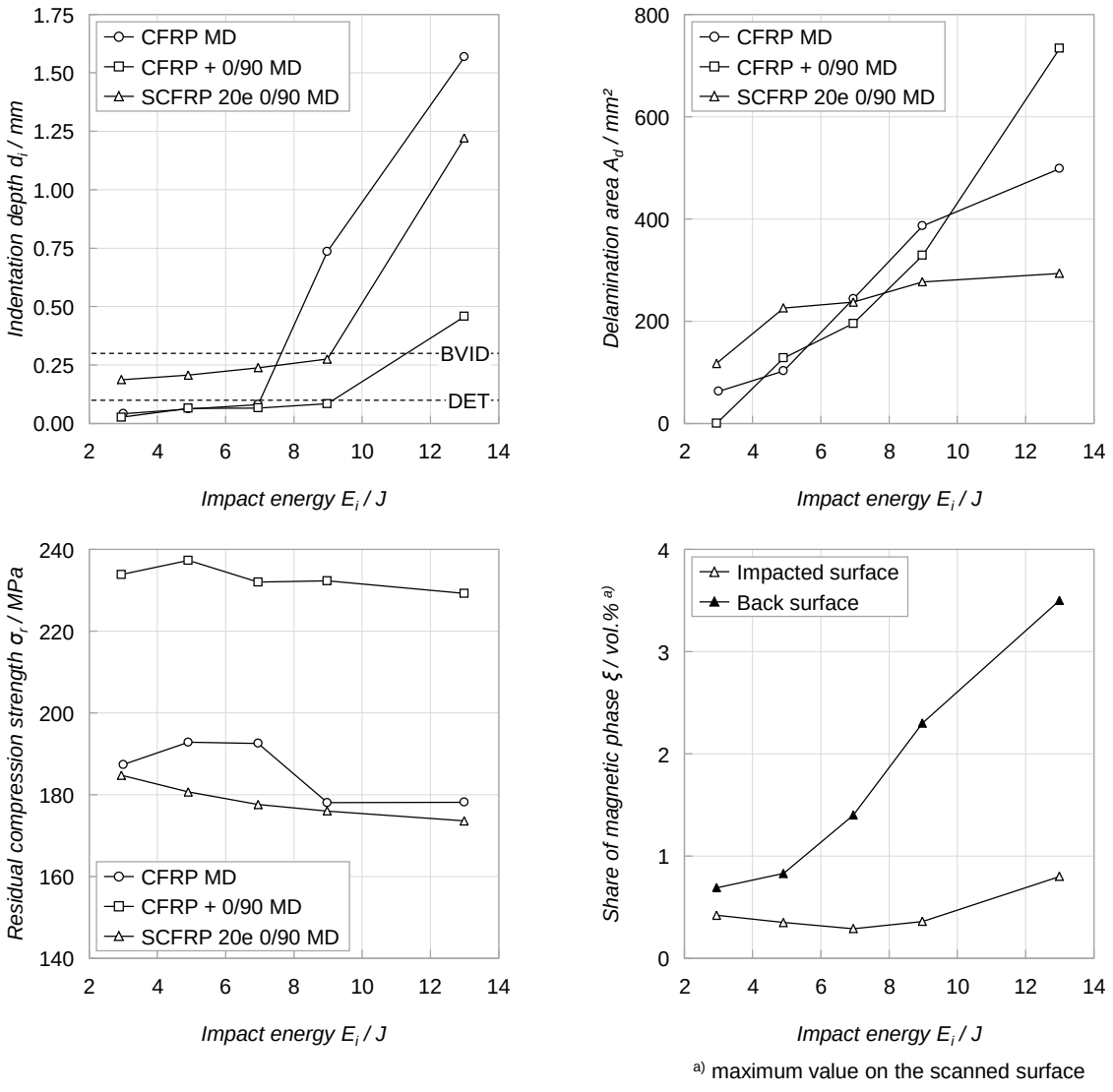

a) maximum value on the scanned surface

Figure 8.15 Results of the CAI tests on multiaxial reinforced (hybrid) laminates

calculated by dividing the maximum compression load experienced by the initial cross-sectional area of the specimen. A summary of the obtained test results is given in figure 8.15.

As shown by figure 8.10, increasing impact energy intensifies the load to the tested coupons. The damage threshold load of CFRP, which indicates onset of damage propagation, is (1589 ± 75) N. Increasing the laminate thickness of CFRP from 1.60 mm to 2.12 mm raises the DTL to (2238 ± 175) N. This is in good agreement (deviation: -6 %) with the theoretical approach deduced by Davies et al. (cf. chapter 2.4). By contrast, despite a similar laminate thickness as CFRP + 0/90 MD, the DTL of SCFRP 20e 0/90 MD of (1570 ± 135) N is even slightly lower than that of the reference CFRP. As the contact force increases, the deflection of the laminates rises and thus the impact-induced damages. This is verified both by measurement of the indentation depth and by determination of the delamination area. The larger the impact energy, the more pronounced are the damages introduced. In case of CFRP + 0/90 MD, the impact energy of 3 J is, however, insufficient to exceed the damage threshold load, which prevents any detectable damage (cf. figure 8.11 and figure 8.15 (top right)). At minor impact events, the indentation depth generally enlarges linearly but only slightly with increasing impact energy. At this region, the dents on the surface of the hybrid material are more pronounced compared to both CFRP configurations. The impressions on both CFRP laminates are below the DET (detailed inspection) criterion of 0.1 mm. However, from 13 J (in case of the reference CFRP already from 9 J), the indentation depth rises erratically; for each material, the indentation depth then exceeds the critical BVID criterion of 0.3 mm. In addition, permanent spacious warpage of SCFRP remains after the impact and has to be considered regarding the buckling stability of the hybrid laminate.

As shown in figure 8.11, the delamination area in case of CFRP is shaped elliptically while the major axis is orientated in parallel to the fibre orientation of the outermost layers. By contrast, the internal damages of the hybrid composite exhibit a rhombic pattern, again with the diagonals in parallel to the fibre orientation of the top layers of the laminate. Generally, the delamination enlarges with increasing impact energy, figure 8.15. At minor (non-critical) impact energies, the hybrid composite exhibits larger internal damages than both CFRP. At higher energy levels, however, the impact-induced delamination spreads less since most of the introduced impact energy is absorbed by yielding of the steel fibres, in particular at the area of the

indentation, instead of delamination propagation; the gain of the delamination area as a function of the impact energy is thus less pronounced for the hybrid composite in comparison with CFRP. This damage behaviour becomes also apparent by the minor oscillations of the force history trace after exceeding the DTL which are much less pronounced in case of the hybrid laminate compared to CFRP + 0/90 MD (cf. chapter 2.4). In addition, the pronounced plastic deformation of the steel fibres in the area of the impact point is proven by the increased share of (deformation-induced) ferromagnetic phase. From 7 J, the internal damages of SCFRP are smaller compared to CFRP while the difference increases with the intensity of the impact event. Moreover, impact energies of 9 J or more cause chipping of laminate bundles at the impact-averted side of the reference CFRP. The hybrid composite, by contrast, consistently sustains its outer visible integrity.

Due to the impact-induced damages, the residual compressive strength of the laminates generally degrades with increasing impact energy. The strength diminution of CFRP + 0/90 MD (-2 %) is, however, less pronounced compared to CFRP MD (-5 %) or the hybrid composite (-6 %). For CFRP, this is due to the pattern of the internal damages. The diagonal orientation of the delamination area reduces the intact cross-section of the reference CFRP in compression load direction to a greater extent compared to CFRP + 0/90 MD. In case of the hybrid laminate, the absolute lower compressive strength can be attributed to the permanent global warpage of the specimens after impact, which promotes buckling of the sub-laminates and thus compression failure of the specimen.

Moreover, the indentation causes a considerable plastic deformation of the steel fibres as a function of the impact energy both at the top and the bottom SFRP layers of the hybrid material. The associated phase transformation from paramagnetic austenite to ferromagnetic martensite leads to measurable gain of the local magnetisability. This effect rises with increasing impact energy and is more pronounced on the rear side than on the impacted side of the laminate, figure 8.12. Measurement of the share of magnetic phase by a magnetic induction sensor enables to non-destructively locate and assess the significance of the impact event. Even minor impact events are detectable, proving the sensitivity of this technique.

As proven by the test results obtained, the hybrid material principally acts more sensitive to impact events that conventional CFRP. Due to the poor steel fibre-resin-

adhesion (cf. chapter 7.4), inter-fibre-failure (delamination) is initiated at comparatively low impact energies, which becomes apparent by a minor DTL. Unlike CFRP, where impact energy is mostly absorbed by delamination propagation, the hybrid composite absorbs energy by means of yielding of the integrated stainless both locally at the point of impact but also in the form of global warpage. This causes pronounced permanent indentations on the laminate surface but also restrains the size of the impact-induced internal damages. At higher impact energies (above the critical BVID criterion), this leads to a lower impact sensitivity of the hybrid laminate compared to CFRP.

8.8 Perforation resistance

In order to assess the low velocity/high mass impact behaviour, i.e. the penetration resistance (PR) of the laminates, dynamic perforation tests are conducted according to DIN EN ISO 6603-2 [140]. The tests are carried out on a drop tower with a drop weight of 19.965 kg. For this purpose, quadratic specimens with an edge length of 60 mm are fixed by a clamping device to prevent buckling and radial slippage. The clamping device consists of a support ring and a clamping ring, both with an inner diameter of 40 mm and chamfered with a 1 mm radius. Each specimen is punctured at its centre using a hemispherical striker with a diameter of 16 mm perpendicularly to the specimen surface and at a nominally impact velocity of 4.4 m/s. This equates to an impact energy of 193 J. In order to reduce friction between indenter and

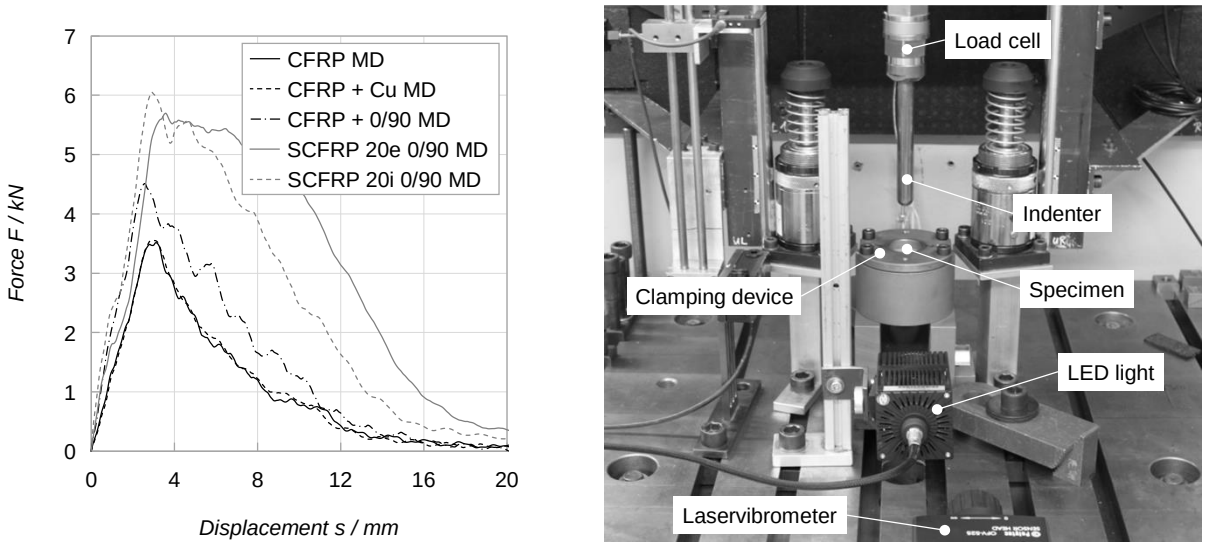

Figure 8.16 (left) Mean force-displacement curves and (right) test setup of the perforation resistance tests on multiaxial reinforced (hybrid) laminates

specimen, the tip of the indenter is lubricated with oil. The force exerted on the specimens is measured by a piezo-electric load cell with a calibrated range of ±60 kN, while the displacement of the impactor slide is captured by a single-point laser vibrometer. For each material configuration, five specimens are tested. The material response is characterised by the maximum force F_{max}, the displacement at which the force has fallen to half its maximum value s_p and the energies which are expended up to maximum force $E_{a,Fmax}$ or to complete penetration of the specimen $E_{a,20\,mm}$. Moreover, the ratio R of the energy absorbed after the maximum load to the energy absorbed prior to the maximum load is determined. Figure 8.16 and table 8.7 summarises the obtained results. Typical failure modes of the different laminate configurations are shown in figure 8.17.

Table 8.7 Results of the perforation resistance tests on multiaxial reinforced (hybrid) laminates

Laminate	F_{max} / kN	s_{Fmax} / mm	$E_{a,Fmax}$ / J	s_p / mm	$E_{a,20\,mm}$ / J	R
CFRP MD	3.56 ± 0.34	2.91 ± 0.22	5.44 ± 0.85	5.76 ± 0.57	20.93 ± 0.73	2.92 ± 0.57
CFRP + Cu MD	3.60 ± 0.06	3.02 ± 0.15	5.71 ± 0.58	6.07 ± 0.60	20.99 ± 0.55	2.71 ± 0.37
CFRP + 0/90 MD	4.52 ± 0.09	2.58 ± 0.05	6.33 ± 0.19	6.95 ± 0.35	29.50 ± 0.28	3.66 ± 0.16
SCFRP 20e 0/90 MD	5.74 ± 0.05	3.91 ± 0.53	12.51 ± 2.90	12.55 ± 0.18	61.51 ± 0.58	4.11 ± 1.06
SCFRP 20i 0/90 MD	6.09 ± 0.17	3.02 ± 0.16	9.88 ± 0.95	9.08 ± 0.46	49.97 ± 2.16	4.09 ± 0.46

The reference CFRP exhibits brittle failure behaviour. The failure mode is dominated by inter-fibre-failure, fibre fracture, fragmentation and delamination. After exceeding a peak load of (3.56 ±0.34) kN, cracks propagate mostly at an angle of ±45°, i.e. in direction of the majority of the reinforcing carbon fibres, which is accompanied by continuous diminution of the load-bearing capacity. An additional copper mesh on the impacted side of the reference CFRP has no beneficial influence on the penetration performance. Both failure pattern and penetration resistance (maximum force and energy absorption capacity) remain unaffected. Increasing the thickness of the laminate from 1.60 mm to 2.12 mm (CFRP + 0/90 MD) causes an increase of the bending stiffness and therefore of the maximum force (+27 %) and of the total energy absorption capacity (+41 %). The failure mode is, however, basically similar to that of the reference CFRP. By contrast, both hybrid composites exhibit ductile characteristics in their failure pattern. On the impacted side of SCFRP 20e 0/90 MD, yielding of the steel fibres occurs in particular at the edge of the perforation hole in

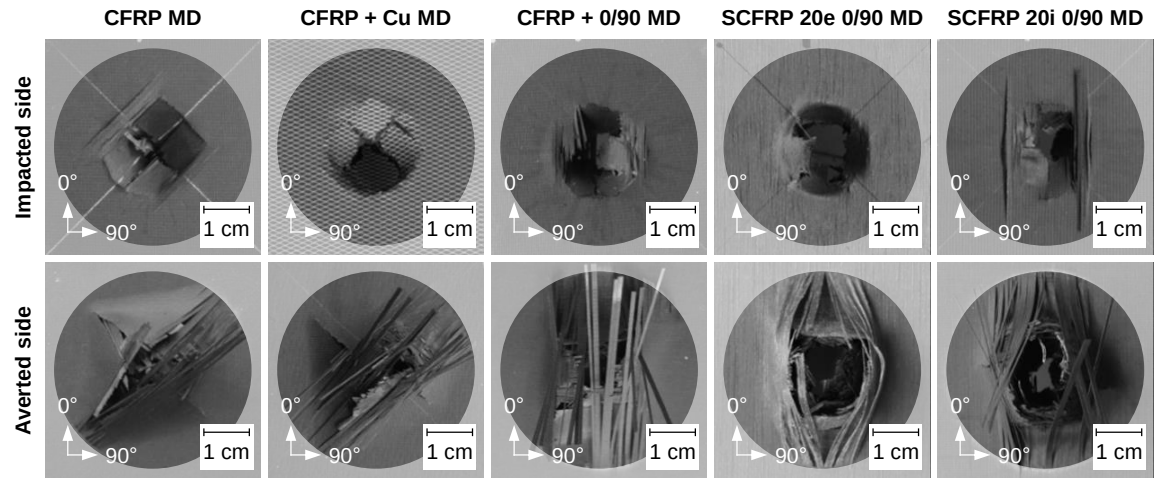

Figure 8.17 Representative failure modes after perforation tests on multiaxial reinforced (hybrid) laminates

form of plastic hinges. On the rear side, bundles of steel fibres detach from the CFRP core and are able to yield along their entire length. More extensive deformations are only hindered by the circular fixture of the coupon. Since the elongation at break of the steel fibres is significantly higher than that of the applied carbon fibres, the bending stiffness of the composite degrades significantly slower compared to pure CFRP. As a consequence, the hybrid composite can bear larger deformation at higher levels of load. The maximum force increases by 61 %. The total energy absorption capacity rises by 194 % compared to the reference CFRP and still by 108 % compared to CFRP + 0/90 MD. In case of the hybrid composite with the steel fibres at the core layers of the laminate (SCFRP 20i 0/90 MD), the high elongation at break of the stainless steel fibres sustains the moment of inertia, i.e. the bending stiffness of the hybrid laminate up to larger deflection compared to unmodified CFRP. This causes an increase of the maximum force by 71 %. However, since the steel fibres are aligned close to the neutral axis of the laminate, the beneficial effect of the intact steel fibres on the bending stiffness of the laminate is less pronounced compared to SCFRP 20e 0/90 MD; the bending stiffness degrades faster in the post-damage stage after failure of the carbon fibres. Still, the energy absorption is 139 % higher compared to the reference CFRP and 69 % higher compared to CFRP + 0/90 MD.

9 Discussion

Within this chapter, the results of the previous investigations on steel fibre bundles, uni- and multiaxial reinforced laminates are discussed with regard to the damage tolerance, crashworthiness, bolted joint suitability, impact performance and electrical conductivity of the hybrid material. Based on this discussion, load case dependent design principles for a beneficial spatial arrangement of the metal fibres are derived.

9.1 Result interpretation

9.1.1 Post-damage behaviour

Both the stainless steel and the copper cladded low carbon steel fibres exhibit distinct strain rate sensitivity. In case of the stainless steel fibres, increasing load rate causes a small diminution of their elongation at break. This sensitivity is of interest since a spatial confinement of the steel fibre elongation (cf. concept of the fracture zone of influence) inevitably causes an increase in local strain rate. As a consequence, even quasi-static loading of the hybrid laminate can result in highly dynamic elongation of the embedded steel fibres. Moreover, the fracture gap generation itself, which is accompanied by deformation of the steel fibres, is a highly transient process. Reduction of the elongation at break of the steel fibres, however, negatively affects the post-failure performance of the hybrid material; the critical length of the fracture zone of influence is increased, while the ultimate strain at failure of the hybrid composite is reduced. Consequently, diminution of the strain at failure of the steel fibres with increasing strain rate detrimentally affects the post-damage performance of the hybrid composite and should be less pronounced.

In theory, even uniaxial reinforced hybrid composites with minor stainless steel fibre share are able to demonstrate pronounced post-failure behaviour under plain tensile load. For this purpose, the integrated steel fibres have to offer sufficiently high elongation at break and/or poor fibre-resin-adhesion. In principle, the introduced failure model provides an indication of the necessary extent of the fracture zone of influence, i.e. of a proper grade of steel fibre-resin-adhesion. According to the analytical approach, a minimum length of the fracture zone of influence of 4.89 % is estimated for SCFRP 20h UD (cf. appendix A.4). For a clamping length of 150 mm,

this corresponds to an absolute value of 7.33 mm. This theoretical value is basically feasible (e.g. by an appropriate treatment of the filament's surface) but with regard to other composite properties, such as the transverse tensile strength, impact resistance or fatigue performance, inappropriate for actual applications.

However, the bending-tensile tests on UD hybrid laminates prove that the aspired post-damage behaviour is feasible even with distinct steel fibre-resin-adhesion and/or minor steel fibre share. Due to the heterogeneous load state (both over the length and the height of the coupon), significantly less elastic energy is generated in the material up to fracture initiation. As a consequence, the load of the steel fibres bridging the fracture gap during failure of the carbon fibres is reduced. Moreover, the restoring force during fracture gap generation which acts on the steel fibres within the FZI is lower. In addition, by placing the steel fibres at beneficial (tensile loaded) areas of the laminate, their ductility can specifically be addressed. Proper spatial arrangement of the applied stainless steel fibres as well as a reduced number of equally loaded carbon and steel fibres thus enables to achieve the aspired enhancement of the damage tolerance of a UD hybrid composite without modification of the steel fibre surface or inappropriate increase in steel fibre share.

This knowledge can be transferred to multiaxial laminates. Accumulation of steel fibres in distinct plies (separated layer concept) enables to vary the orientation of the (exclusively) carbon fibre reinforced plies relatively to the SFRP layers. Different to UD hybrid composites, this lowers the proportion of equally aligned (loaded) carbon and steel fibres and thus reduces the effective stiffness of CFRP relatively to the integrated steel fibres[24]. Due to the reduced effective stiffness of the CFRP portion, less elastic energy is generated during plain tensile load. As a consequence, less elastic energy has to be dissipated by means of inter-fibre-failure, fibre fracture, laminate fragmentation and/or yielding of the steel fibres during failure initiation. In addition, the lower stiffness of the fracture halves reduces the restoring force which acts on the steel fibres within the fracture zone of influence during fracture gap generation. Moreover, different to pure CFRP, the steel fibres absorb a considerable

[24] For comparison: According to the rule of mixtures, classical laminate theory and the properties of the fibres and the resin listed in table A.1, uniaxial reinforced CFRP (φ_{CF} = 60 vol.%) exhibits an effective stiffness E_1 of 145 GPa. By contrast, the effective stiffness of multiaxial CFRP (stacking sequence according to chapter 8) is 46 GPa. The stiffness E_1 of a stainless steel fibre reinforced UD layer (φ_{SF} = 60 vol.%) is 107 GPa. For a hybrid composite (φ_{CF} = 50 vol.%, φ_{SF} = 10 vol.%) following the separated layer approach, this yields a stiffness ratio E_{CFRP} to E_{SFRP} of 6.78 in case of a uniaxial and of only 2.15 in case of a multiaxial reinforced hybrid laminate.

amount of released elastic energy, which is otherwise transferred to the ±45° CFRP plies. As a consequence, the ±45° CFRP layers of the hybrid laminate are not entirely destructed during failure of the 0° CFRP layers. In addition, inter-fibre-failure of the angularly aligned plies is bypassed by the intact adjacent SFRP layers. By this means, ±45° CFRP layers can be included for load carrying purposes in the after-damage stage of the hybrid laminate. The post-failure performance is therefore characterised by both progressive yielding of the ductile steel fibres and shear deformation of angularly aligned CFRP plies. By this means, multiaxial hybrid laminates are able to demonstrate pronounced post-failure behaviour despite minor steel fibre percentage and/or proper steel fibre-resin-adhesion. Compared to conventional CFRP, the enhanced ultimate strain at failure increases the energy absorption capacity of the hybrid material and ensures its structural integrity after failure initiation in case of plain tensile load.

9.1.2 Bolted joints

As shown by the filled hole tensile tests and in compliance with the plain tensile tests, the specific stiffness and bypass strength of CFRP is lowered by the incorporation of steel fibres. This effect rises with increasing steel fibre share and deviation of the steel fibre orientation from the load direction. Regarding the design of the borehole pattern, this diminution increases the minimum hole spacing of adjacent bolted joints. However, different to the brittle failure mode of CFRP, bypass failure of the hybrid material can be considered as “forgiving”; after exceedance of the bypass strength (failure of CFRP plies with fibre orientation in parallel or transverse to the load direction), load is relocated to the reinforcing steel fibres aligned in load direction. By means of plastic elongation, the steel fibres preserve the structural integrity of the laminate and sustain a considerable load carrying capacity, albeit on a reduced level of load. This post-damage behaviour is particularly pronounced if the additional SFRP layers are arranged in ±45° to the load direction.

Moreover, the integration of stainless steel fibres has no considerable effect on the bearing strength as long as the fibres are orientated in pin load direction. Basically, the high elongation at break of the steel fibres provides no advantage over carbon fibres since the initial bearing failure is essentially characterised by (compressive) buckling failure of the fibres aligned in load direction. The buckling stability of the fibres again relies on their cross-section, their modulus of elasticity and their support

by the surrounding matrix. In case of the steel fibres, the advantage of their large filament diameter is compromised by their lower stiffness in comparison with carbon fibres. Also, the steel fibre-resin-adhesion should be maximised to reduce the unrestrained column length and thus to increase the buckling stability of the steel fibres. As in case of carbon fibres, steel fibres which are aligned vertically or angularly to the bolt load direction do not contribute to the bearing strength of the composite but impede intralaminar inter-fibre-failure in parallel to the load direction. In this regard, carbon fibres are, however, to be preferred due to their higher stiffness and significantly higher ultimate tensile strength.

Considerable enhancement due to the integration of steel fibres arises in terms of the post-damage stage after exceedance of the bearing strength. Different to the bearing strength, the post-damage performance is positively affected by steel fibres which are arranged perpendicularly to the bolt load direction. Steel fibres integrated in this way are primarily subjected to tensile load during progressive pin displacement. In contrast to the brittle, anisotropic carbon fibres, the steel fibres can be plastically elongated by the bolt displacement prior to fibre failure. This effect is emphasised if the steel fibres are able to detach extensively from the laminate as in case of steel fibre reinforced top layers. By this means, spacious areas of the laminate can be addressed for energy absorption purposes. If the transversely aligned steel fibres are covered by differently orientated plies, the plastic deformation is confined to the area nearby the fastener. This, by trend, lowers the mean bearing stress and finally the energy absorption capacity of the hybrid material during progressive bearing failure. Steel fibres which are aligned in parallel to the load direction (independently of the location within the laminate) do not significantly contribute to the post-damage performance. Due to the fragment wedge accumulating in front of the pin, both the longitudinally arranged carbon and steel fibres are bent or laterally displaced. By this means, the high specific energy absorption capacity of the steel fibres cannot be entirely exploited. By contrast: energy absorption is mainly limited to inter- or intralaminar cracking.

In addition, minor enhancements are feasible in terms of the head pull-through resistance. Although the bending stiffness as well as the first failure load of the hybrid laminate are reduced due to the minor stiffness and offset yield strength of the integrated steel fibres, the pull-through strength is comparable to pure CFRP with identical stacking sequence (or laminate thickness). However, after exceeding the

maximum load, the carbon fibres underneath the fastener head subjected to bending load fail in a brittle manner. The remaining load-bearing capacity of the laminate mainly results from friction between the fastener head and CFRP fragments or the breaking edge. The soft-annealed steel fibres, by contrast, continuously yield. By this means, the steel fibre reinforced layers maintain a considerable moment of inertia. In case of the hybrid composite, the load-bearing capacity therefore results from sustained structural bending stiffness as well as friction between the fastener head and laminate fragments. During the further course of the fastener pull-through, this increases the resistance of the hybrid material against progressive penetration of the fastener head; compared to CFRP, the energy required for complete pull-through of the fastener is therefore higher. In this regard, steel fibre reinforced top layers exhibit the best bolt pull-through performance for the investigated case of protruding heads. The performance of the hybrid composite with SFRP layers at the centre of the laminate is, however, only slightly worse. This might be relevant for the application of countersunk heads.

9.1.3 Impact tolerance

As demonstrated by the transverse tensile tests on UD hybrid layers, the high transverse stiffness of the integrated steel fibres facilitates the formation of intralaminar inter-fibre-failure. These defects act as initial point for further damage in the form of (interlaminar) delamination, e.g. in case of impact events, which results in greater susceptibility of the hybrid composite to delamination. Compared to CFRP, even minor impact energies can cause detectable internal damages. This sensitivity is also reflected by a diminution of the damage threshold load. In addition, plastic deformation of the steel fibres at the point of impact causes permanent indentations, which are more pronounced compared to the dents on the surface of conventional CFRP. However, the damages remain below the critical BVID criterion. In case of CFRP, increasing intensity of the impact event causes a dramatic rise of the damage extent. In addition to a significant increase in delamination area, fibre fractures and fibre chipping occur on the impact-averted side of the laminate. By contrast, in case of the hybrid laminate, steel fibres arranged on top of the laminate absorb a significant amount of impact energy by means of plastic deformation. As a result, less impact energy has to be dissipated in the form of crack propagation; delamination is thus less pronounced. The impairment of the laminate (formation of sub-laminates) is

circularly confined to the area around the impact location. In comparison with CFRP, the improved integrity of the laminate reduces the weakening of the structure. SFRP top layers thus provide the chance of improving the damage tolerance in case of critical impact events. However, the plastic deformation of the steel fibres can also cause a permanent global warpage of the hybrid structure, which reduces its buckling stability, i.e. its compressive strength after impact.

The findings of the impact tests basically correlate with the improved perforation resistance of the hybrid material. In principle, the penetration resistance test equates to dynamic bending-tensile load. In case of CFRP, fibre chipping and the great extent of internal laminate damages (e.g. delamination, inter-fibre-failure, fibre fracture) lower the bending stiffness and consequently the load carrying capacity of the laminate. During advanced penetration of CFRP, the brittle fragmentation of the laminate causes a rapid decrease in penetration resistance. By contrast, due to their high elongation at break, the steel fibre reinforced top layers of the hybrid laminate enable larger deflection without failure of the reinforcing fibres. Moreover, as shown by the impact tests, delamination within SCFRP spreads less in the initial stage of the perforation (initial contact, global laminate deflection). This maintains the bending stiffness of the laminate, which again enables significantly higher maximum loads. Subsequent detachment of the steel fibre bundles from the CFRP core during penetration of the hybrid laminate allows further plastic deformation of the steel fibres without fracture. Different to CFRP, this causes a slower degradation of the bending stiffness, which finally increases the total energy absorption capacity of the hybrid material in case of perforation load. Similar improvements are feasible by arranging SFRP layers at the centre of the laminate. Due to the position at or close to the neutral axis of the laminate, the steel fibre layers are included for load transfer primarily after failure of the outer CFRP layers. Prior to that, the initial bending performance is similar to pure CFRP; the minor stiffness of the steel fibres in comparison with the carbon fibres can be neglected due to the proximity to the neutral axis of the laminate (cf. Huygens-Steiner theorem). After failure of the outer CFRP layers, load is redistributed to the inner SFRP plies which remain as load-carrying cross-section. However, the arrangement at or close to the neutral axis of the laminate causes a lower moment of inertia in the after-damage stage, which finally leads to a smaller load-bearing capacity, hence minor overall energy absorption capacity in case of penetration load.

9.1.4 Electrical conductivity

From a mechanical point of view, the copper cladded low carbon steel fibres are not of interest for the considered hybrid material concept due to their embrittlement during laminate manufacturing. However, the electrical investigations on these fibre bundles demonstrate the potential of highly conductive metal coatings in terms of specific electrical conductivity enhancement. In principle, such metal coating is also applicable to austenitic steel fibres[25]. This provides the chance of combining the beneficial mechanical performance and corrosion resistance of the stainless steel fibres with the high electrical conductivity of the coating material. The coating is, however, also accompanied by a (detrimental) change in the mean filament density (Zn: 7.14 g/cm^3, Ni: 8.91 g/cm^3, Cu: 8.92 g/cm^3) and material cost.

All structural investigations carried out consistently demonstrate the isolated function of the LSP copper mesh on top of the laminate. The mesh only provides lightning strike protection without contributing to the mechanical performance of the composite (function separation). This state-of-the-art solution thus clearly differs from the hybrid material concept investigated in this work, which aims for a combination of electrical and mechanical tasks (function integration).

9.2 Effects of the steel fibre integration

Table 9.1 and table 9.2 summarise the effects of the steel fibre integration on the properties of CFRP. The tables indicate whether the steel fibre incorporation causes an increase (↑), decrease (↓) or negligible change (→) of the respective property. Changes by trend are tagged by diagonal arrows (↗, ↘). The assessment is carried out each for the best performing hybrid material configuration and in comparison to unmodified CFRP with similar stacking sequence. In addition, the tables advise the

Table 9.1 Effects of the steel fibre integration on the properties of uniaxial reinforced hybrid layers

Direction	E	σ_{max}	ε_{max}	$e_{a,max}$	ρ^*	Reference	Recommendation
1-direction	↓	↓	→/↑↑ [a)]	↘/↑↑ [a)]	↑↑	CFRP UD	mid
2-/3-direction	↑	↓↓	↓↓	↓↓	(↑) [b)]	CFRP UD	homogeneous

[a)] depending on the steel fibre-resin-adhesion and/or steel fibre share

[b)] expected but experimentally not demonstrated

[25] According to the supplier, metal coatings of the stainless steel fibre are basically feasible but have not been realised yet.

Table 9.2 Effects of the steel fibre integration on the properties of multiaxial reinforced hybrid laminates

Load case	E	σ_{max}	$\varepsilon_{\sigma max}$	ε_{max}	$e_{a,max}$	Reference	Recommendation
PT	↓	↓	↗	↑↑	↑↑	CFRP + 0 MD	mid, load direction
FHT	↓	↓	↗	↑↑	↑↑	CFRP + 0/90 MD	mid, load direction

Load case	E	σ_{max}	σ_{mean}	$E_{a,max}$	Reference	Recommendation
PLB	↘	↘	-	-	CFRP + 0/90 MD	mid, load direction
PLB (cont.)	↘	↓	↑↑	↑↑	CFRP + 0/90 MD	top, transverse direction

Load case	EI	F_{int}	F_{max}	s_{Fmax}	s_{max}	$E_{a,max}$	Reference	Recommendation
BPT	↓	↓	→	↗	↗	↑	CFRP + 0/90 MD	top, multiaxial
PR	↘	-	↑↑	↗	↗	↑↑	CFRP + 0/90 MD	top, multiaxial

Load case	DTL	d_i	A_d	σ_r	E_a	Reference	Recommendation
CAI	↓	↑	↑/↓↓ [a)]	→	↑	CFRP + 0/90 MD	top, multiaxial

[a)] depends on the impact energy

preferable spatial arrangement of the steel fibres within the composite.

By trend, incorporation of steel fibres diminishes the composite's specific stiffness and strength but increases its ultimate strain at failure and energy absorption capacity. Major improvements arise in terms of electrical conductivity, impact and penetration resistance. Enhancements regarding the plain tensile behaviour or bolted joint suitability mainly concern the post-damage stage.

9.3 Design recommendation

Table 9.1 and table 9.2 indicate that the ideal fibre arrangement depends on the considered load case. Based on the investigations carried out, the following design principles for steel/carbon fibre hybrid composites can be concluded:

(1) In order to increase the electrical in-plane conductivity of the hybrid composite, the steel fibres should be arranged in direction of the electrical load. The spatial distribution of the steel fibres is of subordinate importance, albeit minor conductivity enhancements based on a percolation process are feasible by accumulating the steel fibres in adjacent plies. The specific electrical resistance of the applied steel fibres should be as low as possible. Especially in case of high frequency signal transfer, highly conductive coatings (e.g. copper, nickel, zinc)

are of interest due to the skin effect.

(2) In order to enable a considerable post-damage performance in case of plain tensile load, the steel fibres should be orientated in load direction. Accumulating the steel fibres in distinct plies enables to reduce the proportion of similarly aligned carbon and steel fibres by means of multiaxial stacking sequences. The steel fibre reinforced layers should then be arranged at the laminate centre to minimise deterioration by the burst (energy release) of adjacent CFRP plies during failure of the carbon fibres. Moreover, the steel fibre-resin-adhesion should be reduced in order to allow plastic deformation at spacious areas of the laminate and thus to increase the laminate's ultimate strain at failure and energy absorption capacity. In principle, the strain at failure of the steel fibres as well as the steel fibre share should be maximised to emphasise the post-damage performance of the hybrid material. Conversely, the share of steel fibres should be only as high as necessary in order to minimise the specific stiffness- and strength-reducing effect of the steel fibre integration.

(3) In plies subjected to transverse (tensile) load, the share of steel fibres should be minimised in order to ease the strength-reducing effect of strain magnification. In this context, present steel fibres should be distributed as homogeneously as possible while the transverse stiffness of the integrated steel fibres should be minimal. Moreover, the steel fibre-resin-adhesion should be maximised in order to impede adhesive inter-fibre-failure.

(4) In case of bending load and with regard to the damage tolerance of the hybrid material, the steel fibres should primarily be arranged at the outermost layers of the laminate. This increases the flexural stiffness of the laminate after failure of the carbon fibres and finally the maximum energy absorption capacity. However, if the bending stiffness at minor deflection is of superordinate meaning, the steel fibres should be located at the neutral axis of the laminate. The detrimental effect of this steel fibre arrangement (compared to the outer arrangement) on the post-damage performance of the hybrid material is of minor significance.

(5) In case of bolted joints, the steel fibre arrangement basically follows the guidelines for conventional CFRP. In consideration of the bearing and bypass strength, the steel fibres should be aligned in load direction. The tensile and compressive stiffness of the steel fibres should be as high as possible to reduce any detrimental influence of the hybridisation on the bolted joint performance. In

order to emphasise the post-damage behaviour in case of bypass failure, the steel fibres should be aligned at ±45° to the load direction. If the fastener joint is designated for energy absorption purposes under progressive bearing load, the steel fibres should primarily be arranged transverse to the pin load direction and at the outermost layers of the laminate. In this case, the steel fibre-resin-adhesion should be minimised to allow plastic deformation of the steel fibres at extensive areas of the laminate.

(6) Fastener pull-through is related to bending load; the steel fibres should therefore be located at the outermost layers of the laminate in order to maximise the energy required for complete fastener pull-through. If the initial bending stiffness is of superordinate meaning, the steel fibres should primarily be applied to the centre of the laminate. In any case, uniform load distribution to the laminate and best possible support of the fastener head is achieved by multiaxial (quasi-isotropic) steel fibre alignment.

(7) Aiming for a good drill-hole (edge) quality, the steel fibres should be distributed homogeneously in the laminate. If possible, pure steel fibre reinforced layers should be covered on both sides by CFRP plies. In any case, adjacent layers should be orientated in deviant direction in order to maximise their mutual support. This reduces the risk of shear deformation of the steel fibres and/or intralaminar (fibre parallel) crack propagation.

(8) Impact or penetration events are related to bending-tensile load; in order to increase the energy absorption capacity of the laminate, the steel fibres should be located at the outermost layers of the laminate. Arranging the steel fibres in multiple in-plane directions ensures homogeneous load distribution to the material. In case of minor impact events, the steel fibre-resin-adhesion should be maximised to impede interlaminar crack formation (delamination). By contrast, in order to facilitate extensive plastic deformation of the steel fibres and thus to maximise the energy absorption capacity of the laminate in case of high impact energies (penetration), the steel fibre-resin-adhesion should be reduced.

(9) From a processing point of view, spatial concentration of the steel fibres in individual plies of the laminate is preferable. The hybridisation can then efficiently be achieved by combining exclusively carbon or steel fibre reinforced non-crimp fabrics, while complex manufacturing of hybrid rovings or hybrid fabrics is avoided. The position in thickness direction of the laminate is insignificant.

9.4 Exemplary application

In order to exemplify the potential of the considered multifunctional material concept, basic mechanical and electrical properties of a generic stiffening element are analytically estimated. As reference, an omega-stringer made of multiaxial CFRP with a laminate thickness of 1.125 mm is considered. The stacking sequence and the geometry of the stiffener are shown in figure 9.1.

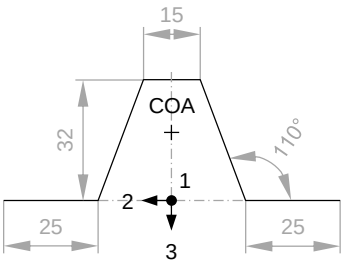

CFRP laminate (reference)

$(45^C/90^C/0^C/-45^C/\bar{0}^C)_s$

SCFRP laminate (at the modified sections)

$(45^C/90^C/0^C/-45^C/0^S_{nSFRP}/\bar{0}^C)_s$

with n_{SFRP} = 1, 2, 4, 9 or 18

Figure 9.1 Geometry (centre line of the structure) and laminate stacking sequences of the considered omega-stringer [6]

The baseline stringer is partially reinforced at its webs and/or flanges by additional unidirectional SFRP layers orientated in 1-direction (configuration 1 to 3, cf. table 9.4). For each configuration, an overall steel fibre share of approximately 10 or 20 vol.% is considered, adjusted by the number of additional SFRP plies. Both CFRP and SFRP layers have a CPT of 125 µm and comprise 60 vol.%. of reinforcing fibres. The properties of the constituent materials basically correspond to those of the carbon fibres, stainless steel fibres and epoxy resin discussed in chapter 4. Poisson ratios v of the constituent materials as well as shear modulus G of the carbon fibres are appraised by generally accepted values. Using these properties and applying the rule of mixtures and classical laminate theory, the homogenised mechanical properties of the laminates and finally of the stringer (longitudinal stiffness in 1-direction E_1, bending stiffness in 3-direction with respect to the centre of area (COA)

Table 9.3 Assigned properties of the constituent materials

Constituent	E_1 / GPa	E_2 / GPa	G_{12} / GPa	v_{12}	ρ_1^* / Ωm	Reference
Carbon fibre	240	24	50	0.23	1.60×10^{-5}	[7, 13]
Steel fibre	176	176	67.69	0.30	1.48×10^{-7} a)	[141]
Epoxy resin	3.52	3.52	-	0.35	1.00×10^{13}	[7, 13]

a) assuming a copper coating with a mean thickness of 3 µm and a specific electrical resistance of 1.70×10^{-7} Ωm [17]

EI_2) are determined. For the calculation of the electrical conductivity of the stringer along its longitudinal axis G_1, only reinforcing fibres aligned in 1-direction are considered. The remaining fibres are assumed to laterally leave the stringer, hence do not contribute to its electrical conductivity. Moreover, the stainless steel fibres are assumed to be copper cladded (mean coating thickness of 3 µm) in order to emphasise the full potential of the considered hybrid material concept. A summary of the assigned properties is given in table 9.3.

Table 9.4 Comparison of the mechanical and electrical properties of an omega-stringer made of CFRP or different SCFRP configurations

	 Reference	 1.1	 1.2	 2.1	 2.2	 3.1	 3.2
Property	CFRP	SCFRP 10	SCFRP 20	SCFRP 10	SCFRP 20	SCFRP 10	SCFRP 20
n_{SFRP} [a)]	-	2	4	4	8	18	36
φ_{CF} / vol.%	60.0	49.1	41.5	49.3	41.8	49.0	41.4
φ_{SF} / vol.%	-	10.9	18.5	10.7	18.2	11.0	18.6
φ_R / vol.%	40.0	40.0	40.0	40.0	40.0	40.0	40.0
E_1 / GPa	67.34	74.55 (+11 %)	79.55 (+18 %)	74.42 (+11 %)	79.35 (+18 %)	74.64 (+11 %)	79.67 (+18 %)
EI_2 / 10^9 Nmm^2	1.52	2.06 (+35 %)	2.60 (+71 %)	2.21 (+45 %)	2.88 (+89 %)	2.65 (+74 %)	3.34 (+120 %)
G_1 / S/m	1.87	136.78 (73×)	271.68 (145×)	133.63 (71×)	265.39 (142×)	138.70 (74×)	275.52 (147×)

[a)] number of additional SFRP layers at the modified sections (feet, webs and/or flange) of the stringer

The calculated stringer characteristics are listed in table 9.4. The integration of SFRP layers results in an increase in longitudinal and bending stiffness of the stringer. Regarding the flexural stiffness, concentration of steel fibres at the upper and/or lower flanges of the stringer is of particular interest (duplication of the bending stiffness compared to the CFRP reference). In principle, ductile steel fibres at the tensile loaded areas of the stringer (either at the upper cap or lower feet, depending on the bending direction) are expected to increase the energy absorption capacity in case of supercritical bending load (crash). Moreover, the additional SFRP layers could improve the bearing performance of the stringer, which again could be utilised for energy absorption purposes (cf. progressive bearing failure). Simultaneously, the electrical conductivity of the stringer is increased by a factor of up to 147 relatively to the CFRP reference. The configurations 2.1 and 2.2 additionally facilitate three individual conductive pathways, e.g. for realisation of separated electrical functions.

10 Conclusion

Within the present work, a novel hybrid composite consisting of continuous steel and carbon fibres embedded in an epoxy resin is introduced and analysed. The incorporation of ductile steel fibres into CFRP aims to improve both the electrical and mechanical performance of the composite. For this purpose, analytical and experimental investigations are gradually performed on steel fibre bundles as well as on unidirectional and multiaxial laminates in order to understand the micromechanical interaction between the constituents and the macroscopic functionality of such hybrid material in dependence on the load case.

For the introduced material concept, austenitic steel fibres are of particular interest. In soft-annealed condition, the stainless steel fibres offer an excellent trade-off between beneficial tensile properties (high elongation at break, high ultimate tensile strength) and sufficient electrical conductivity. Latter can be further enhanced by means of copper, nickel or zinc cladding. Moreover, the alloy composition (high amount of chromium and nickel) prevents the steel fibres from galvanic corrosion when in contact with carbon fibres or exposed to corrosive media. In principle, the selected steel fibre bundles can be processed without any need for spreading the individual filaments. However, for efficiency reasons, established technologies such as weaving or prepreg manufacturing should be used to prepare dry or pre-impregnated (non-crimp) fabrics. The prefabricated textiles can then be integrated into conventional lay-up processes without limitations in terms of part geometry or laminate stacking design.

Measurements of the electrical in-plane conductivity on UD hybrid laminates verify a correlation of the volume conductivity of the composite with the volume share and the specific electrical resistance of the incorporated steel fibres. Compared to pure CFRP, the electrical conductivity in parallel to the fibre orientation can be increased by one to two orders of magnitude even for minor percentages (10 to 20 vol.%) of (cladded) steel fibres. Adapting the share and the orientation of the steel fibres allows adjusting the composite’s conductivity to fit specific application requirements. Smart metal fibre arrangements generating a three-dimensional conductor network could additionally enable improvement of the out-of-plane conductivity. The analysis carried out, however, also discloses the challenge of establishing a sufficient and consistent connection to the hybrid composite in order to exploit its full electrical conductivity.

This is of particular meaning for future applications. Further investigations must therefore comprise proper connection design principles (e.g. self-tapping screws, interference fit bolts, welding spots, excavated metal fibres [142]). Moreover, capacitive effects caused by alternating current in case of the separated layer approach as well as the influence of mechanical damage or repair on the electrical performance of the hybrid laminate need to be analysed.

Simultaneously, the hybridisation of CFRP by means of annealed steel fibres enables significant enhancement of the composite's damage tolerance. The high elongation at break of the steel fibres ensures the structural integrity of the composite and provides a considerable load-bearing capacity after failure of the brittle carbon fibres. However, in order to achieve such quasi-ductile behaviour, both the steel fibre-resin-adhesion and the laminate stacking sequence are crucial. The outcome of the mechanical analysis generally suggests that a spatial concentration of the steel fibres at distinct plies is advantageous over a homogeneous distribution in the entire composite. In case of tensile load, the steel fibres should be arranged at the centre, while for bending load the steel fibres should primarily be applied to the outermost layers of the laminate. The overall material response is then not only a simple superimposition but a complex interaction of the mechanical behaviour of the composite's constituents; even pre-damaged, angularly (e.g. ±45°) aligned carbon fibre reinforced plies can be included in the post-damage stage for load transmission. Minor steel fibre-resin-adhesion additionally facilitates to exploit the ductility of the steel fibres at spacious areas of the laminate after failure initiation. This increases the ultimate elongation at break of the hybrid material to over 11 % and finally its energy absorption capacity by a factor of 6. However, the integration of steel fibres simultaneously diminishes the specific stiffness and strength of the composite. Moreover, weakening of the steel fibre-resin-interface intensifies the affinity of the hybrid composite to adhesive inter-fibre-failure and consequently also the laminate's susceptibility to delamination. This sensitivity is jointly responsible for the low damage threshold load in case of impact events; internal damages occur even for minor impact energies. However, compared to CFRP, impact-induced delamination spreads less since a considerable amount of impact energy is dissipated by yielding of the steel fibres instead of interlaminar crack propagation. This significantly reduces the extent of damage caused by critical impact events by up to 60 %. In combination with the penetration resistance of the hybrid material twice as high compared to CFRP,

this opens the possibility for a reduction of the prescribed minimum skin thickness and should be subjected to detailed future investigations. Improvements in terms of bolted joints mainly concern the post-damage stage, i.e. the fail-safe behaviour; the steel fibre integration does thus not facilitate considerable enhancements with respect to a strength- or stiffness-orientated dimensioning of such connections. However, by appropriate steel fibre arrangement, the bolted joints suit for structural energy absorption purposes in case of overload (improvement of 63 % under bearing load and of 81 % in case of bolt pull-through). Not considered in this work but highly recommended for future researches is the influence of the different coefficients of thermal expansion of carbon and steel fibres on residual stresses within the laminate.

Also, the hybridisation enables to add a novel feature to the composite material. Plastic deformation of the integrated metastable austenitic steel fibres arising during overstraining of the hybrid composite is accompanied by phase transformation from paramagnetic γ-austenite to ferromagnetic α'-martensite. Exemplarily shown for impact and fatigue [176], the change of the magnetic properties of austenitic steel fibres placed at near-surface layers suits to detect and assess damage of the hybrid material. However, in order to develop this method to a mature non-destructive testing application, comprehensive investigations regarding sensitivity, damage correlation, temperature dependence and stability, spatial resolution, reproducibility and proper fibre arrangement are mandatory. The compactness of the necessary test equipment could then enable on-site application.

Concluding, the present study proves the basic feasibility of the introduced multifunctional hybrid material concept and the aspired simultaneous structural and electrical enhancements of the composite with acceptable steel fibre shares. The findings of the fracture mechanics, in particular of the interaction between ductile steel and brittle carbon fibres during failure initiation and in the after-damage stage, provide crucial knowledge for further developments in the field of fibre hybrid composites, e.g. in terms of hybridisation concepts or selection of proper material combinations. The explicated analytical concept of the fracture zone of influence can serve as origin for the development of an appropriate material (degradation) model for prognostic simulation of SCFRP or comparable hybrid materials. Such model could be used to design a non-generic element allowing for well-known specifications in order to demonstrate the potential of the multifunctional hybrid material concept over state-of-the-art CFRP solutions with respect to the overall weight of the aircraft structure.

Appendix

Appendix A.1: Numerical simulation of UD layers

In order to numerically calculate the effective stiffness of uniaxial reinforced (hybrid) layers in parallel and transverse to the fibre orientation, the software package GeoDict [143] is used. The package includes the software tools FiberGeo and ElastoDict. In a first step, FiberGeo is applied to automatically generate a representative volume element (RVE) with a random distribution of circularly shaped carbon and metal fibres. The edge length of the RVE is set to 1 mm in order to ensure a statistically significant but overall homogeneous fibre distribution. The RVE is meshed by 1000 × 1000 × 1 cubic elements, which corresponds to an element edge length of 1 µm. The generated model disregards the hexagonal structure of the steel fibre bundles, which, however, is also neglected in the analytical derivation of

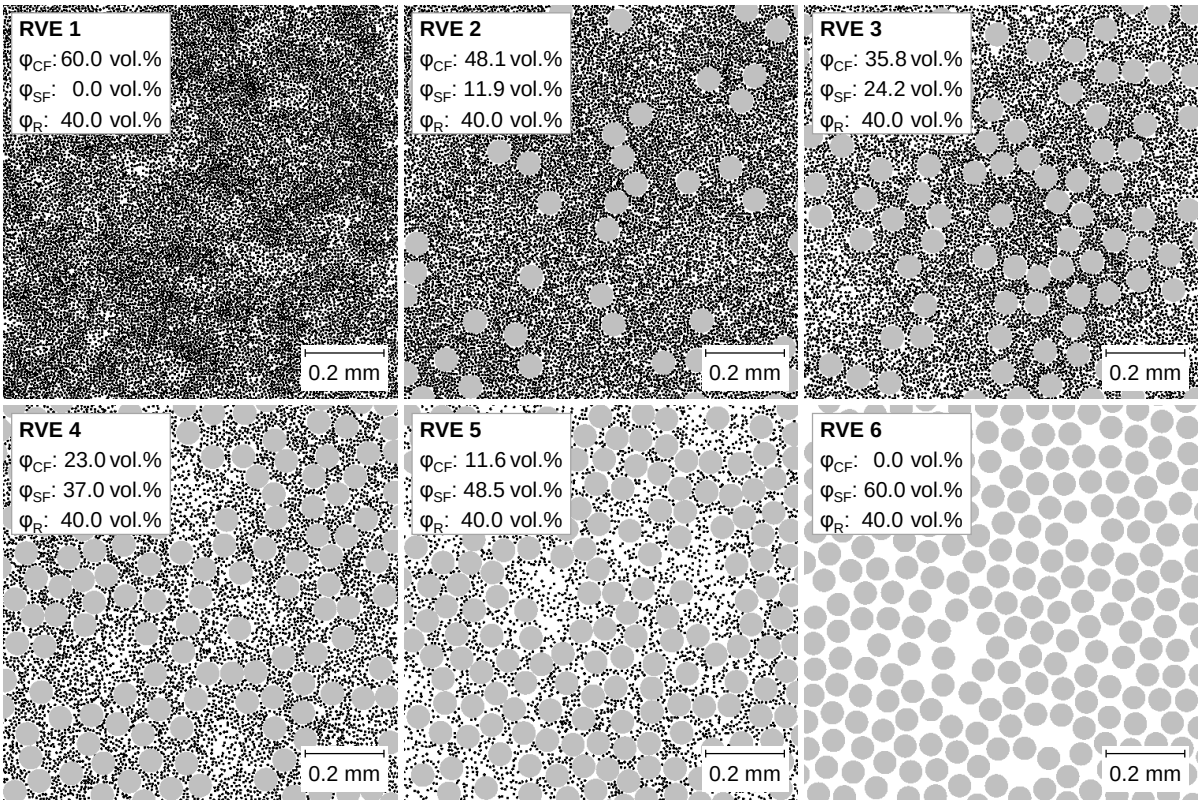

black: carbon fibre, grey: steel fibre, white: epoxy resin, 1-direction: normal, 2-direction: horizontal, 3-direction: vertical

Figure A.1 Representative volume elements with different carbon and steel fibre proportions for the numerical calculation of the effective elastic moduli of uniaxial reinforced (hybrid) layers

the mechanical ply properties. Six different material configurations each with an overall fibre share of 60 vol.% are considered. The corresponding models are shown in figure A.1. The elastic material behaviour of the transverse isotropic carbon fibres and the isotropic resin and steel fibres is modelled in compliance with the analytical approach (cf. chapter 5.2) and according to the properties listed in table 4.4. If required by the calculation, Poisson ratios v as well as shear modulus G of the constituent materials are appraised by generally accepted values due to the lack of the exact properties. An overview of the assigned properties of the constituent materials is given in table A.1.

Table A.1 Assigned properties of the constituent materials

Constituent	E_1 / GPa	E_2 / GPa	E_3 / GPa	G_{12} / GPa	v_{12}	v_{23}	Reference
Carbon fibre	240	24	24	50	0.23	0.10	[7, 13]
Steel fibre	176	176	176	-	0.30	0.30	[141]
Epoxy resin	3.52	3.52	3.52	-	0.35	0.35	[7, 13]

The fibre-resin-adhesion is set to be ideally tied. A failure model is not implemented since the simulation simply aims to predict the elastic behaviour of the composite. Three different load cases (i.e. discrete elongation of 0.005 % in each of the three spatial directions) are simulated. For each of these load cases, ElastoDict calls the FeelMath solver of Fraunhofer ITWM that sets up the system of Lamé equations of linear elasticity and solves this system. By appropriate integration, ElastoDict finally provides the effective stiffness of the RVE. The calculated moduli of elasticity in parallel E_1 and transverse to the fibre orientation E_2 and E_3 are summarised in table A.2. The minor deviation between E_2 and E_3 results from the uneven distribution of

Table A.2 Numerically calculated effective moduli of elasticity of a uniaxial reinforced hybrid layer for different carbon and metal fibre proportions

Property	RVE 1	RVE 2	RVE 3	RVE 4	RVE 5	RVE 6
φ_{CF} / vol.%	60.00	48.08	35.81	23.00	11.60	0.00
φ_{SF} / vol.%	0.00	11.92	24.19	37.00	48.50	60.00
φ_{R} / vol.%	40.00	40.00	40.00	40.00	40.00	40.00
E_1 / GPa	145.52	137.90	130.03	121.81	114.40	107.03
E_2 / GPa	10.14	11.00	11.96	13.46	15.42	15.84
E_3 / GPa	10.13	10.92	11.98	13.42	14.65	15.38

reinforcement fibres in the respective spatial directions but also indicates a secondary influence of the exact fibre arrangement on the transverse stiffness of the composite.

The application of GeoDict is beneficial for efficient analysis of micromechanical problems. Typically, finite element analysis (FEA) runs on mesh sizes which are much larger than the diameter of the embedded reinforcing fibres. As a consequence, each element exhibits an effective (homogenised) material behaviour. The exact number of fibres and their orientation intricately determines the usually anisotropic behaviour of each element. Standard FEA tools can account for this complexity; difficulties typically arise from determining the microstructural parameters. A high-resolution meshing of the RVE with differentiation of individual fibres, however, requires a large number of (finite) elements, hence computational effort. The applied FeelMath solver overcomes this difficulty. The limitation to cubic elements simplifies the compiled system of equations, which allows application of FFT (fast Fourier transform) and thus efficient computation of large numbers of elements, i.e. a detailed simulation of the composite's microstructure.

Appendix A.2: Thermal analysis of the epoxy resin

In order to investigate the thermal behaviour of the applied epoxy resin (Cytec Cycom 977-2), temperature-modulated differential scanning calorimetry (TMDSC) is carried out according to DIN EN ISO 11357-5 [144]. TMDSC is based on determination of the quantity of heat that is either absorbed or released by the polymer sample undergoing a physical or chemical change caused by an imposed temperature profile. This change corresponds to an alteration of the specimen's internal energy. Processes such as melting, evaporation or glass transition are endothermic (negative enthalpy), while crystallisation, progressive curing and decomposition are exothermic (positive enthalpy). Evaluation of the heat flow consequently allows identifying characteristic processes within the polymer sample. Different to conventional differential scanning calorimetry (DSC), TMDSC superimposes an oscillating temperature component on the prescribed temperature profile. By analysing the oscillating heat flow, the signal can be separated into a reversing (thermal) and a non-reversing (reaction-caused) portion, which again allows distinguishing processes within the thermoset or thermoplastic phase of the resin. A detailed description of the work principles of DSC and TMDSC is given in [145] and [146]. For the present TMDSC, samples of approximately 10 mg of thawed resin film are analysed.

Additionally, dielectric analysis (DEA) is carried out on unfrozen resin film in dependence on ASTM E2039 [147] in order to analyse its rheological behaviour. DEA equals an impedance measurement on the polymer resin which is exposed to a defined temperature profile. In general, polymers exhibit dielectric behaviour due to the lack of free electrons. A certain current flow is, however, given by movement and alignment of ions and dipoles which occur in the form of catalysts or impurities in the polymer. Application of a sinusoidal voltage to the polymer sample therefore results in a sinusoidal current flow. Increasing cross-linking (curing) of the resin reduces the mobility of the ions and dipoles, which increases the phase shift and attenuates the amplitude of the induced current relatively to the excitation. Since the ion viscosity correlates with the dynamic viscosity of the resin, DEA enables to assess the curing behaviour of the polymer resin. One essential advantage of DEA over shear rheology is the ability to analyse the viscosity of the resin up to the entirely cured state. For the present analysis, disposable interdigitated electrodes with a line spacing of 115 µm (Netzsch IDEX) are used as dielectric sensor on resin samples of 100 mg. The excitation frequencies range logarithmically from 1 Hz to 1 kHz. [148]

The considered temperature profile for TMDSC and DEA basically emulates the applied autoclave cycle (cf. figure 6.1 (left)). Additionally, analogue measurements with continuous heating to 300 °C are carried out in order to determine the absolute degree of cure. Figure A.2 depicts the results of the conducted analyses.

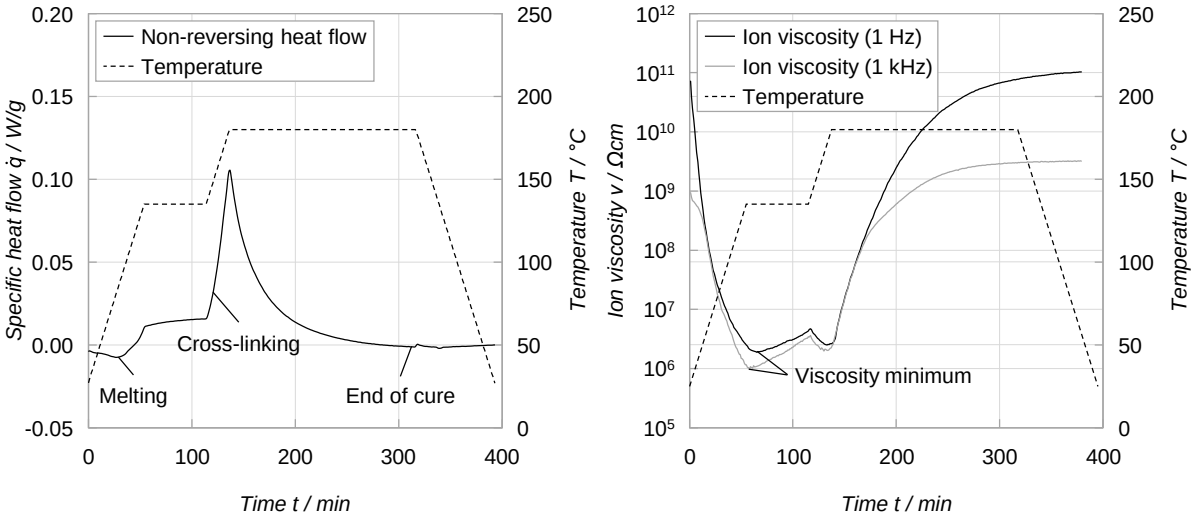

Figure A.2 (left) Heat flow determined by TMDSC and (right) ion viscosity determined by DEA for epoxy resin of type Cytec Cycom 977-2 for the temperature profile used for laminate curing

The heating initially causes softening of the epoxy resin and thus a reduction of its viscosity. For the selected heat-up rate of 2 °C/min, the viscosity minimum is nearly achieved at 135 °C (cf. figure 6.1 (right)). At this point, the resin exhibits optimal flow behaviour. In order to delay gelling of the resin and thus to facilitate impregnation and consolidation of the laminate (in particular of the intermittent steel fibre plies), this temperature is maintained for 60 min. During this isothermal dwell time, viscosity as well as exothermic heat flow due to beginning cross-linking rise only slightly[26]. Subsequent heating to 180 °C initially causes another drop of the viscosity with a local minimum at 165 °C but also a significant increase of the exothermic heat flow, indicating onset of curing. At this stage, softening counteracts the cross-linking of the polymer resin. With increasing temperature, curing starts to predominate; this leads to a rise in viscosity of more than five orders of magnitude to a maximum value of 10^{11} Ωcm (for an excitation frequency of 1 Hz). After approximately 315 min, the heat flow curve as well as the viscosity levels out, indicating that curing is completed. The degree of cure achieved is 94 %.

Appendix A.3: Martensite transformation

The martensite formation is a diffusion-free, lattice-shearing transformation from face-centred cubic (fcc) γ-austenite (high temperature phase) to body-centred cubic (bcc) α‘-martensite and/or hexagonal close-packed (hcp) ε-martensite (low temperature phase). The transformation originates at preformed nuclei, i.e. distorted atomic arrangements in the γ-austenite with α‘-martensite-like microstructure, as for example given at groups of screw dislocation. A detailed description of the crystallographic processes is given by Smaga [149]. Basically, the martensitic phase transformation can be thermal- and/or deformation-induced. A thermodynamical consideration of the γ-α‘-transformation is depicted in figure A.3 (left). At a temperature T_0 γ-austenite and α’-martensite are thermodynamically balanced. With decreasing temperature, the Helmholtz free energy of austenite increases stronger than the Helmholtz free energy of martensite. If a critical potential difference $\Delta G_{\gamma\text{-}\alpha',min}$ is exceeded, γ-austenite transforms into α‘-martensite (principle of minimum energy, c.f. second law of

[26] Increasing the dwell time temperature to approximately 150 °C would lead to an even lower initial viscosity. The higher temperature would, however, also cause a more intense cross-linking of the resin and thus faster re-gain of the viscosity during this stage. Besides, the viscosity re-gain during the isothermal dwell time could principally be decelerated by continuous temperature diminution during that period.

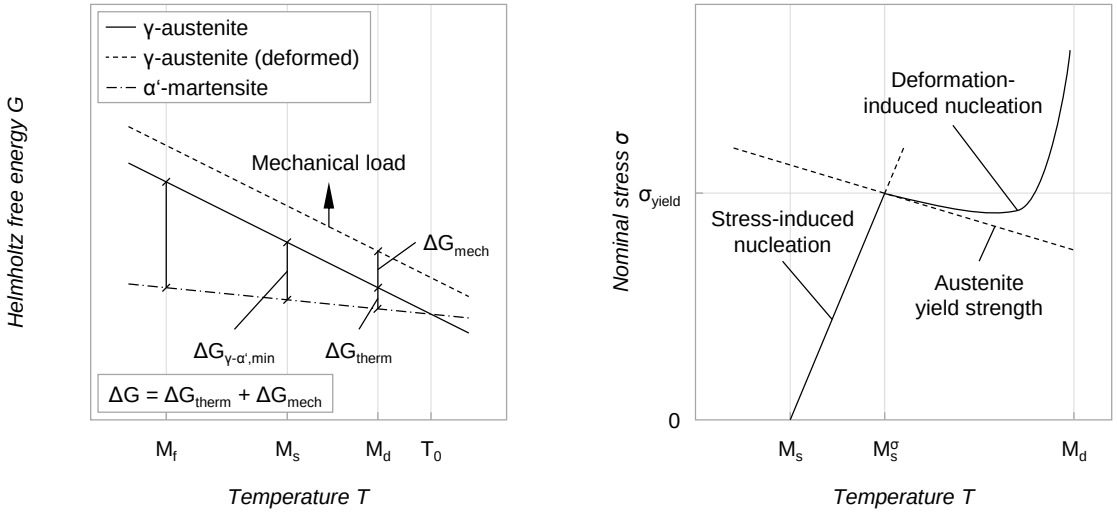

Figure A.3 (left) Consideration of the Helmholtz potential of γ-austenite and α'-martensite during γ-α'-transformation and (right) temperature dependence of stress- and strain-induced martensite formation [150]

thermodynamics [151]), in which the difference of the Helmholtz potentials $\Delta G_{\gamma\text{-}\alpha'}$ acts as driving force. The corresponding temperature is called martensite start temperature M_s. Cooling, however, must be sufficiently fast to suppress diffusion-controlled reactions, such as the formation of ferrite, pearlite or bainite. The transformation ends if the temperature falls below the martensite finish temperature M_f. Above M_s the critical energy of formation can only be achieved by additional external mechanical stress, which shifts the Helmholtz free energy of austenite to a higher level. $\Delta G_{\gamma\text{-}\alpha'}$ is then given by a thermal and a mechanical portion. The higher the temperature, the more mechanical stress is required, figure A.3 (right). At M_s^σ the mechanical stress equals the yield strength of the austenite. Onset of plastic deformation of the austenite and thus additional deformation-induced nucleation initially facilitates martensite formation. However, with increasing temperature, the stress required for martensite formation rises excessively. The maximum temperature up to which deformation-induced martensite formation is possible is defined as M_d temperature. M_d is between M_s and T_0. [149, 150]

M_d is usually replaced by M_{d30} due to a reduction of measurement effort. By definition, M_{d30} is the temperature at which 50 vol.% of austenite is transformed to martensite when subjected to a true strain of 30 %. Both M_s and M_{d30} strongly depend on the chemical composition of the alloy. Elements such as nickel, carbon, manganese, nitrogen or cobalt positively affect the austenite stability and thus lower

M_s and M_{d30}. The limiting temperatures M_s and M_{d30} (in °C) can be estimated by means of empirical equations, as for example eq. A.1 and A.2 [152]. The alloy elements influence the limiting temperatures according to their mass fraction ψ_i (in wt.%) and their reduction factors f_i listed in table A.3.

$$M_s = 1350 - \sum_i f_i \cdot \Psi_i \qquad \text{(Eq. A.1)}$$

$$M_{d30} = 413 - \sum_i f_i \cdot \Psi_i \qquad \text{(Eq. A.2)}$$

Table A.3 Reduction factors for the estimation of M_s and M_{d30} [152]

Property	f_{C+N}	f_{Cr}	f_{Ni}	f_{Si}	f_{Mn}	f_{Mo}
M_s	1665	42	61	28	33	-
M_{d30}	462	13.7	9.5	9.2	8.1	18.5

Other approaches additionally consider the grain size of the microstructure. Considering the alloy composition listed in table 4.1, M_s and M_{d30} are calculated to -38 °C and 47 °C, respectively, for the applied stainless steel fibre. If M_d is above ambient temperature, as given for the alloy 1.4301 of the considered stainless steel fibre bundles, the austenite is denominated as metastable.

As a consequence, plastic deformation of metastable austenitic steel causes hardening due to both strain hardening of the austenite and deformation-induced formation of martensite, accompanied by a considerable increase in yield stress and tensile strength [149]. The hardening, however, also causes a reduction of the uniform elongation and elongation at break. According to Olsen-Cohen analysis [153], the transformation curve (volume fraction of martensite vs. plastic strain) is sigmoidal in shape. Rising deformation temperature causes increasing austenite stability and thus decreasing strain hardening rate. Hecker et al. [154] showed that at low strain levels increasing strain rate promotes α'-martensite formation. With progressive elongation, however, the temperature rise caused by adiabatic heating stabilises austenite and restrains martensite formation. This effect gains in importance with increasing strain rate due to the limited heat release during highly transient processes.

The martensite formation by means of γ-α'-transformation is accompanied by a

change from paramagnetic to ferromagnetic microstructure. This change is eligible to non-destructively ascertain local material variation [155, 156]. Magneto-sensitive sensors suitable to quantify the phase transformation to α‘-martensite include giant magnetoresistance (GMR) sensor, superconducting quantum interference device (SQUID), meandering winding magnetometer (MWM), Hall effect sensor or microelectromechanical (MEMS) based magnetic field sensor. Within the present study, a pen-shaped magnetic induction sensor (Fischer Feritscope® FMP30 [157]) is used. This sensor generates a magnetic field which interacts with the ferromagnetic portion of the specimen. Changes in the magnetic field induce a voltage proportional to the magnetic content in the sensor and can be correlated to the α’-martensite share. Since M_{d30} of the present metastable austenitic steel fibres is 47 °C, this effect is basically applicable to the hybrid composites at relevant, application orientated temperatures. [149, 150]

Appendix A.4: Estimation of the critical failure zone of influence

The analytical approach introduced in chapter 7.3 is applied in order to exemplarily estimate the minimum extent of the fracture zone of influence $f_{FZI,crit}$ which is required to achieve post-failure behaviour in case of a tensile-loaded UD hybrid layer with a stainless steel fibre share of 18.8 vol.% (SCFRP 20h UD). For this purpose, the non-linear stress-strain relation of the stainless steel fibres is approximated by a

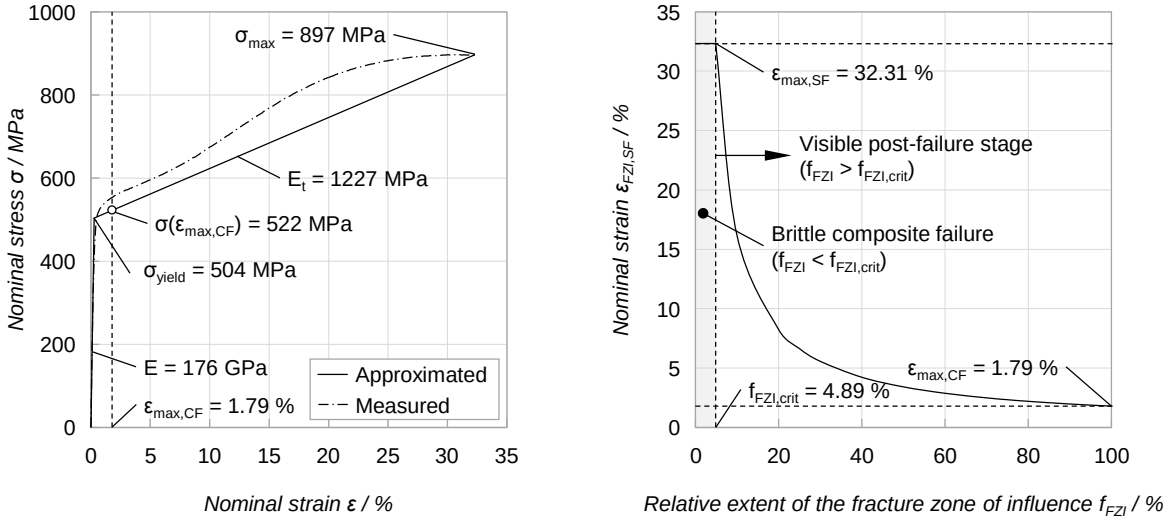

Figure A.4 (left) Bi-linear approximation of the stress-strain relation of the stainless steel fibres and (right) resulting elongation of the stainless steel fibres within the fracture gap as a function of the fracture zone of influence

piecewise linear elastic-plastic material behaviour, figure A.4. The modulus of elasticity as well as the yield strength agree with the experimental data. Compared to the actual stress-strain relation of the dry steel fibre bundles, this conservative approach underestimates the energy absorption capacity by -7.6 %. The carbon fibres and the epoxy resin are assumed to exhibit linear elastic stress-strain relation. Moreover, the epoxy resin is set to fail simultaneously with the carbon fibres. For convenience, both constituents are combined to one phase denominated as (surrounding) CFRP. The corresponding properties are calculated by the linear rule of mixtures. Any strain rate sensitivity is neglected. Furthermore, the analytical model postulates similar stress-strain relation for tensile as well as compression load for each constituent. The assigned characteristics are summarised in table A.4.

Table A.4 Assigned characteristics for the analytical approach

Material	E / GPa	σ_{yield} / MPa	ε_{yield} / %	σ_{max} / MPa	ε_{max} / %	φ / vol.%
Carbon fibre	240	-	-	4300	1.79 [a)]	49.1
Epoxy resin	3.52	-	-	63 [a)]	1.79 [b)]	32.1
CFRP	147	-	-	2625	1.79	81.2
Steel fibre	176	504	0.29	897	32.31	18.8

[a)] adapted for an ideal linear elastic material behaviour abiding Hooke's law ($\varepsilon_{max,CF} = \sigma_{max,CF} / E_{CF}$ and $\sigma_{max,R} = E_R \cdot \varepsilon_{max,R}$)

[b)] adapted to the strain at failure of the carbon fibres ($\varepsilon_{max,R} \stackrel{!}{=} \varepsilon_{max,CF}$)

In principle, two steady states of the hybrid composite must be considered in order to derive the critical extent of the fracture zone of influence: the state immediately before failure initiation (state 1) and after load redistribution (state 2), figure A.5.

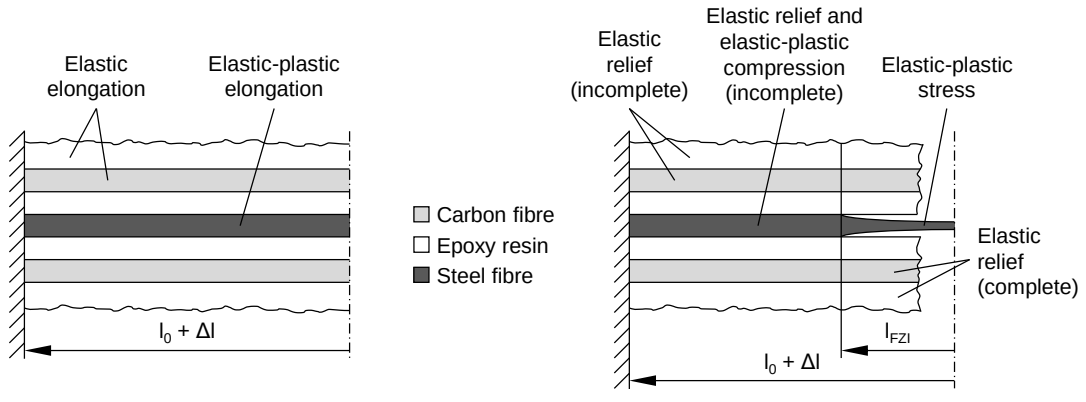

$\Delta l = \varepsilon \cdot l_0$, $\varepsilon \rightarrow \varepsilon_{max,CF}$, $\varepsilon > \varepsilon_{yield,SF}$

State 1: Before failure initiation

$\Delta l = \varepsilon \cdot l_0$, $l_{FZI} = f_{FZI} \cdot (l_0 + \Delta l)$, $\varepsilon = \varepsilon_{max,CF}$, $\varepsilon_{FZI,SF} > \varepsilon$

State 2: After fracture gap generation

Figure A.5 Illustration of the considered states of the loaded hybrid composite

State 1: Right before failure initiation, the elongation of each constituent equates to the global elongation of the composite and corresponds to the elongation at break of the carbon fibres. Both the carbon fibres and the epoxy resin are elastically elongated. The steel fibres, by contrast, are already plastically deformed (uniformly on the entire length of the hybrid composite) since their yield strain is smaller than the current global elongation of the composite.

State 2: Immediately after the load redistribution (no global change in length of the composite since state 1), the carbon fibres and the epoxy resin within the fracture zone of influence are completely relieved (unrestrained elastic relaxation). The steel fibres in this area are conversely further elongated to bypass the generated fracture gap. Outside the fracture zone of influence, the steel fibres (which are perfectly bonded to the surrounding CFRP) are first elastically relieved and then, if necessary, elastic-plastically compressed due to the elastic spring-back of the adhesive CFRP. The relaxation of the CFRP in this area is, however, incomplete due to the permanent deformation of the steel fibres outside and the tensile load exerted by the steel fibres inside the fracture zone of influence.

The critical length of the fracture zone of influence (given as ratio to the length of the composite) is determined iteratively, assuming that the steel fibres within the fracture zone of influence are strained to their maximum elongation and having regard to three principal requirements:

(1) The transition of the limit states occurs exclusively by means of relative displacement between the steel fibres and the surrounding CFRP, i.e. without change in length of the composite (**kinematic boundary condition**).
(2) The normal force executed on the laminate fragments outside the fracture zone of influence equals the normal force of the steel fibres in the fracture zone of influence (**balance of forces**).
(3) The fracture halves return to their steady state without oscillation (**critically damped harmonic oscillator**). Since the relief motion starts without initial velocity, overshoots of the fragments over their final (steady) position do not occur. Damping is given by yielding of the steel fibres as well as inter-fibre-failure, fibre fracture and friction between laminate bundles.

According to this theoretical model, failure is initiated independently of the steel fibre fraction and the size of the fracture zone of influence at a global elongation of

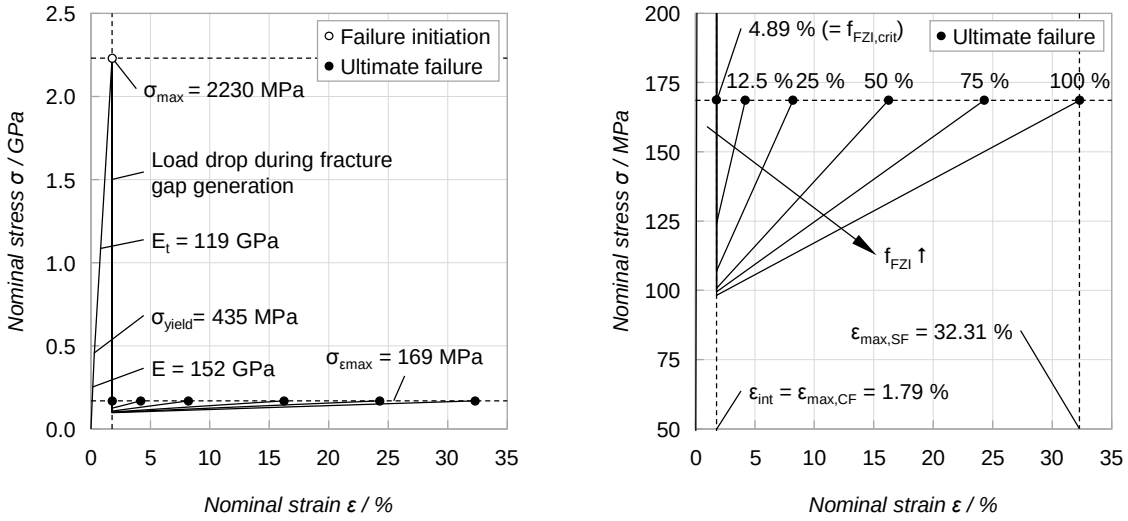

Figure A.6 Stress-strain relation of the considered hybrid composite SCFRP 20h UD as a function of the fracture zone of influence: (left) overall view and (right) close-up view of the post-failure stage

1.79 %. At this elongation, the hybrid composite exhibits a heterogeneous stress distribution with a local stress of 522 MPa at the steel fibres and 2625 MPa at the surrounding CFRP. With the given proportion, this corresponds to an average stress of 2230 MPa. As shown at the end of this section, this stress conforms to the tensile strength of the hybrid composite. The degree of local elongation of the steel fibres within the fracture zone of influence for bridging the propagating fracture gap directly depends on the extent of the fracture zone of influence f_{FZI}, figure A.4 (right). The smaller the fracture zone of influence, the higher is the local elongation of the steel fibres and thus the lower is the residual elongation capacity of the hybrid composite, i.e. its ultimate strain at failure, figure A.6. In case of f_{FZI} = 100 %, the steel fibres and the surrounding CFRP can be considered as independent of each other. Failure initiation is accompanied by complete elastic unloading of the CFRP without affecting the incorporated steel fibres. During the fracture gap generation, the uniform elongation of the steel fibres therefore remains unchanged at 1.79 %. Subsequently, the composite can sustain further elongation up to an ultimate failure strain which equates to the strain at failure of the incorporated steel fibres. In case of $f_{FZI} = f_{FZI,crit}$, the stainless steel fibres within the fracture zone of influence are strained by the elastic spring-back of the fracture halves to their maximum elongation of 32.31 %. According to this definition, a critical length of the fracture zone of influence of

4.89 %[27] is determined for the considered hybrid composite, figure A.4 (right). This value of $f_{FZI,crit}$ corresponds to an absolute length of 7.33 mm for a standard-conform coupon with a clamping length l_0 of 150 mm (cf. DIN EN ISO 527-5 [131]), which is hardly viable for genuine composites. For this limit state, the residual deformability of the hybrid composites becomes minimal; its ultimate strain at failure equals the elongation at break of the carbon fibres. In case of $f_{FZI} < f_{FZI,crit}$, the local elongation of the steel fibres within the fracture zone of influence exceeds their strain at failure during fracture gap generation; the composite consequently exhibits brittle failure. In principle, the elongation of the steel fibres within the fracture zone of influence is accompanied by strain hardening, i.e. a local stress increase. The smaller the fracture zone of influence, the greater is the strain hardening of the steel fibres and thus the less pronounced is the load drop during failure of the carbon fibres, figure A.6. In case of f_{FZI} = 100 %, the stainless steel fibres show a local stress of 522 MPa immediately after the fracture gap generation, which corresponds to a global stress of 98 MPa (considering the steel fibre volume share). If the fracture zone of influence is reduced to $f_{FZI} = f_{FZI,crit}$, the steel fibres are stressed to 897 MPa, which equates to a global stress of 169 MPa. Independently of f_{FZI}, total failure of the composite occurs at a local stress of the steel fibres of 897 MPa, which again corresponds to a global stress of 169 MPa. The tensile strength of the considered hybrid material is therefore

Table A.5 Characteristic values of the hybrid composite at different states of elongation as a function of the extent of the fracture zone of influence

f_{FZI} / %	ε_{int} / %	σ_{max} / MPa	σ_{SF} / MPa [a)]	ε_r / % [b)]	$\sigma_{FZI,SF}$ / MPa [c)]	σ / MPa [c)]	ε_{max} / %	$\sigma_{\varepsilon max}$ / MPa
< $f_{FZI,crit}$	1.79	2230	522	-	-	-	1.79 (= $\varepsilon_{max,CF}$)	169
4.89 (= $f_{FZI,crit}$)	1.79	2230	522	0.22	897 (= $\sigma_{max,SF}$)	169	1.79 (= $\varepsilon_{max,CF}$)	169
12.5	1.79	2230	522	0.19	660	124	4.34	169
25	1.79	2230	522	0.18	582	109	8.35	169
50	1.79	2230	522	0.17	542	102	16.38	169
75	1.79	2230	522	0.17	529	99	24.42	169
100	1.79	2230	522	0.00	522	98	32.31 (= $\varepsilon_{max,SF}$)	169

[a)] right before failure of the carbon fibres (state 1)

[b)] elongation of the fracture halves in steady state 2

[c)] immediately after fracture gap generation (state 2)

[27] For comparison: The approximation formula for $f_{FZI,crit}$ (ratio of $\varepsilon_{max,CF}$ to $\varepsilon_{max,SF}$, cf. chapter 7.3) yields a value of 5.55 %. In fact, this value corresponds to a hybrid composite with a negligible steel fibre share ($\varphi_{SF} \rightarrow 0$ vol.%) or to the case of complete spring-back of the fracture halves ($\varepsilon_r \rightarrow 0$).

defined by the (higher) stress at the moment of failure initiation. In addition to the critical length of the fracture zone of influence, this iterative approach yields all essential characteristic values to approximate the stress-strain relation of the UD hybrid layer in parallel to its fibre direction as a function of the fracture zone of influence, figure A.6.

Appendix A.5: Specimen geometries

The specimen geometries used in this thesis are depicted in the figures below. All dimensions are given in millimetres. The laminate thickness t depends on the tested laminate configuration and is therefore not specified (cf. figure 7.1 and figure 8.1).

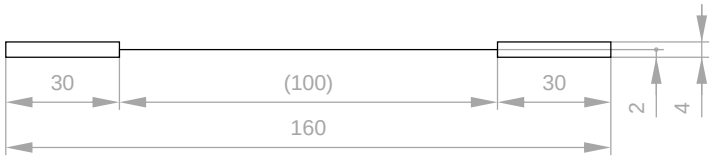

Figure A.7 Specimen geometries used for the fibre characterisation

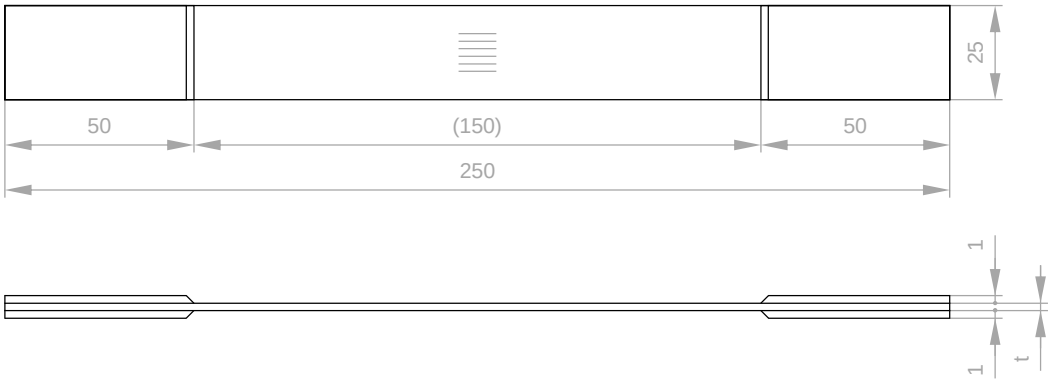

Longitudinal tensile tests on UD layers (DIN EN ISO 527-5)

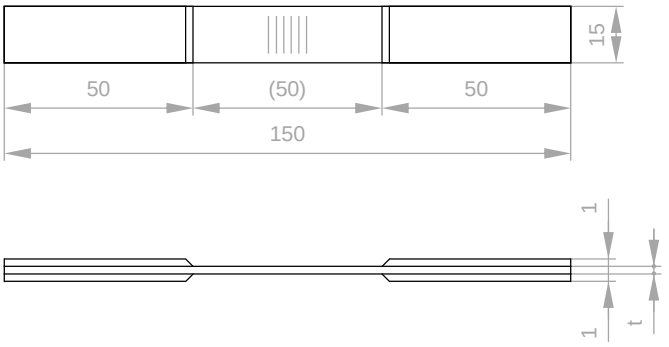

Transverse tensile tests on UD layers (DIN EN ISO 527-5)

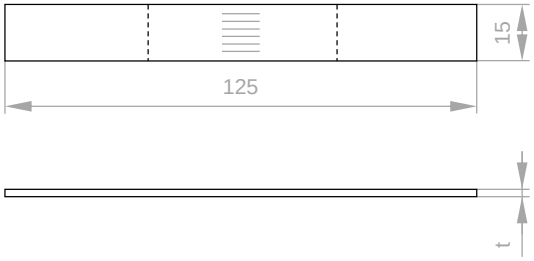

Bending-tensile tests on UD layers (non-standardised)

Figure A.8 Specimen geometries used for the uniaxial layer characterisation

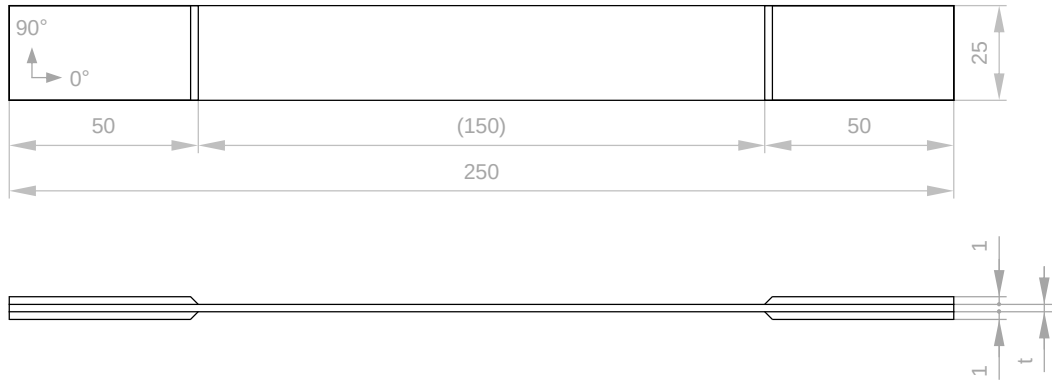

Plain tensile tests on multiaxial laminates (DIN EN ISO 527-4)

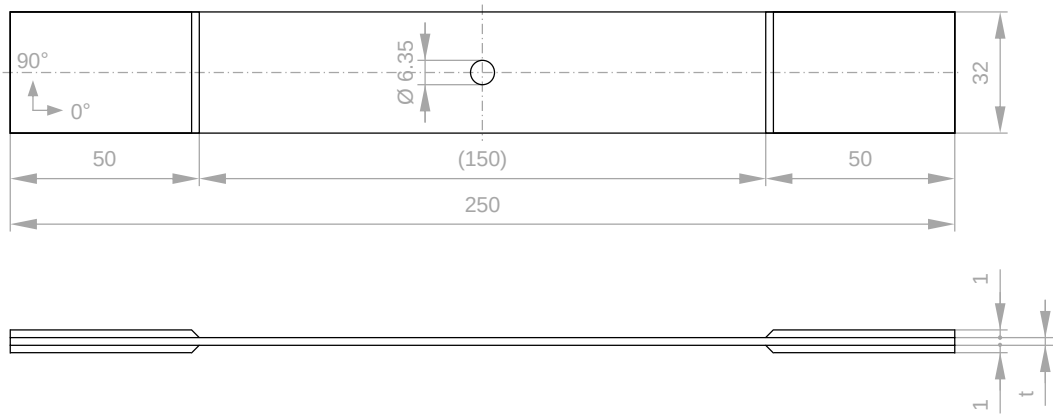

Filled hole tensile tests on multiaxial laminates (AITM 1-0007)

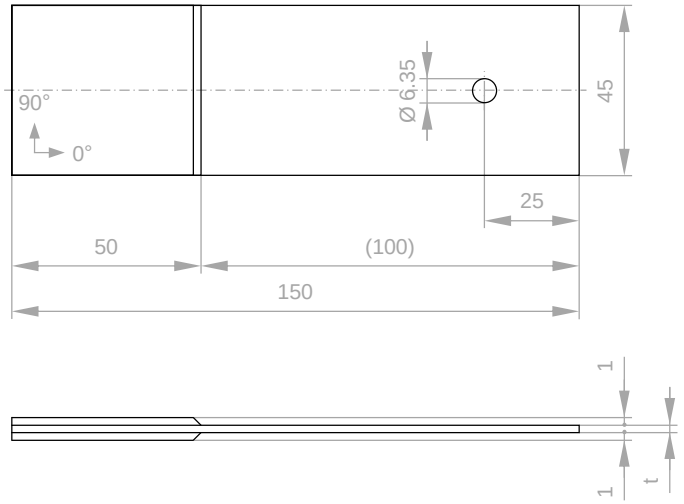

Bearing strength tests on multiaxial laminates (AITM 1-0009)

Figure A.9 Specimen geometries used for the multiaxial laminate characterisation

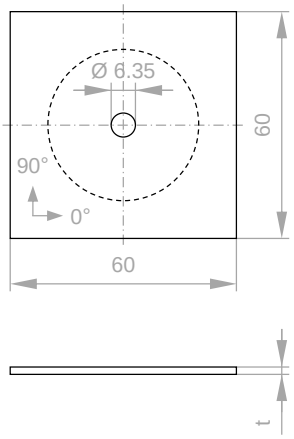

Bolt pull-trough tests on multiaxial laminates (AITM 1-0066)

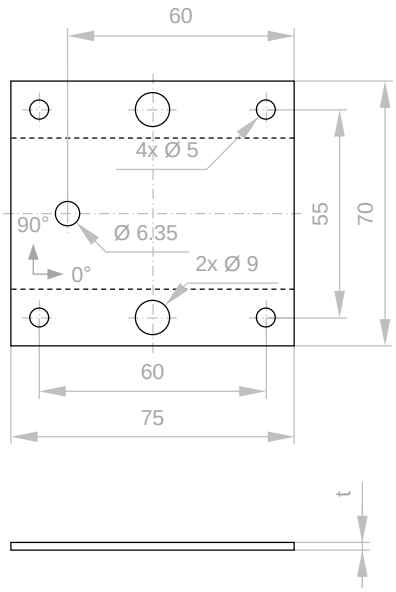

Progressive bearing strength tests on multiaxial laminates (non-standardised)

Figure A.10 Specimen geometries used for the multiaxial laminate characterisation

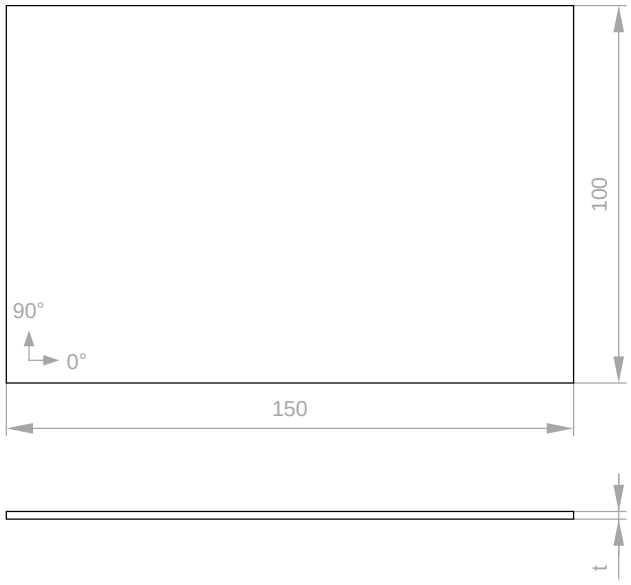

Compression strength after impact tests on multiaxial laminates (AITM 1-0010)

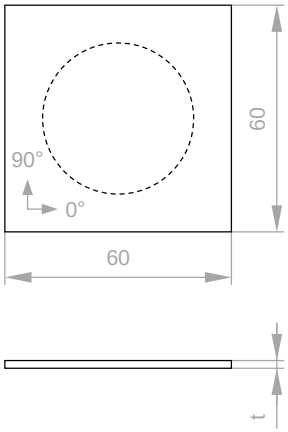

Penetration resistance tests on multiaxial laminates (DIN EN 6603-2)

Figure A.11 Specimen geometries used for the multiaxial laminate characterisation

References

[1] Breuer, U. P.: Commercial aircraft composite technology. 1st edition, Springer International, 2016.

[2] Hübler, M.: Methodik zur Auslegung und Herstellung von aktiven SMA-FKV-Hybridverbunden. Dissertation, Kaiserslautern, IVW Schriftenreihe, 2015, 118.

[3] Hellard, G.: Composites in Airbus. A long story of innovations and experiences. EADS Global Investor Forum, Sevilla, 17.-18.01.2008.

[4] Bold, J.: Airbus composite training: Skills for composites. Virtual Product Development Conference, Frankfurt, 17.-18.10.2007.

[5] Toray Industries: Strategic business expansion of carbon fiber. 12.04.2005

[6] Noebel, T.: CFRP fuselage sizing/design. Commercial Aircraft Composite Technology. Guest lecture, Kaiserslautern, 24.01.2013.

[7] Schürmann, H.: Konstruieren mit Faser-Kunststoff-Verbunden. 2nd edition, Springer, Berlin, 2005.

[8] Baker, A. A.; Scott M. L.: Composite materials for aircraft structures. 3rd edition, American Institute of Aeronautics and Astronautics Education Series, Reston, 2016.

[9] Böttger-Hiller, F.; Kleiber, J.; Böttger, T.; Lampke, T.: Multimetallic electrodeposition on carbon fibers. Materials Science and Engineering, 2016, 118 (1), 1-6.

[10] Conductive Composites: Nickel CVD coated carbon fiber (NiFiber). Heber City, 2015.

[11] Ha, M. S.; Kwon, O. Y.; Choi, H. S.: Improved electrical conductivity of CFRP by conductive silver nano-particles coating for lightning strike protection. 17th International Conference on Composite Materials, Edinburgh, 27.-31.07.2009.

[12] Toho Tenax: Produkt Datenblatt Tenax HTS Filamentgarn, nickelbeschichtet. Wuppertal, 2014.

[13] Toho Tenax: Produktprogramm und Eigenschaften für Tenax HTS Filamentgarn. Wuppertal, 2011.

[14] Spitalsky, Z.; Tasis, D.; Papagelis, K.; Galiotis, C.: Carbon nanotube-polymer composites: Chemistry, processing, mechanical and electrical properties. Progress in Polymer Science, 2010, 35 (3), 357-401.

[15] Schulte, K.; Schüler, R.; Kupke, M.; Joshi, S. B.: Ermittlung der Schädigung in CFK-Platten durch systematische Aufzeichnung der elektrischen Leitfähigkeit. Deutsche Gesellschaft für zerstörungsfreie Prüfung, Jahrestagung, Berlin, 21.-23.05.2001.

[16] CES EduPack 2012, version 11.9.9.

[17] Deutsches Kupferinstitut: Werkstoff-Datenblatt Cu-0FE. Düsseldorf, 2005.

[18] Roebroeks, G. H. J. J.: Glare features. In: Vlot, A.; Gunnink, J. W. (eds.): Fibre metal laminates. 1st edition, Springer Science and Business Media, 2001.

[19] Zhang, D.; Ye, L.; Deng, S.; Zhang, J.; Tang, Y.; Chen, Y.: CF/EP composite laminates with carbon black and copper chloride for improved electrical conductivity and interlaminar fracture toughness. Composites Science and Technology, 2012, 72 (3), 412-420.

[20] Elimat, Z. M.; Hamideen, M. S.; Schulte, K. I.; Wittich, H.; de la Vega, A.; Wichmann, M.; Buschhorn, S.: Dielectric properties of epoxy/short carbon fiber composites. Journal of Materials Science, 2010, 45 (19), 5196-5203.

[21] Xing, Y.; Cao, W.; Li, W.; Chen, H.; Miao, W.; Wei, H.; Hu, D.; Chen, M.; Li, Q.: Carbon nanotube/Cu nanowires/epoxy composite materials with improved thermal and electrical conductivity. Journal of Nanoscience and Nanotechnology, 2015, 15 (4), 3265-3270.

[22] Al-Saleh, M. H.; Sundararaj, U.: A review of vapor grown carbon nanofiber/polymer conductive composites. Carbon, 2009, 47 (1), 2-22.

[23] Noll, A.: Effektive Multifunktionalität von monomodal, bimodal und multimodal mit Kohlenstoff-Nanoröhren, Graphit und kurzen Kohlenstofffasern gefülltem Polyphenylensulfid. Dissertation, Kaiserslautern, IVW Schriftenreihe, 98, 2010.

[24] Sandler, J. W. K.; Kirk, J. E.; Kinloch, I. A.; Shaffer, M. S. P.; Windle, A. H.: Ultra-low electrical percolation threshold in carbon-nanotube-epoxy composites. Polymer, 2003, 44 (19), 5893-5899.

[25] Li, N.; Huang, Y.; Du, F.; He, X.; Lin, X.; Gao, H.; Ma, Y.; Li, F.; Chen, Y.; Eklund, P. C.: Electromagnetic interference (EMI) shielding of single-walled carbon nanotube epoxy composites. Nano Letters, 2006, 6 (6), 1141-1145.

[26] Kim, H. S.; Hahn, H. T.: Graphite fiber composites interlayered with single-walled carbon nanotubes. Journal of Composite Materials, 2011, 45 (10), 1109-1120.

[27] Reia da Costa, E. F.; Skordos, A. A.; Partridge, I. K.; Rezai, A.: RTM processing and electrical performance of carbon nanotube modified epoxy/fibre composites. Composites Part A: Applied Science and Manufacturing, 2012, 43 (4), 593-602.

[28] Causse, N.; Benchimol, S.; Martineau, L.; Carponcin, D.; Lonjon, A.; Fogel, M.; Dandurand, J.; Dantras, E.; Lacabanne, C.: Polymerization study and rheological behavior of a RTM6 epoxy resin system during preprocessing step. Journal of Thermal Analysis and Calorimetry, 2015, 119 (1), 329-336.

[29] Qin, W.; Vautard, F.; Drzal, L. T.; Yu, J.: Mechanical and electrical properties of carbon fiber composites with incorporation of graphene nanoplatelets at the fiber-matrix interphase. Composites Part B: Engineering, 2015, 69, 335-341.

[30] Wajid, A. S.; Ahmed, H. S. T.; Das, S.; Irin, F.; Jankowski, A. F.; Green, M. J.: High-performance pristine graphene/epoxy composites with enhanced mechanical and electrical properties. Macromolecular Materials and Engineering, 2013, 298 (3), 339-347.

[31] Tang, Y.; Gou, J.: Synergistic effect on electrical conductivity of few-layer graphene/multi-walled carbon nanotube paper. Materials Letter, 2010, 64 (22), 2513-2516.

[32] Moosa, A. A.; Ramazani, A.; Ibrahim, M. N.: Mechanical and electrical properties of graphene nanoplates and carbon-nanotubes hybrid epoxy nanocomposites. American Journal of Materials Science, 2016, 6 (6), 157-165.

[33] Guo, M.; Yi, X.; Liu, G.; Liu, L.: Simultaneously increasing the electrical conductivity and fracture toughness of carbon-fiber composites by using silver nanowires-loaded interleaves. Composites Science and Technology, 2014, 97, 27-33.

[34] Rehbein, J.; Wierach, P.; Gries, T.; Wiedemann, M.: Improved electrical conductivity of NCF-reinforced CFRP for higher damage resistance to lightning strike. Composites Part A: Applied Science and Manufacturing, 2017, 100, 352-360.

[35] Lengsfeld, H.; Wolff-Fabris, F.; Krämer, J.; Lacalle, J.; Altstädt, V.: Faserverbundwerkstoffe: Prepregs und ihre Verarbeitung. Carl Hanser, München, 2014.

[36] Rivenc, J.; Perraud, R.; Peres, G.; Zink, T.; Andissac, D.; Mills, R.; Cinquin, J.: A multiphysic approach to predict the degradation of a composite material due to current injection. 17th European Conference on Composite Materials, München, 26.-30.06.2016.

[37] Lochot, C.; Slomianowski, D.: A350 XWB electrical structure network. Fast, 2014, 53, 10-25.

[38] Gagné, M.; Therriault, D.: Lightning strike protection of composites. Progress in Aerospace Sciences, 2014, 64, 1-16.

[39] Karch, C.; Metzner, C.: Lightning protection of carbon fibre reinforced plastics - An overview. 33rd International Conference on Lightning Protection, Estoril, 25.-30.09.2016.

[40] Rupke, E.: Lightning direct effects handbook. AGATE-WP3.1-031027-043-Design Guideline. 2002.

[41] Feraboli, P.; Miller, M.: Damage resistance and tolerance of carbon/epoxy composite coupons subjected to simulated lightning strike. Composites Part A: Applied Science and Manufacturing, 2009, 40 (6), 954-967.

[42] Chemartin, L.; Lalande, P.; Peyrou, B.; Chazottes, A.; Elias, P. Q.; Delalondre, C.; Cheron, B. G.; Lago, F.: Direct effects of lightning on aircraft structure: Analysis of the thermal, electrical and mechanical constraints. AerospaceLab Journal, 2012, 5, 1-15.

[43] Feraboli, P.; Kawakami, H.: Damage of carbon/epoxy composite plates subjected to mechanical impact and simulated lightning. Journal of Aircraft, 2010, 47 (3), 999-1012.

[44] Plumer, J. A.; Robb, J. D.: The direct effects of lightning on aircraft. IEEE Transactions on Electromagnetic Compatibility, 1982, EMC-24 (2), 158-172.

[45] Shulin, L.; Junjie, Y.; Xueling, Y; Fei, C.; Xiaopeng, S.: Damage analysis for carbon fiber/epoxy composite exposed to simulated lightning current. Journal of Reinforced Plastics and Composites, 2016, 35 (15), 1201-1213.

[46] Hirano, Y.; Katsumata, S.; Iwahori, Y.; Todoroki, A.: Fracture behaviour of CFRP specimen after lightning test. 17th International Conference on Composite Materials, Edinburgh, 27.-31.07.2009.

[47] Ogasawara, T.; Hirano, Y.; Yoshimura, A.: Coupled thermal-electrical analysis for carbon fiber/epoxy composites exposed to simulated lightning current. Composites Part A: Applied Science and Manufacturing, 2010, 41 (8), 973-981.

[48] Soulas, F.; Espinosa, C.; Lachaud, F.; Guinard, S.; Lepetit, B.; Revel, I.: Equivalent impact set-up for lightning strike damage on composite coupons. 20th International Conference on Composite Materials, Copenhagen, 19.-24.07.2015.

[49] Dexmet: Microgrid for composite aircraft, wind turbine blades and structures.

[50] Niles: Expanded metal lightning strike protection.

[51] Kawakami, H.; Feraboli, P.: Lightning strike damage resistance and tolerance of scarf-repaired mesh-protected carbon fiber composites. Composites Part A: Applied Science and Manufacturing, 2011, 42 (9), 1247-1262.

[52] Gou, J.; Tang, Y.; Liang, F.; Zhao, Z.; Firsich, D.; Fielding, J.: Carbon nanofiber paper for lightning strike protection of composite materials. Composite Part B: Engineering, 2010, 41 (2), 192-198.

[53] Soykasap, O.; Karakaya, S.; Colakoglu, M.: Simulation of lightning strike damage in carbon nanotube doped CFRP composites. Journal of Reinforced Plastics and Composites, 2016, 35 (6), 504-515.

[54] Cantwell, W. J.; Morton, J.: Comparison of the low and high velocity impact response of CFRP. Composites, 1989, 20 (6), 545-551.

[55] Yashiro, S.; Ogi, K.: High-velocity impact damage on CFRP laminates. In: Silberschmidt, V. V. (ed.): Dynamic deformation, damage and fracture in composite materials and structures. Woodhead, Amsterdam, 2016.

[56] Bouvet, C.; Rivallant, S.: Damage tolerance of composite structures under low-velocity impact. In: Silberschmidt, V. V. (ed.): Dynamic deformation, damage and fracture in composite materials and structures. Woodhead, Amsterdam, 2016.

[57] Minak, G.; Fotouhui, M.; Ahmadi, M.: Low-velocity impact on laminates. In: Silberschmidt, V. V. (ed.): Dynamic deformation, damage and fracture in composite materials and structures. Woodhead, Amsterdam, 2016.

[58] Wagner, H.; Drechsler, K.; Bansemir, H.: Impactverhalten unterschiedlicher FVW-Bauweisen und Fertigungstechniken. Deutscher Luft- und Raumfahrtkongress, Aachen, 08.-10.09.2009.

[59] Cartié, D. D. R.; Irving, P. E.: Effect of resin and fibre properties on impact and compression after impact performance of CFRP. Composites Part A: Applied Science and Manufacturing, 2002, 33 (4), 483-493.

[60] Abrate, S.: Damage in laminates from low-velocity impacts. In: Silberschmidt, V. V. (ed.): Dynamic deformation, damage and fracture in composite materials and structures. Woodhead, Amsterdam, 2016.

[61] Schoeppner, G. A.; Abrate, S.: Delamination threshold loads for low velocity impact on composite laminates. Composites Part A: Applied Science and Manufacturing, 2000, 31 (9), 903-915.

[62] Davies, G. A. O.; Olsson, R.: Impact on composite structures. The Aeronautical Journal, 2004, 108 (1089), 541-563.

[63] Heimbs, S.; Heller, S.; Middendorf, P.; Hähnel, F.; Weiße, J.: Low velocity impact on CFRP plates with compressive preload: Test and modelling. International Journal of Impact Engineering, 2009, 36 (10-11), 1182-1193.

[64] Stavropoulos, C. D.; Papanicolaou, G. C.: Effect of thickness on the compressive performance of ballistically impacted carbon fibre reinforced plastic (CFRP) laminates. Journal of Materials Science, 1997, 32 (4), 931-936.

[65] Tong, L.; Mouritz, A. P.; Bannister, M. K.: 3d fibre reinforced polymer composites. 1st edition, Elsevier, Amsterdam, 2002.

[66] Gilliot, A.: Matrix influence on the impact tolerance of carbon composites made of non-crimp fabric. Dissertation, Magdeburg, DLR-Forschungsberichte, 2010-03, 2009.

[67] Domun, N.; Hadavinia, H.; Zhang, T.; Sainsbury, T.; Liaghat, G. H.; Vahid, S.: Improving the fracture toughness and the strength of epoxy using nanomaterials - A review of the current status. Nanoscale, 2015, 7, 10294-10329.

[68] Borowski, E.; Soliman, E.; Kandil, U. F.; Taha, M. R.: Interlaminar fracture toughness of CFRP laminates incorporating multi-walled carbon nanotubes. Polymers, 2015, 7, 1020-1045.

[69] Partridge, I. K.; Cartié, D. D. R.: Delamination resistant laminates by z-fiber pinning: Part I manufacture and fracture performance. Composites Part A: Applied Science and Manufacturing, 2005, 36 (1), 55-64.

[70] Knaupp, M.; Scharr, G.: Manufacturing process and performance of dry carbon fabrics reinforced with rectangular and circular z-pins. Journal of Composite Materials, 2014, 48 (17), 2163-2172.

[71] Choi, I. H.; Ahn, S. M.; Yeom, C. H.; Hwang, I. H.; Lee, D. S.: Manufacturing of z-pinned composite laminates. 17th International Conference on Composite Materials, Edinburgh, 27.-31.07.2009.

[72] Rezai, A.; Cartié, D. D. R.; Partridge, I.; Irving, P.; Ashton, T.; Negre, P.; Langer, J.: Interlaminar damage resistance of z-fiber reinforced structural CFRP. 13th International Conference on Composite Materials, Beijing, 25.-29.06.2001.

[73] Childress, J.; Freitas, G.: Z-direction pinning of composite laminates for increased survivability. Aerospace Design Conference, Irvine, 03.-06.02.1992.

[74] Freitas, G.; Magee, C.; Dardzinski, P.; Fusco, T.: Fiber insertion process for improved damage tolerance in aircraft laminates. Journal of Advanced Materials, 1994, 25, 36-43.

[75] Liu, H.-Y.; Li, X.; Gu, B.; Mai, Y.-W.; Bai, S.-L.: Fatigue performance of z-pin reinforced delamination. 17th International Conference on Composite Materials, Edinburgh, 27.-31.07.2009.

[76] Mouritz, A. P.; Leong, K. H.; Herszberg, I.: A review of the effect of stitching on the in-plane mechanical properties of fibre-reinforced polymer composites. Composites Part A: Applied Science and Manufacturing, 1997, 28 (12), 979-991.

[77] Chang, P.; Mouritz, A. P.; Cox, B. N.: Properties and failure mechanisms of z-pinned laminates in monotonic and cyclic tension. Composites Part A: Applied Science and Manufacturing, 2006, 37 (10), 1501-1513.

[78] Schmidt, H.: Experimentelle Charakterisierung und rechnerische Vorhersage der mechanischen Eigenschaften strukturell vernähter Multiaxialgelege-Laminate. Dissertation, Kaiserslautern, IVW Schriftenreihe, 2013, 105.

[79] Ermanni, P.: Composite Technologien. Skript zur ETH-Vorlesung 151-0307-00L. Zürich, 2007.

[80] Hart-Smith, L. J.: Bolted joint analyses for composite structures - Current empirical methods and future scientific prospects. In: Kedward, K. T.; Kim, H. (eds.): Joining and repair of composite structures. ASTM International, West Conshohocken, 2004, 126-160.

[81] Fink, A.; Camanho, P. P.; Andrés, J. M.; Pfeiffer, E.; Obst, A.: Hybrid CFRP/titanium bolted joints: Performance assessment and application to a spacecraft payload adaptor. Composites Science and Technology, 2010, 70 (2), 305-317.

[82] Lopes, J.; Stefaniak, D.; Camanho, P. P.; Freitas, M.; Reis, L.: Fatigue behaviour of CFRP/steel hybrid composites. 10th International Conference on Composites Science and Technology, Lisbon, 02.-04.09.2015.

[83] Fink, A.; Camanho, P. P.: Reinforcement of composite bolted joints by means of local metal hybridization. In: Camanho, P. P.; Tong, L. (eds.): Composite joints and connections: Principles, modelling and testing. Woodhead Publishing, Oxford, 2011, 3-34.

[84] Molitor, P.; Barron, V.; Young, T.: Surface treatment of titanium for adhesive bonding to polymer composites: A review. International Journal of Adhesion and Adhesives, 2001, 21 (2), 129-136.

[85] Lopes, J.; Freitas, M.; Stefaniak, D.; Camanho, P. P.: Inter-laminar shear stress in hybrid CFRP/austenitic steel. Fracture and Structural Integrity, 2015, 31, 67-79.

[86] Bosbach, B.; Liebig, W. V.; Fiedler, B.: Bearing response of fibre metal laminates consisting of GFRP and woven metallic fabrics. 20th International Conference on Composite Materials, Copenhagen, 19.-24.07.2015.

[87] Farley, G. L.; Jones, R. M.: Crushing characteristics of continuous fiber-reinforced composite tubes. Journal of Composite Materials, 1992, 26 (1), 37-50.

[88] Bergmann, T.: Beitrag zur Charakterisierung und Auslegung zugbelasteter Energieabsorberkonzepte mittels experimenteller, analytischer und numerischer Methoden. Dissertation, Kaiserslautern, IVW-Schriftenreihe, 2016, 122.

[89] De Boer, T.: Next generation fibre metal laminates. In: Vlot, A.; Gunnink, J. W. (eds.): Fibre metal laminates. 1st edition, Springer Science and Business Media, 2001.

[90] Voll, N.: Experimentelle Untersuchung, Simulation und Materialmodellierung von edelstahltextilverstärkten Langfaserthermoplasten. Dissertation, Kaiserslautern, IVW-Schriftenreihe, 2010, 95.

[91] Meichsner, A.: Herstellung, Charakterisierung, Modellierungsansätze und Simulation von edelstahltextilverstärktem Polypropylen (ETV-PP) und Langglasfaserthermoplasten mit PP-Matrix (ETV-PP/GF). Dissertation, Kaiserslautern, IVW-Schriftenreihe, 2009, 87.

[92] Schmeer, S.; Steeg, M.; Maier, M.; Mitschang, P.: Metal fibre reinforced composite - Potentialities and tasks. Advanced Composite Letters, 2009, 18 (2), 45-52.

[93] Callens, M. G.; Gorbatikh, L.; Verpoest, I.: Damage development in steel fibre composites with unidirectional and quas-unidirectional woven architectures. 20th International Conference on Composite Materials, Copenhagen, 19.-24.07.2015.

[94] Callens, M. G.; De Cuyper, P.; Gorbatikh, L.; Verpoest, I.: Effect of fibre architecture on the tensile and impact behaviour of ductile stainless steel fibre polypropylene composites. Composite Structures, 2015, 119, 528-533.

[95] Callens, M. G.; Gorbatikh, L.; Verpoest, I.: Ductile steel fibre composites with brittle and ductile matrices. Composites Part A: Applied Science and Manufacturing, 2014, 61, 235-244.

[96] Allaer, K.; De Baere, I.; Lava, P.; Van Paepegem, W.; Degrieck, J.: On the in-plane mechanical properties of stainless steel fibre reinforced ductile composites. Composites Science and Technology, 2014, 100, 34-43.

[97] McBride, A. K.; Turek, S. L.; Zaghi, A. E.; Burke, K. A.: Mechanical behavior of hybrid glass/steel fiber reinforced epoxy composites. Polymers, 2017, 9 (4), 1-16.

[98] Swolfs, Y.; De Cuyper, P.; Callens, M. G.; Verpoest, I.; Gorbatikh, L.: Hybridisation of two ductile materials - Steel fibre and self-reinforced polypropylene composites. Composites Part A: Applied Science and Manufacturing, 2017, 100, 48-54.

[99] Van den Abeele, F.: Impact damage models for steel fibre reinforced composite materials. Dissertation, Gent, 2006.

[100] Ahmed, T. J.: Hybrid composite structures: Multifunctionality through metal fibres. Dissertation, Delft, 2009.

[101] Callens, M. G.: Development of ductile stainless steel fibre composites. Dissertation, Leuven, 2014.

[102] Mosleh, Y.; Clemens, D.; Gorbatikh, L.; Verpoest, I.; van Vuure, A. W.: Penetration impact resistance of novel tough steel fibre-reinforced polymer composites. Journal of reinforced plastics and composites, 2015, 34 (8), 624-635.

[103] Lehmann, B.; Selvarayan, S. K.; Ghomeshi, R.; Gresser, G. T.: Carbon fiber reinforced composite - Toughness and structural integrity enhancement by integrating surface modified steel fibers. Materials Science Forum, 2015, 825, 425-432.

[104] QinetiQ Group: QinetiQ unveils new material to protect aircraft from impacts. Farnborough, 25.07.2016.

[105] Breuer, U. P.; Schmeer, S.; Eberth, U.: Carbon and metal fibre reinforced airframe structures - A new approach to composite multifunctionality. Deutscher Luft- und Raumfahrtkongress, Stuttgart, 10.-12.09.2013.

[106] Swolfs, Y.; Gorbatikh, L.; Verpoest, I.: Fibre hybridisation in polymer composites: A review. Composites Part A: Applied Science and Manufacturing, 2014, 67, 181-200.

[107] Manders, P. W.; Bader, M. G.: The strength of hybrid glass/carbon fibre composites. Journal of Materials Science, 1981, 16 (8), 2233-2245.

[108] Deutsches Kupferinstitut: Werkstoff-Datenblatt CuSn6. Düsseldorf, 2005.

[109] Deutsches Kupferinstitut: Werkstoff-Datenblatt CuZn37. Düsseldorf, 2005.

[110] Aleris: Aerospace aluminum AA5028 AlMgSc. Cleveland, 2015.

[111] Black, J. T.; Kohser, R. A.: Degarmo's materials and processes in manufacturing. 11th edition, John Wiley & Sons, Hoboken, 2012.

[112] Hofmann, H.; Spindler, J.: Verfahren in der Beschichtungs- und Oberflächentechnik. 2nd edition, München, 2004.

[113] Cytec Engineered Materials: Cycom 977-2 Epoxy resin system. Technical data sheet. Tempe, 2012.

[114] DIN EN 10088-3:2014-12: Stainless steels. Part 3: Technical delivery conditions for semi-finished products, bars, rods, wire, sections and bright products of corrosion resisting steels for general purposes.

[115] DIN EN 10025-2:2011-04: Hot rolled products of structural steels. Part 2: Technical delivery conditions for non-alloy structural steels.

[116] Spektralanalytisches Labor: Inspection certificate. 12765/0614/1809. Linkenheim-Hochstetten, 2014.

[117] Spektralanalytisches Labor: Inspection certificate. 12766/0614/1809. Linkenheim-Hochstetten, 2014.

[118] DIN EN 10088-1:2014-12. Stainless steels. Part 1: List of stainless steels.

[119] ASTM B227-15: Standard specification for hard-drawn copper-clad steel wire.

[120] ISO 10119:2002-05. Carbon fibre. Determination of density.

[121] Rude, T. J.; Strait, L. H.; Ruhala, L. A.: Measurement of fibre density by helium pycnometry. Journal of Composite Materials, 2000, 34 (22), 1948-1958.

[122] Motion Studio, version 2.12.02.

[123] Powell, R. G.: Introduction to electric circuits. 1st edition, Arnold, 1995.

[124] Airbus: Airbus material specification. Carbon fibre reinforced epoxy prepreg. Unidirectional tape / 180 °C curing. Standard modulus fibre. AIMS 05-01-001. Blagnac Cedex, 2004.

[125] Tygavac: Nylon non-woven release fabric 60B, 60BR. Chadderton, 2009.

[126] Sheikh-Ahmad, J. Y.: Machining of polymer composites. 1st edition. Springer, New York, 2009.

[127] UHU: Technical data sheet. UHU endfest 300. Bühl.

[128] Adams, D. O.; Adams D. F.: Tabbing guide for composite test specimens. Federal Aviation Administration, Washington, 2002.

[129] Henkel: Loctite Frekote 770-NC. Technical data sheet. Düsseldorf, 2014.

[130] DIN EN 2563:1997-03: Aerospace series. Carbon fibre reinforced plastics. Unidirectional laminates. Determination of the apparent interlaminar shear strength.

[131] DIN EN ISO 527-5:2010-01: Plastics. Determination of tensile properties. Part 5: Test conditions for unidirectional fibre-reinforced plastic composites.

[132] Lackmann, J.; Mertens, H.; Liebich, R.: Beanspruchung stabförmiger Bauteile. In: Grote, K. H.; Feldhusen, J. (eds.): Dubbel. Springer, Berlin, 2011.

[133] DIN EN ISO 527-4:1997-07: Plastics. Determination of tensile properties. Part 4: Test condition for isotropic and orthotropic fibre-reinforced plastic composites.

[134] DIN EN 2379:1995-04: Aerospace series. Fluids for assessment of non-metallic materials.

[135] DIN EN 2489:1995-11: Aerospace series. Fibre reinforced plastics. Determination of the action of test fluids.

[136] AITM 1-0007:2004-12: Airbus test method. Fibre reinforced plastics. Determination of plain, open hole and filled hole tensile strength.

[137] AITM 1-0009:2003-11: Airbus test method. Fibre reinforced plastics. Determination of bearing strength by either pin or bolt bearing configuration.

[138] AITM 1-0066:2013-12: Airbus test method. Fibre reinforced plastics. Determination of pull-through strength of mechanical joints.

[139] AITM 1-0010:2005-10: Airbus test method. Fibre reinforced plastics. Determination of compression strength after impact.

[140] DIN EN ISO 6603-2:2002-04: Plastics. Determination of puncture impact behaviour of rigid plastics. Part 2: Instrumented puncture test.

[141] Gross, D.; Hauger, W.; Schröder, J.; Wall, W. A.: Technische Mechanik 2. Elastostatik. 12th edition, Springer Vieweg, Berlin, 2014.

[142] Böttger-Hiller, F.; Jahn, P.; Trautmann, M.; Lindner, T.; Nickel, D.; Lampke, T.: Electrically conductive carbon-fiber-reinforced plastics (CFRP) with accessible functional layer. Materials Science and Engineering Technology, 2015, 46 (8), 844-851.

[143] GeoDict 2017, service pack 2, rev. 17381.

[144] DIN EN ISO 11357-5:2014-07: Plastics. Differential scanning calorimetry (DSC). Part 5: Determination of characteristic reaction-curve temperatures and times, enthalpy of reaction and degree of conversion.

[145] Ehrenstein, G. W.; Riedel, G.; Trawiel, P.: Thermal analysis of plastics. Theory and praxis. Carl Hanser, München, 2004.

[146] Stark, W.; Jaunich, M.; McHugh, J.: Cure state detection for pre-cured carbon-fibre epoxy prepreg (CFC) using temperature-modulated differential scanning calorimetry (TMDSC). Polymer Testing, 2013, 32, 1261-1272.

[147] ASTM E2039-04: Standard test method for determining and reporting dynamic dielectric properties. *(withdrawn 2009)*

[148] Karcher, M.; Chaloupka, A.; Henning, F.; Schmölzer, S.; Moukhina, E.: Determination of curing kinetics of a two-stage curing epoxy resin for high performance composites. Journal of Plastics Technology, 2016, 2, 80-111.

[149] Smaga, M.: Experimentelle Untersuchung der Mikrostruktur sowie des Verformungs- und Umwandlungsverhaltens zyklisch beanspruchter metastabiler austenitischer Stähle. Dissertation, Kaiserslautern, Werkstoffkundliche Berichte, 15, 2005.

[150] Nebel, T.: Verformungsverhalten und Mikrostruktur zyklisch beanspruchter austentitischer Stähle. Dissertation, Kaiserslautern, Werkstoffkundliche Berichte, 9, 2002.

[151] Callen, H. B.: Thermodynamics and an introduction to thermostatistics. 2nd edition, John Wiley & Sons, New York, 1985.

[152] Becker, H.; Brandis, H.; Küppers, W.: Zur Verfestigung instabil austenitischer nichtrostender Stähle und ihre Auswirkung auf das Umformverhalten von Feinblechen. Thyssen-Edelstahl Technische Berichte, 1986, 12 (1), 35-54.

[153] Olsen, G.; Cohen, M.: Kinetics of strain-induced martensitic nucleation. Metallurgical and Materials Transactions A, 1975, 6 (4), 791-795.

[154] Hecker, S. S.; Stout, M. G.; Staudhammer, K. P.; Smith, J. L.: Effects of strain state and strain rate on deformation-induced transformation in 304 stainless steel: Part I. Magnetic measurements and mechanical behaviour. Metallurgical and Materials Transactions A, 1982, 13 (4), 619-626.

[155] Schoß, V.: Martensitische Umwandlung und Ermüdung austentischer Edelstähle, Gefügeveränderungen und Möglichkeiten der Früherkennung von Ermüdungsschäden. Dissertation, Freiberg, 2001.

[156] Grigorescu, A. C.; Hilgendorff, P.-M.; Zimmermann, M.; Fritzen, C.-P.; Christ, H.-J.: Cyclic deformation behavior of austenitic Cr-Ni-steels in the VHCF regime: part I - Experimental study. International Journal of Fatigue, 2016, 93 (2), 250-260.

[157] Helmut Fischer: Feritscope FMP30. Measurement of the ferrite content in austenitic and duplex steel. Sindelfingen, 2014.

Student theses

Within the scope of this work, the following student theses have been edited and supervised.

[158] Netz, J.: Simulative Analyse von metallfaserverstärktem FKV. Projektarbeit, Kaiserslautern, IVW-Bericht, 2013, 13-026.

[159] Reisdörfer, C.: Charakterisierung und Modifikation der Oberflächen von Endlosfasern aus Stahl. Studienarbeit, Kaiserslautern, IVV-Bericht, 2015, 15-003.

[160] Oswald, F.: Prozessoptimierung zur Herstellung von stahlfaserverstärktem CFK. Studienarbeit, Kaiserslautern, IVW-Bericht, 2015, 15-034.

[161] Seifert, C.: Mechanische und elektrische Eigenschaften von Metall-FKV-Hybridlaminaten: Stand der Technik. Studienarbeit, Kaiserslautern, IVW-Bericht, 2016, 16-037.

Publication and conferences

Contents of this work have been published in the books, journals and conference proceedings listed below.

[162] Hannemann, B.; Breuer, U. P.; Schmeer, S.; Backe, S.; Balle, F.: Metal and carbon united: Electrical function integration. In: Breuer, U. P. (ed.): Commercial aircraft composite technology. 1st edition, Springer International Publishing, 2016, 220-234.

[163] Hannemann, B.; Backe, S.; Schmeer, S.; Balle, F.; Breuer, U. P.: Metal fibre incorporation in CFRP for improved electrical conductivity. Materials Science and Engineering Technology, 2016, 47 (11), 1015-1023.

[164] Hannemann, B.; Backe, S.; Schmeer, S.; Balle, F.; Breuer, U. P.; Schuster, J.: Hybridisation of CFRP by use of continuous metal fibres (MCFRP) for damage tolerant and electrically conductive lightweight structures. Composite Structures, 2017, 172, 374-382.

[165] Hannemann, B.; Schmeer, S.; Breuer, U. P.: Entwicklung multifunktionaler Faser-Hybrid-Werkstoffe für Rumpfanwendungen in der Luftfahrt. Carbon Composites Magazin, 2017, 2, 41-42.

[166] Utzig, L.; Karch, C.; Rehra, J.; Hannemann, B.; Schmeer, S.: Modelling and simulation of effective strength of hybrid polymer composites reinforced by carbon and steel fibres. Journal of Materials Science, 2017, 53 (1), 667-677.

[167] Schmeer, S.; Hannemann, B.; Breuer, U. P.; Backe, S.; Balle, F.: Steel fiber reinforced CFRP: Challenges and potentials of a new hybrid material. 25 Years IVW Anniversary Colloquium, Kaiserslautern, 11.-12.06.2015.

[168] Hannemann, B.; Backe, S.; Schmeer, S.; Balle, F.; Breuer, U. P.: New multifunctional hybrid polymer composites reinforced by carbon and steel fibres. 20th International Conference on Composite Materials, Copenhagen, 19.-24.07.2015.

[169] Breuer, U. P.; Schmeer, S.; Hannemann, B.: New multifunctional composites for airframe structures - Carbon and metal united. 7th Asia-Europe Symposium on Processing and Properties of Reinforced Polymers, Madrid, 04.-06.02.2015.

[170] Backe, S.; Hannemann, B.: Multifunctionality by embedded steel fibres for improved aircraft composites. Young Researchers Symposium, Kaiserslautern, 14.-15.04.2016.

[171] Hannemann, B.; Backe, S.; Schmeer, S.; Balle, F.; Breuer, U. P.: Multifunctional metal-carbon-fibre composites for damage tolerant and highly conductive lightweight structures. 2nd International Conference Euro Hybrid Materials and Structures, Kaiserslautern, 20.-21.04.2016.

[172] Hannemann, B.; Backe, S.; Schmeer, S.; Balle, F.; Breuer, U. P.: Improved mechanical and electrical properties of CFRP multiaxial laminates by embedded metal fibres. 17th European Conference on Composite Materials, München, 26.-30.06.2016.

[173] Breuer, U. P.; Hannemann, B.; Schmeer, S.; Balle, F.; Backe, S.: Metall und Carbon - Ein neuer Multifunktionswerkstoff für Primärstrukturen entsteht. Deutscher Luft- und Raumfahrtkongress, Braunschweig, 13.-15.09.2016.

[174] Hannemann, B.; Backe, S.; Schmeer, S.; Balle, F.; Breuer, U. P.: Intrinsic hybridisation of CFRP by incorporation of endless metal fibres for damage tolerant and highly conductive lightweight structures. 25th International Conference on Processing and Fabrication of Advanced Materials, Auckland, 22.-25.01.2017.

[175] Hannemann, B.; Backe, S.; Schmeer, S.; Balle, F.; Breuer, U. P.: Hybridisation of CFRP with continuous metal fibres for damage tolerant and highly conductive lightweight structures. 21st International Conference on Composite Materials, Xi'an, 20.-25.08.2017.

[176] Backe, S.; Hannemann, B.; Balle, F.; Schmeer, S.; Breuer, U. P.: Fatigue behaviour of multifunctional CFRP laminates and intrinsic capabilities for damage monitoring. 21st International Conference on Composite Materials, Xi'an, 20.-25.08.2017.

[177] Bauer, C.; Hannemann, B.; Glatt, E.; Schmeer, S.: Micromechanical simulation of a multifunctional hybrid composite with continuous steel and carbon fibre reinforcement. 17th Automotive Composites Conference and Exhibition, Detroit, 06.-08.09.2017.

[178] Hausmann, J.; Hannemann, B.; Schmeer, S.; Breuer, U. P.: Electrically conductive and damage tolerant fibre-hybrid-composite developed as skin material in aeronautics. European Congress and Exhibition on Advanced Materials and Processes, Thessaloniki, 17.-22.09.2017.

Symposia

Contents of this work have been discussed at the symposia listed below.

[179] Hannemann, B.; Schmeer, S.; Maier, M.: Potentialstudie zu metallfaserverstärktem CFK mittels analytischen und numerischen Methoden. PfalzMetall-Tag, Neustadt a. d. W., 14.06.2012.

[180] Backe, S.; Balle, F.; Eifler, D.; Hannemann, B.; Schmeer, S.; Breuer, U. P.: Multifunktionale Metall-C-Faser-Kunststoff-Verbunde (MCFK): Konzepte und Potentiale. Deutsche Gesellschaft für Materialkunde, Fachausschusssitzung “Hybride Werkstoffe und Strukturen”, Attendorn, 23.10.2014.

[181] Backe, S.; Balle, F.; Hannemann, B.; Schmeer, S.; Breuer, U. P.: Elektrische und mechanische Eigenschaften von UD-Laminaten mit Metall- und C-Faserverstärkung. Deutsche Gesellschaft für Materialkunde, Fachausschusssitzung “Hybride Werkstoffe und Strukturen”, Braunschweig, 02.12.2015.

[182] Hannemann, B.; Rehra, J.; Backe, S.; Schmeer, S.; Balle, F.; Breuer, U. P.: Verbesserung der mechanischen und elektrischen Eigenschaften von CFK durch zusätzliche Stahlfaserverstärkung. Carbon Composites, Thementag „Funktionsintegration in der Praxis“, Leipzig, 27.09.2016.

[183] Hannemann, B.; Rehra, J.; Backe, S.; Schmeer, S.; Balle, F.; Breuer, U. P.: Experimentelle Untersuchungen zur Schadenstoleranz von multiaxial metallfaserverstärktem CFK. Deutsche Gesellschaft für Materialkunde, Fachausschusssitzung “Hybride Werkstoffe und Strukturen”, Darmstadt, 29.09.2016.

[184] Rehra, J.: Funktionsintegration mittels metallischen Endlosfasern - Beschreibung des Materialverhaltens. Deutsche Gesellschaft für Materialkunde, Fachausschusssitzung “Hybride Werkstoffe und Strukturen”, Clausthal-Zellerfeld, 15.-16.05.2017.

[185] Bauer, C.; Hannemann, B.: Simulation of steel and carbon fiber reinforced composites. Math2Market, GeoDict User Meeting, Kaiserslautern, 26.-27.09.2017.